

SEMICLASSICAL TREATMENT OF INTERFERENCE PHENOMENA IN BOSONIC QUANTUM MANY-BODY SYSTEMS



Dissertation

zur Erlangung des Doktorgrades
der Naturwissenschaften (Dr. rer. nat.)
der Fakultät für Physik
der Universität Regensburg

vorgelegt von

Josef Rammensee geb. Michl

aus

Stamsried

März 2019

Promotionsgesuch eingereicht am: 04.10.2018

Die Arbeit wurde angeleitet von: Prof. Dr. Klaus Richter

Prüfungsausschuss:

Vorsitzender:	Prof. Dr. Jascha Repp
Erstgutachter:	Prof. Dr. Klaus Richter
Zweitgutachter:	Prof. Dr. Gregor Tanner
Weiterer Prüfer:	Prof. Dr. Christoph Lehner

Termin Promotionskolloquium: 20.05.2019

Contents

1	Introduction	5
2	Classical Hamiltonian dynamics	15
2.1	Hamiltonian systems	15
2.2	Linear stability of Hamiltonian systems	18
2.2.1	The stability matrix	18
2.2.2	Lyapunov exponents and the decomposition of the stability matrix	19
2.2.3	Pairing rule of the Lyapunov exponents	21
2.2.4	Constants of motion and their relation to neutral directions	23
2.3	Properties of chaotic Hamiltonian dynamics	25
2.3.1	Mixing and ergodicity	25
2.3.2	Hyperbolicity	27
3	Semiclassical treatment of bosonic quantum many-body systems described by the Bose-Hubbard model	29
3.1	Bosonic Fock space and its representations	30
3.1.1	Bosonic Fock states	30
3.1.2	Creation and annihilation operators	31
3.1.3	Quadrature operators and quadrature states	32
3.1.4	Coherent states	37
3.2	Bose-Hubbard models	39
3.3	The semiclassical approximation for the propagator	40
3.3.1	The time-evolution operator	40
3.3.2	Feynman path integral representation of the propagator	42
3.3.3	The semiclassical approximation of the propagator	46
4	Semiclassical analysis of out-of-time-order correlators (OTOCs)	51
4.1	The OTOCs and their expected behaviour for short times	51
4.1.1	Wigner-Weyl transformations	52
4.1.2	Expected behavior of OTOCs	54
4.2	Semiclassical treatment of OTOCs for bosonic many-body systems	57
4.2.1	The trajectory-based semiclassical representation of the OTOC . .	58
4.2.2	Identification of the main contributions to the OTOC	60
4.2.3	Geometry of encounters in phase space	62
4.2.4	Density, amplitudes and action difference of diagrams with encounters	66

4.3	Calculation of diagrammatic contributions	67
4.3.1	Contributions of four-leg diagrams	67
4.3.2	Contributions of two-leg diagrams	70
4.3.3	Contributions of zero-leg diagrams	72
4.4	Summary	74
4.4.1	Pre-Ehrenfest behaviour	74
4.4.2	Post-Ehrenfest behaviour	74
4.5	Further remarks and implications	76
4.5.1	Generalization of the methods to OTOCs with more generic operators	76
4.5.2	Generalization towards a Lyapunov spectrum and general hyperbolicity	78
4.5.3	Non-ergodic many-body dynamics	81
4.5.4	Time-reversal invariance and higher-order quantum corrections	81
4.5.5	Small-h limit and single-particle systems	82
5	Al'tshuler-Aronov-Spivak oscillations for interacting bosonic atoms	85
5.1	The Aharonov-Bohm ring with cold atoms	86
5.1.1	Bose-Hubbard Hamiltonian	86
5.1.2	Mean-field equations	90
5.1.3	Reflection and Transmission	91
5.1.4	Green's function approach and the role of disorder	93
5.2	Numerical predictions for Al'tshuler-Aronov-Spivak (AAS) oscillations	98
5.2.1	The noninteracting case	98
5.2.2	Inversion of peaks of the AAS oscillations for interacting cold atoms	101
5.2.3	Truncated Wigner approximation and its relation to the mean-field approach	102
6	Diagrammatic approach towards Al'tshuler-Aronov-Spivak oscillations	107
6.1	The noninteracting case	108
6.1.1	Basic resummation of diagrams	108
6.1.2	Symmetry arguments to derive other resummed diagrams	110
6.1.3	Further resummed diagrams	111
6.1.4	Full reflection and transmission amplitude in the noninteracting case	113
6.2	The interacting case	115
6.2.1	Perturbative treatment of interaction	115
6.2.2	Effective reflection and transmission amplitudes in linear order in the interaction strength	120
6.2.3	Disorder averaged reflection and transmission probabilities in linear order in the interaction strength	121
6.2.4	Discussion of the results	124
7	Summary and outlook	127

Appendices	133
A.1 Evaluation of matrix elements of the Bose-Hubbard Hamiltonian	133
A.2 Stationary phase approximation applied to the Feynman path integral . .	137
A.3 Calculation of the action difference	144
A.4 Calculation of encounter-related integrals	147
A.4.1 Frequently used integrals in the calculations of encounters	147
A.4.2 Encounter integral of the four-leg diagram	148
A.4.3 Encounter integral of the two-leg diagram with the encounter at the beginning	150
A.4.4 Encounter integral of the two-leg diagram with the encounter at the end	153
A.4.5 Encounter integral of the zero-leg diagram	154
A.5 Scattering matrix elements for a discretized Y-junction	156
A.6 List of resummed diagrams	158
A.7 Numerical averaging of reflection and transmission probabilities	159
List of publications	163
Notation	165
Bibliography	167
Acknowledgments	177
Index	179

1 Introduction

Wave interference and the semiclassical theory

The formation of waves is an omnipresent feature found in nature, taking place in a variety of scenarios and length scales. Waves in water are observable in any amount of the liquid, from glasses of water up to the ocean. The humans hearing relies on capturing acoustic waves with the ears. Applications of electromagnetic waves are found in numerous fields, such as in communication, in imaging, and in the manipulation of matter. Finally, one of the fundamental axioms underlying the quantum theory is that of particle-wave duality, *i.e.* particles behave as waves and waves admit a description in terms of particles.

For the study of waves one in general employs a suitable theory describing in an efficient way their formation and propagation in the system of interest. For instance, we have Maxwell equations for classical electromagnetic waves or the Schrödinger equation for non-relativistic quantum mechanical systems. They all have in common that they comprise the interference of waves, leading to a lot of interesting phenomena such as the formation of standing stationary solutions. Within the quantum theory, such solutions, for instance, are what yield orbitals of an atom.

As one might imagine, using the wave equations becomes more cumbersome and even impossible if the scales of the system, such as its diameter, are many orders of magnitude larger than the wavelength or other scales provided by the wave. This raises the need for effective theories, and their derivation relies on an analysis of the wave equation in a formal limit of “ $\hbar_{\text{eff}} \rightarrow 0$ ”, where an effective Planck’s constant \hbar_{eff} is used as a small parameter comprising the relation of scales between the wave and the system. In case of a single-particle wave described by the Schrödinger equation, this parameter is related to Planck’s constant, $\hbar_{\text{eff}} \propto \hbar$, and the according limit is found to be the classical limit governed by the Hamilton’s equations of motion. The theory responsible for drawing the connection between classical and quantum physics is known as semiclassical theory [1, 2], and not only explains the emergence of classical dynamics from the quantum description, but also provides means to treat wave interference in quantum systems in the semiclassical limit “ $\hbar_{\text{eff}} \ll 1$ ”, for which a purely classical description is not yet sufficient.

The semiclassical theory relates the description of the quantum system to the dynamics found in its corresponding classical limit. Its basic method is to take classical paths, *i.e.* solutions of the Hamilton’s equations of motion, and associate them with a weighting amplitude and with a phase accumulated along. Interference phenomena as

a consequence of the quantum nature of the systems are in the semiclassical formalism captured through the interference of contributions of multiple paths sharing the same boundary conditions. This way, the semiclassical theory goes beyond the purely classical description of the system, and even more, the picture of “interfering classical paths” provides valuable insight into the interference mechanism leading to the observed phenomena.

For instance, a typical system where the assumptions of classical physics are brought to its limits are mesoscopic systems, where the length and energy scales are large compared to atomic scales, but the coherence length is small compared to the system size. This makes even a numerical treatment of the full-fledged quantum-mechanical problem rather unfavorable, while a purely classical treatment is not able to capture the interference of the still coherent particle wave. The use of powerful semiclassical theories for these systems allowed to successfully explain effects such as weak localization [3], where, in comparison to the classically expected value, the interference contribution of a path with its time-reversed partner leads to an enhancement of back-reflection (and therefore to an enhanced resistance) in the transport of particles through disordered media or mesoscopic phase-coherent conductors. Due to the conservation of current, this enhancement is accompanied by a reduction of transmission (or conductivity), which could semiclassically be attributed to the interference contribution of trajectories undergoing self-crossings. The reduction of transmission is then explained by trajectory pairs, which traverse the loop formed by the self-crossing in time-reversed directions [4].

Yet another prominent effect in mesoscopic systems is found in the electronic transport through a ring penetrated by a magnetic field [5]. Within the semiclassical picture, the magnetic field contributes an additional phase accumulated along the paths – an effect known as Aharonov-Bohm effect [6]. It is observable through oscillations of the conductivity as a function of the flux encircled by the ring, which again within the semiclassical theory can be quantitatively understood through the interference of paths. If the ring is additionally subject to a disorder potential, which is weak and smooth enough to avoid wave localization, the Aharonov-Bohm oscillations turn into Al’tshuler-Aronov-Spivak oscillations [7] seen in the disorder-averaged transmission as a function of the encircled flux. Interestingly, these oscillations show half the period of the conventional Aharonov-Bohm oscillations. Its semiclassical explanation, which we will also re-encounter for a different setup within this thesis, yields a similar mechanism as the one underlying weak localization: the interference of time-reversed partners.

Bosonic quantum many-body systems and their mean-field description

Like for mesoscopic systems, the question of effective theories also arises in the context of quantum systems containing many interacting particles. For bosonic quantum many-body systems, which are the focus of this thesis, the still growing interest emerged from the first realization of Bose-Einstein condensates (BECs) with rubidium (^{87}Rb) [8] and sodium atoms (^{23}Na) [9] using magnetic trapping potentials and laser cooling techniques. Since then, numerous experimental techniques have been developed to provide devices to explore the properties of BECs, see for instance Refs. [10, 11] for a review.

Potential landscapes can be generated using laser fields whose frequency is slightly detuned to an internal transition frequency of the atoms. Through interference of multiple high-intensity laser fields in opposite directions one can create standing waves, thereby forming optical lattices in three, two, and one dimension [12–14], or continuous ring-shaped structures [15]. Furthermore, rapidly moving laser beams allow the creation of optical billiards [16] or ring-shaped lattices [17]. Transport experiments are also feasible through so-called atom lasers [18, 19], where through a controlled and coherent outcoupling process, a beam of atoms at well-defined energy and particle current density can be released from a BEC into an optical waveguide. The generated structures have in common that they are free of defects and allow a high experimental accessibility of its parameters. If instead a highly controllable randomized disorder potential is needed, this can be achieved, for instance, by a laser field passing through a diffusive plate to produce an optical speckle field [20]. Finally, one can create synthetic gauge fields [21, 22], which play a similar role for the uncharged atoms than magnetic fields for electrons.

Apart from the above mentioned properties, possibly one of the most intriguing features of cold atoms is that the strength of an effective particle-particle interaction is highly tunable through means of Feshbach resonances (see Ref. [23] for a review): an external magnetic field changes the internal structure through the (anomalous) Zeeman effect such that in the scattering of two bosonic particles an excited molecular binding state comes in resonance. This significantly changes the scattering length, and can be understood as an effective interaction. While this is known as magnetic Feshbach resonance, the optical Feshbach resonance relies on an optical transition to an excited rotational-vibrational level of the molecular state. In any case, near the resonance, the strength of the effective interaction significantly grows but can also undergo a sign change when tuning the field strength near the resonance condition.

As one of the many means to theoretically treat the quantum many-body problem, effective theories are used, which replace the interacting many-body problem by an effective wave description of the system. For bosonic systems, such an effective theory is found within the Gross-Pitaevskii equation [24, 25], obtained by the assumptions that relevant single-particle states are occupied by a large number of bosons. This allows to substitute the Heisenberg picture of bosonic quantum field operators in second quantization by scalar complex field, whose squared modulus is interpreted as the associated occupation of the single-particle state – an approximation also known as mean-field approach. The dynamics is then described by an effective wave equation similar to the single-particle Schrödinger equation, however with a term nonlinear in the matter wave as a consequence of interaction.

The validity of the mean-field approach is in the limit of a large number N of particles, “ $N \rightarrow \infty$ ”, while the energy comprised in interaction amongst particles remains small compared to the kinetic energy. Such a description is already enough to explain many interference phenomena also known from electronic systems, such as the experimental observation of coherent back-scattering for matter waves of noninteracting bosons [26], and Anderson localization [20, 27]. Even more, the possibility to have a weak particle-particle interaction allows to raise the interesting question how interaction influences

these well-known effects. Due to the resemblance of an effective single-particle theory, one can again employ semiclassical techniques in the formal limit “ $\hbar \rightarrow 0$ ” to find and investigate the solution of the mean-field problem, provided the same assumptions as in the single-particle case are met. This led, for instance, to the prediction of an inversion of the peak in the coherent back-scattering probability due to weak particle-particle interaction [28], while in the transport of cold bosonic atoms through chaotic cavities the weak localization peak shows an interaction-based reduction [29].

A part of this thesis makes a new addition to this list by studying Al’tshuler-Aronov-Spivak oscillations in the coherent transport of interacting bosons through a ring with disorder, penetrated by a synthetic gauge field for bosons. There, numerical studies by R. Chrétien *et al.* [30] indicate an inversion of the oscillations when the interaction strength is increased, and it is one of the aims of this thesis to use semiclassical techniques in the formal limit “ $\hbar \rightarrow 0$ ” to develop an understanding of this behaviour in terms of interfering scattering paths.

For larger interaction strength, the nonlinear nature of the mean-field description leads to instabilities of the solutions of the mean-field equations [29, 31, 32]. The situation becomes then comparable to single-particle quantum systems in a scenario, where the quantum dynamical behaviour does not follow effectively a single classical trajectory any more. One has to take into account contributions arising from other classical trajectories, or, in the context of bosonic quantum many-body systems, of other solutions of the mean-field or Gross-Pitaevskii equation. This thinking ultimately led to the development of a semiclassical theory, here taking the inverse number of particles as effective Planck’s constant, $\hbar_{\text{eff}} = 1/N$ [33, 34]. Within this theory the mean-field equations emerge as Hamilton’s equations of motion of a Hamilton function found as the complementary classical “ $\hbar_{\text{eff}} = 1/N \rightarrow 0$ ” limit of the bosonic quantum many-body Hamiltonian. Remarkably, since this semiclassical theory associates the wave solutions of the mean-field equations with an additional phase accumulated along the solution, we can have interference phenomena happen both at the mean-field level to produce the distinct solutions, and at the semiclassical level through the interference of contributions of multiple mean-field solutions. The truncated Wigner method, which is commonly used to obtain results beyond the Gross-Pitaevskii description, is re-derived in this semiclassical theory as diagonal contribution, which is the semiclassical contribution arising from many-body interference of mean-field solutions with themselves [33, 35, 36].

Thinking of the mean-field equations as classical equations in the limit “ $1/N \rightarrow 0$ ” quite naturally raises the question whether the unstable behaviour seen in the mean-field dynamics for stronger interactions can be related to what is known from studies of unstable dynamics in chaotic classical systems. Indeed, once the kinetic energy of the individual particles becomes comparable to the energy stored in the interaction, signatures of chaotic dynamics in the mean-field description are seen [37–39]. Quite generally in the study of interacting many-body systems, not limited to just bosonic ones, the observation of similar features as those that are known from single-particle systems with a classical chaotic limit, known as quantum chaos [1], led to an increased interest into this field in the recent years, and ultimately to the emergence of the field

“many-body quantum chaos”.

Out-of-time-order correlators as probes of many-body quantum chaos

A particular attention to many-body quantum chaos started with the proposal of Kitaev [40] and related works [41–43] that addresses the question of what is the mechanism behind the “scrambling” of quantum information, the spreading of initially localized information across the many degrees of freedom of an interacting many-body system. It is conjectured that chaotic dynamics in a suitable (and in some models yet to understand) classical limit of the quantum many-body system produces the unstable dynamics which lead to a fast distribution of information across the system. A central object which aims at probing this many-body quantum-to-classical correspondence is the so-called *out-of-time-order correlator* (OTOC) [43–45]

$$F(t) = \langle \Psi | \hat{V}^\dagger(t) \hat{W}^\dagger(0) \hat{V}(t) \hat{W}(0) | \Psi \rangle , \quad (1.1)$$

for which several experimental protocols [46–48] and first experiments [49, 50] are available. Its name originates from the unusual ordering of the involved operators in time.

An interpretation of the OTOC $F(t)$ is possible by explicitly writing the Heisenberg picture of the operator $\hat{V}(t) = e^{(i/\hbar)\hat{H}t}\hat{V}e^{-(i/\hbar)\hat{H}t}$ and understanding $F(t)$ as the overlap of two states [51]: one of the states takes the initial state $|\Psi\rangle$ and applies \hat{W} , then evolves the obtained state forward in time with $e^{-(i/\hbar)\hat{H}t}$, applies \hat{V} , and evolves back in time with $e^{(i/\hbar)\hat{H}t}$. The second state applies \hat{W} at the end of this sequence instead of the beginning. Within this description the OTOC bears similarities to the Loschmidt echo [52], however here with twice the number of forward and backward evolutions in time. Even if \hat{V} and \hat{W} are taken as local, commuting operators with an initial overlap $F(t=0) = 1$, when time evolves, $\hat{V}(t)$ becomes a non-local operator, and the growing complexity of $\hat{V}(t)$ encodes the unstable dynamics within the quantum system. As a consequence, \hat{W} and $\hat{V}(t)$ cease to commute, and consequently $F(t)$ decreases in time. Since the rate of decrease relates to the growing complexity of $\hat{V}(t)$, this makes $F(t)$ a quantum probe for chaos in the classical limit.

This last conclusion, the connection to the dynamics in the classical limit of the quantum system, can even more easily be seen with a closely related object, which is also dubbed out-of-time-order correlator. It is the expectation value of the squared commutator [43, 44],

$$C(t) = \left\langle \left[\hat{V}(t), \hat{W}(0) \right]^\dagger \left[\hat{V}(t), \hat{W}(0) \right] \right\rangle , \quad (1.2)$$

in which $F(t)$ appears as one of the terms when carrying out the products of operators. Here, we can apply the quantum-to-classical correspondence principle which replaces the commutator of the two operators by the Poisson bracket of their classical analogues. The evaluation of the latter then results in an intuition for the dynamical behaviour and the role of OTOCs as a many-body quantum analogue of classical measures for instability

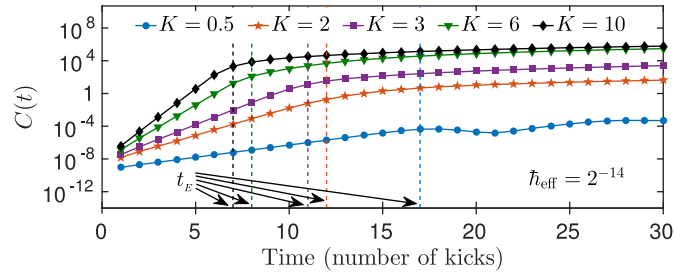


Figure 1.1: Dynamical behaviour of the OTOC $C(t) = -\langle [\hat{p}(t), \hat{p}]^2 \rangle$ for the one-dimensional kicked rotor for different kicking strengths K . The average is performed over a Gaussian wave packet with initial momentum $p_0 = 0$. (Figure adapted from Ref. [53])

of chaotic many-body dynamics. For instance, if the operators are the momentum and the position operator for a single particle, $\hat{W} = \hat{p}_i$, $\hat{V} = \hat{q}_j$, we have [43, 44, 47]

$$C(t) = \langle [\hat{p}_i, \hat{q}_j(t)][\hat{q}_j(t), \hat{p}_i] \rangle \approx -(i\hbar)^2 \langle \{p_i, q_j(t)\}^2 \rangle_{\text{cl}} = \hbar^2 \left\langle \left(\frac{\partial q_j^{(f)}(t)}{\partial q_i^{(i)}} \right)^2 \right\rangle_{\text{cl}}, \quad (1.3)$$

where $\langle \cdot \rangle_{\text{cl}}$ denotes a classical phase space average related to the quantum expectation value in Eq. (1.2). Here, the evaluation of the Poisson bracket directly results in an element of the so-called stability matrix. The stability matrix describes the variation of a trajectory's final point upon changes of its initial condition, and can be used to distinguish regular from unstable dynamics. If the motion takes place in an integrable system, the growth of the elements of the stability matrix is at most polynomial. Contrarily, in chaotic systems, the motion is hyperbolic and leads to an exponential separation of trajectories. This is observed in an exponential growth of the elements of the stability matrix, whose rate defines the classical Lyapunov exponent λ . Consequently, the growth rate of the OTOC is given by twice of λ ,

$$C(t) \approx \hbar^2 e^{2\lambda t}. \quad (1.4)$$

Indeed, an exponential growth of the OTOC has been observed in numerical studies of single particle systems [53], see also figure 1.1 at times $t \leq t_E$. Hence, the OTOCs $C(t)$ or $F(t)$ allow, as quantum objects, an immediate access to classical measures of chaos in the classical limit of the quantum system.

The OTOC is studied both for single particle [53] and many-body systems, for instance in analytical works for Sachdev-Ye-Kitaev models [54, 55] or through random matrix theory [56–58] where $\lambda \rightarrow \infty$. Attempts to identify the many-body Lyapunov exponent from Eq. (1.2) by numerical means still remains a challenge [59–61]. This difficulty can be attributed to quantum mechanical unitarity, which prevents the OTOC $C(t)$

from performing an unbounded classical growth as predicted by Eq. (1.4), but rather enforces an eventual bound. This is indeed seen in numerical studies of $C(t)$ [53, 59], where the OTOC is found to saturate, see Fig. 1.1 at times $t \geq t_E$. Quite interestingly, the characteristic time scale at which the exponential growth ceases and the saturation commences is found to be a time scale known as Ehrenfest time t_E [62, 63], and is dubbed scrambling time [43, 64] in the many-body context. The Ehrenfest time t_E is the time needed for details of the order of the quantum mechanical wavelength to grow under classical dynamics to a typical system size. This time separates the classical regime, where the initial quantum evolution essentially follows the classical motion, from the quantum mechanical one, where interference effects have to be taken into account. Quite generally for quantum chaotic systems, this time scale for the classical-to-quantum crossover can be formalized by $t_E \propto (1/\lambda) \log(1/\hbar_{\text{eff}})$ involving the classical Lyapunov exponent λ and the effective Planck's constant \hbar_{eff} , whose definition, as we have seen, can denote complementary classical limits: for a fixed, finite particle number N , we have $\hbar_{\text{eff}} \sim \hbar$ and λ is the characteristic Lyapunov exponent of the limiting classical particle dynamics. For many-body systems with a large number N of particles, we discover the mean-field description as classical limit with “ $\hbar_{\text{eff}} \simeq 1/N \rightarrow 0$ ”. Here, the Lyapunov exponent λ characterizes the instability of the corresponding nonlinear mean-field solutions.

Due to the appearance of the Ehrenfest time t_E , the saturation of OTOCs has been attributed to the onset of quantum many-body interference [41, 53, 54, 61], without so far identifying its underlying dynamical interference mechanism.

The Moyal expansion [55, 57] of commutators in powers of \hbar_{eff} , which is implicitly used to find Eq. (1.3), is not able to go beyond the Ehrenfest time, and can therefore not capture the interference-based saturation of OTOCs beyond t_E . To adequately describe the post-Ehrenfest behaviour of OTOCs, other techniques are needed. Such are available through the semiclassical theory, and have been originally developed for single particle [65–72], and recently also adapted to many-body systems [34, 73–77].

A major part of this thesis aims at extending these approaches to develop a semiclassical theory for OTOCs and provide a unifying understanding of both the pre-Ehrenfest exponential growth and the interference mechanism leading to the post-Ehrenfest saturation of OTOCs. Moreover, it explicitly identifies the Lyapunov exponent and explains its emergence, as well as the role of the Ehrenfest time within this theory. Our focus here lies on bosonic large- N systems, for which the classical “ $N \rightarrow \infty$ ” limit can be defined, and for which the basis for a semiclassical theory, the semiclassical approximation for the many-body propagator in bosonic Fock space [33, 34], is at hand.

Outline of this thesis

The thesis is structured as follows:

Chapters 2 to 4 are devoted in the detailed presentation of the semiclassical theory to understand and explain the dynamical behaviour of out-of-time-order correlators. This derivation is rather generic, and we choose to present it for the many-body scenario of many interacting bosonic atoms contained in an optical lattice with a finite number of

sites.

In chapter 2 we provide the basic understanding of unstable classical Hamiltonian dynamics, as this is both needed for the technical parts deriving the theory, as well as for the understanding of the dynamical behaviour of OTOCs themselves. Therefore, we review the relevant concepts from classical Hamiltonian formalism, with a special emphasize on the description of the stability of trajectories upon changes of their initial conditions. There we learn about Lyapunov exponents, which encode the rate of exponential separation of two trajectories starting nearby. Through the directions of the stable, unstable and neutral manifold, we obtain a possibility to describe the local phase space in the near vicinity of a given trajectory, which proves essential for the technical derivation of the semiclassical theory for the OTOC. We end the chapter by a discussion of the defining properties of classically chaotic systems.

In chapter 3 we turn to the Bose-Hubbard Hamiltonian as a model for bosonic atoms in an optical lattice. Starting from second quantization, we introduce quadrature operators, which, in the same spirit as position and momentum operators in single particle systems, represent the quantum analogue of conjugate variables for the classical “ $\hbar_{\text{eff}} = 1/N \rightarrow 0$ ” limit of the many-body system. Based on those operators, we derive the semiclassical approximation of the propagator in Fock space which is our main tool in the semiclassical study of OTOCs. Here we see that the mean-field, Gross-Pitaevskii equations emerge as Hamilton’s equations of motion from the Hamilton function found as the classical “ $\hbar_{\text{eff}} \rightarrow 0$ ” limit of the quantum Hamiltonian.

Chapter 4 is devoted to the semiclassical analysis of the dynamical behaviour of OTOCs. For intuition we derive the short-time limit of the OTOC through a detailed review of the Moyal-bracket expansion underlying Eq. (1.3). We then start the semiclassical analysis of OTOCs by expressing them through semiclassical propagators in Fock space. This introduces summations over mean-field solutions, weighted by amplitudes and phases accumulated along. By considering subtle classical correlations amongst these solutions we identify and compute the dominant contributions to the OTOC, which prove responsible for the exponential growth at times smaller than the Ehrenfest time, and for the saturation after the Ehrenfest time.

Chapters 5 and 6 are devoted to a discussion of the effect of interaction on Al’tshuler-Aronov-Spivak oscillations in the coherent transport of cold atoms through an Aharonov-Bohm ring. This work requires the detailed studying of a single mean-field solution rather than the interference of multiple solutions such as for the OTOC. It is a work done in collaboration with R. Chrétien, J. Dujardin, C. Petitjean and P. Schlagheck.

Chapter 5 summarizes the work performed by my collaborators. We introduce the Aharonov-Bohm setup, a ring structure with waveguides attached to it at opposite sites. The ring is penetrated by a synthetic gauge field and contains a Gaussian correlated disorder potential within its arms. We show numerical results for the transmission probability, which is obtained from solving the mean-field equations. These results display Al’tshuler-Aronov-Spivak oscillations in the noninteracting case. In the presence

of a weak particle-particle interaction inside the ring, an inversion of the oscillation is observed, which motivated my study of the mean-field problem in chapter 6. As preparation for the analytical treatment of the system, we show how to relate the reflection and transmission probabilities to the Green's function of the noninteracting mean-field problem, and derive a semiclassical representation of this Green's function in the form of a summation of weighted phases accumulated along scattering paths, which perform multiple oscillations within the ring.

Chapter 6 marks my contribution to the collaboration and shows how to perform the summation over scattering paths in the noninteracting case. Interaction is then incorporated in a perturbative manner, and we present the calculation of the reflection and transmission probabilities up to linear order in the interaction strength, leading to interaction-based corrections to the Al'tshuler-Aronov-Spivak oscillations.

2 Classical Hamiltonian dynamics

This chapter reviews classical Hamiltonian dynamics, with special emphasis on the stability of trajectories. In order to describe the local phase space in the vicinity of a given trajectory we introduce the concept of stable, unstable, and neutral manifolds, together with Lyapunov exponents as quantities encoding the exponential sensitivity of trajectories towards changes in its initial conditions. The chapter ends with the defining properties of classical chaotic systems.

Throughout this thesis we will consider quantum systems which allow for the notion of a classical limit. For such systems, the semiclassical theory provides powerful tools to explain and interpret interference phenomena in the semiclassical limit by exclusively using information from the classical realm. It is through these methods that we are able to understand OTOCs and to confirm that these correlators are suitable tools to quantify and identify chaos in the classical limit of a quantum system.

For the systems considered within this thesis the classical limit of the quantum system is described by the Hamiltonian formalism. A proper understanding of this formalism is needed both for the semiclassical theory in general and for understanding the dynamical behavior of OTOCs. This chapter aims to provide the reader with the necessary mathematical framework of classical Hamiltonian dynamics, with special emphasis on classical chaotic systems.

Many books containing a general introduction into classical Hamiltonian dynamics exist, see for instance [78–80]. For the subsequent chapter, we choose to follow the introductory chapter in the dissertation of Marko Turek [81], together with its main reference, the first chapter of the book by Gaspard [82], as these references provide the details in the description of the local phase space structure needed for this thesis. Additional sources are cited when they appear in the manuscript.

2.1 Hamiltonian systems

Within the Hamiltonian formalism a classical system is fully described by a single function, the *Hamilton function* $\mathcal{H}(\mathbf{q}, \mathbf{p}, t)$. The arguments of this function are the “time” t and vectors \mathbf{q} and \mathbf{p} of the same dimension d .¹ The dimension d is referred to as the

¹In a more rigorous mathematical treatment using the language of differential geometry, \mathbf{q} is an element of a d -dimensional manifold Ω , known as *configuration space*, and \mathbf{p} is a vector from the dual space of its tangent space, see *e.g.* [83]. However, for readability, we only consider here Hamiltonian systems whose configuration space is represented by a real vector space. This simplifies the presentation and representation of the stability matrix \mathbf{M} in the subsequent section.

number of degrees of freedom. Often, one denotes \mathbf{q} as “position” and \mathbf{p} as “momentum vector”, but depending on the actual physical system described by \mathcal{H} these variables do not necessarily represent a position in space and the mechanical momentum of physical particles.²

We can combine the two vectors into a single vector of dimension $2d$, the *phase space point*

$$\mathbf{x} = \begin{pmatrix} \mathbf{q} \\ \mathbf{p} \end{pmatrix}, \quad (2.1)$$

and we call the set of all these vectors *phase space* \mathcal{X}^3 . A phase space point holds the current state of the system, and the dynamics of the system is given by a set of ordinary differential equations, the *Hamilton’s equations of motion*,

$$\dot{\mathbf{q}}(t) = \left[\frac{\partial \mathcal{H}}{\partial \mathbf{p}}(\mathbf{q}(t), \mathbf{p}(t), t) \right]^\top, \quad \dot{\mathbf{p}}(t) = - \left[\frac{\partial \mathcal{H}}{\partial \mathbf{q}}(\mathbf{q}(t), \mathbf{p}(t), t) \right]^\top, \quad (2.2)$$

where the dot denotes a derivative w.r.t. the time t . Any function solving Hamilton’s equations of motion is referred to as a *trajectory (in phase space)*.

We can combine the above expressions into a single expression for the phase space point,

$$\dot{\mathbf{x}}(t) = \Sigma \cdot \left[\frac{\partial \mathcal{H}}{\partial \mathbf{x}}(\mathbf{x}(t), t) \right]^\top, \quad (2.3)$$

where we used the *fundamental matrix of the symplectic structure*,

$$\Sigma = \begin{pmatrix} \mathbf{0} & \mathbf{1} \\ -\mathbf{1} & \mathbf{0} \end{pmatrix}. \quad (2.4)$$

As Eq. (2.3) is an ordinary first order differential equation, one and only one solution of these equations can be found for a given initial condition $\mathbf{x}_0 = (\mathbf{q}_0, \mathbf{p}_0)$ at time t_0 , and we write $\mathbf{x}(t; \mathbf{x}_0, t_0)$ for the function solving (2.3) subject to these initial conditions. An (infinitesimally) small variation of the initial conditions leads to a smooth variation of the found solution, rendering the solution a smooth function of the boundary conditions. Finding the solution to a given initial condition is (in the general context of differential equations) referred to as an *initial value problem*.

Contrarily, the property of uniqueness and existence of solutions is lost in the case of a *boundary problem*, where one searches for trajectories fulfilling conditions both at an initial time t_0 and a final time $t_1 > t_0$. For instance, by fixing the initial and final position vector, $\mathbf{q}(t_0) = \mathbf{q}^{(i)}$, $\mathbf{q}(t_1) = \mathbf{q}^{(f)}$. For boundary problems, it is possible to have any number of solutions, with the extreme cases being no solution and an

²Indeed, as we see in section 3.3.3, in the classical limit for Bose-Hubbard models \mathbf{q} and \mathbf{p} even lack a direct physical interpretation. However, the squared absolute value of components of the phase space point, $|x_i|^2 = |q_i|^2 + |p_i|^2$ is associated to the particle density at the site i , as seen from Eq. (3.22).

³In the context of differential geometry, the phase space is the co-tangent bundle, $\mathcal{X} = \mathcal{T}^*\Omega$, with Ω denoting the configuration space.

uncountable infinite number of solutions⁴. Different trajectories found in a boundary problem are distinguished by Greek letters as subscript, *e.g.* γ , and we write $\mathbf{x}_\gamma(t) \equiv \mathbf{x}_\gamma(t; \mathbf{q}^{(f)}, \mathbf{q}^{(i)}, t_1, t_0)$ for the corresponding solution of Hamilton's equations of motion. Note that solutions of the initial value problem can be distinguished from those of the boundary value problem through the presence of the label γ in the notation. Similar to the initial value problem, an (infinitesimally) small variation of the boundary conditions leads to a smooth variation of the found solution, rendering the solution a smooth function of the boundary conditions.

There is an important function associated with a solution of the boundary value problem. In order to define this function, the *action functional* $R[\mathbf{x}(t)]$ is used, which returns the integral of the Lagrange function along the path $\mathbf{x}(t)$ in phase space. The action is well-defined for any smooth enough path $\mathbf{x}(t)$ in phase space, not necessarily a solution of Hamilton's equations of motion. However, evaluating the action of a classical trajectory γ introduces *Hamilton's principal function* $R_\gamma(\mathbf{q}^{(f)}, \mathbf{q}^{(i)}, t_1, t_0) = R[\mathbf{x}_\gamma(t)]$, which is a function associated with the trajectory γ , with the boundary conditions as arguments. Expressing the Lagrange function in phase space variables through the Hamilton function, we find

$$\begin{aligned} R_\gamma(\mathbf{q}^{(f)}, \mathbf{q}^{(i)}, t_1, t_0) &= R[\mathbf{x}_\gamma(t; \mathbf{q}^{(f)}, \mathbf{q}^{(i)}, t_1, t_0)] \\ &= \int_{t_0}^{t_1} dt [(\mathbf{p}_\gamma(t))^\top \dot{\mathbf{q}}_\gamma(t) - \mathcal{H}(\mathbf{q}_\gamma(t), \mathbf{p}_\gamma(t), t)]. \end{aligned} \quad (2.5)$$

where in the last line we dropped the dependence on $\mathbf{q}^{(f)}$, $\mathbf{q}^{(i)}$, t_1 , t_0 from the trajectory-related function \mathbf{q}_γ , \mathbf{p}_γ . The derivatives with respect to initial and final position result in the conjugate momenta,

$$\left[\frac{\partial R_\gamma}{\partial \mathbf{q}^{(f)}}(\mathbf{q}^{(f)}, \mathbf{q}^{(i)}, t_1, t_0) \right]^\top = \mathbf{p}_\gamma^{(f)}(\mathbf{q}^{(f)}, \mathbf{q}^{(i)}, t_1, t_0), \quad (2.6)$$

$$\left[\frac{\partial R_\gamma}{\partial \mathbf{q}^{(i)}}(\mathbf{q}^{(f)}, \mathbf{q}^{(i)}, t_1, t_0) \right]^\top = -\mathbf{p}_\gamma^{(i)}(\mathbf{q}^{(f)}, \mathbf{q}^{(i)}, t_1, t_0), \quad (2.7)$$

which formally allows the interpretation of R_γ as a local generating function for the canonical transformation from initial to final phase space coordinates along γ . Hamilton's principal function is of central importance within the semiclassical approximation of the time evolution operator, as we will see in chapter 3.3.

So far, our considerations include Hamilton functions with an explicit time dependence. To simplify the subsequent presentations, we, from now on, limit our considerations to time-independent Hamilton functions $\mathcal{H}(\mathbf{q}, \mathbf{p})$. Note that this is not a restriction, as any time-dependent Hamilton function of spatial dimension d can be transformed into

⁴As examples consider a single-particle Hamiltonian system in standard form. If the potential energy separates two areas by a wall of infinite potential, no solution can be found linking the separate areas. Contrarily, if in an elliptical billiard the boundary conditions are such that initial and final position are the focal points the other extreme case of an uncountable infinite number of solutions is produced.

a time-independent Hamiltonian system of dimension $d + 1$ by introducing energy and time as an additional set of conjugate variables [79],

$$\mathcal{K}(\mathbf{Q}, \mathbf{P}) = \mathcal{H}(\mathbf{q}, \mathbf{p}, t) - E \quad \text{where } \mathbf{Q} = \begin{pmatrix} \mathbf{q} \\ t \end{pmatrix}, \quad \mathbf{P} = \begin{pmatrix} \mathbf{p} \\ -E \end{pmatrix}. \quad (2.8)$$

In this picture t becomes a component of the coordinate vector and loses its interpretation as “time” in the dynamical equations governed by the new Hamilton function K .

For a time-independent Hamilton function, it can be shown that only the difference $t - t_0$ between initial time t_0 and final time t appears in a dynamical quantity. It is thus justified to take the initial time $t_0 = 0$ as the zero of time and drop it from the arguments of dynamical quantities.

2.2 Linear stability of Hamiltonian systems

In this section we discuss the stability of trajectories, *i.e.* the change of the trajectory due to infinitesimal changes in its initial conditions.

2.2.1 The stability matrix

Let \mathbf{x}_0 be an arbitrary phase-space point, and $\delta\mathbf{x}_0$ be an infinitesimally small initial perturbation such that the perturbed trajectory $\mathbf{x}(t; \mathbf{x}_0 + \delta\mathbf{x}_0)$ stays infinitesimally close to the trajectory $\mathbf{x}(t; \mathbf{x}_0)$. A treatment in the linearizable regime is thus justified, and we obtain by linearization around the initial phase space point

$$\begin{aligned} \delta\mathbf{x}(t; \mathbf{x}_0, \delta\mathbf{x}_0) &= \mathbf{x}(t; \mathbf{x}_0 + \delta\mathbf{x}_0) - \mathbf{x}(t; \mathbf{x}_0) \\ &= \frac{\partial\mathbf{x}}{\partial\mathbf{x}_0}(t; \mathbf{x}_0) \cdot \delta\mathbf{x}_0 = \mathbf{M}(t; \mathbf{x}_0) \cdot \delta\mathbf{x}_0, \end{aligned} \quad (2.9)$$

where we introduced the *stability matrix*

$$\mathbf{M}(t; \mathbf{x}_0) = \frac{\partial\mathbf{x}}{\partial\mathbf{x}_0}(t; \mathbf{x}_0). \quad (2.10)$$

As the derivative of the phase space point w.r.t. the initial phase space point, the stability matrix, by definition, encodes the stability of a trajectory towards infinitesimal variations of its initial conditions. Utilizing Hamilton’s equations of motion, Eq. (2.3), we can derive equations of motion for the stability matrix. On the one hand, we find

$$\begin{aligned} \delta\dot{\mathbf{x}}(t; \mathbf{x}_0, \delta\mathbf{x}_0) &= \Sigma \cdot \left(\frac{\partial\mathcal{H}}{\partial\mathbf{x}}(\mathbf{x}(t; \mathbf{x}_0 + \delta\mathbf{x}_0), t) - \frac{\partial\mathcal{H}}{\partial\mathbf{x}}(\mathbf{x}(t; \mathbf{x}_0), t) \right)^\top \\ &= \Sigma \cdot \frac{\partial^2\mathcal{H}}{\partial\mathbf{x}\partial\mathbf{x}}(\mathbf{x}(t; \mathbf{x}_0)) \cdot \mathbf{M}(t; \mathbf{x}_0) \cdot \delta\mathbf{x}_0. \end{aligned} \quad (2.11)$$

On the other hand, by a direct differentiation of Eq. (2.9) with respect to time, we get

$$\delta\dot{\mathbf{x}}(t; \mathbf{x}_0, \delta\mathbf{x}_0) = \dot{\mathbf{M}}(t; \mathbf{x}_0) \cdot \delta\mathbf{x}_0. \quad (2.12)$$

The above equations hold true for any infinitesimal perturbation $\delta\mathbf{x}_0$. Thus, by comparing Eqs. (2.11) and (2.12), we obtain the equations of motion

$$\dot{\mathbf{M}}(t; \mathbf{x}_0) = \boldsymbol{\Sigma} \cdot \frac{\partial^2 \mathcal{H}}{\partial \mathbf{x} \partial \mathbf{x}}(\mathbf{x}(t; \mathbf{x}_0)) \cdot \mathbf{M}(t; \mathbf{x}_0), \quad (2.13)$$

which are formally solved by

$$\begin{aligned} \mathbf{M}(t; \mathbf{x}_0) &= \mathcal{T} \exp \left(\int_0^t ds \boldsymbol{\Sigma} \cdot \frac{\partial^2 \mathcal{H}}{\partial \mathbf{x} \partial \mathbf{x}}(\mathbf{x}(s; \mathbf{x}_0)) \right) \\ &= \sum_{l=0}^{\infty} \int_0^t ds_1 \int_0^{s_1} ds_2 \cdots \int_0^{s_{l-1}} ds_l \boldsymbol{\Sigma} \cdot \frac{\partial^2 \mathcal{H}}{\partial \mathbf{x} \partial \mathbf{x}}(\mathbf{x}(s_1; \mathbf{x}_0)) \cdots \boldsymbol{\Sigma} \cdot \frac{\partial^2 \mathcal{H}}{\partial \mathbf{x} \partial \mathbf{x}}(\mathbf{x}(s_l; \mathbf{x}_0)), \end{aligned} \quad (2.14)$$

where we introduced and utilized the time-ordered exponential function $\mathcal{T} \exp$.

2.2.2 Lyapunov exponents and the decomposition of the stability matrix

An important property of the stability matrix is the so-called *multiplicative cocycle*, i.e. \mathbf{M} satisfies the relation

$$\mathbf{M}(t + t'; \mathbf{x}_0) = \mathbf{M}(t; \mathbf{x}(t'; \mathbf{x}_0)) \cdot \mathbf{M}(t'; \mathbf{x}_0), \quad (2.15)$$

for any positive time t' . In view of Eq. (2.9), this property contains the observation that an initial perturbation $\delta\mathbf{x}_0$ can also be translated to the final one $\delta\mathbf{x}(t + t'; \mathbf{x}_0, \delta\mathbf{x}_0)$ through the determination of the intermediate perturbation at time t' .

Both Eq. (2.14) and Eq. (2.15) imply that an infinitesimal perturbation $\delta\mathbf{x}_0$ can at most grow exponentially in time. We can characterize the strength of such an exponential growth by the *Lyapunov exponent* associated with a perturbation vector $\delta\mathbf{x}_0$

$$\lambda(\mathbf{x}_0, \delta\mathbf{x}_0) = \lim_{t \rightarrow \infty} \frac{1}{t} \log \left[\frac{\|\mathbf{M}(t; \mathbf{x}_0) \cdot \delta\mathbf{x}_0\|}{\|\delta\mathbf{x}_0\|} \right]. \quad (2.16)$$

However, the Lyapunov exponent is not a smooth function of the perturbation vector $\delta\mathbf{x}_0$, as is concluded from the theorem of Oseledets (see for instance [84]). This theorem requires the property of the multiplicative cocycle, and implies that the limit in Eq. (2.16) takes its values only from a discrete set of exponents. The set of all Lyapunov exponents $\{\lambda_1(\mathbf{x}_0), \dots, \lambda_r(\mathbf{x}_0)\}$ found for a given initial phase space point \mathbf{x}_0 is called the *spectrum of Lyapunov exponents*. Each of these Lyapunov exponents $\lambda_i(\mathbf{x}_0)$ comes with a multiplicity $m_i(\mathbf{x}_0)$ which add up to the dimension of the phase space,

$$\sum_{i=1}^r m_i(\mathbf{x}_0) = 2d. \quad (2.17)$$

Depending on the sign of the Lyapunov exponent, we obtain one of three possible cases:

- Exponential growth of perturbations is equivalent to $\lambda_i(\mathbf{x}_0) > 0$. The corresponding vectors $\delta\mathbf{x}_0$ leading to these Lyapunov exponent are denoted *unstable directions*.

- Exponential decrease is equivalent to $\lambda_i(\mathbf{x}_0) < 0$. The corresponding vectors are called *stable directions*.
- An at most polynomial growth or decrease results in $\lambda_i(\mathbf{x}_0) = 0$, and we call the corresponding vectors *neutral directions*.

Note that the Lyapunov exponents depend, in general, on the phase space point \mathbf{x}_0 , or more precisely on the trajectory through \mathbf{x}_0 , as the definition (2.16) is invariant under translation in time.

A more thorough understanding of the exponential growth is obtained by representing the stability matrix $\mathbf{M}(t; \mathbf{x}_0)$ by a decomposition of the form

$$\mathbf{M}(t; \mathbf{x}_0) = \sum_{i=1}^{2d} \mathbf{e}_i[\mathbf{x}(t; \mathbf{x}_0)] \cdot \Lambda_i(t; \mathbf{x}_0) \cdot \mathbf{f}_i^\top[\mathbf{x}_0], \quad (2.18)$$

where the exponential growth in time is now captured by scalar functions, the *local stretching rates* $\Lambda_i(t, \mathbf{x}_0)$, with corresponding normalized vector fields $\mathbf{e}_i[\mathbf{x}]$, $\mathbf{f}_i[\mathbf{x}]$. For fixed \mathbf{x} the tangent vectors obtained from these vector fields fulfill the relations

$$\sum_{i=1}^{2d} \mathbf{e}_i[\mathbf{x}] \cdot \mathbf{f}_i^\top[\mathbf{x}] = \mathbf{1}, \quad \mathbf{f}_i[\mathbf{x}]^\top \mathbf{e}_j[\mathbf{x}] = \delta_{ij}. \quad (2.19)$$

Geometrically, for a fixed phase space point \mathbf{x} , the set of tangent vectors $\{\mathbf{e}_i[\mathbf{x}]\} = \{\mathbf{e}_i[\mathbf{x}] : i = 1, \dots, 2d\}$ forms a basis of the tangent space $\mathcal{T}_{\mathbf{x}}(\mathcal{X})$ at \mathbf{x} . According to the second relation in Eq. (2.19), the second family of vector fields $\{\mathbf{f}_i[\mathbf{x}]\}$ is just the dual basis to $\{\mathbf{e}_i[\mathbf{x}]\}$.

Using Eq. (2.19) one immediately confirms that the vector fields evaluated at different phase space points along a classical trajectory are related to each other according to

$$\mathbf{M}(t; \mathbf{x}_0) \cdot \mathbf{e}_i[\mathbf{x}] = \Lambda_i(t; \mathbf{x}_0) \cdot \mathbf{e}_i[\mathbf{x}(t; \mathbf{x}_0)]. \quad (2.20)$$

Note that, despite its similarity, this relation is not an eigenvalue equation as the basis vectors $\mathbf{e}_i[\mathbf{x}] \in \mathcal{T}_{\mathbf{x}_0}(\mathcal{X})$ and $\mathbf{e}_i[\mathbf{x}(t; \mathbf{x}_0)] \in \mathcal{T}_{\mathbf{x}(t; \mathbf{x}_0)}(\mathcal{X})$ are, in general, elements of different tangent vectors spaces.

Eq. (2.20) is important for the interpretation of the vector fields $\{\mathbf{e}_i[\mathbf{x}]\}$. Along a trajectory we find a co-traveling basis of the tangent space, which we can use to describe the local phase space in the vicinity of this trajectory within the linearizable regime. Moreover, a perturbation of the initial conditions in the direction $\mathbf{e}_i[\mathbf{x}_0]$ is growing with the corresponding stretching factor $\Lambda_i(t, \mathbf{x}_0)$. Through the decomposition Eq. (2.18) of the stability matrix, we can thus at any initial phase space point \mathbf{x}_0 associate directions to the exponential growth and contraction in phase space.

The spectrum of Lyapunov exponents is easily obtained from the stretching rates $\Lambda_i(t, \mathbf{x}_0)$. Using $\delta\mathbf{x}_0 = \mathbf{e}_i[\mathbf{x}_0]$ in (2.16) and utilizing (2.20), one finds

$$\lambda_i(\mathbf{x}_0) = \lambda(\mathbf{x}_0, \mathbf{e}_i[\mathbf{x}_0]) = \lim_{t \rightarrow \infty} \frac{1}{t} \log (|\Lambda_i(t; \mathbf{x}_0)|). \quad (2.21)$$

Since through Eq. (2.18) a Lyapunov exponent is accompanied by a vector field we can also divide the tangent space $\mathcal{T}_{\mathbf{x}}\mathcal{X}$ into the sum of three linear independent subspaces,

$$\mathcal{T}_{\mathbf{x}}\mathcal{X} = \mathcal{E}_u(\mathbf{x}_0) \oplus \mathcal{E}_s(\mathbf{x}_0) \oplus \mathcal{E}_n(\mathbf{x}_0), \quad (2.22)$$

where each of the vector spaces on the r.h.s. is spanned by the subset of basis vectors $\{\mathbf{e}_i[\mathbf{x}_0]\}$ corresponding to stable ($\lambda_i(\mathbf{x}_0) < 0$), unstable ($\lambda_i(\mathbf{x}_0) > 0$) and neutral ($\lambda_i(\mathbf{x}_0) = 0$) directions.

It is very common to also refer to the vectors in $\mathcal{E}_s(\mathbf{x}_0)$ and $\mathcal{E}_u(\mathbf{x}_0)$ as vectors pointing into the direction of the *local stable and unstable manifold* at the phase space point \mathbf{x}_0 . In this context, the stable and unstable manifolds are submanifolds of phase space which contain all phase space points \mathbf{x} , whose trajectories defined by \mathbf{x} and \mathbf{x}_0 converge to each other in the limit $t \rightarrow \infty$ (stable) or $t \rightarrow -\infty$ (unstable), with the distance between the trajectories' phase space points at equal times decreasing exponentially with time.

It is important to note that the property of exponential convergence is omitted in mathematical definitions of the stable and unstable manifold, see *e.g.* [82]. Only convergence towards the trajectory through \mathbf{x}_0 is demanded. Consequently, while in these definitions the tangent space of $W_s(\mathbf{x}_0)$ ($W_u(\mathbf{x}_0)$) at \mathbf{x}_0 still contains the vector space $\mathcal{E}_s(\mathbf{x}_0)$ ($\mathcal{E}_u(\mathbf{x}_0)$), we may additionally also find vectors of neutral directions which lead to an at most polynomial convergence of trajectories.

2.2.3 Pairing rule of the Lyapunov exponents

An important property of the stability matrix for Hamiltonian systems is that it belongs to the class of symplectic matrices, *i.e.* it fulfills the matrix relations

$$\mathbf{M}^\top(t; \mathbf{x}_0) \cdot \boldsymbol{\Sigma} \cdot \mathbf{M}(t; \mathbf{x}_0) = \boldsymbol{\Sigma}. \quad (2.23)$$

In order to prove this relation we use the equation of motion for \mathbf{M} , Eq. (2.13), together with $\boldsymbol{\Sigma}^\top = -\boldsymbol{\Sigma} = \boldsymbol{\Sigma}^{-1}$ to show that

$$\frac{d}{dt}[\mathbf{M}^\top(t; \mathbf{x}_0) \cdot \boldsymbol{\Sigma} \cdot \mathbf{M}(t; \mathbf{x}_0)] = 0, \quad (2.24)$$

i.e. the left hand side of Eq. (2.23) is a constant matrix. Since for $t = 0$ we have $\mathbf{M}(0; \mathbf{x}_0) = \mathbf{1}$, this constant matrix is equal to $\boldsymbol{\Sigma}$.

By a simple transformation of Eq. (2.23) we find the inverse of the stability matrix,

$$\mathbf{M}^{-1}(t; \mathbf{x}_0) = \boldsymbol{\Sigma} \cdot \mathbf{M}^\top(t; \mathbf{x}_0) \cdot \boldsymbol{\Sigma}^\top. \quad (2.25)$$

Using further the decomposition Eq. (2.18) we obtain

$$\mathbf{M}^{-1}(t; \mathbf{x}_0) = \sum_{i=1}^{2n} (\boldsymbol{\Sigma} \mathbf{f}_i[\mathbf{x}_0]) \cdot \Lambda_i(t; \mathbf{x}_0) \cdot (\boldsymbol{\Sigma} \mathbf{e}_i[\mathbf{x}(t; \mathbf{x}_0)])^\top. \quad (2.26)$$

Alternatively, by directly checking $\mathbf{M}^{-1}(t; \mathbf{x}_0) \cdot \mathbf{M}(t; \mathbf{x}_0) = \mathbf{M}(t; \mathbf{x}_0) \cdot \mathbf{M}^{-1}(t; \mathbf{x}_0) = \mathbf{1}$ with the subsequent equation, one also finds

$$\mathbf{M}^{-1}(t; \mathbf{x}_0) = \sum_{i=1}^{2d} \mathbf{e}_i[\mathbf{x}_0] \cdot \Lambda_i^{-1}(t; \mathbf{x}_0) \cdot \mathbf{f}_i^\top[\mathbf{x}(t; \mathbf{x}_0)]. \quad (2.27)$$

The comparison⁵ with Eq. (2.26) implies the *pairing rule* that for each direction i we find a corresponding direction j with

$$\Lambda_i^{-1}(t; \mathbf{x}_0) = \Lambda_j(t; \mathbf{x}_0). \quad (2.28)$$

This has an important consequence for the Lyapunov spectrum, as for every positive Lyapunov $\lambda_i(\mathbf{x}_0)$ there must exist a negative one of equal absolute value. As a consequence, each positive Lyapunov exponent $\lambda_i(\mathbf{x}_0)$ can be associated with two elements of the set $\{\mathbf{e}_i(\mathbf{x}_0)\}$ – an unstable direction with Lyapunov exponent $\lambda_i(\mathbf{x}_0)$, and a stable one with exponent $-\lambda_i(\mathbf{x}_0)$. Moreover, again comparing Eqs. (2.26) with Eq. (2.27) we also find that the dual basis vectors $\{\mathbf{f}_i[\mathbf{x}_0]\}$ are related to $\{\mathbf{e}_i[\mathbf{x}_0]\}$ through the symplectic structure according to

$$\mathbf{e}_i[\mathbf{x}_0] = \pm \Sigma \mathbf{f}_j[\mathbf{x}_0], \quad \mathbf{f}_i[\mathbf{x}_0] = \pm \Sigma \mathbf{e}_j[\mathbf{x}_0], \quad (2.29)$$

where the signs have to be chosen such that they fulfill

$$(\Sigma \mathbf{f}_j[\mathbf{x}_0]) \cdot (\Sigma \mathbf{e}_j[\mathbf{x}(t; \mathbf{x}_0)])^\top = \mathbf{e}_i[\mathbf{x}_0] \cdot \mathbf{f}_i^\top[\mathbf{x}(t; \mathbf{x}_0)]. \quad (2.30)$$

It is convenient to reorder the set of basis vectors $\{\mathbf{e}_i[\mathbf{x}_0]\}$ in a way that directions are grouped together when their stretching factors fulfill the pairing rule $\Lambda_i^{-1}(t; \mathbf{x}_0) = \Lambda_j(t; \mathbf{x}_0)$. We then relabel the basis vectors in such a way, that a pair of stable and unstable directions shares the same integer index (i), while the vectors are now distinguished through additional subscripts s/u. Neutral directions are indicated by the subscript n. To be more precise, we assume we have $k \leq d$ stable and unstable directions. There, the new notation is

$$\{\mathbf{e}_i[\mathbf{x}_0]\} = \{\mathbf{e}_s^{(i)}(\mathbf{x}_0), \mathbf{e}_u^{(i)}(\mathbf{x}_0) : i = 1, \dots, k\} \cup \{\mathbf{e}_n^{(i)}(\mathbf{x}_0) : i = 1, \dots, 2(d-k)\}. \quad (2.31)$$

The same naming convention can be applied to the dual basis $\{\mathbf{f}_i[\mathbf{x}_0]\}$.

Finally, to also fix the signs in Eq. (2.29) we can demand that

$$\mathbf{f}_s^{(i)}(\mathbf{x}_0) = \Sigma \mathbf{e}_u^{(i)}(\mathbf{x}_0), \quad \mathbf{f}_u^{(i)}(\mathbf{x}_0) = -\Sigma \mathbf{e}_s^{(i)}(\mathbf{x}_0), \quad (2.32)$$

which transforms the second relation in Eq. (2.19) into

$$\mathbf{e}_u^{(i)}(\mathbf{x})^\top \Sigma \mathbf{e}_s^{(j)}(\mathbf{x}) = \delta_{ij}, \quad \mathbf{e}_s^{(i)}(\mathbf{x})^\top \Sigma \mathbf{e}_s^{(j)}(\mathbf{x}) = \mathbf{e}_u^{(i)}(\mathbf{x})^\top \Sigma \mathbf{e}_u^{(j)}(\mathbf{x}) = 0. \quad (2.33)$$

⁵To be precise here, to use the comparison as a proof would require that the decomposition Eq. (2.18) of the stability matrix is unique up to ordering, the signs in front of the vectors and degeneracies in the stretching factors. However, a proof of uniqueness is not known to the author, and this chapter should in this case rather be understood as a motivation for the pairing rule, for which a suitable decomposition of the stability matrix fulfilling the properties Eqs. (2.28), (2.19) can be found.

2.2.4 Constants of motion and their relation to neutral directions

In many physical systems the dynamics in phase space is restricted to a submanifold due to the existence of constants of motion. Let $\mathcal{I} \subset \mathcal{X}$ be a subset of phase space which is invariant under the Hamiltonian flow. We then call a time-independent, differentiable function $\mathcal{C}(\mathbf{x})$ defined on \mathcal{I} a *constant of motion*, if it fulfills

$$\mathcal{C}(\mathbf{x}(t, \mathbf{x}_0)) = \mathcal{C}(\mathbf{x}_0), \quad (2.34)$$

for all initial phase space points \mathbf{x}_0 , *i.e.* the function remains constant along trajectories. If $\mathcal{I} = \mathcal{X}$ we call $\mathcal{C}(\mathbf{x})$ a *global constant of motion*.

By differentiating Eq. (2.34) with respect to time, and using Hamilton's equation of motion, Eq. (2.3), we identify an equivalent criterion for a constant of motion,

$$0 = \frac{\partial \mathcal{C}}{\partial \mathbf{x}}(\mathbf{x}(t; \mathbf{x}_0)) \cdot \Sigma \cdot \left[\frac{\partial \mathcal{H}}{\partial \mathbf{x}}(\mathbf{x}(t; \mathbf{x}_0)) \right]^\top = -\{\mathcal{H}, \mathcal{C}\}(\mathbf{x}(t; \mathbf{x}_0)), \quad (2.35)$$

where we introduced the *Poisson bracket*

$$\{\mathcal{H}, \mathcal{C}\}(\mathbf{x}) = \frac{\partial \mathcal{H}}{\partial \mathbf{p}}(\mathbf{x}) \left[\frac{\partial \mathcal{C}}{\partial \mathbf{q}} \right]^\top - \frac{\partial \mathcal{H}}{\partial \mathbf{q}}(\mathbf{x}) \left[\frac{\partial \mathcal{C}}{\partial \mathbf{p}} \right]^\top. \quad (2.36)$$

Thus, a time-independent function \mathcal{C} is a constant of motion if and only if the Poisson bracket between the function \mathcal{C} and the Hamilton function \mathcal{H} vanishes. Quite obviously, for systems with a time-independent Hamilton function, \mathcal{H} itself is a constant of motion since $\{\mathcal{H}, \mathcal{H}\} = 0$, *i.e.* energy is a conserved quantity.

To be able to work, in a reasonable way, with a set of $m \leq d$ constants of motion $\{\mathcal{C}^{(i)}\} = \{\mathcal{C}^{(i)} : i = 1, \dots, m\}$ the functions are assumed to be chosen such that they fulfill two further properties [80]:

1. The set of constants of motion $\{\mathcal{C}^{(i)}\}$ is *functionally independent* in any open subset of their defining set \mathcal{I} , *i.e.* locally none of the constants of motion can be expressed as a function of the others and thus, none of the functions can be treated as obsolete. This property is equivalent to demanding that there is only the trivial linear combination of the differentials $d\mathcal{C}^{(i)}$ to zero, *i.e.* the problem of finding $\alpha_i \in \mathbb{R}$ with

$$0 = \sum_{i=1}^m \alpha_i d\mathcal{C}^{(i)} \quad (2.37)$$

has only the trivial solution $\forall_i \alpha_i = 0$.

2. The set of constants of motion $\{\mathcal{C}^{(i)}\}$ should be *in involution*, *i.e.* we require for the Poisson brackets $\{\mathcal{C}^{(i)}, \mathcal{C}^{(j)}\} = 0$ for all $i, j = 1, \dots, m$. As will become clear before long, this property is important to find a basis for the subspace $\mathcal{E}_n(\mathbf{x})$ of neutral directions which complies with the demands in Eq. (2.19) for a basis used in the decomposition Eq. (2.18) of the stability matrix.

Each constant of motion can be associated with two neutral directions. To see this, we first differentiate both sides of Eq. (2.34) with respect to the trajectory's initial PS point \mathbf{x}_0 . We then use the definition of the stability matrix $M = \partial\mathbf{x}/\partial\mathbf{x}_0$, as well as Eq. (2.25), to transform the equation into

$$\mathbf{M}(t; \mathbf{x}_0) \cdot \boldsymbol{\Sigma} \cdot \left[\frac{\partial \mathcal{C}^{(i)}}{\partial \mathbf{x}}(\mathbf{x}_0) \right]^\top = \boldsymbol{\Sigma} \cdot \left[\frac{\partial \mathcal{C}^{(i)}}{\partial \mathbf{x}}(\mathbf{x}(t; \mathbf{x}_0)) \right]^\top. \quad (2.38)$$

By defining

$$\mathbf{e}_n^{(i)}(\mathbf{x}_0) = \frac{\boldsymbol{\Sigma} \left[\frac{\partial \mathcal{C}^{(i)}}{\partial \mathbf{x}}(\mathbf{x}_0) \right]^\top}{\left\| \left[\frac{\partial \mathcal{C}^{(i)}}{\partial \mathbf{x}}(\mathbf{x}_0) \right]^\top \right\|}, \quad (2.39)$$

we see that Eq. (2.38) just expresses relation (2.20), with a stretching factor

$$\Lambda_n^{(i)}(t, \mathbf{x}_0) = \frac{\left\| \left[\frac{\partial \mathcal{C}^{(i)}}{\partial \mathbf{x}}(\mathbf{x}(t; \mathbf{x}_0)) \right]^\top \right\|}{\left\| \left[\frac{\partial \mathcal{C}^{(i)}}{\partial \mathbf{x}}(\mathbf{x}_0) \right]^\top \right\|}. \quad (2.40)$$

For systems in which the constant of motion limits the dynamics to a submanifold of phase space with a finite (and thus compact) volume, this stretching factor has an upper bound and can thus not grow exponentially in time.⁶ Consequently, its Lyapunov exponent is 0, and $\mathbf{e}_n^{(i)}(\mathbf{x}_0)$ is part of the subspace $\mathcal{E}_n(\mathbf{x}_0)$. Moreover, as the constants of motion are functionally independent, the generated vectors $\{\mathbf{e}_n^{(i)}(\mathbf{x}_0) : i = 1, \dots, m\}$ are linearly independent for almost all $\mathbf{x}_0 \in \mathcal{I}$, and use them within the decomposition Eq. (2.18) of the stability matrix. In that case, the pairing rule implies for each direction $\mathbf{e}_n^{(i)}(\mathbf{x}_0)$ the existence of a second direction, whose dual vector is, with $i' \in \{m+1, \dots, 2\}$, given by

$$\mathbf{f}_n^{(i')}(\mathbf{x}) = \boldsymbol{\Sigma} \mathbf{e}_n^{(i)}(\mathbf{x}) = - \frac{\left[\frac{\partial \mathcal{C}^{(i)}}{\partial \mathbf{x}}(\mathbf{x}_0) \right]^\top}{\left\| \left[\frac{\partial \mathcal{C}^{(i)}}{\partial \mathbf{x}}(\mathbf{x}_0) \right]^\top \right\|}. \quad (2.41)$$

A contradiction at this stage is prevented by the involution property of the constants of motion, as relation (2.19) requires us to have $\mathbf{f}_n^{(i')}(\mathbf{x})^\top \mathbf{e}_n^{(j)}(\mathbf{x}) = 0$ for any $j \in \{1, \dots, k\}$, $i' \in \{k+1, \dots, 2k\}$. This is indeed the case, as up to normalization of the vectors, we calculate

$$\mathbf{f}_n^{(i')}(\mathbf{x})^\top \mathbf{e}_n^{(j)}(\mathbf{x}) \propto \frac{\partial \mathcal{C}^{(i)}}{\partial \mathbf{x}}(\mathbf{x}_0) \cdot \boldsymbol{\Sigma} \cdot \left[\frac{\partial \mathcal{C}^{(j)}}{\partial \mathbf{x}}(\mathbf{x}_0) \right]^\top = \left\{ \mathcal{C}^{(i)}, \mathcal{C}^{(j)} \right\}(\mathbf{x}_0) = 0. \quad (2.42)$$

The geometrical interpretation of the vector $\mathbf{e}_n^{(i)}(\mathbf{x}_0) \propto \boldsymbol{\Sigma} \cdot (\partial \mathcal{C}^{(i)} / \partial \mathbf{x})^\top$ is that it corresponds to the direction of the flow generated by Hamilton's equation of motion, with $\mathcal{C}^{(i)}$

⁶An example for an unbounded system, where the constant of motion produces an exponential stretching factor, is the inverted harmonic oscillator, $\mathcal{H}(q, p) = p^2/2m - m\omega^2 q^2/2$, with \mathcal{H} as constant of motion.

used as Hamilton function. $\mathbf{e}_n^{(i)}(\mathbf{x}_0)$ is thus a tangent vector at \mathbf{x}_0 of the submanifold defined by $\mathcal{C}^{(i)}(\mathbf{x}) = \mathcal{C}^{(i)}(\mathbf{x}_0)$.

Contrarily, the vector $\mathbf{f}_n^{(i')}(\mathbf{x}) = \partial\mathcal{C}^{(i)}/\partial\mathbf{x}$ is a normal vector to this submanifold, demanding that the basis vector $\mathbf{e}_n^{(i')}(\mathbf{x}_0)$ has a normal component, too. Perturbations of initial conditions in the direction of $\mathbf{e}_n^{(i')}(\mathbf{x}_0)$ thus lead to a change in the value of the constant of motion $\mathcal{C}^{(i)}$.

2.3 Properties of chaotic Hamiltonian dynamics

Having established the notion of Hamiltonian systems and discussed the stability of trajectories therein in the last sections, we are now at the position to formalize our understanding of *chaotic systems* by stating their main and in a way defining properties. These are

- **Mixing**, which implies **ergodicity**,
- **Hyperbolicity**, and
- **Periodic orbits cover a dense subset of the accessible phase space.**

We will discuss in detail the meaning of the first two properties in the following subsections, as those are the ones relevant for the technical part of this thesis. The third property is stated here for the sake of completeness to arrive at a highly agreed set of properties which, in a physicists view, define classical chaotic systems. A widely accepted precise mathematical definition of the notion “chaos” can be found for maps in the book by Devaney, Ref. [85], with extensions to dynamical flows in Ref. [86]⁷.

2.3.1 Mixing and ergodicity

Contrarily to a single trajectory, the definition of mixing and of ergodicity is a property of ensembles of phase space points. For that reason, we require the definition of *invariant measures*. These are measures μ defined for phase space with the property to be invariant under Hamiltonian flow, *i.e.* for any measurable subset $\mathcal{U}_0 \subset \mathcal{X}$ the measure of the set $\mathcal{U}(t) = \{\mathbf{x}(t; \mathbf{x}_0) | \mathbf{x}_0 \in \mathcal{U}_0\}$ obtained from time-evolving the phase space points in \mathcal{U}_0 remains constant in time,

$$\mu(\mathcal{U}(t)) = \mu(\mathcal{U}_0). \quad (2.43)$$

An obvious example for such a measure is the phase space volume itself, given by the Lebesgue measure $d\mu(\mathbf{x}) = d^{2d}x$. However, since we introduced the complete phase

⁷There are some discussions and works, for instance Refs. [87, 88], which indicate that, under rather general conditions towards the dynamical flow in a chaotic system, one does not need the property of sensitivity to initial conditions in Devaney’s definition, as this property is implied by the other properties of topological transitivity (*i.e.* mixing in our case) and the dense set of periodic orbits. However, since we heavily rely on the properties of hyperbolicity and on mixing, we decided to explicitly mention these properties here, without claiming that there are no possible redundancies.

space \mathcal{X} as the vector space \mathbb{R}^{2d} , the measure $\mu(\mathcal{X}) = \infty$ is infinite. This measure is thus not normalizable and does not support a probabilistic interpretation. However, for Hamiltonian systems subject to a number of functionally independent constants of motions, $\{\mathcal{C}^{(i)}, i = 1, \dots, m\}$ which are in involution, the dynamics of a trajectory is restricted to a $(2d - m)$ -dimensional submanifold \mathcal{X}' of phase space defined by fixing the values for the constants of motion. Depending on the physical system of interest, this submanifold might be bounded to a finite region in phase space. In this case, a common, normalizable measure for the complete phase space, which is widely used to describe the statistical behavior of chaotic submanifolds, is given by

$$d\mu(\mathbf{x}) = \frac{[\prod_{i=1}^m \delta(\mathcal{C}^{(i)}(\mathbf{x}) - c_i)] d^{2d}x}{\int_{\mathcal{X}} [\prod_{i=1}^m \delta(\mathcal{C}^{(i)}(\mathbf{x}) - c_i)] d^{2d}x}. \quad (2.44)$$

We can interpret that measure as an invariant measure for the submanifold \mathcal{X}' , introduced through the embedding of the submanifold into the complete phase space \mathcal{X} . $\mu(A)$ is thus interpreted as the measure of the $2d - m$ dimensional volume $A' = A \cap \mathcal{X}'$. Note that, for a probabilistic interpretation of the invariant measure, we normalized μ to one.

A system with a normalizable measure μ is called *mixing* if for any two sets $\mathcal{A}_0, \mathcal{B}_0 \subset \mathcal{X}$ we have in the limit of long times

$$\lim_{t \rightarrow \infty} \mu(\mathcal{A}(t) \cap \mathcal{B}_0) = \mu(\mathcal{A}_0)\mu(\mathcal{B}_0), \quad \left(\Leftrightarrow \lim_{t \rightarrow \infty} \frac{\mu(\mathcal{A}(t) \cap \mathcal{B}_0)}{\mu(\mathcal{B}_0)} = \frac{\mu(\mathcal{A}_0)}{\mu(\mathcal{X})} \text{ for } \mu(\mathcal{B}_0) \neq 0 \right), \quad (2.45)$$

where $\mathcal{A}(t) = \{\mathbf{x}(t; \mathbf{x}_0) \mid \mathbf{x}_0 \in \mathcal{A}_0\}$ is the phase space volume obtained from time-evolving the phase space points in \mathcal{A}_0 . The interpretation of this relation is such, that in the limit of long times t , the measure of the fraction of the set $\mathcal{A}(t) \cap \mathcal{B}_0$ compares to the full set \mathcal{B}_0 like $\mathcal{A}(t)$ (whose measure $\mu(\mathcal{A}(t)) = \mu(\mathcal{A}_0)$ is invariant in time) compares to the measure of the full phase space $\mu(\mathcal{X}) = 1$.

This property has an important equivalence for functions of the phase space variables. Since through mixing any initially local phase space volume \mathcal{A}_0 is distributed over the whole accessible phase space in the limit of long times, the average of any smooth phase space function over the set $\mathcal{A}(t)$ approaches for long times the average over the accessible phase space, weighted by the fraction $\mu(\mathcal{A}_0)$. Mathematically,

$$\lim_{t \rightarrow \infty} \int_{\mathcal{A}} d\mu(\mathbf{x}_0) g(\mathbf{x}(t; \mathbf{x}_0)) = \mu(\mathcal{A}) \int_{\mathcal{X}} d\mu(\mathbf{x}) g(\mathbf{x}). \quad (2.46)$$

In the extreme case of an almost point like set \mathcal{A}_0 , centered around a phase space point \mathbf{x}_0 , this justifies the following approximation: for long enough times (where one still needs to specify the time scale) functions of a trajectory's phase space point are well approximated by the phase space average of the function,

$$f(\mathbf{x}(t; \mathbf{x}_0)) \approx \int_{\mathcal{X}} d\mu(\mathbf{x}) f(\mathbf{x}). \quad (2.47)$$

For chaotic systems the time scale is given as the time needed to sufficiently feel the exponential sensitivity to changes in initial conditions. A proper time scale is thus

obtained through the *Lyapunov time* $t_L = 1/|\lambda|$, where λ denotes the largest positive Lyapunov exponent of the phase space point \mathbf{x}_0 . Moreover, from the arguments leading to the approximation, the method requires a certain smoothing in the initial condition \mathbf{x}_0 to justify the approximation, *e.g.* $f(\mathbf{x}(t; \mathbf{x}_0))$ is used within another integration. It certainly does not apply if one is interested in the exact numerical value of $f(\mathbf{x}(t; \mathbf{x}_0))$ for fixed \mathbf{x}_0 .

Ergodicity is a weaker property than mixing, in the sense that mixing implies ergodicity. Physically speaking, ergodicity means that during its dynamics a typical trajectory approaches arbitrarily close any phase space point which is accessible on the submanifold \mathcal{X}' fixed by the constants of motion. In the limit of long times an average over time of a function of the trajectory converges to a phase space average of the function,

$$\lim_{T \rightarrow \infty} \frac{1}{T} \int_0^T dt f(\mathbf{x}(t; \mathbf{x}_0)) = \int_{\mathcal{X}} d\mu(\mathbf{x}) f(\mathbf{x}). \quad (2.48)$$

2.3.2 Hyperbolicity

The definition presented here is motivated by the one found in Ref. [82], however adjusted to additionally allow a set of global constants of motion.

Assuming we have $m < d$ global constants of motions $\{\mathcal{C}^{(i)}, i = 1, \dots, m\}$, we call the subset $\mathcal{Y} \subset \mathcal{X}$, which is invariant under the Hamiltonian flow, *hyperbolic* if for almost all phase space points $\mathbf{x} \in \mathcal{Y}$ the tangent space can be decomposed into

$$\mathcal{T}_{\mathbf{x}}\mathcal{X} = \mathcal{E}_u(\mathbf{x}) \oplus \mathcal{E}_s(\mathbf{x}) \oplus \mathcal{E}_n(\mathbf{x}) \quad (2.49)$$

with nonempty subspaces $\mathcal{E}_{u/s}(\mathbf{x})$ of dimension $d - m$ spanned by the stable/unstable directions, and a subspace $\mathcal{E}_n(\mathbf{x})$ of dimension $2m$ of neutral directions completely determined by the constants of motion as described in subsection 2.2.4. Furthermore, we demand that the three subspaces vary continuously with the phase space point \mathbf{x} . To put in words, any initial perturbation of a trajectory can be decomposed into contributions along stable and unstable directions, which decrease and increase exponentially in time, and directions which can be associated to the constants of motion.

A subclass of hyperbolic systems which is very helpful for the analysis of chaotic classical systems are *uniformly hyperbolic* systems. In those systems the spectrum of Lyapunov exponents is independent on the single phase space point in \mathcal{Y}

$$\lambda_i(\mathbf{x}) = \lambda_i, \quad \forall \mathbf{x} \in \mathcal{Y}. \quad (2.50)$$

Within the semiclassical theory, this assumption of uniform hyperbolicity in the chaotic classical limit of a quantum system does not only heavily reduce the amount of calculations, but often even enables them at all.

Furthermore, one approximates the stretching factors in the decomposition Eq. (2.18) of the stability matrix by their asymptotic behaviour. In case of the factors associated to the stable and unstable directions, this means

$$\Lambda_i(t; \mathbf{x}) \approx e^{\lambda_i t}. \quad (2.51)$$

Like the approximation presented in Eq. (2.47), this step is justified for times larger than the Lyapunov time, $t > t_L$.

It is then also repeatedly found that the largest positive Lyapunov exponent dominates the explanation of the observed phenomena. To improve the presentation of the used techniques, one thus assumes a more drastic version of uniform hyperbolic dynamics, where the absolute values of all non-zero Lyapunov-exponents are equal,

$$|\lambda_i| = \lambda > 0 \quad \text{for all } i \text{ with } \lambda_i \neq 0. \quad (2.52)$$

Within this thesis, we also rely on this approximation, and discuss in words what happens when we allow for uniform hyperbolicity with a spectrum of Lyapunov exponents.

3 Semiclassical treatment of bosonic quantum many-body systems described by the Bose-Hubbard model

In this chapter we introduce Bose-Hubbard models to describe interacting bosons populating a lattice. Of special interest is the thermodynamic limit of a large number N of particles where we want to understand the dynamical behavior of out-of-time-order correlators. We show that the thermodynamic limit can be interpreted as a classical limit where the inverse number of particles plays the role of an effective Planck's constant, $\hbar_{\text{eff}} = 1/N$ and introduce a semiclassical theory for the Bose-Hubbard model. During the derivation of the main tool, the semiclassical approximation of the propagator for Bose-Hubbard systems, we are able to identify the Hamilton function for the classical “ $1/N \rightarrow 0$ ” limit, and we see that Hamilton's equations of motion coincide with the nonlinear wave equations obtained from a mean-field treatment of the quantum system. This enables us to interpret quantum many-body interference phenomena as to originate from a coherent summation of contributions. Each of these contributions relates to one of many solutions of the mean-field equations subject to boundary conditions, and thereby leads to the formalism needed to go beyond a mean-field treatment of the system such as the truncated Wigner method, which is based on incoherently summing solutions.

We now turn towards the quantum realm and, in this chapter, introduce Bose-Hubbard models as the interacting many-body quantum models of choice to study out-of-time-order correlators. As we plan to work in the thermodynamic limit of a large number N of particles, our key concept is to interpret this limit as a classical limit, with $\hbar_{\text{eff}} = 1/N$, the inverse number of particles, playing the role of an effective Planck's constant. To pave the way in that direction, we not only review in the first section the formalism of second quantization in the bosonic case, but also introduce bosonic quadrature operators, from which we later obtain a set of conjugate variables to use in the Hamilton function of the classical limit of Bose-Hubbard model. In section 2, we briefly discuss the generic Bose-Hubbard Hamiltonian and the minimal assumptions we have to make to ensure the existence of a classical limit. Finally, in the last section of this chapter, we review in detail the derivation of our main tool for the semiclassical theory, the semiclassical approximation of the propagator (the matrix elements of the time-evolution operator, with quadrature eigenstates chosen as basis). We start by writing the propagator in its

Feynman path integral representation, and, following steps pioneered by Gutzwiller [1, 33], identify then in the semiclassical limit and by the means of the stationary phase approximation the classical paths significantly contributing to the propagator. During this procedure, we are able to explicitly identify the Hamilton function of the classical limit.

3.1 Bosonic Fock space and its representations

We start with a brief review of the notion of second quantization, restricting ourselves to bosonic particles only as this is the class of particle considered within the scope of this work. This section is not aiming at a complete treatment of the topic of second quantization, and for more details, as well as the according theory for fermions, we refer the reader to one of the many introductory book towards many-body quantum theory, such as [89, 90].

3.1.1 Bosonic Fock states

The defining property of bosonic many-body quantum states is that interchanging the indistinguishable bosonic particles leaves the wave function unchanged. As a consequence and contrarily to fermions, many bosonic particles can occupy the same single-particle state. Rather than focusing on the single particles, it is thus much more convenient to aim at a description of quantum many-body systems in terms of numbers of occupations of single-particle states. This is the idea at the heart of *second quantization*, also coined the *occupation number representation*.

In this formalism, the bosonic many-body Hilbert space \mathcal{B}_N for a fixed number N of indistinguishable particles is related to single-particle modes by taking as a basis for \mathcal{B}_N the symmetrized products of the basis states of the single-particle Hilbert space. If we denote by $\{|l\rangle : l \in \mathcal{I}\}$ a complete orthonormal basis¹ of the single-particle Hilbert space, then these symmetrized states are given by

$$|\mathbf{n}\rangle = |(n_l)_{l \in \mathcal{I}}\rangle = S^+ \left[\bigotimes_{l \in \mathcal{I}} \underbrace{(|l\rangle \otimes \dots \otimes |l\rangle)}_{n_l \text{ times}} \right], \quad (3.1)$$

where the label \mathbf{n} is a vector with non-negative integer components $n_l \in \mathbb{N}_0$ and with the size of the index set \mathcal{I} as dimension. The function S^+ on the r.h.s. takes a product state as an input and returns the normalized, symmetrized permanent. From the definition, Eq. (3.1), it is easy to interpret the state $|\mathbf{n}\rangle$ as the bosonic many-body state where for $l \in \mathcal{I}$ the single-particle mode $|l\rangle$ is populated by n_l particles. We will refer to states defined by Eq. (3.1) as *number states* or *Fock states*.

It is easy to show that the orthogonality of the single-particle basis states translates directly into orthogonality of Fock states. Consequently, we can write the many-body

¹In view of the Bose-Hubbard model presented in section 3.2 we excluded in our considerations systems which require including non-normalizable scattering states for a full description of the quantum system.

Hilbert space \mathcal{B}_N as the span of all Fock states with fixed total number N of particles,

$$\mathcal{B}_N = \text{span} \left\{ |\mathbf{n}\rangle : \sum_{l \in \mathcal{I}} n_l = N \right\}. \quad (3.2)$$

By lifting the restriction of fixing the total number of particles we can also allow a superposition of states with different N . The Hilbert space containing these more general states is known as *Fock space* and is defined as the direct sum of the Hilbert spaces \mathcal{B}_N ,

$$\mathcal{B} = \bigoplus_{N=0}^{\infty} \mathcal{B}_N = \text{span} \{ |\mathbf{n}\rangle \}. \quad (3.3)$$

Note that the Fock space also contains the Hilbert space of no particles, spanned by a single, special Fock state, the *vacuum state* $|\mathbf{0}\rangle$ where the occupation of any single-particle state is $n_l = 0$ for all $l \in \mathcal{I}$.

We can identify Fock states as the basis states produced by the common eigenstates of the mutually commuting set of the Hermitian *occupation number operators* \hat{n}_l , $l \in \mathcal{I}$, with occupation numbers of the single-particle modes being the eigenvalues,

$$\hat{n}_l |\mathbf{n}\rangle = n_l |\mathbf{n}\rangle. \quad (3.4)$$

Using the occupation number operators, we can define an operator counting the total number of particles in the system through

$$\hat{N} = \sum_{i \in \mathcal{I}} \hat{n}_i. \quad (3.5)$$

Using this operator, it is easy to prove by contradiction that the overlap of Fock states differing in the total number of particles is zero. The set of all Fock states thus forms a complete orthonormal basis of Fock space.

3.1.2 Creation and annihilation operators

We have seen that the construction of Fock states requires the symmetrization of a product state. This step is formally simplified using *creation and annihilation operators*,

$$\hat{b}_l^\dagger, \hat{b}_l, l \in \mathcal{I}. \quad (3.6)$$

These operators are a set of operator pairs, where each pair relates to one of the single-particle basis states in $\{|l\rangle : l \in \mathcal{I}\}$. The action of these operators is such that they add (or “create”), respectively remove (or “annihilate”) from a quantum many-body state a particle in the single particle state they are labeled with, thereby increasing or decreasing the number of particles described by the state. Acting on Fock states, we obtain²

$$\hat{b}_l |\dots, n_l, \dots\rangle = \sqrt{n_l} |\dots, n_l - 1, \dots\rangle, \quad (3.7)$$

²In case of a Fock state with $n_l = 0$, the result of an application of \hat{b}_l in Eq. (3.7) formally results in an unphysical state with $n_l - 1 = -1$. However, this state is multiplied with $\sqrt{n_l} = 0$, and we can define the final result to be the correct value 0. This way, we can continue using Eq. (3.7) without the need to distinguish the cases $n_l = 0$ from $n_l > 0$.

$$\hat{b}_l^\dagger |\dots, n_l, \dots\rangle = \sqrt{n_l + 1} |\dots, n_l + 1, \dots\rangle. \quad (3.8)$$

The normalization is such that we can express the occupation number operator as the product of a creation and annihilation operator,

$$\hat{n}_l = \hat{b}_l^\dagger \hat{b}_l. \quad (3.9)$$

Developing the formalism in terms of these operators converts the bosonic symmetry upon permutation of particles into in a relation of operators, the *bosonic commutation relations*

$$[\hat{b}_l, \hat{b}_{l'}] = [\hat{b}_l^\dagger, \hat{b}_{l'}^\dagger] = 0, \quad [\hat{b}_l, \hat{b}_{l'}^\dagger] = \delta_{ll'}, \quad (3.10)$$

where the last relation indicates that creation and annihilation do not commute with each other, ultimately as a consequence that the attempt of removing a particle from an unoccupied state has to result in 0, see Eq. (3.7).

The great advantage of working with creation and annihilation operators lies in the fact that both the Fock states as well as quantum operators acting on many-body states can be very elegantly re-expressed in terms of these operators, thus allowing an interpretation of the many-body scenario in terms of changes in the occupations of single-particle states. Fock states can be constructed by an appropriate successive application of creation operators upon the vacuum state,

$$|\mathbf{n}\rangle = \prod_{l \in \mathcal{I}} \frac{(\hat{b}_l^\dagger)^{n_l}}{\sqrt{n_l!}} |\mathbf{0}\rangle. \quad (3.11)$$

The action of quantum operators is interpreted such that particles found in single-particle modes are annihilated, and then created in other modes to transform a Fock state into a superposition of Fock states. Operators can then be classified by the number of particles involved, and whether the operator conserves the total number of particles.

3.1.3 Quadrature operators and quadrature states

Of central interest in this thesis are bosonic systems in the thermodynamic limit of a large number N of particles. The main idea for the concepts to be derived is to interpret this limit as a classical limit, with $\hbar_{\text{eff}} = 1/N$, the inverse number of particles, playing the role of an effective Planck's constant. However, for describing the classical limit in terms of a Hamiltonian formalism, it is necessary for us to re-express the Hamiltonian in second quantization in terms of Hermitian operators which lead to conjugate variables in the classical limit.

To find such operators, let us note that the way creation and annihilation operators act upon many-body states reminds with intent of the use of ladder operators \hat{a} , \hat{a}^\dagger in the algebraic treatment of the harmonic oscillator. By understanding how one can arrive at the classical limit of the harmonic oscillator starting from the Hamiltonian expressed through ladder operators, we not only obtain a procedure which we can lift to the bosonic many-body scenario, but also can get additional fruitful intuition.

Expressed through ladder operators, the Hamiltonian and its eigenstates and -energies of the one-dimensional quantum harmonic oscillator of frequency ω are given by [91, 92]

$$\hat{H}_{\text{HO}} = \hbar\omega \left(\hat{a}^\dagger \hat{a} + \frac{1}{2} \right), \quad E_n = \hbar\omega \left(n + \frac{1}{2} \right), \quad |n\rangle = \frac{(\hat{a}^\dagger)^n}{\sqrt{n!}} |0\rangle, \quad n \in \mathbb{N}_0. \quad (3.12)$$

In view of bosonic many-body systems, the spectrum and the corresponding eigenstates of the harmonic oscillator can equivalently be interpreted as adding bosonic quasi-particles to the ground state. Writing the Hamiltonian for the quantum harmonic oscillator in terms of ladder operators is thus a way to elegantly solve the quantum problem. However, the question of the classical limit, in the sense of formally sending “ $\hbar \rightarrow 0$ ”, is better addressed with the Hamiltonian represented by the Hermitian position and momentum operators \hat{q} and \hat{p} . From the abstract point of view of ladder operators, these operators are related to the Hermitian and anti-Hermitian part of the lowering operator \hat{a} . In the common scaling including the particle’s mass m , we have

$$\hat{q} = \frac{1}{\sqrt{m\omega}} \hat{Q} = \frac{1}{\sqrt{m\omega}} \sqrt{\frac{\hbar}{2}} (\hat{a}^\dagger + \hat{a}), \quad (3.13)$$

$$\hat{p} = \sqrt{m\omega} \hat{P} = i\sqrt{m\omega} \sqrt{\frac{\hbar}{2}} (\hat{a}^\dagger - \hat{a}), \quad (3.14)$$

or equivalently,

$$\hat{a} = \frac{1}{\sqrt{2\hbar}} \left(\sqrt{m\omega} \hat{x} + i \frac{\hat{p}}{\sqrt{m\omega}} \right). \quad (3.15)$$

While the normalization with $\sqrt{m\omega}$ is due to a (canonical) scaling of the operators \hat{Q} and \hat{P} (with dimension $\sqrt{\text{Js}}$) towards position and momentum operators associated with the dimensions length and momentum, the more interesting scaling is with $\sqrt{\hbar/2}$. Through this factor, the Hamiltonian of the quantum harmonic oscillator transforms to an expression not directly depending on the Planck constant \hbar any more,

$$\hat{H}_{\text{HO}} = \frac{\hat{p}^2}{2m} + \frac{m\omega^2 \hat{q}^2}{2}. \quad (3.16)$$

while Planck’s constant \hbar is now included in the commutation relations of the position and momentum operator

$$[\hat{q}, \hat{p}] = [\hat{Q}, \hat{P}] = i\hbar. \quad (3.17)$$

This last commutator expression is extremely important in the discussion of the classical limit, where the commutator is translated into the Poisson bracket³, with the classical limits of the operators in its argument,

$$i\hbar = [\hat{q}, \hat{p}] \rightarrow i\hbar\{q, p\}. \quad (3.18)$$

³To be more precise, the Wigner-Weyl transformation of the commutator $[\hat{A}, \hat{B}]$ is the Moyal bracket of the Wigner-Weyl transforms of the operators \hat{A}, \hat{B} , see our discussion in section 4.1.1. The Poisson bracket emerges from the Moyal bracket as the lowest order in an expansion in powers of \hbar .

Comparing both sides we see that the Poisson bracket of the position and the momentum variable is unity. The classical limit of the position and momentum operator thus leads to a pair of conjugate variables and can thus be used to formalize the classical limit. Indeed, the Hamilton function describing the dynamics in the classical harmonic oscillator in terms of these conjugate variables is obtained from the quantum Hamiltonian essentially by substituting the operators with their classical correspondents. However, it should be noted that this simple substitution is a consequence of the structure of the quantum harmonic oscillator which does not contain products of position and momentum operators and therefore does not address the question of ordering.

Turning back to quantum bosonic many-body systems now, the above reasoning motivates the use of the Hermitian and anti-Hermitian part of the creation and annihilation operators. These operators have been well known as *quadrature operators* in the field of Quantum Optics [93]. They have also been used in the original works which introduced the semiclassical approximation for Bose-Hubbard models [33, 34]. The remainder of this section is indeed motivated from the presentation of quadrature states in the latter works, however explicitly discussing and including the effective Planck's constant, thus improving [33, 34].

As motivated in the beginning, for bosonic many-body systems we are interested in the classical/thermodynamic limit of a large total number of particles N . To be more precise here, we treat N as a parameter of the system, assuming that the many-body states of interest support an average particle number of $\mathcal{O}(N)$ ⁴. This way, we can define the effective Planck's constant

$$\hbar_{\text{eff}} = \frac{1}{N} \quad (3.19)$$

as the quantity for which “ $\hbar_{\text{eff}} \rightarrow 0$ ” defines the classical limit and which identifies the criterion when semiclassical tools are applicable to describe phenomena in the quantum system.

Using a scaling in accordance to the quantum harmonic oscillator, we define *position* and *momentum quadrature operators* by

$$\begin{aligned} \hat{q}_i &= \sqrt{\frac{\hbar_{\text{eff}}}{2}} (\hat{b}_i^\dagger + \hat{b}_i) = \frac{1}{\sqrt{2N}} (\hat{b}_i^\dagger + \hat{b}_i), \\ \hat{p}_i &= i\sqrt{\frac{\hbar_{\text{eff}}}{2}} (\hat{b}_i^\dagger - \hat{b}_i) = \frac{i}{\sqrt{2N}} (\hat{b}_i^\dagger - \hat{b}_i), \end{aligned} \quad (3.20)$$

or equivalently

$$\hat{b}_i = \sqrt{\frac{N}{2}} (\hat{q}_i + i\hat{p}_i), \quad \hat{b}_i^\dagger = \sqrt{\frac{N}{2}} (\hat{q}_i - i\hat{p}_i). \quad (3.21)$$

The occupation number operator \hat{n}_i uncovers the equivalence to the harmonic oscillator,

$$\frac{1}{2} (\hat{q}_i^2 + \hat{p}_i^2) = \frac{1}{N} \left(\hat{n}_i + \frac{1}{2} \right). \quad (3.22)$$

⁴In single-particle semiclassical physics one employs a similar reasoning by demanding that the de Broglie wave length λ_{dB} (as a parameter) is small compared to the smallest length scales of the system. The states are then chosen such that their wavelengths are $\mathcal{O}(\lambda_{\text{dB}})$.

In view of Eqs. (3.7) and (3.22), the scaling of quadrature operators with the total number of particles also gains a physical interpretation. Application of an annihilation or creation operator on an N -body bosonic state results in an additional prefactor of the order $\mathcal{O}(\sqrt{N})$, containing information about the total number of particles in the system. By choosing a scaling with the expected total number of particles N , we substitute these absolute occupations by the fraction of all particles found in the labeled single-particle state. It is through that step we are able to find a Hamiltonian formalism independent of N which is meaningful in the classical limit “ $N \rightarrow \infty$ ”.

It is easy to derive the commutator relations of position and momentum quadrature operators from the commutator relations of creation and annihilation operators,

$$[\hat{q}_i, \hat{q}_j] = [\hat{p}_i, \hat{p}_j] = 0, \quad [\hat{q}_i, \hat{p}_j] = i\hbar_{\text{eff}}\delta_{ij} = \frac{i}{N}\delta_{ij}. \quad (3.23)$$

Each of the sets of position and momentum quadrature operators, $\{\hat{q}_i \mid i \in I\}$ and $\{\hat{p}_i \mid i \in I\}$, forms a complete set of commuting Hermitian operators. Each of them thus allow us to find a basis of Fock space consisting of the common eigenstates of the operators in the set, with the corresponding eigenvalues as their labels. This leads to sets of so-called *position* and *momentum quadrature states*

$$\{|\mathbf{q}\rangle = |(q_i)_{i \in I}\rangle : \forall_{i \in I} q_i \in \mathbb{R}\}, \quad \{|\mathbf{p}\rangle = |(p_i)_{i \in I}\rangle : \forall_{i \in I} p_i \in \mathbb{R}\}, \quad (3.24)$$

where the states fulfill

$$\hat{q}_i |\mathbf{q}\rangle = q_i |\mathbf{q}\rangle, \quad \hat{p}_i |\mathbf{p}\rangle = p_i |\mathbf{p}\rangle, \quad i \in I. \quad (3.25)$$

Moreover, identically to the single-particle case and as a consequence from the commutation relations Eq. (3.23), the position quadrature representation of the momentum quadrature operator (and vice versa) is a differential operator⁵,

$$\begin{aligned} \langle \mathbf{q} | \hat{p}_i &= \frac{\hbar_{\text{eff}}}{i} \frac{\partial}{\partial q_i} \langle \mathbf{q} | = \frac{1}{iN} \frac{\partial}{\partial q_i} \langle \mathbf{q} |, \\ \langle \mathbf{p} | \hat{q}_i &= -\frac{\hbar_{\text{eff}}}{i} \frac{\partial}{\partial p_i} \langle \mathbf{p} | = -\frac{1}{iN} \frac{\partial}{\partial p_i} \langle \mathbf{p} |. \end{aligned} \quad (3.26)$$

The basis states are orthonormal in the sense that the overlap of two quadrature states is proportional to a Dirac- δ distribution

$$\begin{aligned} \langle \mathbf{q} | \mathbf{q}' \rangle &= \prod_{i \in I} \mathcal{N}^{(q)} \delta(q_i - q'_i), \\ \langle \mathbf{p} | \mathbf{p}' \rangle &= \prod_{i \in I} \mathcal{N}^{(p)} \delta(p_i - p'_i), \end{aligned} \quad (3.27)$$

⁵One way to proof this utilizes the translation operators $\exp[(i/\hbar_{\text{eff}})\hat{p}_i y]$ generated by the momentum quadrature operator. First one shows, that the operators $\exp[(i/\hbar_{\text{eff}})\hat{p}_i y]\hat{q}_i \exp[-(i/\hbar_{\text{eff}})\hat{p}_i y]$ and $\hat{q}_i + y$ are identical as solutions of the differential equation $d\hat{Q}_i/dy(y) = [\hat{p}_i, \hat{Q}_i(y)]$ with initial condition $\hat{Q}_i(0) = \hat{q}_i$. From this, one can conclude that $\langle \mathbf{q} + y\hat{\mathbf{e}}_i | = \langle \mathbf{q} | \exp[(i/\hbar_{\text{eff}})\hat{p}_i y]$, with $\hat{\mathbf{e}}_i$ the i -th standard basis vector, is again a (left) eigenstate of all position quadrature operators. Differentiating the last equality with respect to y and setting $y = 0$ leads to the result in the first line Eq. (3.26). The second identity follows analogously.

where $\mathcal{N}^{(q)}$, $\mathcal{N}^{(p)}$ denote arbitrary choices of normalization. This freedom in the choice of normalization is a consequence of the fact that quadrature states are unphysical states in the sense that they elude a physical interpretation through probability densities. However, quadrature states are useful tools for the intermediate steps of a technical treatment of an actual physical problem. We can therefore take for granted that quadrature states have been introduced into any calculation through the quadrature state representation of the unit operator,

$$\mathbf{1} = \left(\prod_{i \in \mathcal{I}} \int_{-\infty}^{\infty} \frac{dq_i}{\mathcal{N}^{(q)}} \right) |\mathbf{q}\rangle\langle\mathbf{q}|, \quad \mathbf{1} = \left(\prod_{i \in \mathcal{I}} \int_{-\infty}^{\infty} \frac{dp_i}{\mathcal{N}^{(p)}} \right) |\mathbf{p}\rangle\langle\mathbf{p}|. \quad (3.28)$$

Within this logic, the arbitrary normalizations $\mathcal{N}^{(q)}$, $\mathcal{N}^{(p)}$ are then compensated by the integration measure.

Finally, the normalization factors also appear in the overlap of a position with a momentum quadrature state. By solving either of the differential equations

$$\begin{aligned} \langle\mathbf{q}|\hat{p}_i|\mathbf{p}\rangle &= p_i \langle\mathbf{q}|\mathbf{p}\rangle = \frac{\hbar_{\text{eff}}}{i} \frac{\partial}{\partial q_i} \langle\mathbf{q}|\mathbf{p}\rangle \\ \langle\mathbf{p}|\hat{q}_i|\mathbf{q}\rangle &= q_i \langle\mathbf{p}|\mathbf{q}\rangle = -\frac{\hbar_{\text{eff}}}{i} \frac{\partial}{\partial p_i} \langle\mathbf{p}|\mathbf{q}\rangle \end{aligned} \quad (3.29)$$

we find

$$\langle\mathbf{q}|\mathbf{p}\rangle = \prod_{i \in \mathcal{I}} \frac{\mathcal{N}^{(q)}\mathcal{N}^{(p)}}{2\pi\hbar_{\text{eff}}} \exp\left(\frac{i}{\hbar_{\text{eff}}} q_i p_i\right) \quad (3.30)$$

where the additional factors within the overall normalization originate from the constraint that position with the momentum quadrature representation of states are related with each other through a Fourier transformation.

Like the overlap between quadrature states of the same type, Eq. (3.27), the overlap of quadrature states of different types, Eq. (3.30), should be understood in an distributional sense. This is most important in the case of an infinite set of indices \mathcal{I} , as otherwise, if naively combined to a single prefactor would result in 0, 1 or infinite, depending on the choice of normalizations $\mathcal{N}^{(q)}$, $\mathcal{N}^{(p)}$. Moreover, the scalar product $\mathbf{q}\mathbf{I}\mathbf{p}$ in the phase might also not lead to a finite value. For the construction of a semiclassical theory for bosonic systems with a countable infinite and uncountable index set, further discussions of these issues are needed. However, since the systems of choice to study OTOCs in this thesis are Bose-Hubbard models with a finite number of sites and thus a finite index set \mathcal{I} , we omit such a discussion here.

From now on we thus assume a finite index set $\mathcal{I} = \{1, \dots, d\}$ of size $\#\mathcal{I} = d$. This turns the labels of quadrature states to vectors in \mathbb{R}^d . Furthermore, to keep the notation identical to the d -dimensional quantum harmonic oscillator, we set the normalizations $\mathcal{N}^{(q)} = \mathcal{N}^{(p)} = 1$. Then, the different overlaps between quadrature states are given by

$$\langle\mathbf{q}|\mathbf{q}'\rangle = \delta^d(\mathbf{q} - \mathbf{q}'), \quad \langle\mathbf{p}|\mathbf{p}'\rangle = \delta^d(\mathbf{p} - \mathbf{p}'), \quad \langle\mathbf{q}|\mathbf{p}\rangle = \frac{\exp\left(\frac{i}{\hbar_{\text{eff}}}\mathbf{q}\mathbf{I}\mathbf{p}\right)}{(2\pi\hbar_{\text{eff}})^d}, \quad (3.31)$$

while the expansions of the unit operator become

$$\mathbf{1} = \int_{\mathbb{R}^d} d^d q |\mathbf{q}\rangle\langle\mathbf{q}|, \quad \mathbf{1} = \int_{\mathbb{R}^d} d^d p |\mathbf{p}\rangle\langle\mathbf{p}|. \quad (3.32)$$

Since in the following sections any integration over quadratures is over the integration volume \mathbb{R}^d , we drop the integration volume from our notations.

From its construction Fock states $|\mathbf{n}\rangle$ and quadrature states $|\mathbf{q}\rangle$ and $|\mathbf{p}\rangle$ in quantum bosonic many-body systems are formally equivalent to the eigenstates $|\mathbf{n}\rangle$ of the d -dimensional harmonic oscillator and the position and momentum states $|\mathbf{q}\rangle$ and $|\mathbf{p}\rangle$. This allows us to immediately identify the overlap of a Fock state with a position or a momentum quadrature state with the position and momentum representation of the corresponding eigenstate of the d -dimensional quantum harmonic oscillator. We thus find for the quadrature state representations of Fock states [91, 92]

$$\begin{aligned} \langle\mathbf{q}|\mathbf{n}\rangle &= \prod_{i=1}^d \left(\frac{1}{\pi \hbar_{\text{eff}}} \right)^{\frac{1}{4}} \frac{1}{\sqrt{2^{n_i} n_i!}} H_{n_i} \left(\frac{q_i}{\sqrt{\hbar_{\text{eff}}}} \right) e^{-\frac{1}{2} \frac{q_i^2}{\hbar_{\text{eff}}}}, \\ \langle\mathbf{p}|\mathbf{n}\rangle &= \prod_{i=1}^d \left(\frac{1}{\pi \hbar_{\text{eff}}} \right)^{\frac{1}{4}} \frac{i^{n_i}}{\sqrt{2^{n_i} n_i!}} H_{n_i} \left(\frac{p_i}{\sqrt{\hbar_{\text{eff}}}} \right) e^{-\frac{1}{2} \frac{p_i^2}{\hbar_{\text{eff}}}}, \end{aligned} \quad (3.33)$$

where H_n denote the Hermite polynomials defined by

$$H_n(y) = \exp\left(\frac{y^2}{2}\right) \left(y - \frac{\partial}{\partial y}\right)^n \exp\left(-\frac{y^2}{2}\right). \quad (3.34)$$

We see that beside being non-normalizable, quadrature states $|\mathbf{q}\rangle$ and $|\mathbf{p}\rangle$ have an in general non-vanishing overlap with Fock states of arbitrary number of particles.

The opposite interpretation is that a Fock state can be considered as delocalized in the quadrature state representation. To quantify this, we express quadrature operators through creation and annihilation operators to show that the expectation value of a quadrature operator in an arbitrary Fock state is 0, while the variance is growing with the relative number of occupation, n_i/N , of the single-particle state i

$$\begin{aligned} \langle\mathbf{n}|\hat{q}_i|\mathbf{n}\rangle &= \langle\mathbf{n}|\hat{p}_i|\mathbf{n}\rangle = 0, \\ \langle\mathbf{n}|\hat{q}_i^2|\mathbf{n}\rangle &= \langle\mathbf{n}|\hat{p}_i^2|\mathbf{n}\rangle = \hbar_{\text{eff}} \left(n_i + \frac{1}{2} \right) = \frac{n_i}{N} + \frac{1}{2N}. \end{aligned} \quad (3.35)$$

For the Fock states of interest, *i.e.* those with a particle number in the vicinity of N , the variance is of order 1, indicating delocalization of the Fock states in both the position and momentum quadratures.

3.1.4 Coherent states

A class of states which are localized in the quadrature variables is found to be given by *coherent states*, for which we present a small collection of properties in this subsection.

The details in the derivation of the following statements can be found in any standard reference, which discusses coherent states, *e.g.* [89, 94], but also in the main reference of the last section [33].

Coherent states are defined as the common eigenstates of the annihilation operators,

$$\hat{b}_i |\Phi\rangle = \Phi_i |\Phi\rangle, \quad i \in \{1, \dots, d\}, \quad \Phi \in \mathbb{C}^d, \quad (3.36)$$

with, since annihilation operators are non-Hermitian, in general complex eigenvalues Φ_i . It is found that for any complex vector $\Phi \in \mathbb{C}^d$ the eigenvalue equation can be solved and yields the eigenstate

$$|\Phi\rangle = \exp\left(-\frac{1}{2}\|\Phi\|^2 + \sum_{i=1}^d \hat{b}_i^\dagger \Phi_i\right) |0\rangle. \quad (3.37)$$

Contrary to quadrature states, coherent states are normalizable, and for Eq. (3.37) the prefactor has been chosen such that coherent states normalize to unity,

$$\langle \Phi | \Phi \rangle = 1. \quad (3.38)$$

The overlap with Fock states is easily calculated using Eq. (3.37)

$$\langle \mathbf{n} | \Phi \rangle = \exp\left(-\frac{1}{2}\|\Phi\|^2\right) \prod_{i=1}^d \frac{\Phi_i^{n_i}}{\sqrt{n_i!}}. \quad (3.39)$$

In principle, the normalization of coherent states would allow a physical interpretation in terms of a probability density. However, like quadrature states, coherent states in general have a nonzero overlap with Fock states with an arbitrary number of particles, and thus are non-physical, experimentally not realizable many-body states. The mean value and the variance in the relative occupation numbers \hat{n}_i/N are controlled by the modulus of the components Φ_i of the vector Φ labeling the coherent state,

$$\begin{aligned} \left\langle \Phi \left| \frac{\hat{n}_i}{N} \right| \Phi \right\rangle &= \frac{|\Phi_i|^2}{N}, \\ \left\langle \Phi \left| \left(\frac{\hat{n}_i}{N} \right)^2 \right| \Phi \right\rangle - \left(\left\langle \Phi \left| \frac{\hat{n}_i}{N} \right| \Phi \right\rangle \right)^2 &= \frac{|\Phi_i|^2}{N^2}. \end{aligned} \quad (3.40)$$

Finally, the position and momentum quadrature representations are found to be

$$\langle \mathbf{q} | \Phi \rangle = \left(\frac{1}{\pi \hbar_{\text{eff}}} \right)^{\frac{d}{4}} \exp\left[-\frac{1}{2}\|\Phi\|^2 + \frac{1}{2}\Phi^\top \Phi - \left(\frac{\mathbf{q}}{\sqrt{2\hbar_{\text{eff}}}} - \Phi \right)^\top \left(\frac{\mathbf{q}}{\sqrt{2\hbar_{\text{eff}}}} - \Phi \right)\right], \quad (3.41)$$

$$\langle \mathbf{p} | \Phi \rangle = \left(\frac{1}{\pi \hbar_{\text{eff}}} \right)^{\frac{d}{4}} \exp\left[-\frac{1}{2}\|\Phi\|^2 - \frac{1}{2}\Phi^\top \Phi - \left(\frac{\mathbf{p}}{\sqrt{2\hbar_{\text{eff}}}} + i\Phi \right)^\top \left(\frac{\mathbf{p}}{\sqrt{2\hbar_{\text{eff}}}} + i\Phi \right)\right]. \quad (3.42)$$

We gain a better understanding of the latter equations by expressing the components of the complex vector Φ by its real and imaginary part, in a similar way as we did for the annihilation operator, Eq. (3.21),

$$\Phi = \frac{1}{\sqrt{2\hbar_{\text{eff}}}}(\mathbf{q}_0 + i\mathbf{p}_0). \quad (3.43)$$

This converts Eqs. (3.41), (3.42) into a more intuitive form,

$$\begin{aligned} \langle \mathbf{q} | \Phi \rangle &= \left(\frac{1}{\pi\hbar_{\text{eff}}} \right)^{\frac{d}{4}} \exp \left[-\frac{(\mathbf{q} - \mathbf{q}_0)^\top (\mathbf{q} - \mathbf{q}_0)}{2\hbar_{\text{eff}}} + \frac{i\mathbf{p}_0^\top (\mathbf{q} - \mathbf{q}_0)}{\hbar_{\text{eff}}} + \frac{i\mathbf{p}_0^\top \mathbf{q}_0}{2\hbar_{\text{eff}}} \right], \\ \langle \mathbf{p} | \Phi \rangle &= \left(\frac{1}{\pi\hbar_{\text{eff}}} \right)^{\frac{d}{4}} \exp \left[-\frac{(\mathbf{p} - \mathbf{p}_0)^\top (\mathbf{q} - \mathbf{q}_0)}{2\hbar_{\text{eff}}} - \frac{i\mathbf{q}_0^\top (\mathbf{p} - \mathbf{p}_0)}{\hbar_{\text{eff}}} - \frac{i\mathbf{p}_0^\top \mathbf{q}_0}{2\hbar_{\text{eff}}} \right]. \end{aligned} \quad (3.44)$$

These last equations show that indeed the quadrature state representation of coherent states are Gaussian wave packets centered around the point $(\mathbf{q}_0, \mathbf{p}_0)$ with a width $\sqrt{\hbar_{\text{eff}}/2}$. In the classical limit $\hbar_{\text{eff}} \rightarrow 0$ these states become highly localized. Similar to coherent states for single-particle systems, these states can be interpreted as the quantum equivalent of the classical phase space point $(\mathbf{q}_0, \mathbf{p}_0)$ with a minimal Heisenberg uncertainty in the conjugate variables.

3.2 Bose-Hubbard models

The model for quantum many-body systems we want to consider in the context of OTOCs are *Bose-Hubbard models*. These are models describing a fixed number of sites, for instance in an optical lattice, which support interacting bosonic atoms. In its most generic form the Hamiltonian for these models is given in second quantization by

$$\hat{H} = \sum_{i,j=1}^d h_{ij} \hat{b}_i^\dagger \hat{b}_j + \sum_{i,j,k,l=1}^d U_{ijkl} \hat{b}_i^\dagger \hat{b}_j^\dagger \hat{b}_k \hat{b}_l, \quad (3.45)$$

where \hat{b}_i^\dagger and \hat{b}_i denote creation and annihilation operators of bosonic particles at site i . The first term contains hopping between single sites due to single-particle kinetics and external potentials, while the second one encodes interaction among the particles, both on- and offsite. In order for \hat{H} to be Hermitian the coefficients have to fulfill

$$h_{ij} = h_{ji}^*, \quad U_{ijkl} = U_{lkji}^*. \quad (3.46)$$

Furthermore due to the commutation relation of the bosonic creation and annihilation operators, Eq. (3.10) we can additionally choose the interaction matrix elements to fulfill

$$U_{ijkl} = U_{jikl} = U_{ijlk} = U_{jilk}. \quad (3.47)$$

Dealing with the classical/thermodynamic limit of a large number of particles N , or equivalently “ $\hbar_{\text{eff}} = 1/N \rightarrow 0$ ”, requires additional assumptions towards the Bose-Hubbard Hamiltonian. When acting on a Fock-state of N particles in the system,

creation and annihilation operators each gain a prefactor of the order $\mathcal{O}(\sqrt{N})$. This implies, that by increasing the number of particles N , the product $\hat{b}_i^\dagger \hat{b}_j$ of a creation and an annihilation operator in the single-particle term in Eq. (3.45) will scale with N , while the product $\hat{b}_i^\dagger \hat{b}_j^\dagger \hat{b}_k \hat{b}_l$ related to the interaction energy gains N^2 as a prefactor. If the parameters h_{ij} , U_{ijkl} in the interacting model are not themselves functions of the number of particles N , in the limit “ $N \rightarrow \infty$ ” the interaction term governs the dynamics of the system, leading to either a Mott insulating or a clustering state.

To avoid this trivial scenario, we thus require that when the N is increased, the strength of the interaction $U_{ijkl} = V_{ijkl}/N$ is simultaneously decreased by the inverse number of particles. Like for the definition of quadrature states, this requires to treat the number of particles N as a system parameter, with the underlying assumption that the states of interest in the later treatment of problems support a mean number of particles in the vicinity of N . The class of Bose-Hubbard models underlying this assumption is thus described by the Hamiltonian

$$\hat{H} = \sum_{i,j=1}^d h_{ij} \hat{b}_i^\dagger \hat{b}_j + \frac{1}{N} \sum_{i,j,k,l=1}^d V_{ijkl} \hat{b}_i^\dagger \hat{b}_j^\dagger \hat{b}_k \hat{b}_l, \quad (3.48)$$

where the parameters h_{ij} , V_{ijkl} are assumed to be of equal size in the limit $N \rightarrow \infty$.

3.3 The semiclassical approximation for the propagator

In this section we derive our main tool, the semiclassical approximation of the propagator for Bose-Hubbard models. This approximation of the position quadrature representation of the time-evolution operator enables us to link the dynamics in the quantum regime with that found to be the system’s classical limit “ $\hbar_{\text{eff}} = 1/N \rightarrow 0$ ”.

The derivation presented here follows the original derivation in Refs. [33, 34], which repeats in its techniques the derivation of the Van Vleck-Gutzwiller propagator for single-particle systems in the semiclassical limit “ $\hbar \rightarrow 0$ ”, see *e.g.* Refs. [1, 2]. The reason why it is presented here again in detail is that a precise discussion of the role of \hbar_{eff} in the arguments of the derivation of the semiclassical approximation of the propagator in quadrature state representation is missing in the original work. By including this carefully in the subsequent subsections we see that we obtain a different Hamilton function in the classical limit which does not contain terms due to ordering and which differs in the interaction term. Furthermore, we find that terms produced from ordering quadrature operators in the Hamiltonian result in an additional slowly varying phase.

3.3.1 The time-evolution operator

Our derivation starts rather generically by introducing the *time evolution operator* in the general sense for a system described by the (possibly time-dependent) Hamiltonian $\hat{H}(t)$. Only when we need details of system in the next subsection we restrict to the time-independent Bose-Hubbard models.

The action of the time-evolution operator $\hat{U}(t^{(f)}, t^{(i)})$ is such that, it transforms an initial state $|\Psi(t^{(i)})\rangle$ of the system at initial time $t^{(i)}$ into the state $|\Psi(t^{(f)})\rangle$ at later or final time $t^{(f)}$,

$$|\Psi(t^{(f)})\rangle = \hat{U}(t^{(f)}, t^{(i)}) |\Psi(t^{(i)})\rangle. \quad (3.49)$$

Using the Schrödinger equation one finds that the time evolution operator solves the initial value problem

$$i\hbar \frac{d}{dt} \hat{U}(t, t^{(i)}) = \hat{H}(t) \hat{U}(t, t^{(i)}), \quad \hat{U}(t^{(i)}, t^{(i)}) = \hat{\mathbf{1}}, \quad (3.50)$$

From Eq. (3.50) we can find a formal expression for the time-evolution operator, involving a time-ordered exponential,

$$\begin{aligned} \hat{U}(t, t') &= \mathcal{T} \exp \left(-\frac{i}{\hbar} \int_{t'}^t ds \hat{H}(s) \right) \\ &= \sum_{l=0}^{\infty} \left(-\frac{i}{\hbar} \right)^l \int_{t'}^t dt_1 \int_{t'}^{t_1} dt_2 \cdots \int_{t'}^{t_{l-1}} dt_l \hat{H}(t_1) \cdots \hat{H}(t_l). \end{aligned} \quad (3.51)$$

This expression simplifies to an ordinary exponential of an operator if the Hamiltonians at different times commute with each other. In such a case of no explicit time-dependence of the Hamiltonian, for instance for the Bose-Hubbard models considered within this work, we can choose $t^{(i)} = 0$ to be the zero of time and obtain

$$\hat{U}(t) \equiv \hat{U}(t, 0) = \exp \left(-\frac{i}{\hbar} \hat{H} t \right). \quad (3.52)$$

The time evolution operator fulfills the property

$$\hat{U}(t^{(f)}, t') \hat{U}(t', t^{(i)}) = \hat{U}(t^{(f)}, t^{(i)}), \quad (3.53)$$

reflecting the physical interpretation that a subsequent evolution in time for time spans $t^{(f)} - t'$ and $t' - t^{(i)}$ is identical to a single one of a time span $t^{(f)} - t^{(i)}$. In case of a time-independent Hamiltonian the above relation even allows us to interpret the set of all time-evolution operators mathematically as a semi-group, which coined the name “*semigroup property*” for Eq. (3.53).

Finally, from Eq. (3.50) and for an Hermitian Hamiltonian, one can conclude unitarity of the time evolution operator,

$$\hat{U}^\dagger(t^{(f)}, t^{(i)}) \hat{U}(t^{(f)}, t^{(i)}) = \hat{\mathbf{1}}. \quad (3.54)$$

The matrix element of $\hat{U}(t)$ in a continuous basis representation is denoted the *propagator*. For instance, in coordinate space representation \mathbf{q} , the propagator of a single-particle system is defined by

$$K(\mathbf{q}^{(f)}, t^{(f)}, \mathbf{q}^{(i)}, t) = \langle \mathbf{q}^{(f)} | \hat{U}(t^{(f)}, t^{(i)}) | \mathbf{q}^{(i)} \rangle. \quad (3.55)$$

The propagator is a scalar function which, in the time evolution of a state given in the chosen basis representation, plays the role of an integration kernel. Here,

$$\Psi(\mathbf{q}, t) = \langle \mathbf{q} | \Psi(t) \rangle = \int d^d q' K(\mathbf{q}, t, \mathbf{q}', t') \Psi(\mathbf{q}', t'). \quad (3.56)$$

In the context of Bose-Hubbard models, the representation we are interested in is in the basis of the position quadrature states $|\mathbf{q}\rangle$.

3.3.2 Feynman path integral representation of the propagator

The semi-group property of the time-evolution operator is extremely useful to rewrite this operator as the product of infinitely many, infinitesimal small time steps. This allows for a treatment of the time-ordering inherent in the formal result Eq. (3.51) since for small enough time steps we can not only treat the propagator as if the Hamiltonian is static, but also further replace the operator exponential through its Taylor expansion up to linear order in the time step.

To formalize this procedure we start by writing the time-evolution operator as the limit of a product of time-evolution operators, while assuming at the individual times a static Hamiltonian. Using Eq. (3.52), as well as the linearization of the matrix exponential, we find [95]

$$\begin{aligned} \hat{U}(t^{(f)}, t^{(i)}) &= \lim_{L \rightarrow \infty} \prod_{l=1}^L \exp \left[-\frac{i\tau_L}{\hbar} \hat{H}(t^{(f)} - l\tau_L) \right] \\ &= \lim_{L \rightarrow \infty} \prod_{l=1}^L \left[\hat{\mathbf{1}} - \frac{i\tau_L}{\hbar} \hat{H}(t^{(f)} - l\tau_L) \right], \end{aligned} \quad (3.57)$$

with time steps $\tau_L = (t^{(f)} - t^{(i)})/L \rightarrow 0$. The product has to be understood as an ordered matrix product through

$$\prod_{l=1}^L \hat{A}_l = \hat{A}_1 \hat{A}_2 \dots \hat{A}_L. \quad (3.58)$$

For a time-independent Hamiltonian, such as the one presented in Eq. (3.48), this ordered product reduces to

$$\hat{U}(t) = \lim_{L \rightarrow \infty} \left[\hat{\mathbf{1}} - \frac{i}{\hbar} \hat{H} \frac{t}{L} \right]^L. \quad (3.59)$$

In what follows we now restrict ourselves to Bose-Hubbard models with its propagator expressed in the basis of position quadrature states $|\mathbf{q}\rangle$. Furthermore, for reasons to become clear in a moment, we take the number of time steps to be even, $L = 2M$, and thus obtain an even number of factors in the product shown in Eq. (3.59).

Within the propagator in position quadrature representation, we alternately insert

unit operators in position and momentum quadrature representation to obtain

$$\begin{aligned}
K(\mathbf{q}^{(f)}, \mathbf{q}^{(i)}, t) &= \langle \mathbf{q}^{(f)} | \hat{U}(t) | \mathbf{q}^{(i)} \rangle \\
&= \lim_{M \rightarrow \infty} \int d^d p^{(M)} \int d^d q^{(M-1)} \int d^d p^{(M-1)} \dots \int d^d q^{(1)} \int d^d p^{(1)} \\
&\quad \times \prod_{m=1}^M \left\langle \mathbf{q}^{(m)} \left| \hat{\mathbf{1}} - \frac{i}{\hbar} \hat{H} \frac{t}{2M} \right| \mathbf{p}^{(m)} \right\rangle \left\langle \mathbf{p}^{(m)} \left| \hat{\mathbf{1}} - \frac{i}{\hbar} \hat{H} \frac{t}{2M} \right| \mathbf{q}^{(m-1)} \right\rangle
\end{aligned} \tag{3.60}$$

where we used $\mathbf{q}^{(M)} = \mathbf{q}^{(f)}$ and $\mathbf{q}^{(0)} = \mathbf{q}^{(i)}$ to simplify the notation. Due to the linearization of the single intermediate operators, the factors in the integrand only require the evaluation of a matrix element of the Hamiltonian. By using the normal ordered form, where momentum quadrature operators are found left of the position quadrature operators, the evaluation of these matrix element becomes trivial, and we present this calculation in the Appendix A.1. We find

$$\begin{aligned}
&\left\langle \mathbf{p} \left| \hat{\mathbf{1}} - \frac{i}{\hbar} \hat{H} \frac{t}{2M} \right| \mathbf{q} \right\rangle \\
&= \left(1 - \frac{i}{\hbar_{\text{eff}}} \left[\mathcal{H}(\mathbf{q}, \mathbf{p}) + \hbar_{\text{eff}} \left(\mathcal{H}_{\text{R}}^{(\text{ord})}(\mathbf{q}, \mathbf{p}) + i\mathcal{H}_{\text{I}}^{(\text{ord})}(\mathbf{q}, \mathbf{p}) \right) \right] \frac{t}{2M} \right) \langle \mathbf{p} | \mathbf{q} \rangle,
\end{aligned} \tag{3.61}$$

$$\begin{aligned}
&\left\langle \mathbf{q} \left| \hat{\mathbf{1}} - \frac{i}{\hbar} \hat{H} \frac{t}{2M} \right| \mathbf{p} \right\rangle = \left(\left\langle \mathbf{p} \left| \hat{\mathbf{1}} + \frac{i}{\hbar} \hat{H} \frac{t}{2M} \right| \mathbf{q} \right\rangle \right)^* \\
&= \left(1 - \frac{i}{\hbar_{\text{eff}}} \left[\mathcal{H}(\mathbf{q}, \mathbf{p}) + \hbar_{\text{eff}} \left(\mathcal{H}_{\text{R}}^{(\text{ord})}(\mathbf{q}, \mathbf{p}) - i\mathcal{H}_{\text{I}}^{(\text{ord})}(\mathbf{q}, \mathbf{p}) \right) \right] \frac{t}{2M} \right) \langle \mathbf{q} | \mathbf{p} \rangle,
\end{aligned} \tag{3.62}$$

where we expressed the results in terms of the real-valued functions $\mathcal{H}(\mathbf{q}, \mathbf{p})$, $\mathcal{H}_{\text{R}}^{(\text{ord})}(\mathbf{q}, \mathbf{p})$ and $\mathcal{H}_{\text{I}}^{(\text{ord})}(\mathbf{q}, \mathbf{p})$. Using the complex linear superposition $\Phi = (\mathbf{q} + i\mathbf{p})/\sqrt{2}$ for abbreviation, these function are given by

$$\begin{aligned}
\mathcal{H}(\mathbf{q}, \mathbf{p}) &= \sum_{i,j=1}^d \frac{h_{ij}}{\hbar} \Phi_i^* \Phi_j + \sum_{i,j,k,l=1}^d \frac{V_{ijkl}}{\hbar} \Phi_i^* \Phi_j^* \Phi_k \Phi_l, \\
\mathcal{H}_{\text{R}}^{(\text{ord})}(\mathbf{q}, \mathbf{p}) &= \sum_{i=1}^d \frac{h_{ii}}{2\hbar} + \sum_{i,j,l=1}^d \frac{2V_{ijjl}}{\hbar} \Phi_i^* \Phi_l + \hbar_{\text{eff}} \sum_{i,l=1}^d \left(\frac{V_{illi}}{2\hbar} - \frac{V_{iill}}{4\hbar} \right), \\
\mathcal{H}_{\text{I}}^{(\text{ord})}(\mathbf{q}, \mathbf{p}) &= \frac{1}{2i} \sum_{i,j,k,l=1}^d V_{ijkl} (\delta_{ij} \Phi_k \Phi_l - \delta_{kl} \Phi_i^* \Phi_j^*).
\end{aligned} \tag{3.63}$$

As we will see in the next subsection, the first function \mathcal{H} turns out to represent the Hamilton function⁶ of the classical limit of the Bose-Hubbard model, with \mathbf{q}, \mathbf{p} playing

⁶In this Hamilton function Planck's constant \hbar appears as a constant parameter and may not be confused with the effective Planck's constant $\hbar_{\text{eff}} = 1/N$, which defines with the classical limit.

the role of the conjugate variables. The other terms $\mathcal{H}_R^{(\text{ord})}$, $\mathcal{H}_I^{(\text{ord})}$ originate from the ordering process, which brings the products of quadrature operators in the Hamiltonian in normal order. Since this ordering requires the application of the commutation relations Eqs. (3.23), these functions are joined by an additional factor \hbar_{eff} in Eqs. (3.61), (3.62).

Inserting the matrix elements Eqs. (3.61), (3.62) back into Eq. (3.60) results in a product of the matrix elements. In the limit $M \rightarrow \infty$, we can express this product by an exponential since generally for large M and bounded factors A_m we have

$$\begin{aligned} \prod_{m=1}^M \left(1 - \frac{A_m}{M}\right) &= \exp\left(\sum_{m=1}^M \log\left(1 - \frac{A_m}{M}\right)\right) = \exp\left(-\sum_{m=1}^M \left(\frac{A_m}{M} + \mathcal{O}\left(\frac{1}{M^2}\right)\right)\right) \\ &= \exp\left(-\sum_{m=1}^M \frac{A_m}{M}\right) \left(1 + \mathcal{O}\left(\frac{1}{M}\right)\right). \end{aligned} \quad (3.64)$$

Using further Eq. (3.30) for the overlap $\langle \mathbf{q} | \mathbf{p} \rangle$ of a position with a momentum quadrature state, we get for the propagator

$$\begin{aligned} K(\mathbf{q}^{(f)}, \mathbf{q}^{(i)}, t) &= \langle \mathbf{q}^{(f)} | \hat{U}(t) | \mathbf{q}^{(i)} \rangle \\ &= \lim_{M \rightarrow \infty} \frac{1}{\sqrt{2\pi\hbar_{\text{eff}}}} \int d^d p^{(M)} \int d^d q^{(M-1)} \int d^d p^{(M-1)} \dots \int d^d q^{(1)} \int d^d p^{(1)} \\ &\quad \times \exp\left[\frac{i}{\hbar_{\text{eff}}} \sum_{m=1}^M \left(\mathbf{p}^{(m)} \cdot (\mathbf{q}^{(m)} - \mathbf{q}^{(m-1)})\right)\right] \\ &\quad \times \exp\left[-\frac{i}{\hbar_{\text{eff}}} \sum_{m=1}^M \frac{\mathcal{H}(\mathbf{q}^{(m)}, \mathbf{p}^{(m)}) + \mathcal{H}(\mathbf{q}^{(m-1)}, \mathbf{p}^{(m)})}{2} \frac{t}{M}\right] \\ &\quad \times \exp\left[-i \sum_{m=1}^M \frac{\mathcal{H}_R^{(\text{ord})}(\mathbf{q}^{(m)}, \mathbf{p}^{(m)}) + \mathcal{H}_R^{(\text{ord})}(\mathbf{q}^{(m-1)}, \mathbf{p}^{(m)})}{2} \frac{t}{M}\right] \\ &\quad \times \exp\left[-\sum_{m=1}^M \frac{\mathcal{H}_I^{(\text{ord})}(\mathbf{q}^{(m)}, \mathbf{p}^{(m)}) - \mathcal{H}_I^{(\text{ord})}(\mathbf{q}^{(m-1)}, \mathbf{p}^{(m)})}{2} \frac{t}{M}\right]. \end{aligned} \quad (3.65)$$

Upon integration, large differences in neighboring (labeled by m and $m+1$), quadrature variables of the same type lead to large oscillations in the phase factors and thus to cancellations. It is therefore reasonable to assume that non-canceling contributions to the multidimensional integration arises from vectors $(\mathbf{q}^{(m)}, \mathbf{p}^{(m)})_{m=1, \dots, M}$ each of which can be understood as the discretization of a sufficiently smooth path $\mathbf{q}(s)$, $\mathbf{p}(s)$, with $\mathbf{q}(s)$ fulfilling the boundary condition $\mathbf{q}(0) = \mathbf{q}^{(i)}$, $\mathbf{q}(t) = \mathbf{q}^{(f)}$. Under this assumption⁷ it is possible to interpret the arguments of the exponential as the Riemann sums of integrations of sufficiently smooth functions. Note that within these sums, the effective

⁷To be precise, the assumption is reasonable in view of constructing a semiclassical approximation of the propagator. When working directly with the Feynman path integral, this assumption has to be questioned as different derivations of the path integral may lead to non-equivalent results [96].

time-step is t/M , the elapsed time between two subsequent position, respective momentum quadrature variables in Eq. (3.60), which is twice the time step used in the slicing of the time evolution operator. In the limit $M \rightarrow \infty$, we find

$$\sum_{m=1}^M \mathbf{p}^{(m)} \frac{\mathbf{q}^{(m)} - \mathbf{q}^{(m-1)}}{\frac{t}{M}} \frac{t}{M} \xrightarrow{M \rightarrow \infty} \int_0^t ds \mathbf{p}(s) \cdot \dot{\mathbf{q}}(s), \quad (3.66)$$

$$\begin{aligned} \sum_{m=1}^M \frac{\mathcal{H}(\mathbf{q}^{(m)}, \mathbf{p}^{(m)}) + \mathcal{H}(\mathbf{q}^{(m-1)}, \mathbf{p}^{(m)})}{2} \frac{t}{M} \\ \xrightarrow{M \rightarrow \infty} \int_0^t ds \frac{\mathcal{H}(\mathbf{q}(s), \mathbf{p}(s)) + \mathcal{H}(\mathbf{q}(s), \mathbf{p}(s))}{2} = \int_0^t ds \mathcal{H}(\mathbf{q}(s), \mathbf{p}(s)), \end{aligned} \quad (3.67)$$

$$\begin{aligned} \sum_{m=1}^M \frac{\mathcal{H}_R^{(\text{ord})}(\mathbf{q}^{(m)}, \mathbf{p}^{(m)}) + \mathcal{H}_R^{(\text{ord})}(\mathbf{q}^{(m-1)}, \mathbf{p}^{(m)})}{2} \frac{t}{M} \\ \xrightarrow{M \rightarrow \infty} \int_0^t ds \mathcal{H}_R^{(\text{ord})}(\mathbf{q}(s), \mathbf{p}(s)), \end{aligned} \quad (3.68)$$

$$\begin{aligned} \sum_{m=1}^M \frac{\mathcal{H}_I^{(\text{ord})}(\mathbf{q}^{(m)}, \mathbf{p}^{(m)}) - \mathcal{H}_I^{(\text{ord})}(\mathbf{q}^{(m-1)}, \mathbf{p}^{(m)})}{2} \frac{t}{M} \\ \xrightarrow{M \rightarrow \infty} \int_0^t ds \frac{\mathcal{H}_I^{(\text{ord})}(\mathbf{q}(s), \mathbf{p}(s)) - \mathcal{H}_I^{(\text{ord})}(\mathbf{q}(s), \mathbf{p}(s))}{2} = 0. \end{aligned} \quad (3.69)$$

Quite interestingly, we see that in the limit $M \rightarrow \infty$, the argument associated with the function $\mathcal{H}_I^{(\text{ord})}(\mathbf{q}, \mathbf{p})$, originating from the imaginary part of the overlap $\langle \mathbf{p} | \hat{H} | \mathbf{q} \rangle$, converges to zero and thus does not result in an exponential growth or decay of the integrand. Within the limit $M \rightarrow \infty$, we can therefore safely neglect $\mathcal{H}_I(\mathbf{q}, \mathbf{p})$ and end up with

$$\begin{aligned} K(\mathbf{q}^{(f)}, \mathbf{q}^{(i)}, t) \\ = \lim_{M \rightarrow \infty} \frac{1}{\sqrt{2\pi\hbar_{\text{eff}}}} \int d^d p^{(M)} \int d^d q^{(M-1)} \int d^d p^{(M-1)} \dots \int d^d q^{(1)} \int d^d p^{(1)} \\ \times \exp \left[\frac{i}{\hbar_{\text{eff}}} \sum_{m=1}^M \left(\mathbf{p}^{(m)} \cdot (\mathbf{q}^{(m)} - \mathbf{q}^{(m-1)}) \right) \right] \\ \times \exp \left[-\frac{i}{\hbar_{\text{eff}}} \sum_{m=1}^M \frac{\mathcal{H}(\mathbf{q}^{(m)}, \mathbf{p}^{(m)}) + \mathcal{H}(\mathbf{q}^{(m-1)}, \mathbf{p}^{(m)})}{2} \frac{t}{M} \right] \\ \times \exp \left[-i \sum_{m=1}^M \frac{\mathcal{H}_R^{(\text{ord})}(\mathbf{q}^{(m)}, \mathbf{p}^{(m)}) + \mathcal{H}_R^{(\text{ord})}(\mathbf{q}^{(m-1)}, \mathbf{p}^{(m)})}{2} \frac{t}{M} \right], \end{aligned} \quad (3.70)$$

In view of our interpretation in terms of smooth paths, we can use an abbreviating

formal notation

$$K(\mathbf{q}^{(f)}, \mathbf{q}^{(i)}, t) = \int_{\substack{\mathbf{q}(t)=\mathbf{q}^{(f)} \\ \mathbf{q}(0)=\mathbf{q}^{(i)}}} \mathcal{D}[\mathbf{q}(s), \mathbf{p}(s)] \exp\left(\frac{i}{\hbar_{\text{eff}}} R[\mathbf{q}(s), \mathbf{p}(s)] + i\varphi[\mathbf{q}(s), \mathbf{p}(s)]\right), \quad (3.71)$$

with the action functional

$$R[\mathbf{q}(s), \mathbf{p}(s)] = \int_0^t ds [\mathbf{p}(s) \cdot \dot{\mathbf{q}}(s) - \mathcal{H}(\mathbf{q}, \mathbf{p})], \quad (3.72)$$

and an additional phase due to ordering of operators,

$$\varphi[\mathbf{q}(s), \mathbf{p}(s)] = \int_0^t ds \mathcal{H}_{\text{R}}^{(\text{ord})}(\mathbf{q}(s), \mathbf{p}(s)). \quad (3.73)$$

This final representation, Eq (3.71), is referred to as the *path integral representation of the propagator*, formally displayed as an integration over all possible and sufficiently smooth paths $(\mathbf{p}(s), \mathbf{q}(s))$ with the position quadrature component of the path fulfilling the boundary conditions $\mathbf{q}(0) = \mathbf{q}^{(i)}$, $\mathbf{q}(t) = \mathbf{q}^{(f)}$. For the actual calculation of the path integral, one has of course to understand the path integral in the version with discretized paths, Eq. (3.70).

3.3.3 The semiclassical approximation of the propagator

The stationary phase approximation

A direct evaluation of the multidimensional integration is not possible since the components of integration vectors $\mathbf{q}^{(m)}$, $\mathbf{p}^{(m)}$ appear as a fourth order polynomial in the arguments of the oscillating exponential functions. However, within the semiclassical limit “ $\hbar_{\text{eff}} = 1/N \rightarrow 0$ ” we can employ a powerful technique known by the name *stationary phase approximation*, see for instance Refs. [95, 97]. Generally speaking, this method provides a recipe to approximate integrals of the form

$$F(\lambda) = \int_{-\infty}^{\infty} dx g(x) \exp(i\lambda f(x)), \quad (3.74)$$

with real-valued smooth functions $f(x)$, $g(x)$ in the limit $\lambda \gg 1$. In that regime the argument of the phase factor $\exp(i\lambda f(x))$ is varying rapidly as a function of x , leading to destructive interference of the phases and thus to a negligible contribution to the integration. It is only when this variation in the frequency becomes small that we obtain constructive interference, and consequently a significant contribution to the integral. To identify areas with a slowly varying phase is formalized to solving the *stationarity condition*

$$\frac{df}{dx}(x^{(s)}) = 0 \left(\text{while } \frac{d^2f}{dx^2}(x^{(s)}) \neq 0 \right). \quad (3.75)$$

We denote the solutions $x^{(s)}$ of this extreme value problem as *stationary points*, and the magnitude of contributions to the integration Eq. (3.74) arises from the close vicinity

of these points.⁸ We can thus split the integration $F(\lambda)$ into a sum of integrations, each around an appropriate vicinity of one of the stationary points. In this vicinity of stationary point, we can use Taylor expansions to write

$$\begin{aligned} g(x^{(s)} + y) &\approx g(x^{(s)}) \\ f(x^{(s)} + y) &\approx f(x^{(s)}) + \frac{1}{2} \frac{d^2 f}{dx^2} y^2, \end{aligned} \quad (3.76)$$

Finally, we extend the integration over the vicinity of the stationary points to an integration over the whole real space to obtain a sum of Gaussian integrals, which we can easily evaluate,

$$\begin{aligned} F(\lambda) &\approx \sum_{\substack{\text{stationary} \\ \text{points } x^{(s)}}} g(x^{(s)}) \exp(i\lambda f(x^{(s)})) \int_{-\infty}^{\infty} dy \exp\left(i \frac{\lambda}{2} \frac{d^2 f}{dx^2}(x^{(s)}) y^2\right) \\ &= \sum_{\substack{\text{stationary} \\ \text{points } x^{(s)}}} g(x^{(s)}) \sqrt{\frac{2\pi}{\lambda \left| \frac{d^2 f}{dx^2}(x^{(s)}) \right|}} \exp\left(i\lambda f(x^{(s)}) + i \frac{\pi}{4} \text{sign}\left(\frac{d^2 f}{dx^2}(x^{(s)})\right)\right) \end{aligned} \quad (3.77)$$

As is discussed in Ref. [95], the combined effect of our approximations is to neglect terms approaching 0 as $\mathcal{O}(1/\lambda)$ in the limit $\lambda \rightarrow \infty$. Asymptotically these contributions vanish faster than the result of the stationary phase approximation which is $\mathcal{O}(1/\sqrt{\lambda})$. This is also the reason, why the Taylor expansion of g terminates after the zeroth order in Eq. (3.76).

The method can be easily generalized to multidimensional integrals of the form

$$F(\lambda) = \int_{\mathbb{R}^d} d^d x g(\mathbf{x}) \exp(i\lambda f(\mathbf{x})), \quad (3.78)$$

for which the intermediate result is a sum over stationary points $\mathbf{x}^{(s)}$ of multidimensional Gaussian integrals,⁹

$$F(\lambda) \approx \sum_{\substack{\text{stationary} \\ \text{points } \mathbf{x}^{(s)}}} g(\mathbf{x}^{(s)}) \exp(i\lambda f(\mathbf{x}^{(s)})) \int_{\mathbb{R}^d} d^d y \exp\left(i \frac{\lambda}{2} \mathbf{y}^\top \frac{\partial^2 f}{\partial \mathbf{x} \partial \mathbf{x}}(\mathbf{x}^{(s)}) \mathbf{y}\right). \quad (3.79)$$

Through a transformation, which diagonalized the Jacobi matrix $\frac{\partial^2 f}{\partial \mathbf{x} \partial \mathbf{x}}(\mathbf{x}^{(s)})$, the d -dimensional Gaussian integral is converted into a product of d one-dimensional Gaussian

⁸To be more precise, as discussed in Ref. [95], the major contributions stem from a distance of the order $\mathcal{O}(1/\sqrt{\lambda})$ from stationary points and, as we see in a moment, result in contributions behaving asymptotically like $1/\sqrt{\lambda}$ for $\lambda \gg 1$. Contrarily, the contributions from the surroundings of a generic point x , which is sufficiently far away from a stationary point, behaves asymptotically like $1/\lambda$, which vanishes faster than $1/\sqrt{\lambda}$.

⁹This results holds, if the stationary points are isolated from each other. In case of a manifold of stationary points, one first needs to perform a change of variables including directions within the manifold, and treat the integration within the set of stationary points exactly. An example is Gutzwiller's trace formula, where the set of stationary points is given by periodic orbits [1, 2].

integrals. The product of eigenvalues, which we find in the denominator, is identified with the determinant of the Jacobi matrix. We obtain

$$\begin{aligned}
F(\lambda) &\approx \sum_{\substack{\text{stationary} \\ \text{points } \mathbf{x}^{(s)}}} g(\mathbf{x}^{(s)}) \sqrt{\frac{(2\pi)^d}{\lambda^d \left| \det \left(\frac{\partial^2 f}{\partial \mathbf{x} \partial \mathbf{x}}(x^{(s)}) \right) \right|}} \exp\left(i\lambda f(\mathbf{x}^{(s)}) + i\frac{\pi}{4}\beta(\mathbf{x}^{(s)})\right) \\
&= \sum_{\substack{\text{stationary} \\ \text{points } \mathbf{x}^{(s)}}} g(\mathbf{x}^{(s)}) \sqrt{\frac{(2\pi i)^d}{\lambda^d \left| \det \left(\frac{\partial^2 f}{\partial \mathbf{x} \partial \mathbf{x}}(x^{(s)}) \right) \right|}} \exp\left(i\lambda f(\mathbf{x}^{(s)}) - i\frac{\pi}{2}\nu(\mathbf{x}^{(s)})\right),
\end{aligned} \tag{3.80}$$

where $\beta(\mathbf{x})$ denotes the difference in the number of positive and negative eigenvalues, and $\nu(\mathbf{x})$ the number of negative eigenvalues of the Jacobi matrix. These numbers are related to each other and the dimension d through the identity

$$\beta(\mathbf{x}) = d - 2\nu(\mathbf{x}). \tag{3.81}$$

Stationarity condition for the path integral

We now apply the stationary phase approximation to solve the multidimensional integral over all position and momentum quadratures in Eq. (3.70) in the semiclassical limit of “ $\hbar_{\text{eff}} = 1/N \rightarrow 0$ ”, whose inverse will play the role of $\lambda = 1/\hbar_{\text{eff}}$ in the approximation.

While we perform the actual calculation for the discretized integral, Eq. (3.70), to get an understanding of the physical implication of this approximation, it is useful to formally examine the stationarity condition at the level of the continuous path integral, Eq. (3.71). There the set of partial derivatives turns into a set of functional derivatives or variations. Note that the boundary conditions, which fix the position quadrature component at initial and final time, $\mathbf{q}(0) = \mathbf{q}^{(i)}$, $\mathbf{q}(t) = \mathbf{q}^{(f)}$, has to be considered within this variation. We obtain

$$\begin{aligned}
0 &= \frac{\delta}{\delta p_i(s')} R[\mathbf{q}(s), \mathbf{p}(s)] = \dot{q}_i(s') - \frac{\partial \mathcal{H}}{\partial p_i}(\mathbf{q}(s'), \mathbf{p}(s')), \\
0 &= \frac{\delta}{\delta q_i(s')} R[\mathbf{q}(s), \mathbf{p}(s)] = -\dot{p}_i(s') - \frac{\partial \mathcal{H}}{\partial q_i}(\mathbf{q}(s'), \mathbf{p}(s')),
\end{aligned} \tag{3.82}$$

for $i = 1, \dots, d$. Comparing these equations with Eq. (2.2) we can interpret the solutions of the stationarity condition as trajectories solving Hamilton’s equations of motion with \mathcal{H} as the underlying Hamilton function and with the position and momentum quadratures \mathbf{q} , \mathbf{p} playing the role of the pair of conjugate variables.

The actual full calculation of the propagator in stationary phase approximation, including the calculation of the amplitude weighting the contribution of the single paths, as well as additional phases, is performed at the level of the discretized version of the path integral, Eq. (3.70) and is presented in detail in appendix A.2. From this calculation we obtain the *semiclassical approximation for the propagator in position quadrature*

state representation, given by

$$K^{(\text{sc})}(\mathbf{q}^{(\text{f})}, \mathbf{q}^{(\text{i})}, t) = \sum_{\gamma: \mathbf{q}^{(\text{i})} \xrightarrow{t} \mathbf{q}^{(\text{f})}} A_{\gamma}(\mathbf{q}^{(\text{f})}, \mathbf{q}^{(\text{i})}, t) \exp\left(\frac{i}{\hbar_{\text{eff}}} R_{\gamma}(\mathbf{q}^{(\text{f})}, \mathbf{q}^{(\text{i})}, t)\right), \quad (3.83)$$

where the summation runs over all classical trajectories, *i.e.* solutions of Hamilton's equations of motion, Eq. (3.82), with the boundary conditions $\mathbf{q}_{\gamma}(0) = \mathbf{q}^{(\text{i})}$, $\mathbf{q}_{\gamma}(t) = \mathbf{q}^{(\text{f})}$. The phase factor contains Hamilton's principal function R_{γ} , as defined in Eq. (2.5), and the (complex) amplitude A_{γ} is given by

$$\begin{aligned} & A_{\gamma}(\mathbf{q}^{(\text{f})}, \mathbf{q}^{(\text{i})}, t) \\ &= \sqrt{\frac{1}{(2\pi\hbar_{\text{eff}})^d} \left| \det\left(\frac{\partial^2 R_{\gamma}}{\partial \mathbf{q}^{(\text{f})} \partial \mathbf{q}^{(\text{i})}}(\mathbf{q}^{(\text{f})}, \mathbf{q}^{(\text{i})}, t)\right) \right|} \exp\left[-i\left(\frac{\pi}{4}\mu_{\gamma} + \phi_{\gamma}(\mathbf{q}^{(\text{f})}, \mathbf{q}^{(\text{i})}, t)\right)\right]. \end{aligned} \quad (3.84)$$

The absolute value of A_{γ} contains second order derivatives of R_{γ} with respect to the boundary conditions. Through that amplitude, the contribution of the trajectory γ to the coherent sum in Eq. (3.83) is weighted by its stability upon variations of the boundary conditions. The phase of A_{γ} contains the *Maslov index* μ_{γ} counting the number of divergences of the prefactor, which are interpreted as number of conjugate points along the trajectory, *i.e.* points, for which a bundle of classical trajectories fulfilling the boundary problem can be found [1, 2]. The second contribution to the phase is the function

$$\phi_{\gamma}(\mathbf{q}^{(\text{f})}, \mathbf{q}^{(\text{i})}, t) = \frac{1}{4} \int_0^t ds \text{tr} \left[\frac{\partial^2 \mathcal{H}}{\partial \mathbf{q} \partial \mathbf{q}}(\mathbf{q}_{\gamma}(s), \mathbf{p}_{\gamma}(s)) + \frac{\partial^2 \mathcal{H}}{\partial \mathbf{p} \partial \mathbf{p}}(\mathbf{q}_{\gamma}(s), \mathbf{p}_{\gamma}(s)) \right] \quad (3.85)$$

and originates from the phase space function $\mathcal{H}_{\text{R}}^{(\text{ord})}$ (re-expressed here in terms of second derivatives of the Hamilton function). This phase is thus attributed to the normal ordering of the Hamiltonian. This phase has been also found in the derivation of a semiclassical approximation for the propagator in coherent state representation [98, 99], and is called *Solari-Kochetov phase*. Within the scope of this work, a detailed knowledge of the Maslov index and the phase due to ordering is not necessary, and thus, for a deeper understanding of these quantities, we like to refer the reader towards the existing literature, for instance Refs. [1, 2, 100]

As a concluding remark, it is possible to view the equations of motion, Eq. (3.82), as the real and imaginary part of a dynamical equation for the complex function $\Phi(t) = (\mathbf{q} + i\mathbf{p})/\sqrt{2}$,

$$i \frac{\partial \Phi_i}{\partial t} = \frac{\partial \mathcal{H}}{\partial \Phi_i^*}(\Phi, \Phi^*) = \sum_{j=1}^d \frac{h_{ij}}{\hbar} \Phi_j + 2 \sum_{j,k,l=1}^d \frac{V_{ijkl}}{\hbar} \Phi_j^* \Phi_k \Phi_l, \quad (3.86)$$

which is the well-known Gross-Pitaevskii equation [24, 25, 101], here in its discrete form as consequence of the finite number of sites in the Bose-Hubbard model. Within our reasoning, any solution of the Gross-Pitaevskii equation can thus be interpreted as the classical wave equation describing the dynamics of the Bose-Hubbard model in the classical limit.

4 Semiclassical analysis of out-of-time-order correlators (OTOCs)

In this chapter we study out-of-time-order correlators (OTOCs), which can be used as sensitive probes for chaos in the classical limit of an interacting many-body quantum system. To gain intuition, we provide an explanation for the short-time behaviour of OTOCs based on the quantum-classical correspondence principle. We see that for suitably chosen OTOCs the short-time dynamics is able to discriminate a chaotic classical limit, where OTOCs experience an exponential growth, from an integrable one with an at most polynomial growth of OTOCs.

For systems with a chaotic classical limit, it is observed that the growth saturates after the so-called Ehrenfest time t_E , a time which marks the onset of quantum interference not captured by the quantum-classical correspondence principle. For N -particle Bose-Hubbard models in the semiclassical limit of a large number of particles, “ $\hbar_{\text{eff}} = 1/N \rightarrow 0$ ”, we develop, based on the semiclassical approximation of the propagator, a semiclassical theory, which is able to capture both the pre- and the post-Ehrenfest time behaviour of OTOCs. We show that the initial exponential growth is related to the Lyapunov exponent of the classical mean-field dynamics, thus justifying the intuitive picture by Maldacena *et al.* [43]. Finally, we identify the underlying interference mechanism leading to the saturation and the classical quantities involved in the latter.

Having introduced the necessary concepts in classical dynamics and our main tool for a semiclassical treatment, the semiclassical approximation for the propagator, we are now ready to start our discussion of OTOCs. The results presented in this chapter have been published in Ref. [102], and we follow the presentation in this article to a large extent. Especially the sections containing the details of the involved calculations of diagrams show a substantial overlap with the corresponding sections I wrote for the supplemental material in the above publication.

4.1 The OTOCs and their expected behaviour for short times

A possible definition of an out-of-time-order correlator (OTOC) is given by the average of the squared commutator of two operators in the Heisenberg picture, where the operators

are taken at different times [43–45, 103],

$$C(t) = \left\langle \left| \left[\hat{V}(0), \hat{W}(t) \right] \right|^2 \right\rangle \equiv \left\langle \left[\hat{V}(0), \hat{W}(t) \right]^\dagger \left[\hat{V}(0), \hat{W}(t) \right] \right\rangle. \quad (4.1)$$

The average can be over an initial state Ψ , or thermal over the canonical ensemble, $\langle \cdot \rangle = \text{tr}(\exp(-\beta \hat{H}) \cdot) / Z(\beta)$, with the partition function $Z(\beta) = \text{tr}(\exp(-\beta \hat{H}))$, and with $\beta = 1/(kT)$ as the inverse temperature T with Boltzmann's constant k . Especially for thermal averages, one often finds a second version of the OTOC's definition [43, 49],

$$F(t) = \langle \hat{V}^\dagger(0) \hat{W}^\dagger(t) \hat{V}(0) \hat{W}(t) \rangle, \quad (4.2)$$

which appears as one of the terms when carrying out the products involved in the squared commutator in Eq. (4.1).

4.1.1 Wigner-Weyl transformations

The importance of OTOCs as sensitive probes for chaos in quantum systems arises from its dynamical behaviour for short times. To understand this, we can employ arguments based on the quantum-classical correspondence principle to obtain a first, simple intuitive picture. As we formalize this in detail in a moment, this principle replaces the operators in the averaged squared commutator $C(t)$ in Eq. (4.1) operators by their classical counterparts and the commutator by the classical Poisson bracket. The evaluation of the Poisson bracket introduces elements of the stability matrix \mathbf{M} , Eq. (2.10), whose dynamical behaviour is able to discriminate a chaotic from an integrable classical limit of the quantum system [43].

While quantum-classical correspondence directly yields a first prediction of the dynamical behaviour of $C(t)$ as the leading order in a power expansion in \hbar_{eff} , for the OTOC $F(t)$ in Eq. (4.2) one needs to include the next to leading order, requiring further arguments¹. In both cases, the conclusions drawn from the application of OTOCs on quantum chaotic systems are the same, but require more work for $F(t)$. For the remainder of this thesis we thus focus directly on OTOCs of the form given in Eq. (4.1).

We want to put the above reasoning into an exact statement which we can later also use to check the results of the semiclassical treatment of OTOCs. To do so, we first specify the exact meaning of the quantum-classical correspondence principle by reviewing the concepts of *Wigner-Weyl transformation*. An introduction to the formalism of Wigner-Weyl transformations is found in Refs. [94, 104, 105]. Here, we briefly summarize the results found in these references.

¹For these arguments one takes $F(t)$ as one of the terms appearing in $C(t)$. For $C(t)$ one argues in the same way as we do here, but on top of that an interpretation of the other terms next to $F(t)$ is required. The common arguments rely on a regularization of the thermal average [43] to be able to apply the cycling property of the trace. Furthermore, time-ordered products like $\langle \hat{V}^\dagger(0) \hat{V}(0) \hat{W}^\dagger(t) \hat{W}(t) \rangle$, are assumed to factorize after the ergodic time t_L and thus to contribute a constant. This leads to the prediction that $F(t) \propto c_1 - \hbar_{\text{eff}}^2 \exp(2\lambda t)$ for times $t \ll t_E$.

For an operator \hat{A} , the Wigner-Weyl transformation in d dimensions is defined as²

$$A(\mathbf{q}, \mathbf{p}) \equiv [\hat{A}]_{\text{W}}(\mathbf{q}, \mathbf{p}) = \frac{1}{\sqrt{2\pi\hbar_{\text{eff}}^d}} \int d^d y \left\langle \mathbf{q} - \frac{y}{2} \left| \hat{A} \right| \mathbf{q} + \frac{y}{2} \right\rangle \exp\left(\frac{i}{\hbar_{\text{eff}}} \mathbf{p}^\top \mathbf{y}\right), \quad (4.3)$$

where \hbar_{eff} is the effective Planck's constant controlling the classical limit of the quantum system. In this formalism the *Wigner function* appears as the Wigner-Weyl transformation of the density operator $\hat{\rho}$,

$$W(\mathbf{q}, \mathbf{p}) \equiv [\hat{\rho}]_{\text{W}}(\mathbf{q}, \mathbf{p}) = \frac{1}{\sqrt{2\pi\hbar_{\text{eff}}^d}} \int d^d y \left\langle \mathbf{q} - \frac{y}{2} \left| \hat{\rho} \right| \mathbf{q} + \frac{y}{2} \right\rangle \exp\left(\frac{i}{\hbar_{\text{eff}}} \mathbf{p}^\top \mathbf{y}\right). \quad (4.4)$$

The common interpretation of this function is that it represent the density operator as a classical quasi-distribution in phase space. Here, the name quasi-distribution indicates that the Wigner function has similar properties like a probability distribution. Indeed, it is a real function, which is normalized to one, and quantum mechanical averages of an observable are identical to phase space averages of the Wigner-Weyl transformation of that operator,

$$\langle \hat{A} \rangle = \text{Tr}(\hat{\rho} \hat{A}) = \int d^d q \int d^d p W(\mathbf{q}, \mathbf{p}) A(\mathbf{q}, \mathbf{p}). \quad (4.5)$$

However, since it may admit negative values, the Wigner function is not a proper probability distribution. In the Wigner-Weyl formalism, a product of operators transforms to the so-called *star product* of the individual transformations of operators. The definition of this non-commutative product is given by

$$\begin{aligned} [\hat{A}\hat{B}]_{\text{W}}(\mathbf{q}, \mathbf{p}) &= A(\mathbf{q}, \mathbf{p}) \star B(\mathbf{q}, \mathbf{p}) \\ &= A(\mathbf{q}, \mathbf{p}) \exp\left(\frac{i\hbar_{\text{eff}}}{2} \sum_{i=1}^d \left[\overleftarrow{\frac{\partial}{\partial q_i}} \overrightarrow{\frac{\partial}{\partial p_i}} - \overleftarrow{\frac{\partial}{\partial p_i}} \overrightarrow{\frac{\partial}{\partial q_i}} \right]\right) B(\mathbf{q}, \mathbf{p}), \end{aligned} \quad (4.6)$$

where the exponential has to be understood through its Taylor expansion, and arrows above the derivatives indicate that it either acts on the function A to the left or B to the right. In lowest order in an expansion in powers of \hbar_{eff} , the star product simplifies to a simple product $A(\mathbf{q}, \mathbf{p})B(\mathbf{q}, \mathbf{p})$ of the functions.

The star product allows us to immediately identify the Wigner-Weyl transformation of the commutator. The obtained object is coined Moyal bracket and, for instance, as transformation of the commutator $[\hat{A}, \hat{B}]$ given by

$$\begin{aligned} \{\{A(\mathbf{q}, \mathbf{p}), B(\mathbf{q}, \mathbf{p})\}\} &= \left[[\hat{A}, \hat{B}] \right]_{\text{W}}(\mathbf{q}, \mathbf{p}) \\ &= A(\mathbf{q}, \mathbf{p}) \star B(\mathbf{q}, \mathbf{p}) - B(\mathbf{q}, \mathbf{p}) \star A(\mathbf{q}, \mathbf{p}) \\ &= i\hbar_{\text{eff}} \{A(\mathbf{q}, \mathbf{p}), B(\mathbf{q}, \mathbf{p})\} + \mathcal{O}(\hbar_{\text{eff}}^2), \end{aligned} \quad (4.7)$$

²There is also a more abstract definition of the Wigner-Weyl transformation which involves so-called displacement operators. This allows certain generalizations to other choices of phase space variables, see Ref. [94]. However, for our application here, the two definitions coincide, and we chose the better known classic approach.

where in the last equality we discovered the classical Poisson bracket, $\{.,.\}$, Eq. (2.36), as the leading order in the \hbar_{eff} -expansion of the Moyal bracket.

Finally, let us make an important observation for the Wigner-Weyl transformation $\tilde{A}(t; \mathbf{q}, \mathbf{p})$ of an operator $\hat{A}(t)$ in the Heisenberg picture. The equation of motion for this time-dependent function is obtained by performing the Wigner-Weyl transformation on both sides of the equations of motion for $\hat{A}(t)$, $d\hat{A}(t)/dt = i/\hbar_{\text{eff}}[\hat{H}, \hat{A}(t)] + \partial\hat{A}/\partial t$. In leading order in the \hbar_{eff} -expansion, this resembles the classical equation of motion for a phase space function $A(t, \mathbf{q}^{(f)}(t), \mathbf{p}^{(f)}(t)) = A(t, \mathbf{q}^{(f)}(t; \mathbf{q}, \mathbf{p}), \mathbf{p}^{(f)}(t; \mathbf{q}, \mathbf{p}))$ transported along classical trajectories³,

$$\frac{dA}{dt} = -\left\{ \mathcal{H}(\mathbf{q}^{(f)}(t), \mathbf{p}^{(f)}(t)), A(t; \mathbf{q}^{(f)}(t), \mathbf{p}^{(f)}(t)) \right\} + \frac{\partial A}{\partial t}. \quad (4.8)$$

The initial conditions are $\tilde{A}(0; \mathbf{q}, \mathbf{p}) = A(0, \mathbf{q}, \mathbf{p})$, and thus we conclude

$$\tilde{A}(t; \mathbf{q}, \mathbf{p}) = A(t; \mathbf{q}^{(f)}(t, \mathbf{q}, \mathbf{p}), \mathbf{p}^{(f)}(t, \mathbf{q}, \mathbf{p})) + \mathcal{O}(\hbar_{\text{eff}}). \quad (4.9)$$

This explains the name ‘‘quantum-classical correspondence principle’’, since in leading order operators within the Wigner-Weyl formalism are replaced by their classical counterparts.

4.1.2 Expected behavior of OTOCs

We want to apply the Wigner-Weyl formalism to OTOCs and discuss its consequences. To be more explicit in an example, let us take a single-particle system and choose $\hat{V} = \hat{p}_i$ and $\hat{W} = \hat{q}_j$, the components of the momentum and the position operator of the particle. The OTOC we want to consider is thus given by

$$C(t) = \langle [\hat{p}_i(0), \hat{q}_j(t)] [\hat{q}_j(t), \hat{p}_i(0)] \rangle = \text{tr}(\hat{\rho}[\hat{p}_i(0), \hat{q}_j(t)] [\hat{q}_j(t), \hat{p}_i(0)]). \quad (4.10)$$

Using the above results from the Wigner-Weyl formalism $C(t)$ can be transformed into

$$C(t) = \hbar_{\text{eff}}^2 \int d^d q \int d^d p W(\mathbf{q}, \mathbf{p}) \{ \{ p_i, \tilde{q}_j(t; \mathbf{q}, \mathbf{p}) \} \} \star \{ \{ p_i, \tilde{q}_j(t; \mathbf{q}, \mathbf{p}) \} \}, \quad (4.11)$$

where we used that the Wigner-Weyl transformation of \hat{p}_i is p_i . At this stage, $\tilde{q}_j(t; \mathbf{q}, \mathbf{p})$ does not denote the final point of a classical trajectory starting at (\mathbf{q}, \mathbf{p}) , but the transformation of $\hat{q}_j(t)$.

³The Hamilton function here is the leading order of the Wigner-Weyl transformation of the Hamiltonian \hat{H} . It is obtained by simply replacing operators by scalars. Ordering of the operators is not required here, since this only introduces corrections in higher orders of \hbar_{eff} .

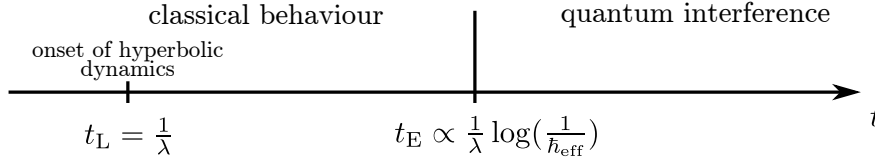


Figure 4.1: Time scales and their influence on the dynamical behaviour of OTOCs.

The classical counterparts are introduced by evaluating the above average in the leading order in the expansion in powers of \hbar_{eff} . We find⁴

$$\begin{aligned} C(t) &= \hbar_{\text{eff}}^2 \int d^d q \int d^d p W(\mathbf{q}, \mathbf{p}) \left(\left\{ p_i, q_j^{(f)}(t; \mathbf{q}, \mathbf{p}) \right\} \right)^2 + \mathcal{O}(\hbar_{\text{eff}}^3) \\ &= \hbar_{\text{eff}}^2 \int d^d q \int d^d p W(\mathbf{q}, \mathbf{p}) \left(\frac{\partial q_j^{(f)}}{\partial q_i^{(i)}}(t; \mathbf{q}, \mathbf{p}) \right)^2 + \mathcal{O}(\hbar_{\text{eff}}^3). \end{aligned} \quad (4.12)$$

In the integrand we recover the derivative of a trajectory's final position component $q_j^{(f)}$ w.r.t. its initial position component $q_i^{(i)}$. This derivative is identified as one matrix element of the stability matrix \mathbf{M} , Eq. (2.10), and thus, Eq. (4.12) represents a phase space average of the squared stability matrix element, with the Wigner function used as weight.

So far we did not make any assumption on the quantum system, as long as it allows for the notion of a classical limit in which \mathbf{q}, \mathbf{p} play the role of conjugate variables. In case of an integrable limit, the above matrix elements are expected to grow at most polynomially. Contrarily, for a chaotic classical limit, the unstable directions soon govern the dynamical behaviour of the stability matrix elements. More exactly, this is expected to happen after the time scale set by the Lyapunov time $t_L = 1/|\lambda|$, with λ denoting the largest Lyapunov exponent found for the phase space points involved in the average. After this time scale, the derivatives grow exponentially in time, with λ as rate of growth, as a consequence of the hyperbolic nature of chaotic systems. Thus

$$\left(\frac{\partial q_j^{(f)}}{\partial q_i^{(i)}}(t; \mathbf{q}, \mathbf{p}) \right)^2 \underset{t > t_L}{\sim} \exp(2\lambda t). \quad (4.13)$$

Thus, we expect that the OTOC behaves as

$$C(t) \approx \left\langle \left(\frac{\partial q_j^{(f)}}{\partial q_i^{(i)}}(t; \mathbf{q}, \mathbf{p}) \right)^2 \right\rangle_W \approx \langle c \hbar_{\text{eff}}^2 e^{2\lambda t} \rangle_W \quad (4.14)$$

where $\langle \cdot \rangle_W$ denotes a phase space average using the Wigner function, and c a proportionality constant.

⁴In order to reduce the danger of confusing phase space variables, we decided here, to differ from the notation introduced in chapter 2 and add superscripts ^(f) and ⁽ⁱ⁾ to a phase space point and its components to make explicit that it denotes a trajectory's final or initial phase space point.

So far, higher orders in the expansion of the Moyal bracket and the Wigner transforms of the operators have not been considered, and it is expected that those are causing deviations from the behaviour in Eq. (4.14). This ultimately culminates in the breakdown of the \hbar_{eff} expansion of the Moyal bracket at the Ehrenfest time $t_E \propto (1/\lambda) \log((1/\hbar_{\text{eff}}))$, since then, roughly speaking, the powers in \hbar_{eff} are compensated by the exponential growth, $\hbar_{\text{eff}} \exp(\lambda t_E) = 1$. For that reason, Eq. (4.14) is only a valid approximation for the OTOC for times $t \ll t_E$, thus reflecting the short-time or pre-Ehrenfest time behaviour of OTOCs.

Physically, the Ehrenfest time marks the time scale at which details of the order of \hbar_{eff} have grown to a significant size. At this time, a purely classical treatment of the dynamics breaks down and interference phenomena have to be included into the considerations. For the OTOC this means a breakdown of the expected exponential growth. Many works, for instance Refs. [53, 61, 106, 107], reported a saturation of the OTOC after the Ehrenfest time as a consequence of quantum interference, without stating the exact nature of interference mechanism. It is one of the major aims of our semiclassical theory of OTOCs to clarify this mechanism.

Before we go beyond this classical picture in the semiclassical treatment of OTOCs, it is worth to specify the proportionality c contained in Eq. (4.14) for a later check of the short-time limit of our theory. We use again $\mathbf{x}' = (\mathbf{q}', \mathbf{p}')$ [see Eq. (2.1)] to abbreviate the notation for a phase space point, and we introduce $[\cdot]_{q_j}$ and $[\cdot]_{p_i}$ to indicate the corresponding components of a vector of phase space. For instance, for real vectors $\mathbf{u}, \mathbf{v} \in \mathbb{R}^d$,

$$\left[\begin{pmatrix} \mathbf{u} \\ \mathbf{v} \end{pmatrix} \right]_{q_j} = u_j, \quad \left[\begin{pmatrix} \mathbf{u} \\ \mathbf{v} \end{pmatrix} \right]_{p_i} = v_i. \quad (4.15)$$

Analogously we use $[\cdot]_{q_j, q_i}$ to indicate an element of matrix operating on phase space vectors. We reformulate $\partial q_j^{(f)} / \partial q_i^{(i)}$ using the decomposition Eq. (2.18) of the stability matrix. For times longer than t_L , we have

$$\begin{aligned} \frac{\partial q_j^{(f)}}{\partial q_i^{(i)}}(t; \mathbf{x}) &= [\mathbf{M}(t; \mathbf{x})]_{q_j, q_i} \underset{t > t_L}{\approx} \sum_{i=1}^k \left[\mathbf{e}_u^{(i)}(\mathbf{x}^{(f)}(t; \mathbf{x})) \right]_{q_j} \exp(\lambda^{(i)}(\mathbf{x})t) \left[\mathbf{f}_u^{(i)}(\mathbf{x}) \right]_{q_i} \\ &= - \sum_{i=1}^k \left[\mathbf{e}_u^{(i)}(\mathbf{x}^{(f)}(t; \mathbf{x})) \right]_{q_j} \exp(\lambda^{(i)}(\mathbf{x})t) \left[\mathbf{e}_s^{(i)}(\mathbf{x}) \right]_{p_i}, \end{aligned} \quad (4.16)$$

where k denotes the number of unstable directions. We neglected terms in the decomposition which relate to stable and neutral directions, since for $t > t_L$ those are exponentially suppressed against the contributions of the unstable directions. For the last equality, we further used the relations Eq. (2.32) to re-express the dual vector of the unstable direction, $\mathbf{f}_u^{(i)}(\mathbf{x}) = -\Sigma \mathbf{e}_s^{(i)}(\mathbf{x})$ by the corresponding vector towards the stable direction, as obtained by the pairing rule (see subsection 2.2.3). Ultimately, we also replaced the stretching rates by their asymptotic form, $\Lambda_u^{(i)}(t; \mathbf{x}) \approx \exp(\lambda_i(\mathbf{x})t)$. This introduces the spectrum of the Lyapunov exponents $\lambda_l(\mathbf{x})$ of the phase space point \mathbf{x} . By

inserting Eq. (4.16) into Eq. (4.12) we obtain an expression representing the short-time dynamics of OTOCs for times $t_L < t < t_E$.

It is quite clear from Eq. (4.16) that the largest Lyapunov exponent soon governs the exponential growth, while its prefactor in the integrand is given by the sum of products $[\mathbf{e}_u^{(i)}(\mathbf{x}^{(f)}(t, \mathbf{x}))]_{q_j} [\mathbf{e}_s^{(i)}(\mathbf{x})]_{p_i}$ of all directions corresponding to this largest Lyapunov exponent. To simplify the subsequent considerations, we assume a uniformly hyperbolic system, in which additionally all Lyapunov exponents have the same absolute value. For that scenario, the expected behaviour boils down to the expression

$$C(t) \underset{t_L < t < t_E}{\approx} \hbar_{\text{eff}}^2 e^{2\lambda t} \int d^d p \int d^d q W(\mathbf{q}, \mathbf{p}) \left(\sum_{i=1}^k [\mathbf{e}_u^{(i)}(\mathbf{x}^{(f)}(t, \mathbf{x}))]_{q_j} [\mathbf{e}_s^{(i)}(\mathbf{x})]_{p_i} \right)^2. \quad (4.17)$$

As a final remark, the above arguments indicate that for the exponential growth of OTOCs only the property of hyperbolicity is needed. For instance in the work by Geiger *et al.* [108] investigating the integrable Lieb-Liniger model, the wave function Ψ involved in the average is chosen such that the Wigner function favors an area of phase space which is subject to *local* hyperbolic dynamics. There, an exponential growth of OTOCs is also observed, even though the classical phase space is integrable. However, due to the absence of the mixing property, the OTOC does not saturate immediately after the Ehrenfest time, but rather shows an oscillatory behaviour.

4.2 Semiclassical treatment of OTOCs for bosonic many-body systems

Our aim is to study OTOCs in an interacting many-body scenario. Since we have a well-controlled semiclassical theory in which we also identify the classical/thermodynamic limit of a large number N of particles, the system we choose to study OTOCs in is a generic Bose-Hubbard models whose d sites support a state with an average of N interacting bosons. The Hamiltonian for such a system is stated in Eq. (3.45). For convenience,

$$\hat{H} = \sum_{i,j=1}^d h_{ij} \hat{b}_i^\dagger \hat{b}_j + \frac{1}{N} \sum_{ijkl=1}^d V_{ijkl} \hat{b}_i^\dagger \hat{b}_j^\dagger \hat{b}_k \hat{b}_l, \quad (4.18)$$

where \hat{b}_i^\dagger (\hat{b}_i) are creation (annihilation) operators at sites $i = 1, \dots, d$, see section 3.1.2. The parameters h_{ij} contain on-site energies and hopping terms, and V_{ijkl} denote interactions. The expected number of particles N is included as a parameter into the system to balance the energies in the kinetic, single-particle part of the Hamiltonian against the interaction energy. This is needed to avoid the trivial behavior in the classical or thermodynamic limit $N \rightarrow \infty$.

Taking $\hbar_{\text{eff}} = 1/N$ as the effective Planck's constant, we identified the Hamiltonian formalism describing this limit in section 3.3 during the derivation of the semiclassical approximation for the propagator in quadrature state representation. These latter states

are the eigenstates of the position and a momentum quadrature operator defined in Eq. (3.20). For convenience,

$$\hat{q}_i = \frac{1}{\sqrt{2}} (\hat{b}_i + \hat{b}_i^\dagger), \quad \hat{p}_i = \frac{1}{\sqrt{2i}} (\hat{b}_i - \hat{b}_i^\dagger), \quad i \in \{1, \dots, d\}. \quad (4.19)$$

The classical analogues of these operators are naturally used as phase space variables, and in Eq. (3.63) we identify the Hamilton function of the classical “ $\hbar_{\text{eff}} = 1/N$ ” limit to be

$$\mathcal{H}(\mathbf{q}, \mathbf{p}) = \sum_{i,j=1}^d \frac{h_{ij}}{\hbar} \Phi_i^* \Phi_j + \sum_{i,j,k,l=1}^d \frac{V_{ijkl}}{\hbar} \Phi_i^* \Phi_j^* \Phi_k \Phi_l, \quad (4.20)$$

where the vector $\Phi = (\mathbf{q} + i\mathbf{p})/\sqrt{2}$ contains as a complex combination of the conjugate position and momentum quadrature vectors.

To support the intuition developed in the last section we choose for our studies an OTOC whose commutator contains the position and a momentum quadrature operator and formally resembles the one in Eq. (4.10). The average is taken over an initial state $|\Psi\rangle$. Explicitly writing the time-evolution operators used for the Heisenberg picture, the OTOC we are about to study is given by

$$C(t) = \left\langle \Psi \left| \left[\hat{p}_i, \hat{U}^\dagger(t) \hat{q}_j \hat{U}(t) \right] \left[\hat{U}^\dagger(t) \hat{q}_j \hat{U}(t), \hat{p}_i \right] \right| \Psi \right\rangle. \quad (4.21)$$

The arguments of the last section still formally apply and immediately grant us a prediction for the short-time limit of the correlator through Eqs. (4.12) and (4.17). We can use these predictions to benchmark the semiclassical theory we develop in the next subsections. OTOCs with more generic operators are discussed in section 4.5.

4.2.1 The trajectory-based semiclassical representation of the OTOC

Our semiclassical theory relies on using the semiclassical approximation for the many-body propagator for Bose-Hubbard models, Eq. (3.83). In a first step, we thus transform the time evolution operators into propagators by inserting multiple unit operators, expressed in the basis of position quadrature states. This results in a multidimensional integral, whose integrand contains the product of four propagators. Furthermore, the position and momentum quadrature operator are replaced by their position quadrature representations, which are an integration variable and a differential operator as seen in Eqs. (3.25) and (3.26). Thus,

$$\begin{aligned} C(t) &= \left\langle \Psi \left| \mathbf{1} \cdot \left[\hat{p}_i, \hat{U}^\dagger(t) \cdot \mathbf{1} \cdot \hat{q}_j \cdot \hat{U}(t) \right] \cdot \mathbf{1} \cdot \left[\hat{U}^\dagger(t) \cdot \mathbf{1} \cdot \hat{q}_j \cdot \hat{U}(t), \hat{p}_i \right] \cdot \mathbf{1} \right| \Psi \right\rangle \\ &= \int d^d q_1 \int d^d q_2 \int d^d q_3 \int d^d q_4 \int d^d q_5 \Psi^*(\mathbf{q}_1) \Psi(\mathbf{q}_5) \\ &\quad \times \left[\left(\frac{\hbar}{i} \frac{\partial}{\partial q_{1,i}} + \frac{\hbar}{i} \frac{\partial}{\partial q_{3,i}} \right) K^*(\mathbf{q}_2, \mathbf{q}_1, t) q_{2,j} K(\mathbf{q}_2, \mathbf{q}_3, t) \right] \\ &\quad \times \left[\left(-\frac{\hbar}{i} \frac{\partial}{\partial q_{5,i}} - \frac{\hbar}{i} \frac{\partial}{\partial q_{3,i}} \right) K^*(\mathbf{q}_4, \mathbf{q}_3, t) q_{4,j} K(\mathbf{q}_4, \mathbf{q}_5, t) \right]. \end{aligned} \quad (4.22)$$

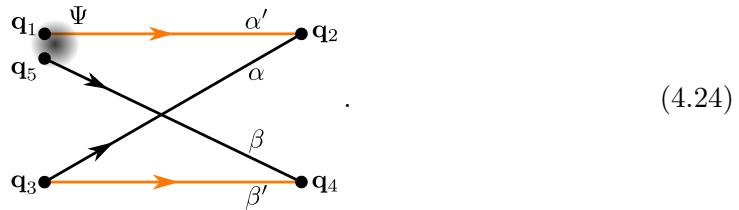
Next, we replace the propagators involved in this integral representation by their semiclassical approximation $K^{(\text{sc})}$, Eq. (3.83). The derivatives w.r.t. $q_{1,i}$, $q_{3,i}$ and $q_{5,i}$ are only acting on the phase factors containing the classical action R_γ in K , not the amplitude A_γ , since in the latter case we obtain contributions which are of the same order in \hbar_{eff} than the terms we neglected within the stationary phase approximation in section 3.3.3. Using further the identity $\partial R_\gamma / \partial \mathbf{q}^{(i)} = -\mathbf{p}_\gamma^{(i)}$ [see Eq. (2.6)], the integral representation of the OTOC Eq. (4.21) transforms into

$$C(t) \approx \int d^d q_1 \int d^d q_2 \int d^d q_3 \int d^d q_4 \int d^d q_5 \Psi^*(\mathbf{q}_1) \Psi(\mathbf{q}_5) \quad (4.23)$$

$$\times \sum_{\substack{\alpha': \mathbf{q}_1 \xrightarrow{t} \mathbf{q}_2 \\ \alpha: \mathbf{q}_3 \rightarrow \mathbf{q}_2 \\ \beta': \mathbf{q}_3 \rightarrow \mathbf{q}_4 \\ \beta: \mathbf{q}_5 \rightarrow \mathbf{q}_4}} A_{\alpha'}^* A_\alpha A_{\beta'} A_\beta e^{\frac{i}{\hbar_{\text{eff}}}(-R_{\alpha'} + R_\alpha - R_{\beta'} + R_\beta)} \left(p_{\alpha',i}^{(i)} - p_{\alpha,i}^{(i)} \right) q_{\alpha,j}^{(f)} \left(p_{\beta,i}^{(i)} - p_{\beta',i}^{(i)} \right) q_{\beta,j}^{(f)}.$$

The four time evolution operators in Eq. (4.21) have been transformed into a fourfold sum over contributions from trajectories of temporal length t linking different initial and final position quadratures. The initial and final position quadratures, which define the boundary conditions for the trajectory, are indicated in the indices of the summation. Note that in principle, these boundary conditions, as well as the time t , would also appear as argument of any of the trajectory-labeled quantities, but for the ease of reading we dropped these arguments in our notations. Finally, to aide our argumentation towards generalizing the results later in section 4.5, we also re-expressed the integration variables appearing in the integrand as final position quadrature of trajectories, for instance $q_{2,j} = q_{\alpha',j}^{(f)}(\mathbf{q}_2, \mathbf{q}_3, t)$.

Some of the initial and final boundary conditions of the trajectories, represented by the integration variables \mathbf{q}_2 , \mathbf{q}_3 and \mathbf{q}_4 , are each shared by two trajectories. Furthermore, the initial position quadratures \mathbf{q}_1 and \mathbf{q}_5 are associated to the variables used within the wave function. By introducing a schematic representation, in which black and orange arrows refer to contributions of a trajectory contained in the coherent sum in $K^{(\text{sc})}$ and $K^{(\text{sc})*}$, we can visualize the geometrical arrangement of the trajectories quadruplet with respect to their boundary conditions,



The initial state $|\Psi\rangle$ is indicated by a gray shaded spot. By taking a state which is localized in both quadrature states, such as a coherent state (see section 3.1.4) we can assume that contributions to the OTOC arise from trajectory constellations where \mathbf{q}_1 and \mathbf{q}_5 are close to each other.

As we can see from Eq. (4.23), the effect of using semiclassical techniques is so far to replace the operators appearing in the OTOC by their classical analogues – here the initial momentum quadrature $p_{\gamma,i}^{(i)}$ and the final position quadrature $q_{\gamma,j}^{(f)}$ of trajectories $\gamma \in \{\alpha, \beta, \alpha', \beta'\}$. The commutators themselves translate into differences of the initial momentum quadratures.

To simplify the presentation of the technical details we work with a set of assumptions:

- The initial wave packet $|\Psi\rangle$ is localized in both quadratures. Such properties are found, for instance, for a many-body coherent state, see section 3.1.4.
- The only two constants of motion for the classical (mean-field) dynamics are the classical energy as the value of the classical Hamilton function,

$$E = \mathcal{H}(\mathbf{q}, \mathbf{p}), \quad (4.25)$$

and the total number of particles in the system, normalized by N . The classical constant of motion for the latter is given by

$$\mathcal{N}(\mathbf{q}, \mathbf{p}) = \sum_{i=1}^d |\Phi_i|^2 = \frac{1}{2} \sum_{i=1}^d (q_i^2 + p_i^2). \quad (4.26)$$

- The $(2d-2)$ -dimensional submanifold of phase space defined by these two constants of motion is chaotic with uniformly hyperbolic dynamics. Furthermore, all positive Lyapunov exponents are assumed to be the same at any phase space point, and we denote it by λ (see subsection 2.3.2).

In section 4.5 we present a discussion of the consequences to expect when the above assumptions are relaxed in order to comply for more realistic implementations of systems described by the Bose-Hubbard model.

4.2.2 Identification of the main contributions to the OTOC

In the semiclassical limit the classical action $R_\gamma(\mathbf{q}^{(f)}, \mathbf{q}^{(i)}; t)$ of a typical trajectory γ , is large compared to \hbar_{eff} , $R_\gamma(\mathbf{q}^{(f)}, \mathbf{q}^{(i)}; t) \gg \hbar_{\text{eff}}$. Thus, the phase factors in Eq. (4.23) are highly oscillatory when varying the initial or final position quadratures within the integrals. Therefore, an arbitrary choice of trajectories within the quadruplet in Eq. (4.24) in general results in a negligible contribution after integration. Only a constellation of correlated trajectories which gives rise to an action difference $R_\alpha - R_{\alpha'} + R_\beta - R_{\beta'} \simeq \mathcal{O}(\hbar_{\text{eff}})$ of the order of \hbar_{eff} leads to a significant contribution to $C(t)$. Since we assume a classical chaotic limit for the Bose-Hubbard model, such constellations only arise in a systematic manner when most of the time trajectories are pairwise almost identical [68, 109]. A change of partners is possible in so-called *encounter regions* in phase space in which all four trajectories stay for a limited time in close vicinity of each other⁵. As we will

⁵While we do not need this for the discussion of OTOCs within this thesis, for completeness we like to note that an encounter region can also contain a time-reversed versions of a trajectory. After such

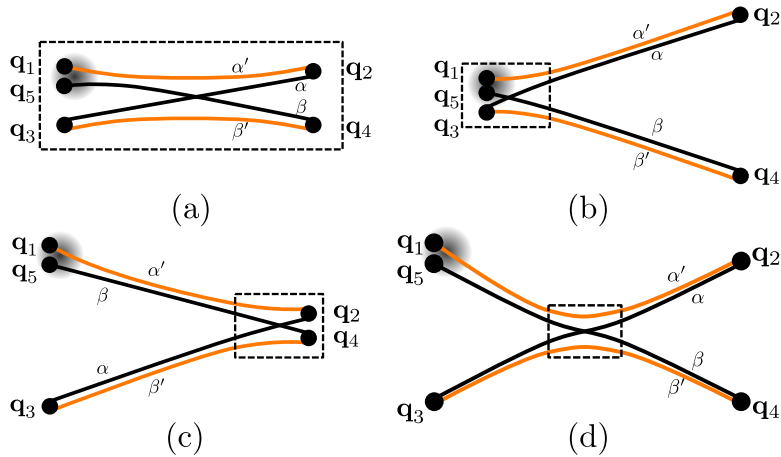


Figure 4.2: Constellations of trajectories that represent the dominant contributions to the OTOC $C(t)$, Eq. (4.23). In (a), the trajectory quadruples are fully contained within a single encounter (marked by a dashed box), and we denote this diagram a “zero-leg” diagram. The subfigures (b) and (c) form a “two-leg” diagram with an encounter (b) at the beginning or (c) at the end. Finally, in (d) a “four-leg” diagram with an intermediate encounter of all trajectories is shown.

see in the next section in detail, forming an encounter heavily relies on the hyperbolic dynamics of the classical chaotic limit, as trajectories need to exponentially approach and diverge from each other within these regions.

For OTOCs the relevant constellations of trajectories involve a single encounter and can be subdivided into four classes, which differ in the role and the position of this encounter region. We depict the four diagram classes in Fig. 4.2, where boxes indicate the encounter region. Diagram (a) shows a “zero-leg” diagram⁶, in which a bundle of four trajectories is staying in close vicinity to each other, thereby forming an encounter during the whole time t . This scenario is slightly more realistically visualized in Fig. 4.3. Panels (b) and (c) display “two-leg” diagrams with an encounter at the beginning or end, and with uncorrelated dynamics of the two trajectory pairs (“legs”) outside the encounter. Finally, the “four-leg” diagrams in (d) are characterized by uncorrelated

a region, a trajectory might follow the path of a time-reversed version of trajectory, a mechanism, which is used to explain, for instance, weak localization [4, 110]. In such scenarios, time-reversal symmetry of the classical system is required, and thus contributions arising from such constellations are sensitive to time-reversal symmetry breaking mechanism, such as magnetic fields in electronic transport scenarios [71, 110], or artificial gauge fields in the Gross-Pitaevskii description of bosonic transport [29].

⁶The names of the classes are motivated, but not equal to the notation found in Ref. [110]. For instance, the authors there might call (d) a 2-leg-loop, since in their picture diagram (d) is obtained by cutting open a closed loop.



Figure 4.3: More realistic graphical representation of diagram (a) in Fig. 4.2. For the whole time t , the four trajectories stay in close vicinity to each other and can be considered as a single solution of the mean-field Gross-Pitaevskii equation, Eq. (3.86).

motion before and after the encounter.

Since the time argument in the semiclassical propagators is fixed to t , legs on the same side of an encounter must have equal times, since otherwise a contradiction arises for the total times of the individual trajectories. This excludes a potential “one-leg” or “three-leg” diagram, and explains, why diagrams (a) to (d) in Fig. 4.2 represent all the configurations containing a single encounter. The contribution of diagram classes which contain more than a single encounter is discussed in section 4.5.

Inside an encounter, the hyperbolic dynamics essentially follows a common mean-field solution. For that reason, diagram (a) in Fig. (4.2) represents the case, where the four trajectories can be interpreted as a single solution of the classical mean-field equations Eq. (3.86). We thus expect this diagram to reproduce results for the OTOC, which are based on solving the mean-field problem. This includes our treatment in section 4.1.2, but also the truncated Wigner method, such as in Ref. [111]. Contrarily, diagrams (b) to (d) are interpreted as two solutions of the Gross-Pitaevskii equation, Eq. (3.86), which are coupled to each other through a fully developed encounter. Their contribution within the interfering sum is a many-body interference phenomenon which goes beyond the above mentioned methods. This mechanism gets quantum mechanically relevant for times beyond t_E since this is the time at which encounter regions with an action difference at the order $\mathcal{O}(\hbar_{\text{eff}})$ start to exist. Indeed, we will see in the next sections that diagrams (b) to (d) are crucial to explain the saturation of OTOCs and its crossover from the pre-Ehrenfest exponential growth.

4.2.3 Geometry of encounters in phase space

For our calculations it is necessary to quantify the encounter of trajectories in a phase space region. This basic understanding has been provided in detailed analyses within single-particle scenarios, and there is already a broad literature available [69, 72, 81, 109, 110, 112]. For convenience, and also to include the explanation of new OTOC-specific modifications, we review and summarize the key steps here.

The main idea is that when two trajectories encounter each other in phase space, the dynamics of their relative motion is well described by linearizing Hamilton’s equations

of motion around one of the trajectories. In this linearized regime, the relative phase space difference of nearby trajectories can be expressed in the local coordinate system spanned by the directions towards the stable and unstable manifolds and the manifolds given by the two constants of motion, as we have seen in our the discussions in section 2.2. However, we have to demand that the encountering trajectories have (within a window of $\mathcal{O}(\hbar_{\text{eff}})$) the same values for their constants of motion, since otherwise a change of the partner trajectory, which is followed outside the encounter region, is not possible. Thus, the relative difference vector is expressed solely in terms of the $2(d-2)$ stable and unstable directions.

To quantitatively describe trajectories $\alpha, \alpha', \beta, \beta'$ encountering each other in phase space, we first choose one of the trajectories as a reference trajectory, say β , and construct the others from that trajectory. We take a time t' at which we want a second trajectory α to be close to β . At the phase space point of β at t' , denoted by $\mathbf{x}_\beta(t')$, we place the origin of a $2(d-2)$ dimensional coordinate system, which is spanned by the local stable and unstable directions $\mathbf{e}_{\beta,s}^{(l)}(t') \equiv \mathbf{e}_s^{(l)}(\mathbf{x}_\beta(t'))$, $\mathbf{e}_{\beta,u}^{(l)}(t') \equiv \mathbf{e}_u^{(l)}(\mathbf{x}_\beta(t'))$. In this frame, an encountering trajectory α , which takes the same values of the constants of motion as β , is uniquely defined by vectors \mathbf{s}, \mathbf{u} through

$$\mathbf{x}_\alpha(t') = \mathbf{x}_\beta(t') + \sum_{l=1}^{d-2} \left[s_l \mathbf{e}_{\beta,s}^{(l)}(t') + u_l \mathbf{e}_{\beta,u}^{(l)}(t') \right]. \quad (4.27)$$

As long as we are working in the linearizable regime of the relative Hamiltonian dynamics, *i.e.* the components of the vectors \mathbf{s}, \mathbf{u} do not reach a given critical (classical) value $\pm c$, Eq. (4.27) results in a well-defined phase space point. Since the Hamilton function \mathcal{H} does not explicitly depend on time this phase space point is sufficient to specify the full trajectory α both for times before and after t' . Since both the stable and the unstable directions are involved, the constructed trajectory α is exponentially diverging from β for times smaller and larger than t' , while it stays close to β around the time t' . The reason why in Eq. (4.27) the phase space points of α and β are taken at the same time t' is the very same which excluded a mismatch of times of legs on the same sides of encounters in Fig. 4.2: Since the partner trajectories α', β' , which we construct in a moment, change from β to α or vice versa within the encounter region, their complete times would differ from t in case of different times in Eq. (4.27). However, since we have to find these partner trajectories in the corresponding sums over trajectories α' and β' in Eq. (4.23) thus leading to a contradiction.

The missing two partner trajectories α', β' , which follow the original trajectories outside the encounter region and interchange the partners inside it, are also uniquely identified by the vectors \mathbf{s}, \mathbf{u} . Their phase space points at time t' are given by

$$\mathbf{x}_{\beta'}(t') = \mathbf{x}_\beta(t') + \sum_{l=1}^{d-2} s_l \mathbf{e}_{\beta,s}^{(l)}(t'), \quad \mathbf{x}_{\alpha'}(t') = \mathbf{x}_\beta(t') + \sum_{l=1}^{d-2} u_l \mathbf{e}_{\beta,u}^{(l)}(t'). \quad (4.28)$$

The trajectory β' exponentially approaches β for times larger than t' , as the difference between $\mathbf{x}_{\beta'}(t')$ and $\mathbf{x}_\beta(t')$ is solely along stable directions. For times smaller than t' ,

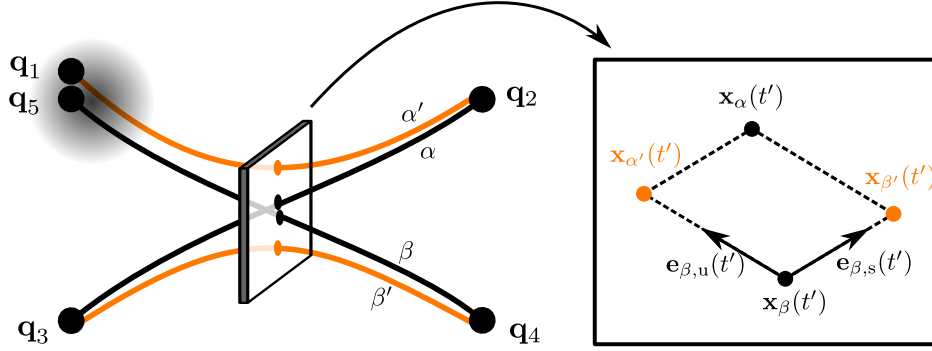


Figure 4.4: Visualization of the local relation between the phase space points of the four trajectories involved in an encounter.

we have to consider time-reversed dynamics, and the stable and unstable manifolds interchange their roles. Thus, for times smaller than t' , β' exponentially separates from β , and exponentially approaches α in the same fashion, since

$$\mathbf{x}_\alpha(t') - \mathbf{x}_{\beta'}(t') = \sum_{l=1}^{d-2} u_l \mathbf{e}_{\beta,u}^{(l)}(t'). \quad (4.29)$$

The same reasoning can be applied to α' .

To summarize, a constellation of trajectories with a single encounter is described by choosing one of the trajectories as a reference trajectory, a time t' as time of the encounter, and vectors \mathbf{s} , \mathbf{u} to quantify the respective distances towards the other trajectories. The whole geometric constellation of the trajectory quadruplet we just constructed is schematically depicted in Fig. 4.4.

So far, we have not yet specified the critical (classical) value c , which controls the linearizable regime. It is chosen such that c^2 has the size of a typical classical action scale and is large compared to \hbar_{eff} . Its exact value is not of importance as diagrams with action differences much larger than \hbar_{eff} essentially do not contribute to the results of semiclassical calculations. Nevertheless, our final results depend on it as it manifests itself through the quantitative definition of the *Ehrenfest time*,

$$t_E = \frac{1}{\lambda} \log\left(\frac{c^2}{\hbar_{\text{eff}}}\right), \quad (4.30)$$

which now admits the physical interpretation of the time scale for which under hyperbolic dynamics details of the order $\mathcal{O}(\hbar_{\text{eff}})$ can grow to a size of the order $\mathcal{O}(c^2)$ of a typical classical action.

Note also that varying the time t' in Eq. (4.27) changes the vectors \mathbf{s} and \mathbf{u} in the co-traveling coordinate system according to the Hamiltonian dynamics. For instance

for t' , t'' inside the encounter region, the phase space points defined by $(t', \mathbf{s}, \mathbf{u})$ and $(t'', \mathbf{s} \exp[-\lambda(t'' - t')], \mathbf{u} \exp[\lambda(t'' - t')])$ are actually describing the very same trajectory α . This produces an overcounting of contributions when we integrate over t' and is associated to the fact, that a constellation of trajectories is more related to the encounter region rather than to the situation at a single time within the region. Such overcounting can be compensated by dividing the contributions through the overall time the trajectories spend inside the encounter region. To identify this time, we note that the borders of the encounter regions are reached when the first components of \mathbf{s} and \mathbf{u} have grown to the classical scale $\pm c$ at which the linearization breaks down. This introduces two time scales, the *stable* and *unstable time*

$$t_s(\mathbf{s}) = \frac{1}{\lambda} \log \left(\frac{c}{\max_{i=1, \dots, d-2} (|s_i|)} \right), \quad t_u(\mathbf{u}) = \frac{1}{\lambda} \log \left(\frac{c}{\max_{i=1, \dots, d-2} (|u_i|)} \right). \quad (4.31)$$

The *encounter time*, the time trajectories spend in a fully developed encounter region as seen in Fig. 4.2 (d), is defined as the sum of these two times,

$$t_{\text{enc}}(\mathbf{s}, \mathbf{u}) = t_s(\mathbf{s}) + t_u(\mathbf{u}). \quad (4.32)$$

Note that if the trajectories start and/or end inside the encounter region, as in Fig. 4.2 (a) to (c), the effective time of the trajectory within an encounter has to be reduced accordingly, since the trajectories terminate before the boundary of the encounter region is reached.

So far, the above considerations are rather general. Regarding encounter contributions to OTOCs, there are further important issues to consider, which are specific to OTOCs and, to the author's knowledge, have not been emerged and not treated so far in the existing works in semiclassical physics. These issues prove crucial in the semiclassical understanding OTOCs and relate to the operators appearing next to the time evolution operators in the definition Eq. (4.21). By introducing the semiclassical formalism, the operators translated to classical, trajectory-related quantities. If the initial points of the trajectories are contained inside the encounter region, we have to treat the corresponding classical quantities which relate to initial points of trajectories in a correlated way, and also use the local coordinates \mathbf{s} , \mathbf{u} to describe them.

In Fig. 4.2 (a) and (b), the beginning of the trajectories is inside the encounter region. This requires to treat the difference of initial momenta in Eq. (4.23) through

$$p_{\alpha', i}^{(i)} - p_{\alpha, i}^{(i)} = - \sum_{l=1}^{d-2} s_l e^{\lambda t'} \left[\mathbf{e}_{\beta, \mathbf{s}}^{(l)}(0) \right]_{p_i}, \quad p_{\beta, i}^{(i)} - p_{\beta', i}^{(i)} = - \sum_{l=1}^{d-2} s_l e^{\lambda t'} \left[\mathbf{e}_{\beta, \mathbf{s}}^{(l)}(0) \right]_{p_i}. \quad (4.33)$$

Similarly, if the final points enter the encounter region, as in Fig. 4.2 (a) and (c), we use

$$q_{\alpha, j}^{(f)} q_{\beta, j}^{(f)} = \frac{1}{2} \left(q_{\alpha, j}^{(f)2} + q_{\beta, j}^{(f)2} \right) - \frac{1}{2} \left(q_{\alpha, j}^{(f)} - q_{\beta, j}^{(f)} \right)^2 \approx q_{\alpha, j}^{(f)2} - \frac{1}{2} \left(\sum_{l=1}^{d-2} u_l e^{\lambda(t-t')} \left[\mathbf{e}_{\beta, \mathbf{u}}^{(l)}(t) \right]_{q_j} \right)^2, \quad (4.34)$$

where we again used $[\cdot]_{p_i}$ and $[\cdot]_{q_j}$ to denote components of the momentum and the position quadrature sector of the phase space vectors, see Eq. (4.15). As we later approximate the square of the final points in Eq. (4.34) by its phase space average due to mixing, we already approximate them here by $q_{\alpha,j}^{(f)2}$ to simplify expressions.

4.2.4 Density, amplitudes and action difference of diagrams with encounters

To obtain all possible contributions to Eq. (4.23) from trajectory constellations undergoing a single encounter, we first introduce integrations over the relative differences \mathbf{s} , \mathbf{u} and time t' at which these differences are employed. The integration volumes are such that the linearizable regime, as limited by the critical values $\pm c$ is covered, and the encounter region around t' is placed according to the diagrammatic class in Fig. 4.2.

Since the partner trajectories α' and β' are uniquely given by the Eqs. (4.28), the four-fold sum over trajectories can be reduced to a two-fold sum. Furthermore, we can correlate the remaining sums over α and β by introducing the density distribution

$$\rho_{\alpha,\beta}(\mathbf{s}, \mathbf{u}, t') = \frac{(2\pi\hbar_{\text{eff}})^2}{t_{\text{enc}}(\mathbf{s}, \mathbf{u})} \delta^{2d}[\mathbf{x}_\alpha(t') - \tilde{\mathbf{x}}(\mathbf{x}_\beta(t'), \mathbf{s}, \mathbf{u})], \quad (4.35)$$

It utilizes a multidimensional Dirac- δ function to implement Eq. (4.27), since for the argument we defined

$$\tilde{\mathbf{x}}(\mathbf{x}, \mathbf{s}, \mathbf{u}) = \mathbf{x} + \sum_{l=1}^{d-2} [s_l \mathbf{e}_s^{(l)}(\mathbf{x}) + u_l \mathbf{e}_u^{(l)}(\mathbf{x})]. \quad (4.36)$$

Note that Eq. (4.35) the encounter time $t_{\text{enc}}(\mathbf{s}, \mathbf{u})$ needs to be adjusted in case of trajectories ending inside the encounter.

The normalization $(2\pi\hbar_{\text{eff}})^2$ in Eq. (4.35) is independently determined by performing similar calculations for the identity $1 = \langle \Psi | \hat{U}^\dagger(t) \hat{U}(t) \hat{U}^\dagger(t) \hat{U}(t) | \Psi \rangle$. It reflects that the paired trajectories should all stay in a window of size \hbar_{eff} near the submanifold defined by the reference trajectory's values for the constants of motion \mathcal{H} and \mathcal{N} .

It can be shown [81] that for the diagrammatic constellations in Fig. 4.2 the product of amplitudes associated with the four trajectories reduces to the product of the squared modulus of the amplitudes of the two trajectories α and β ,

$$A_\alpha A_{\alpha'} A_\beta A_{\beta'} \rightarrow |A_\alpha|^2 |A_\beta|^2, \quad (4.37)$$

where we also implicitly used that, as one can also show [81], the Maslov indices and the sum of phases due to ordering sum up to zero.

Finally, the action difference of this system of four trajectories, as derived in appendix A.3, see also [69, 109] is found to be

$$R_\alpha - R_{\alpha'} + R_\beta - R_{\beta'} \approx \mathbf{s} \cdot \mathbf{u} + \mathbf{p}_\alpha^{(i)} \cdot (\mathbf{q}_1 - \mathbf{q}_5). \quad (4.38)$$

The term related to the initial momentum and the relative distance $\mathbf{y} = \mathbf{q}_1 - \mathbf{q}_5$ is introduced as we substitute the trajectories α , α' , starting at \mathbf{q}_1 and \mathbf{q}_5 , by nearby

trajectories starting at $\mathbf{q} = \frac{1}{2}(\mathbf{q}_1 + \mathbf{q}_5)$. This is required by the pairing of the trajectories α, α' before the encounter. It can, on the one hand, be justified by our demand of a localized state Ψ , which also contains the above variables $\mathbf{q}_1, \mathbf{q}_5$, see Eq. (4.23). On the other hand, we can consistently assume that a large distance of these vectors produces an action difference much larger than \hbar_{eff} and thus a vanishing contribution in the semiclassical limit. The latter argument allows, also to consider the final result of our subsequent calculations for physically realistic many-body states, such as Fock states.

4.3 Calculation of diagrammatic contributions

4.3.1 Contributions of four-leg diagrams

We now turn towards the actual calculations of the contributions of the single diagram classes depicted in Fig. 4.2. For pedagogical reasons we start with the contributions of the four-leg-encounters displayed in subfigure (d). The contribution of this diagram is found by evaluating the integral

$$\begin{aligned}
C^{(4\text{le})}(t) &= \int d^d q \int d^d y \int d^d q_2 \int d^d q_3 \int d^d q_4 \Psi^* \left(\mathbf{q} + \frac{\mathbf{y}}{2} \right) \Psi \left(\mathbf{q} - \frac{\mathbf{y}}{2} \right) \\
&\times \sum_{\substack{\alpha: \mathbf{q}_3 \xrightarrow{t} \mathbf{q}_2 \\ \beta: \mathbf{q} \rightarrow \mathbf{q}_4}} |A_\alpha|^2 |A_\beta|^2 \left(p_{\beta,i}^{(i)} - p_{\alpha,i}^{(i)} \right)^2 q_{\alpha,j}^{(f)} q_{\beta,j}^{(f)} e^{\frac{i}{\hbar_{\text{eff}}} \mathbf{p}_\alpha^{(i)} \cdot \mathbf{y}} \\
&\times \int_{-c}^c d^{d-2} s \int_{-c}^c d^{d-2} u \int_{t_s(\mathbf{s})}^{t-t_u(\mathbf{u})} dt' e^{\frac{i}{\hbar_{\text{eff}}} \mathbf{s} \cdot \mathbf{u}} \Theta[t - t_{\text{enc}}(\mathbf{s}, \mathbf{u})] \rho_{\alpha,\beta}(\mathbf{s}, \mathbf{u}, t'),
\end{aligned} \tag{4.39}$$

where we used the short-hand notation

$$\int_{-c}^c d^{d-2} s \int_{-c}^c d^{d-2} u = \int_{-c}^c ds_1 \int_{-c}^c du_1 \cdots \int_{-c}^c ds_{d-2} \int_{-c}^c du_{d-2} \tag{4.40}$$

to abbreviate the $2(d-2)$ integrations of the stable and unstable coordinates.

Most of the ingredients of Eq. (4.39) have already been discussed in detail in the previous section. The special features of Fig. 4.2 (d) are represented by the boundaries of the integration over t' , which require that the encounter region does neither contain the beginning nor the end of the trajectories. Additionally, the Heaviside step function Θ ensures that encounter regions longer than the available time t are excluded. Finally, following the arguments after Eq. (4.38), and paving the way for later introducing the Wigner function, Eq. (4.4), we already performed the variable transformation

$$(\mathbf{q}_1, \mathbf{q}_5) \rightarrow (\mathbf{q}, \mathbf{y}) = \left(\frac{\mathbf{q}_1 + \mathbf{q}_5}{2}, \mathbf{q}_1 - \mathbf{q}_5 \right), \tag{4.41}$$

to replace the coordinates \mathbf{q}_1 and \mathbf{q}_5 in the arguments of the wave function by their center of mass and the relative coordinates.

We begin the evaluation of Eq. (4.39) by noting that by using Eq. (2.7) in Eq. (3.84) the squared amplitudes $|A_\alpha|^2$ can be interpreted as Jacobian for a variable transformation from final coordinates to initial momenta along a classical trajectory,

$$|A_\alpha|^2 = \frac{1}{(2\pi\hbar_{\text{eff}})^d} \left| \frac{\partial \mathbf{p}_\alpha^{(i)}}{\partial \mathbf{q}^{(f)}} \right|. \quad (4.42)$$

In combination with the sum over trajectories α , this allows us to transform the integrations over $\mathbf{q}_2 = \mathbf{q}_\alpha^{(f)}$ into an integration over initial momenta \mathbf{p}_3 . Trajectory-related quantities labeled by α become then functions of trajectories with initial conditions $\mathbf{x}_3 = (\mathbf{q}_3, \mathbf{p}_3)$. For instance

$$\left(\mathbf{p}_\alpha^{(i)}, \mathbf{q}_\alpha^{(f)} \right) \rightarrow \left(\mathbf{p}_3, \mathbf{q}^{(f)}(\mathbf{x}_3; t) \right). \quad (4.43)$$

In the same spirit we use the sum over β with $|A_\beta|^2$ to transform the integration over \mathbf{q}_4 to \mathbf{p} , and β -labeled quantities become functions of $\mathbf{x} = (\mathbf{q}, \mathbf{p})$.

The δ -function in the density of encounters, Eq. (4.35) can be interpreted as classical probability density for a trajectory starting at \mathbf{x}_3 to be at time t' at a certain phase space point which depends on $\mathbf{q}, \mathbf{p}, \mathbf{s}, \mathbf{u}$ and t' . Within the integration, we can approximate this probability density by a smoothed function. As the initial points \mathbf{x}_3 are not located within the encounter region, it is then justified to utilize the mixing property of the chaotic system, Eq. (2.47) to approximate $\rho_{\alpha,\beta}$ by

$$\rho_{\alpha,\beta} \rightarrow \frac{(2\pi\hbar_{\text{eff}})^2}{t_{\text{enc}}(\mathbf{s}, \mathbf{u})} \frac{\delta^2 \left(\begin{array}{l} \mathcal{H}(\mathbf{x}_3) - \mathcal{H}(\mathbf{x}) \\ \mathcal{N}(\mathbf{x}_3) - \mathcal{N}(\mathbf{x}) \end{array} \right)}{\Sigma(\mathbf{x})}, \quad (4.44)$$

where $\Sigma(\mathbf{x})$ is the volume of the chaotic phase space submanifold,

$$\Sigma(\mathbf{x}) = \int d^{2d}x' \delta^2 \left(\begin{array}{l} \mathcal{H}(\mathbf{x}') - \mathcal{H}(\mathbf{x}) \\ \mathcal{N}(\mathbf{x}') - \mathcal{N}(\mathbf{x}) \end{array} \right). \quad (4.45)$$

The interpretation of Eq. (4.44) is that every phase space point which shares the same values of the constants of motions $\mathcal{H}(\mathbf{x})$ and $\mathcal{N}(\mathbf{x})$ is equally likely to be reached by the classical dynamics of a typical trajectory in the chaotic region.

Together with the integration over initial phase space points \mathbf{x}_3 , Eq. (4.44) introduces an average over the accessible submanifold defined by the constants of motion. This leads to the following substitution of initial momenta and final position:

$$(p_{3,i} - p_i)^2 q_j^{(f)}(\mathbf{x}_3; t) \rightarrow \langle (p'_i - p_i)^2 q_j^{(f)}(\mathbf{x}'; t) \rangle_{\mathbf{x}}, \quad (4.46)$$

where the phase space average is defined as

$$\langle f(\mathbf{x}') \rangle_{\mathbf{x}} = \frac{\int d^{2d}x' \delta^2 \left(\begin{array}{l} \mathcal{H}(\mathbf{x}') - \mathcal{H}(\mathbf{x}) \\ \mathcal{N}(\mathbf{x}') - \mathcal{N}(\mathbf{x}) \end{array} \right) f(\mathbf{x}')}{\Sigma(\mathbf{x})}. \quad (4.47)$$

Note that the phase space point \mathbf{x} , which is also used as label, defines the values of the constants of motion $\mathcal{H}(\mathbf{x})$ and $\mathcal{N}(\mathbf{x})$ in this average. To be able to distinguish this phase space average from the phase space average involving the Wigner function introduced later, we denote Eq. (4.47) an *ergodic phase space average*.

For times larger than the Lyapunov time $t_L = 1/|\lambda|$ the final position of a trajectory is independent of its starting point. This allows us to factorizes the average Eq. (4.46)

$$\langle (p'_i - p_i)^2 q_j^{(f)}(\mathbf{x}'; t) \rangle_{\mathbf{x}} = \langle (p'_i - p_i)^2 \rangle_{\mathbf{x}} \langle q'_j \rangle_{\mathbf{x}}. \quad (4.48)$$

Again using the mixing property, we also approximate the remaining factor $q_j^{(f)}(\mathbf{x}; t)$ by the phase space average $\langle q'_j \rangle_{\mathbf{x}}$.

Combining all the above considerations, and also introducing the Wigner function according to Eq. (4.4) for the pure state $\hat{\rho} = |\Psi\rangle\langle\Psi|$,

$$W(\mathbf{q}, \mathbf{p}) = \frac{1}{(2\pi\hbar_{\text{eff}})^d} \int d^d y \Psi^*\left(\mathbf{q} + \frac{\mathbf{y}}{2}\right) \Psi\left(\mathbf{q} - \frac{\mathbf{y}}{2}\right) e^{\frac{i}{\hbar_{\text{eff}}}\mathbf{p}\cdot\mathbf{y}}, \quad (4.49)$$

we see that the contribution of four-leg encounters can be written in terms of a phase space average weighted with the Wigner function,

$$C^{(4\text{le})}(t) = \int d^d q \int d^d p W(\mathbf{q}, \mathbf{p}) I^{(4\text{le})}(\mathbf{q}, \mathbf{p}; t), \quad (4.50)$$

where the phase space function to be averaged is given by

$$I^{(4\text{le})}(\mathbf{q}, \mathbf{p}; t) = \langle (p'_i - p_i)^2 \rangle_{\mathbf{x}} \langle q'_j \rangle_{\mathbf{x}}^2 F^{(4\text{le})}(t), \quad (4.51)$$

and contains the ergodic phase space averages as discussed above, and the encounter integral

$$F^{(4\text{le})}(t) = \frac{1}{(2\pi\hbar_{\text{eff}})^{d-2}} \int_{-c}^c d^{d-2} s \int_{-c}^c d^{d-2} u e^{\frac{i}{\hbar_{\text{eff}}}\mathbf{s}\cdot\mathbf{u}t - \frac{t_{\text{enc}}(\mathbf{s}, \mathbf{u})}{t_{\text{enc}}(\mathbf{s}, \mathbf{u})} \Theta[t - t_{\text{enc}}(\mathbf{s}, \mathbf{u})]}. \quad (4.52)$$

The calculation of this integral is performed in appendix A.4.2. We find, as exact result

$$F^{(4\text{le})}(t) = \left(\frac{2}{\pi}\right)^{d-2} \lambda t (d-2) \text{Si}^{d-3}\left(e^{\lambda t_{\text{E}}}\right) \sin\left(e^{\lambda t_{\text{E}}}\right) - \left(\frac{2}{\pi}\right)^{d-2} \left[\text{Si}^{d-2}\left(e^{\lambda t_{\text{E}}}\right) - \text{Si}^{d-2}\left(e^{\lambda(t_{\text{E}}-t)}\right) \right], \quad (4.53)$$

where Si denotes the *sine-integral* [113]

$$\text{Si}(z) = \int_0^z dz' \frac{\sin(z')}{z'}. \quad (4.54)$$

The result further contains the Ehrenfest time t_{E} from Eq. (4.30) as an indicator that trajectory constellations with an action difference of the order of \hbar_{eff} or smaller contribute

the most in the diagram class (d) in Fig. 4.2. As we explained in detail in section 4.2.3 such constellations need times larger than the Ehrenfest time to form a close enough encounter of trajectories to produce an action difference equal or smaller than \hbar_{eff} . Indeed, as the further analysis of Eq. (4.53) in appendix A.4.2 shows, in the semiclassical limit $\hbar_{\text{eff}} \ll c^2$, which implies $\lambda t_E = \log(c^2/\hbar_{\text{eff}}) \gg 1$, we can well approximate the above function by the Heaviside step-function Θ ,

$$F^{(4\text{le})}(t) \approx \begin{cases} 0 & \text{if } t < t_E \\ -1 & \text{if } t > t_E \end{cases} \approx -\Theta(t - t_E). \quad (4.55)$$

The physical implication is now obvious, as diagrams depicted in Fig. (4.2) (d) contribute to the OTOC a constant value after the Ehrenfest time.

4.3.2 Contributions of two-leg diagrams

We now turn towards the two-leg diagrams depicted in Fig. 4.2 (b) and (c). These are characterized by an encounter region that contains either the starting or the end points of the quadruplet of trajectories.

Encounter at the beginning

We start with diagram (b). Its contribution $C^{(2\text{le},(b))}$ is calculated from a similar expression as $C^{(4\text{le})}$, Eq. (4.39), however with three major differences:

- Since the encounter region is at the beginning, the integration over t' is over the interval $[0, t_s(\mathbf{s})]$.
- The effective time in the encounter is $t_{\text{enc}}^{(\text{eff})}(t', \mathbf{u}) = t' + t_u(\mathbf{u})$ and thus smaller than the encounter time in Eq. (4.32).
- The difference of initial momenta is expressed through Eq. (4.33) and adds additional terms depend on \mathbf{s} and t' to the integrand.

Apart from a different treatment of the density $\rho_{\alpha,\beta}$, which here can be directly used to cancel the integration over \mathbf{x}_3 , we apply the same steps which led to Eq. (4.50) for the four-leg encounter. Thus, formally we arrive at the same phase space average, however, in this case the phase space function being averaged is given by

$$I^{(2\text{le},(b))}(\mathbf{q}, \mathbf{p}; t) = \langle q_j' \rangle_{\mathbf{x}}^2 \sum_{l,l'=1}^{d-2} \left[\mathbf{e}_s^{(l)}(\mathbf{x}) \right]_{p_i} \left[\mathbf{e}_s^{(l')}(\mathbf{x}) \right]_{p_i} F_{ll'}^{(2\text{le},(b))}(t) \quad (4.56)$$

where the encounter integral reads

$$F_{ll'}^{(2\text{le},(b))}(t) = \frac{1}{(2\pi\hbar_{\text{eff}})^{d-2}} \int_{-c}^c d^{d-2}s \int_{-c}^c d^{d-2}u e^{\frac{i}{\hbar_{\text{eff}}}\mathbf{s}\cdot\mathbf{u}} s_l s_{l'} \times \int_0^{t_s(\mathbf{s})} dt' \frac{\Theta\left[t - t_{\text{enc}}^{(\text{eff})}(t', \mathbf{u})\right]}{t_{\text{enc}}^{(\text{eff})}(t', \mathbf{u})} e^{2\lambda t'}. \quad (4.57)$$

The details of the calculation of this integral are found in appendix A.4.3, and we refer there for the exact analytical result. We further show there that in both the temporal regimes $t > t_E$ and $t < t_E$ the contribution of this diagram is exponentially suppressed compared to contributions of other diagrams. Consequently, diagram (b) in Fig. 4.2 neither contributes to the pre- nor the post-Ehrenfest dynamics of the OTOC.

Non-negligible contributions of this diagram arise in the vicinity of the Ehrenfest-time t_E . We therefore conjecture that this diagram, amongst others, is responsible for the smooth crossover between the early-time exponential growth and the late-time saturation of OTOCs. However, it is not possible to describe this crossover quantitatively within this semiclassical framework, as for times $t \approx t_E$, our results become sensitive to the classical value c we chose as a sharp cutoff for the treatment of encounters.

Encounter at the end

The two-leg diagram class of Fig. 4.2 (c) is similar to the previous one. Here, it is the final points of the quadruplet of trajectories that are contained inside the encounter. In this case, the following modifications to Eq. (4.39) are required:

- The integration interval for t' is $[t - t_u(\mathbf{u}), t]$.
- The effective encounter time is $t_{\text{enc}}^{(\text{eff})}(t', \mathbf{s}) = t_s(\mathbf{s}) + (t - t')$.
- The product of final positions is expressed through Eq. (4.34). In one part of the subsequent calculation, this leads to correlated final points $\langle q_j'^2 \rangle_{\mathbf{x}}$ in the ergodic average. In the other part the integrand admits additional terms which depend on \mathbf{u} and t' .

The contributions are given by

$$I^{(2\text{le},(c))}(\mathbf{q}, \mathbf{p}; t) = \langle (p_i' - p_i)^2 \rangle_{\mathbf{x}} \left(\langle q_j'^2 \rangle_{\mathbf{x}} F^{(2\text{le},(c))}(t) - \frac{1}{2} \sum_{l,l'=1}^{d-2} \left[\mathbf{e}_u^{(l)}(\mathbf{x}^{(f)}(\mathbf{x}; t)) \right]_{q_j} \left[\mathbf{e}_u^{(l')}(\mathbf{x}^{(f)}(\mathbf{x}; t)) \right]_{q_j} F_{l'l'}^{(2\text{le},(c))}(t) \right), \quad (4.58)$$

where the phase space integrals read

$$F^{(2\text{le},(c))}(t) = \frac{1}{(2\pi\hbar_{\text{eff}})^{d-2}} \int_{-c}^c d^{d-2}s \int_{-c}^c d^{d-2}u e^{\frac{i}{\hbar_{\text{eff}}}\mathbf{s}\cdot\mathbf{u}} \times \int_{t-t_u(\mathbf{u})}^t dt' \frac{\Theta[t - t_{\text{enc}}^{(\text{eff})}(t', \mathbf{s})]}{t_{\text{enc}}^{(\text{eff})}(t', \mathbf{s})}, \quad (4.59)$$

$$\begin{aligned}
F_{ll'}^{(2le,(c))}(t) &= \frac{1}{(2\pi\hbar_{\text{eff}})^{d-2}} \int_{-c}^c d^{d-2}s \int_{-c}^c d^{d-2}u e^{\frac{i}{\hbar_{\text{eff}}}\mathbf{s}\cdot\mathbf{u}} u_l u_{l'} \\
&\times \int_{t-t_u(\mathbf{u})}^t dt' \frac{\Theta\left[t - t_{\text{enc}}^{(\text{eff})}(t', \mathbf{s})\right]}{t_{\text{enc}}^{(\text{eff})}(t', \mathbf{s})} e^{2\lambda(t-t')}. \tag{4.60}
\end{aligned}$$

The details of the calculation of these integrals are found in appendix A.4.4. As is argued there, a simple change of variables transforms $F_{ll'}^{(2le,(c))}(t)$ into the very same form as Eq. (4.57), the phase space integral we solved for the two-leg diagram with the encounter at the beginning. It is therefore obvious to conclude that this term is only contributing to the crossover at time $t \approx t_E$.

The contribution for $F^{(2le,(c))}(t)$ is found to be

$$F^{(2le,(c))}(t) = \left(\frac{2}{\pi}\right)^{d-2} \left[\text{Si}^{d-2}\left(e^{\lambda t_E}\right) - \text{Si}^{d-2}\left(e^{\lambda(t_E-t)}\right) \right]. \tag{4.61}$$

The analysis of the latter result uses the same arguments as for the contribution for four-leg-encounters, and we find that $F^{(2le,(c))}(t)$ only contributes for times larger than the Ehrenfest time t_E . It can, like $F^{(2le,(d))}(t)$ be well approximated by the Heaviside step function θ ,

$$F^{(2le,(c))}(t) \approx \theta(t - t_E), \tag{4.62}$$

and thus also contributes to the saturation value of the OTOC.

The difference between the contributions of diagrams (c) and (d) is whether or not the final position quadratures have to be treated correlated. Consequently, the combination of diagrams (c) and (d) results in the variance of position quadrature variable, $\langle q_j^2 \rangle_{\mathbf{x}} - \langle q_j \rangle_{\mathbf{x}}^2$, in the phase space accessible by the trajectory starting at \mathbf{x} .

4.3.3 Contributions of zero-leg diagrams

In this final section we calculate the contribution $C^{(0le)}(t)$ shown in Fig. 4.2 (a), where the quadruplet of trajectories is fully contained within the single encounter, *i.e.* the trajectories stay close to each other for the whole time.

The starting point for the calculation of $C^{(0le)}(t)$ differs from the one of the four-leg-encounter $C^{(4le)}$, Eq. (4.39), in the following items (see also Refs. [114, 115])

- As the encounter stretches over the full time t , the integration interval for t' is $[0, t]$ and the effective encounter time is $t_{\text{enc}}^{(\text{eff})} = t$. There is no Heaviside step function Θ in time any more.
- As the encounter time is fixed, the integration interval for the components of \mathbf{s} is reduced to $[-c \exp(-\lambda t'), c \exp(-\lambda t')]$ to ensure none of the stable components grows larger than the maximal value c in the available time t' . With the same reasoning, the integration intervals for the components of \mathbf{u} have to be taken as $[-c \exp[-\lambda(t-t')], c \exp[-\lambda(t-t')]]$.

- Both, the initial momentum difference and the product of final positions, have to be interpreted in view of Eqs. (4.33), (4.34) and be respected in the integrations over \mathbf{s} , \mathbf{u} and when using arguments leading to the ergodic averages.
- The δ -function in the density $\rho_{\alpha,\beta}$ of partner trajectories can again be directly used to cancel the integration over \mathbf{x}_3 .

After the initial transformations towards a phase space average of the form Eq. (4.50), we find that the phase space function with the contribution of the zero-leg diagram has the form

$$F_{ll'}^{(0le)}(\mathbf{q}, \mathbf{p}; t) = \sum_{l,l'=1}^{d-2} \left[\mathbf{e}_s^{(l)}(\mathbf{x}) \right]_{p_i} \left[\mathbf{e}_s^{(l')}(\mathbf{x}) \right]_{p_i} \left[\langle q_j'^2 \rangle_{\mathbf{x}} F_{ll'}^{(0le,1)}(t) \right. \\ \left. - \frac{1}{2} \sum_{m,m'=1}^{d-2} \left[\mathbf{e}_u^{(m)}(\mathbf{x}^{(f)}(\mathbf{x}; t)) \right]_{q_j} \left[\mathbf{e}_u^{(m')}(\mathbf{x}^{(f)}(\mathbf{x}; t)) \right]_{q_j} F_{ll'mm'}^{(0le,2)}(t) \right], \quad (4.63)$$

with encounter integrals

$$F_{ll'}^{(0le,1)}(t) = \frac{1}{(2\pi\hbar_{\text{eff}})^{d-2}} \int_0^t dt' e^{2\lambda t'} \int_{-ce^{-\lambda t'}}^{ce^{-\lambda t'}} d^{d-2}s \int_{-ce^{-\lambda(t-t')}}^{ce^{-\lambda(t-t')}} d^{d-2}u \frac{e^{\frac{i}{\hbar_{\text{eff}}}\mathbf{s}\cdot\mathbf{u}}}{t} s_l s_{l'}, \quad (4.64)$$

$$F_{ll'mm'}^{(0le,2)}(t) = \frac{1}{(2\pi\hbar_{\text{eff}})^{d-2}} \int_0^t dt' e^{2\lambda t'} \int_{-ce^{-\lambda t'}}^{ce^{-\lambda t'}} d^{d-2}s \int_{-ce^{-\lambda(t-t')}}^{ce^{-\lambda(t-t')}} d^{d-2}u \frac{e^{\frac{i}{\hbar_{\text{eff}}}\mathbf{s}\cdot\mathbf{u}}}{t} s_l s_{l'} u_m u_{m'}. \quad (4.65)$$

The details of the calculation of these integrals are found in appendix A.4.5, including the discussion of their behaviour in the regime $t < t_E$ and $t > t_E$. We find that Eq. (4.64) is exponentially suppressed again for $t < t_E$ and $t > t_E$, but contributes to the crossover regime at $t \approx t_E$. Also the second contribution, Eq. (4.65) is strongly suppressed for times larger than the Ehrenfest time.

For $t < t_E$ the leading contributions are obtained for index sets with pairwise equal indices $\{l, l'\} = \{m, m'\}$. For $l \neq l'$, their contribution is found to be

$$F_{ll'mm'}^{(0le,2)}(t) = - \left(\frac{2}{\pi} \right)^{d-2} c^4 \text{Si}^{d-4}(e^{\lambda(t_E-t)}) e^{2\lambda(t-t_E)} \left[\text{Si}(e^{\lambda(t_E-t)}) - \sin(e^{\lambda(t_E-t)}) \right]^2. \quad (4.66)$$

while for $l = l'$, the result is multiplied by 2 and contains additional terms only contributing for $t \approx t_E$. In the limit $t < t_E$, the above result is well approximated by

$$F_{ll'mm'}^{(0le,2)}(t) \approx -\hbar_{\text{eff}}^2 e^{2\lambda t} \Theta(t_E - t), \quad (4.67)$$

which inserted in Eq. (4.63) reproduces the expected short-time behaviour of OTOCs stated in Eq. (4.17).

4.4 Summary

In the previous section 4.3 we found that each contribution of the diagrams (a) to (d) in Fig. 4.2 to the OTOC takes the form of a phase space average,

$$C(t) \simeq \int d^d q \int d^d p W(\mathbf{q}, \mathbf{p}) I(\mathbf{q}, \mathbf{p}; t), \quad (4.68)$$

where $W(\mathbf{q}, \mathbf{p})$, defined in Eq. (4.49), denotes the Wigner function of the initial state and $I(\mathbf{q}, \mathbf{p}; t)$ comprises all encounter diagrams.

4.4.1 Pre-Ehrenfest behaviour

We found that the dynamics of the OTOCs for $t < t_E$ is fully described by diagram (a) in Fig. 4.2, via Eq. (4.63) together with Eq. (4.66). This diagram represents a quadruplet of trajectories which effectively follow a single, central solution of the mean-field equation. It reproduces the result also obtained from a classical treatment of OTOCs.

To be more precise, the effective phase space function $I_{<}(\mathbf{q}, \mathbf{p}; t)$ corresponding to this diagram is found to be

$$I_{<}(\mathbf{q}, \mathbf{p}; t) \approx \left(\sum_{l=1}^{d-2} \left[\mathbf{e}_s^{(l)}(\mathbf{x}) \right]_{p_i} \left[\mathbf{e}_u^{(l)}(\mathbf{x}^{(f)}(\mathbf{x}; t)) \right]_{q_j} \right)^2 F_{<}(t), \quad (4.69)$$

where the early-time exponential growth of OTOCs is contained in the function

$$\begin{aligned} F_{<}(t) &= \left(\frac{2}{\pi} \right)^{d-2} c^4 e^{2\lambda(t-t_E)} \text{Si}^{d-4} \left(e^{\lambda(t_E-t)} \right) \left[\text{Si} \left(e^{\lambda(t_E-t)} \right) - \sin \left(e^{\lambda(t_E-t)} \right) \right]^2 \\ &\approx \hbar_{\text{eff}}^2 e^{2\lambda t} \Theta(t_E - t). \end{aligned} \quad (4.70)$$

The approximation involving the Heaviside step function θ arises from the detailed analysis of the semiclassical limit $\hbar_{\text{eff}} \ll c^2$, which implies $\lambda t_E = \log(c^2/\hbar_{\text{eff}}) \gg 1$.

The last line in Eq. (4.70) indicates that $F_{<}(t)$ is strongly suppressed for $t > t_E$, which reflects, as a consequence of the unstable mean-field behavior of the classical limit, the vanishing phase space volume of the quadruplet of trajectories remaining close to each other over longer times. Additionally, it explicitly uncovers the expected short-time, classical exponential growth $\exp[2\lambda(t-t_E)]$ of the OTOC for $t < t_E$. This reproduces the expected behavior for short times obtained from expanding the Moyal bracket and the decomposition of the stability matrix, leading to Eq. (4.17). Our result additionally contains the missing cutoff at the Ehrenfest time through $\theta(t_E - t)$ which terminates the exponential growth at the Ehrenfest time.

4.4.2 Post-Ehrenfest behaviour

For $t > t_E$, the only non-negligible contributions to OTOCs are found in the sum of results from diagrams (c) and (d). As seen from Eqs. (4.51), (4.58), with their temporal behavior given in Eqs. (4.53), (A.108), their combined contribution is given by

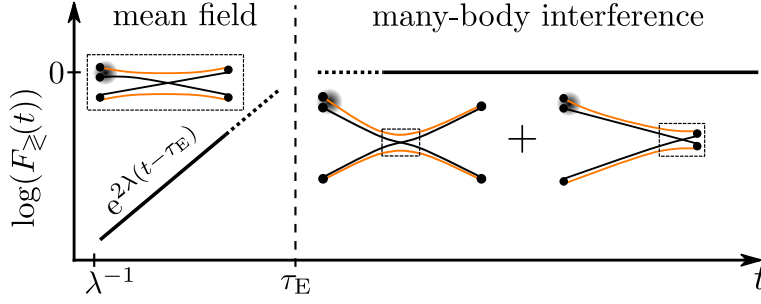


Figure 4.5: Universal contributions to the time evolution of the OTOC $C(t)$ for classically chaotic many-body quantum systems before $[F_{<}(t)$, Eq. (4.70)] and after $[F_{>}(t)$, Eq. (4.72)] the Ehrenfest time $t_E = (1/\lambda) \log(N)$ marked by the vertical dashed line. The insets show diagrams (a), (d), and (c) from Fig. 4.2, representing interfering mean-field solutions. Not shown is the crossover regime at $t \approx t_E$ to which all diagrams from Fig. 4.2 contribute.

(neglecting terms not relevant for $t > t_E$)

$$I_{>}(\mathbf{q}, \mathbf{p}; t) = \langle (p'_i - p_i)^2 \rangle_{\mathbf{x}} \left(\langle q_j'^2 \rangle_{\mathbf{x}} - \langle q_j^2 \rangle_{\mathbf{x}} \right) F_{>}(t), \quad (4.71)$$

where

$$F_{>}(t) = \left(\frac{2}{\pi} \right)^{d-2} \left[\text{Si}^{d-2} \left(e^{\lambda t_E} \right) - \text{Si}^{d-2} \left(e^{\lambda(t_E - t)} \right) \right] \approx \Theta(t - t_E). \quad (4.72)$$

From the last line we see that the diagrams (c) and (d) are responsible for the saturation after the Ehrenfest time, while their contribution is suppressed for $t < t_E$. Its description requires to consider the interference of multiple many-body mean-field solutions and thus cannot be described using mean-field approaches [116]. Physically, the diagrammatic situation depicted in diagrams (c) and (d) corresponds to swapping forth and back along distinctly different encounter-coupled mean-field solutions, thereby creating quantum correlations and entanglement.

The saturation value of the OTOC is associated to classical quantities. The first is the ergodic variance of the j -th position quadrature $(\Delta q_j)^2 = \langle q_j'^2 \rangle_{\mathbf{x}} - \langle q_j^2 \rangle_{\mathbf{x}}$. The second is $\langle (p_i - p'_i)^2 \rangle_{\mathbf{x}} = (\langle p_i'^2 \rangle_{\mathbf{x}} - \langle p_i^2 \rangle_{\mathbf{x}}) + (p_i - \langle p_i \rangle_{\mathbf{x}})^2$, which is summing the ergodic variance of the i -th momentum quadrature and the squared distance of the quadrature p_i , as provided by the Wigner function, to the ergodic average $\langle p_i \rangle_{\mathbf{x}}$. It is possible to evaluate the ergodic averages by assuming that no site i of the Bose-Hubbard model is special and therefore taking $\langle p_i'^2 \rangle_{\mathbf{x}} \approx \langle q_i'^2 \rangle_{\mathbf{x}} \approx \langle p_j'^2 \rangle_{\mathbf{x}} \approx \langle q_j'^2 \rangle_{\mathbf{x}}$ to be equal. Further exploiting the connection between $p_i'^2$ and $q_j'^2$ with the particle density, Eq. (4.26),

$$1 \approx \langle \mathcal{N}(\mathbf{x}') \rangle_{\mathbf{x}} = \frac{1}{2} \sum_{i=1}^d \left(\langle p_i'^2 \rangle_{\mathbf{x}} + \langle q_i'^2 \rangle_{\mathbf{x}} \right), \quad (4.73)$$

we find $\langle p_i'^2 \rangle_{\mathbf{x}} \approx \langle q_i'^2 \rangle_{\mathbf{x}} \approx 1/d$. Further assuming vanishing expectation values, $\langle p_i' \rangle_{\mathbf{x}} \approx \langle q_i' \rangle_{\mathbf{x}} \approx 0$, this yields

$$I_{>}(\mathbf{x}; t) \approx \theta(t - t_E) \left(p_i^2 + \frac{1}{d} \right) \frac{1}{d}. \quad (4.74)$$

For an initial state $|\Psi\rangle$ whose Wigner function is sharply localized in phase space at $\mathbf{x}_0 = (\mathbf{q}_0, \mathbf{p}_0)$, with $\mathcal{N}(\mathbf{x}_0) \approx 1$, we thus find for $t > t_E$

$$C(t) = \int d^d q \int d^d p W(\mathbf{q}, \mathbf{p}) I_{>}(\mathbf{x}; t) \approx \left(p_{0,i}^2 + \frac{1}{d} \right) \frac{1}{d} \approx \frac{2}{d^2} \quad (4.75)$$

where we used the same arguments as after Eq. (4.73) to estimate $p_{0,i}^2 \approx 1/d$. Corrections of $\mathcal{O}(\hbar_{\text{eff}})$ can arise due to the finite width of the wave packet.

Interestingly, the same result, Eq. (4.75), holds if $|\Psi\rangle$ is an extended chaotic many-body state with fixed energy and particle density, since then, the average over the Wigner function equals an ergodic average. This allows again to use the argument after Eq. (4.73).

4.5 Further remarks and implications

4.5.1 Generalization of the methods to OTOCs with more generic operators

The key ingredient to understand OTOCs is to use semiclassical techniques which translate the quantum operators \hat{p}_i and \hat{q}_j to their corresponding classical partners while keeping the quantum mechanical phase information. In the classical phase space, we used the local linearization of Hamilton's equations of motion to connect these classical functions to the hyperbolic property of the chaotic system. Furthermore, the mixing property produced variances of these phase space functions.

In view of these points, generalizing the methods for OTOCs of the form

$$\left\langle \Psi \left| \left[\hat{B}(t), \hat{A} \right]^\dagger \left[\hat{B}(t), \hat{A} \right] \right| \Psi \right\rangle, \quad (4.76)$$

with generic operators \hat{A} and \hat{B} appears to be straightforward if the following assumptions are fulfilled:

- The operators \hat{A} , \hat{B} are smooth functions of the operators \hat{q}_i , \hat{p}_i , $i = 1, \dots, d$, in the sense that we can write \hat{A} , \hat{B} as a sum of products of powers of position and momentum quadrature operators.
- To avoid additional contributions to the overall action difference in the phase factor in Eq. (4.23), which have to be considered within the semiclassical analysis, the operators \hat{A} , \hat{B} are not allowed to depend on \hbar_{eff}^{-1} . Hence, for instance, displacement operators such as $\exp(-i/\hbar_{\text{eff}}) y \hat{p}_i$ would require a refined treatment.

Within the scope of these assumptions, we expect our methods to apply. The classical functions corresponding to the quantum operators are constructed by replacing operators \hat{q}_i, \hat{p}_i in the expansion by the corresponding trajectory-based equivalents, *i.e.* initial position and momentum quadratures in \hat{A} , and final ones in \hat{B} . Any dependence on powers of \hbar_{eff} of single terms in these expansion can be dropped as we are working in the leading order semiclassical limit $\hbar_{\text{eff}} \ll c^2$. We expect these terms to arise from different ordering of the quantum operators \hat{q}_i, \hat{p}_i . They can be avoided from the beginning by using operators and classical functions which are linked to each other by the classical-quantum correspondence principle as provided by Weyl-symbols and Wigner transformations [117].

Denoting the classical functions by $A(\mathbf{q}, \mathbf{p}) = A(\mathbf{x})$ and $B(\mathbf{x})$ it is straightforward to see that in the integrand of Eq. (4.23) we substitute

$$\left(p_{\alpha',i}^{(i)} - p_{\alpha,i}^{(i)}\right) q_{\alpha,j}^{(f)} \left(p_{\beta,i}^{(i)} - p_{\beta',i}^{(i)}\right) q_{\beta,j}^{(f)} \quad (4.77)$$

by

$$\left[A(\mathbf{x}_{\alpha'}^{(i)}) - A(\mathbf{x}_{\alpha}^{(i)})\right] B(\mathbf{x}_{\alpha}^{(f)}) \left[A(\mathbf{x}_{\beta}^{(i)}) - A(\mathbf{x}_{\beta'}^{(i)})\right] B(\mathbf{x}_{\beta}^{(f)}). \quad (4.78)$$

For diagrams (b), (c) and (d) of Fig. 4.2 the beginning and/or the ends of the trajectories are not contained inside an encounter region, and we approximate parts of the above expression by their ergodic averages. Note that as α', β start at phase space points which are associated with the Wigner function in Eq. (4.68), $A(\mathbf{x}_{\alpha'}^{(i)})$, $A(\mathbf{x}_{\beta}^{(i)})$ turn into $A(\mathbf{x})$. Like p_i in Eq. (4.71) they are treated as constants in the ergodic average Eq. (4.48), but are later averaged in the phase space average, Eq. (4.68), involving the Wigner function.

For diagrams (a), (b) and (c) in Fig. 4.2, the initial and/or final points of the trajectories are contained within an encounter, and thus we have to express the corresponding functions through the local hyperbolic variables. Equations (4.33, 4.34) are thus modified to

$$A(\mathbf{x}_{\alpha'}^{(i)}) - A(\mathbf{x}_{\alpha}^{(i)}) \approx - \left[\frac{\partial A}{\partial \mathbf{x}}(\mathbf{x}_{\beta}^{(i)}) \right] \cdot \sum_{l=1}^{d-2} s_l e^{\lambda t'} \mathbf{e}_{\beta,s}^{(l)}(0) \quad (4.79)$$

$$A(\mathbf{x}_{\beta}^{(i)}) - A(\mathbf{x}_{\beta'}^{(i)}) \approx - \left[\frac{\partial A}{\partial \mathbf{x}}(\mathbf{x}_{\beta}^{(i)}) \right] \cdot \sum_{l=1}^{d-2} s_l e^{\lambda t'} \mathbf{e}_{\beta,s}^{(l)}(0) \quad (4.80)$$

$$B(\mathbf{x}_{\alpha}^{(f)}) B(\mathbf{x}_{\beta}^{(f)}) \approx B^2(\mathbf{x}_{\beta}^{(f)}) - \frac{1}{2} \left(\left[\frac{\partial B}{\partial \mathbf{x}}(\mathbf{x}_{\beta}^{(f)}) \right] \cdot \sum_{l=1}^{d-2} u_l e^{\lambda(t-t')} \mathbf{e}_{\beta,u}^{(l)}(t) \right)^2 \quad (4.81)$$

This changes the phase space function $I(\mathbf{q}, \mathbf{p}; t)$ in Eqs. (4.51, 4.56, 4.58, 4.63), since it now uses different ergodic averages and adjusts the terms involving the stable and unstable directions. However, the encounter integrals $F(t)$ in Eqs. (4.52, 4.57, 4.59, 4.60, 4.64, 4.65) remain the same. Therefore, the result of the OTOC for operators fulfilling the above assumptions is thus obtained by adjusting the classical information in the phase space functions $I_{<}$ and $I_{>}$ in Eqs. (4.69, 4.71).

It is straightforward to see, that this reproduces for times $t < t_E$ shorter than the Ehrenfest time

$$C(t) \approx \int d^d q \int d^d p W(\mathbf{q}, \mathbf{p}) \left(\left\{ B(\mathbf{x}^{(f)}(t; \mathbf{x})), A(\mathbf{x}) \right\} \right)^2, \quad (4.82)$$

while for times larger than the Ehrenfest time, $t > t_E$ the saturation value is determined by

$$C(t) \approx \int d^d q \int d^d p W(\mathbf{q}, \mathbf{p}) \left\langle (A(\mathbf{x}) - A(\mathbf{x}'))^2 \right\rangle_{\mathbf{x}} \left(\langle B(\mathbf{x}')^2 \rangle_{\mathbf{x}} - \langle B(\mathbf{x}') \rangle_{\mathbf{x}}^2 \right). \quad (4.83)$$

4.5.2 Generalization towards a Lyapunov spectrum and general hyperbolicity

The assumption of uniformly hyperbolic dynamics, with moreover taking all Lyapunov exponents to be equal, is a very common approximation for the analysis of chaotic classical systems, and is used, for instance, in Ref. [33]. For a physically realistic many-body system, this seems to be rather restrictive, but, as we argue in the subsequent lines, this assumption is only needed to heavily reduce the amount of calculations and to simplify the technical aspects of our work, such that a pedagogical presentation of them is possible. The essential physical interpretations of OTOCs remain valid when lifting this assumption, as our main results for the OTOC in the limits of times much smaller and much larger than the Ehrenfest time still hold true for generic hyperbolic dynamics.

As we discussed in section 2.3.2, within generic hyperbolic dynamics each phase space point \mathbf{x} admits a set $\{ \Lambda_1(t; \mathbf{x}), \dots, \Lambda_{d-2}(t; \mathbf{x}) \}$ of exponentially growing stretching factors, representing unstable hyperbolic dynamics, while their inverses represent stable dynamics, see the decomposition of the stability matrix, Eq. (2.18) and the pairing rule, Eq. (2.28). Within our studies of the OTOC and for times larger than the Lyapunov time t_L (the minimal time required to experience hyperbolic dynamics) we introduced the Lyapunov exponents by approximating the stretching factors by their asymptotic behaviour,⁷

$$\Lambda_i(t; \mathbf{x}) \approx e^{\lambda_i(\mathbf{x})t}. \quad (4.84)$$

For the main contributions to OTOCs depicted in Fig. 4.2, multiple trajectories are coupled to each other within an encounter region. In such regions phase space points of the trajectories are in close vicinity of each other, and by assuming continuity of the stretching factors of nearby trajectories we can conclude that each of the trajectories

⁷Since we do not take the limit $t \rightarrow \infty$ within our considerations of the OTOC, the set of Lyapunov exponents obtained from this approximation might be different from the one obtained from their mathematical definition in Eq. (2.16). A difference might happen if two uniformly hyperbolic classical chaotic systems with different Lyapunov spectra are weakly coupled to each other. For a limited time, a trajectory launched in one of the subsystems is subject to that subsystems hyperbolic dynamics, and the stretching factors report exponential growth with the Lyapunov exponents of the subsystem. For long times, after multiples of the dwell times τ_d , the mean time a typical trajectory stays in the single subsystems, the stretching factors accumulate exponential growth subject to the Lyapunov exponents of both subsystems. In the limit of infinite time this results in a spectrum of Lyapunov exponents which can be interpreted as a weighted average of the spectra of the subsystems.

involved in the encounter admits the same spectrum of Lyapunov exponents. The phase space point \mathbf{x} fixing this spectrum can be taken as one of the starting points of the trajectories. By choosing here the initial conditions of the reference trajectory β , we associate this point to the ones provided by the final phase space average involving the Wigner function, Eq. (4.68). For the analysis of the diagram classes in Fig. (4.2), which lead to the phase space functions $I(\mathbf{x}; t)$, we can thus assume a fixed spectrum of Lyapunov exponents, as its dependence on a phase space point only needs to be considered in this final phase space average.

Let us thus assume \mathbf{x} to be fixed and we take uniform hyperbolic dynamics with a spectrum $\{\lambda_1(\mathbf{x}), \dots, \lambda_{d-2}(\mathbf{x})\}$ of positive Lyapunov exponents. For the subsequent arguments, we drop the dependence on \mathbf{x} . Pairs of stable and unstable directions are associated through their indices with their corresponding Lyapunov exponent λ_i . Finally, the Ehrenfest time is defined as in Eq. (4.30), where λ is taken to be the largest positive Lyapunov exponent of the spectrum.

The consequences of considering a spectrum of Lyapunov exponents in the semiclassical treatment of the OTOC is reflected in two modifications. First, we need to adjust our treatment of the initial momentum quadrature difference and the product of final position quadratures in case of correlated initial or final conditions of the trajectories,

$$\begin{aligned} p_{\alpha',i}^{(i)} - p_{\alpha,i}^{(i)} &= - \sum_{l=1}^{d-2} s_l e^{\lambda_l t'} \left[\mathbf{e}_{\beta,s}^{(l)}(0) \right]_{p_i}, \\ p_{\beta,i}^{(i)} - p_{\beta',i}^{(i)} &= - \sum_{l=1}^{d-2} s_l e^{\lambda_l t'} \left[\mathbf{e}_{\beta,s}^{(l)}(0) \right]_{p_i}, \\ q_{\alpha,j}^{(f)} q_{\beta,j}^{(f)} &\approx q_{\alpha,j}^{(f)2} - \frac{1}{2} \left(\sum_{l=1}^{d-2} u_l e^{\lambda_l(t-t')} \left[\mathbf{e}_{\beta,u}^{(l)}(t) \right]_{q_j} \right)^2. \end{aligned} \quad (4.85)$$

Second, the times t_s (t_u) the first stable (unstable) component needs to grow to the critical value c in Eq. (4.31) are altered to

$$t_s(\mathbf{s}) = \min_i \left(\frac{1}{\lambda_i} \log \left(\frac{c}{|s_i|} \right) \right), \quad t_u(\mathbf{u}) = \min_i \left(\frac{1}{\lambda_i} \log \left(\frac{c}{|s_i|} \right) \right). \quad (4.86)$$

While these modifications do not affect the arguments leading to ergodic phase space averages and the generic structure of the contributions, Eq. (4.68), it does change the encounter integrals. Their calculation requires much more work and further, (so far unknown) techniques to resolve the minima in Eq. (4.86) to be able to calculate the encounter integrals. However, we do not expect that this further complication in the semiclassical treatment of OTOCs results in further information going beyond the physical interpretation we have drawn so far from our semiclassical analysis of OTOCs. To understand this, one can investigate the implications of a spectrum of Lyapunov exponents in the case of the zero-leg diagram, where due to the absence of a dependence on $t_s(\mathbf{s})$ and $t_u(\mathbf{s})$ the evaluation of integrals is still possible.

For instance, we found within our studies that contributions originating from $F_{l'l'mm'}^{(0le,2)}(t)$ for $\{l, l'\} = \{m, m'\}$ contained the short-time exponential growth of OTOCs. For the generic hyperbolic case, also taking $m = l, m' = l', l \neq l'$, this encounter integral is modified to

$$\begin{aligned}
F_{l'l'l'}^{(0le,2)}(t) &= \frac{1}{(2\pi\hbar_{\text{eff}})^{d-2}t} \int_0^t dt' \prod_{\substack{i=1 \\ l \neq i \neq l'}}^{d-2} \left(\int_{-ce^{-\lambda_i t'}}^{ce^{-\lambda_i t'}} ds_i \int_{-ce^{-\lambda_i(t-t')}}^{ce^{-\lambda_i(t-t')}} du_i e^{\frac{i}{\hbar_{\text{eff}}} s_i u_i} \right) \\
&\times \left(\int_{-ce^{-\lambda_l t'}}^{ce^{-\lambda_l t'}} ds_l \int_{-ce^{-\lambda_l(t-t')}}^{ce^{-\lambda_l(t-t')}} du_l e^{\frac{i}{\hbar_{\text{eff}}} s_l u_l} s_l u_l e^{\lambda_l t} \right) \\
&\times \left(\int_{-ce^{-\lambda_{l'} t'}}^{ce^{-\lambda_{l'} t'}} ds_{l'} \int_{-ce^{-\lambda_{l'}(t-t')}}^{ce^{-\lambda_{l'}(t-t')}} du_{l'} e^{\frac{i}{\hbar_{\text{eff}}} s_{l'} u_{l'}} s_{l'} u_{l'} e^{\lambda_{l'} t} \right).
\end{aligned} \tag{4.87}$$

Note that the exponentially growing factor in the integrand contain the Lyapunov exponents labeled by the same indices l, l' as of the encounter integral $F_{l'l'l'}$. They originate from a correlated consideration of the initial and final points according to Eq. (4.85).

Using Eqs. (A.71) and (A.73), the evaluation of the integral is straightforward and yields

$$\begin{aligned}
F_{l'l'l'}^{(0le,2)}(t) &= -\left(\frac{2}{\pi}\right)^{d-2} \hbar_{\text{eff}}^2 e^{(\lambda_l + \lambda_{l'})t} \left[\text{Si}\left(\frac{c^2}{\hbar_{\text{eff}}} e^{-\lambda_l t}\right) - \sin\left(\frac{c^2}{\hbar_{\text{eff}}} e^{-\lambda_l t}\right) \right] \\
&\times \left[\text{Si}\left(\frac{c^2}{\hbar_{\text{eff}}} e^{-\lambda_{l'} t}\right) - \sin\left(\frac{c^2}{\hbar_{\text{eff}}} e^{-\lambda_{l'} t}\right) \right] \prod_{\substack{i=1 \\ l \neq i \neq l'}} \text{Si}\left(\frac{c^2}{\hbar_{\text{eff}}} e^{-\lambda_i t}\right),
\end{aligned} \tag{4.88}$$

where we observe that the multiple Lyapunov exponents different from λ_l and $\lambda_{l'}$ only appear in the arguments of the Sine-functions $\text{Si}(x)$. As we discuss in detail in the appendix A.4, we either approximate this function by a linear Taylor expansion to explain the strong suppression after the Ehrenfest time, or we use the asymptotic value $\text{Si}(z) \approx \pi/2$ for $z \rightarrow \infty$ to obtain a simplified analytic expression for $t < t_E$. In both cases an explicit dependence of the result on these additional Lyapunov exponents is suppressed. Indeed, following the same argumentation as in appendix A.4.5 we can approximate

$$F_{l'l'l'}^{(0le,2)}(t) \approx -\hbar_{\text{eff}}^2 e^{(\lambda_l + \lambda_{l'})t} \theta(t_E - t), \tag{4.89}$$

which, used within Eq. (4.63) reproduces the expected short-time behaviour of OTOCs as stated by Eq. (4.17), however now explicitly including the spectrum of Lyapunov exponents to reproduce the derivative in Eq. (4.16).

Based on this observation, for the other diagrammatic contributions explaining the saturation value of OTOCs, we thus conjecture also a masking of the Lyapunov exponents through functions which are insensitive to their precise values.

4.5.3 Non-ergodic many-body dynamics

For our studies, and more exactly when we introduced ergodic averages in Eq. (4.47), we assumed that the submanifold in phase space defined by the constants of motion \mathcal{H} and \mathcal{N} , see Eqs. (4.25) and (4.26), fulfills the mixing property (see section 2.3.1 for an exact definition). However, the nonlinear mean-field dynamics associated with the classical limit of the many-body Fock space is much less understood [77, 118, 119] than the classical dynamics within single-particle systems, and most likely it admits more complex behaviour such as mixed regular-chaotic dynamics, where regular islands due to local constants of motion emerge within the chaotic sea in the classical phase space, or diffusive behaviour. The propagator Eq. (3.83) is not restricted to chaotic dynamics, but also allows investigating these scenarios.

For times shorter than the Ehrenfest time the result obtained from the expansion of Moyal brackets in section 4.1.2 should still be reproduced. Since this is based on the stability of a single solution of the mean-field equations we expect our semiclassical analysis to produce, for any system, the same interference mechanism as depicted in Fig. 4.2 (a), *i.e.* the dynamics of the involved trajectories in the semiclassical treatment essentially follow a single, central trajectory.

For times larger than the Ehrenfest time one needs, in case of regular motion, the knowledge of all trajectories to investigate the interference mechanism, rendering $C(t)$ strongly system-dependent. Post-Ehrenfest behaviour of the OTOC has thus to be studied individually for each system.

Mixed regular-chaotic or diffusive systems may be treated by a modification of the ergodic phase space average to account for a restricted exploration of the accessible phase space. Ultimately, this can also lead to a time-dependence of the OTOC after the Ehrenfest time in case of a growing accessibility of phase space regions in time, such as, for instance, for Lorentz gases, as we see in our discussion in section 4.5.5.

4.5.4 Time-reversal invariance and higher-order quantum corrections

The diagrams in Fig. 4.2 do not contain trajectory loops, where a trajectory partially follows the time-reversed version of another trajectory, see, for instance, Fig. 4.6 (a). This implies that our results hold for systems both with and without time-reversal symmetry.

Diagrams involving more than one trajectory encounter generally yield further contributions that can be susceptible to time-reversal symmetry breaking. However, note that an encounter region is accompanied by a partner density similar to Eq. (4.35), which is proportional to the inverse volume of the chaotic phase space submanifold, $\Sigma(\mathbf{x})^{-1}$, see Eq. (4.45). This proportionality is a consequence of limiting the free exploration of the individual trajectories in order to produce their encounter in phase space, and ultimately suppresses diagrammatic contributions with n encounters by a factor proportional $\Sigma(\mathbf{x})^{-n+1}$ compared to the contributions of the leading diagrams in Fig. 4.2. Furthermore, since the formation of an encounter with a small enough action difference requires a minimal time, corrections due to multi-encounter diagrams are expected to contribute to the OTOC after times which are multiples of the encounter time t_E .

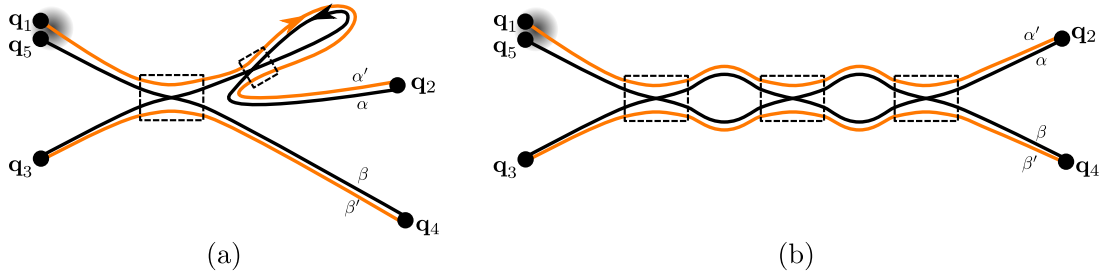


Figure 4.6: Examples for diagrammatic contributions to the OTOC with more than one encounter involved. In (a), one of the legs of Fig. 4.2 (d) is decorated with a loop. During the loop α' follows the time-reversal of α , rendering the contribution of this diagram sensitive to mechanisms breaking time-reversal symmetry.

In (b), in each of the encounters all four trajectories participate and interchange their partners. In order to fulfill the boundary conditions of the trajectories, an odd number of such encounters is required.

As a final remark, for the diagrams with a single encounter depicted in Fig. 4.2, the factor $\Sigma(\mathbf{x})^{-1}$ is compensated by two of the five integrations in the integral representation of the OTOC, Eq. (4.23). This is the reason why at the Ehrenfest time t_E their contributions are of the same order than the results from a classical, mean-field treatment of OTOCs.

Examples for higher order diagrams are shown in Fig. (4.6) and are similar to the diagrams which have been investigated in the context of shot noise in electronic transport through chaotic cavities [110]. Their evaluation for OTOCs requires further research and is beyond the scope of this thesis.

4.5.5 Small- \hbar limit and single-particle systems

To perform our semiclassical calculations for OTOCs we only needed to exploit the formal structure of the semiclassical approximation of the propagator for Bose-Hubbard models, Eq. (3.83), *i.e.* its appearance as coherent sum over mean-field solutions γ , where the phase factor contains Hamilton's principal function R_γ and the amplitude encodes the stability of the solution as a derivative of R_γ w.r.t. the boundary conditions of the trajectory. This structure is not exclusive to the propagator for Bose-Hubbard model, but is also found for the original Van Vleck-Gutzwiller approximation of propagator [1, 2] in the semiclassical limit of small \hbar . Our semiclassical calculation of OTOCs in the large- N limit can therefore be generalized to systems of N particles in f spatial dimensions, including the quantum chaotic single-particle case $N = 1$, treated in the complementary semiclassical " $\hbar \rightarrow 0$ " limit. For such systems, the effective Planck's constant is $\hbar_{\text{eff}} = \hbar/S \sim \lambda_{\text{dB}}/L$, where λ_{dB} is the de Broglie wavelength and S and L are typical actions and length scales of the chaotic classical limit. By using the Van Vleck-

Gutzwiller propagator [1] in $d = f \cdot N$ dimensions in the integral representation of the OTOC, Eq. (4.23), we can immediately conclude from our results that the exponential increase of the OTOC $C_N(t)$ is determined by the leading Lyapunov exponent λ_N of the corresponding classical N -particle system (see, for instance Refs. [53, 120] for $N = 1$). Furthermore, the corresponding Ehrenfest time, at which the OTOC displays the onset of saturation, is identified to be $t_E^{(N)} \sim (1/\lambda_N) \log(\hbar_{\text{eff}}^{-1}) \sim (1/\lambda_N) \log(L/\lambda_{\text{dB}})$.

The saturation value of $C_N(t)$ for $t > t_E^{(N)}$ involves ergodic averages, which we can attempt to evaluate using similar techniques as those used to arrive at Eq. (4.75). For instance, if we consider $C_N(t) = \langle |[\hat{p}_i, \hat{q}_j(t)]|^2 \rangle$ for chaotic billiards, where here \hat{p}_i and \hat{q}_j indeed represent momentum and position operator of particles, then the saturation value is again formally determined by the phase space function in Eq. (4.71). To estimate the ergodic averages involving the momenta, we use the classical Hamilton function of the system,

$$\mathcal{H}(\mathbf{q}, \mathbf{p}) = \frac{\|\mathbf{p}\|^2}{2m} + V(\mathbf{q}), \quad V(\mathbf{q}) = \begin{cases} 0, & \text{if } \mathbf{q} \in \Omega \\ \infty, & \text{else} \end{cases}, \quad (4.90)$$

where Ω denotes the set of points within the bounds of the billiard, and for simplicity, we assume equal masses in case of more than a single particle, $N > 1$. Trivially, since we do not have the system moving as a whole, the momentum averaged over the chaotic energy shell has to be 0, $\langle p'_i \rangle_{\mathbf{x}} = 0$. Furthermore, due to energy conservation

$$\frac{\|p\|^2}{2m} = \mathcal{H}(\mathbf{q}, \mathbf{p}) = \langle \mathcal{H}(\mathbf{q}, \mathbf{p}) \rangle_{\mathbf{x}} = \sum_{i=1}^d \frac{\langle p_i'^2 \rangle_{\mathbf{x}}}{2m}. \quad (4.91)$$

Under the assumption that no component of the momentum vector is preferred in the system, we thus arrive at $\langle p_i'^2 \rangle_{\mathbf{x}} = \|\mathbf{p}^2\|/d$, and therefore

$$\langle (p_i - p'_i)^2 \rangle_{\mathbf{x}} = p_i^2 + \frac{\|\mathbf{p}\|^2}{d}. \quad (4.92)$$

The ergodic variance in position equals the variance in position of the geometry of the billiard, and we can estimate

$$\Delta(q'_j)^2 = \langle q_j'^2 \rangle_{\mathbf{x}} - \langle q_j' \rangle_{\mathbf{x}}^2 \propto (\mathcal{L})^2 = L^2, \quad (4.93)$$

where \mathcal{L} denotes the typical diameter of the system, such that \mathcal{L}^f yields the volume of the billiard in configuration space. Moreover, \mathcal{L} sets the typical length scale L of the system, since this length also estimates the distance the particle travels between two bounces of the boundary.

At last, within the final average involving the Wigner function we can re-express $\|\mathbf{p}\|^2$ through the de Broglie wavelength,

$$\int d^d q \int d^d p W(\mathbf{q}, \mathbf{p}) \|\mathbf{p}\|^2 = \frac{(2\pi\hbar)^2}{\lambda_{\text{dB}}^2}. \quad (4.94)$$

This also indicates that the phase space average of p_i^2 is of the order of $(2\pi\hbar)^2/(d\lambda_{\text{dB}}^2)$, which we can use as a rough estimate.

Combining the above considerations we arrive at the following estimate for the saturation value of $C_N(t)$ for $t > t_E^{(N)}$

$$C_N(t) \approx \frac{2((2\pi\hbar)^2 L^2}{d\lambda_{\text{dB}}^2} \propto \frac{S^2}{d}. \quad (4.95)$$

Note that here we have a different scaling with the dimension d compared to Eq. (4.75), ultimately due to the different role played by \mathbf{q} within the classical Hamilton functions of the billiard and Bose-Hubbard models. Furthermore, the typical action $S = \hbar/\hbar_{\text{eff}}$ appears in the final result. This can be attributed to the fact that the operators \hat{p}_i, \hat{q}_j are scaled such that their commutator, $[\hat{q}_j, \hat{p}_i] = i\delta_{ij}\hbar$, is related to \hbar rather than $\hbar_{\text{eff}} = \hbar/S$.

Employing this line of reasoning, it is further possible to view the results in Ref. [53] as a quantitative numerical confirmation of our semiclassical findings.

Interestingly, while for billiards we have $L = \mathcal{L}$, for many systems we can have $L \ll \mathcal{L}$. An example for such a system is the famous Lorentz gas [82], where a point-like particle scatters off randomly positioned disks or spheres for $d = 2$ or 3 , where the diameter of the scatterers sets the scale L ⁸. In such systems the dynamics is hyperbolic only up to the Ehrenfest time $t_E^{(1)}$. After this time it becomes diffusive, implying in Eq. (4.71) a linear growth in time of the variance $(\Delta q_j')^2 \sim Dt$ with the diffusion constant D . This directly affects our result Eq. (4.71) for the OTOC, as beyond the Ehrenfest time $\tau_E^{(1)}$ we expect $C_1(t)$ to further increase linearly in time before it finally saturates at the Thouless time \mathcal{L}^2/D .

⁸Ehrenfest time effects in Lorentz gases were studied, *e.g.*, in Refs. [66, 121, 122].

5 Al'tshuler-Aronov-Spivak oscillations for interacting bosonic atoms

While in the last chapter many-body interference of multiple, different solutions of the bosonic mean-field equations was needed to explain the saturation of OTOCs, we here turn to a scenario whose explanation requires an explicit study of the mean-field equations themselves: the influence of interaction on Al'tshuler-Aronov-Spivak (AAS) oscillations in the coherent transport of cold atoms through an Aharonov-Bohm (AB) setup. This setup consists of two semi-infinite waveguides attached to a ring structure penetrated by a synthetic gauge field with tunable flux Φ . Within the ring, the atoms are subject to both a weak disorder potential and a weak atom-atom interaction.

In this chapter we present the Bose-Hubbard Hamiltonian we use as model for the discretized AB setup and derive its dynamical mean-field equation, the Gross-Pitaevskii equation, for the coherent transport of cold atoms through the ring. For weak interaction, we show that a scattering approach involving the Green's function of the interaction-free system formally solves the stationary scattering problem. We discuss that for weak disorder the Green's function admits a semiclassical approximation as a sum of scattering paths through the ring, in which disorder is reflected as an additional contribution to the phases accumulated along the paths.

Based on this semiclassical representation we qualitatively explain for the noninteracting case the AAS oscillations observable in the flux-dependent transmission through the ring. To motivate the theoretical study of the system including interaction in chapter 6, we further present results obtained from a numerical treatment by R. Chrétien *et al.*, which show the influence of interaction on these oscillations.

In the last part, we have seen that many-body interference of distinct, but correlated mean-field solutions is the mechanism explaining the saturation of OTOCs. The mean-field problems itself, which is not required to be solved explicitly, appears in the OTOC in the form of classical quantities such as the Lyapunov exponent and phase space averages. However, there are also scenarios where interesting phenomena can already be attributed to wave interference at the level of the mean-field wave equations themselves. In this part, we turn to such a case with the study of Al'tshuler-Aronov-Spivak (AAS) oscillations seen in the flux-dependent reflection and transmission of matter waves of interacting bosonic particles in the Aharonov-Bohm (AB) setup.

A system to study AB and AAS oscillations is an AB setup, where two semi-infinite waveguides are attached at opposite sites to a waveguide ring structure. In the transport of waves through such a structure, a gauge field (*e.g.* a magnetic field for electric waves) encircled by the ring results in additional phases the waves accumulate. These are proportional to the enclosed flux Φ , remarkably, even without the gauge field producing a classical force field in the waveguides. This is known as *Aharonov-Bohm effect*, which is here observable in oscillations in the transmission as a function of the enclosed flux and is attributed to the interference of waves following the two arms of the ring. When introducing an additional disorder potential within the ring, the disorder-averaged transmission reveals *Al'tshuler-Aronov-Spivak oscillations* with double the frequency of the AB oscillations.

In the next two chapters we study AAS oscillations for interacting bosonic matter waves, as here interaction amongst the particles leads to an inversion of AAS oscillations. This work has been done in collaboration with R. Chrétien, J. Dujardin, C. Petitjean and P. Schlagheck and has been published in Ref. [30]. The contents of this chapter are the presentation of the system we study, of the basic theoretical concepts, as well as of the numerical findings, and have been provided to me by my collaborators. My contribution, a semiclassical diagrammatic treatment of the problem, perturbative in the interaction strength, aims at an understanding of the numerical findings and is the subject of chapter 6. It builds on the theoretical framework derived in this chapter.

In order to provide a basic understanding of the underlying interference mechanism leading to AAS oscillations as an effect in general, we want to utilize the theoretical tools we provide for the bosonic matter wave in the limit of vanishing atom-atom interaction. We therefore shift the explanation of AAS oscillations to the second section of this chapter, and first introduce the system with the basic theoretical framework.

5.1 The Aharonov-Bohm ring with cold atoms

5.1.1 Bose-Hubbard Hamiltonian

The bosonic quantum many-body system in which we want to study AAS oscillations is schematically depicted in Fig. (5.1) (a). It is an interferometer setup built by two semi-infinite waveguides for guiding matter waves of cold bosonic atoms, which are attached to a central ring structure encircling an artificial gauge field. Interparticle interaction of the atoms is assumed to be limited to the ring structure, where additionally we assume a weak disorder potential. To generate a steady current of atoms into the waveguides and towards the ring structure, the left waveguide is weakly coupled to a Bose-Einstein condensate (BEC) with initially $N \rightarrow \infty$ particles at temperature $T = 0$ and chemical potential μ . By an adiabatic ramping of the coupling, this results, in the limit of long times, in a well-defined stationary scattering state of the system.

Within the numerical work of R. Chrétien *et al.*, this system is modeled by a Bose-Hubbard Hamiltonian arising from a discretization scheme of the continuous system of the AB setup in Fig. 5.1 (a) as described in Refs. [35, 36]. The semiclassical treatment

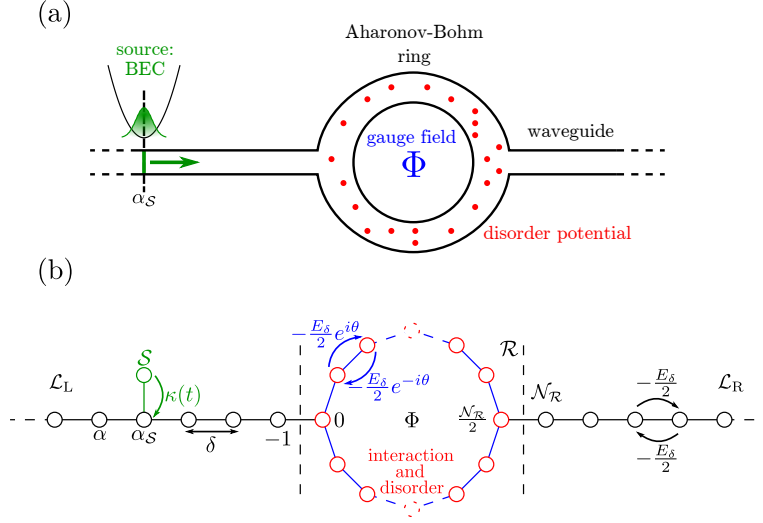


Figure 5.1: (a) Sketch of the investigated AB ring structure. A Bose-Einstein condensed cloud of cold bosonic atoms is coupled to the waveguide left to the ring and acts as a reservoir. Through an outcoupling mechanisms a current of atoms towards the ring structure is produced. Within the ring, the atoms experience a weak disorder potential, a gauge field Φ and a weak particle-particle interaction. (*Figure adapted from Ref. [30]*)

(b) Discretization of the system as preparation for the numerical study by R. Chrétien *et al.* The system is subdivided into four regions, the two waveguides (\mathcal{L}_R , \mathcal{L}_L), the ring structure (\mathcal{R}) and the BEC as the source (\mathcal{S}) of atoms. (*Figure taken from Ref. [30]*)

of AAS oscillations in chapter 6 is based on this Bose-Hubbard Hamiltonian and the parameters contained in that. We therefore use the Bose-Hubbard model as a starting point to derive the theoretical concepts necessary for our study.

The discretized version of the AB setup is schematically depicted in Fig. 5.1 (b). To write the Bose-Hubbard Hamiltonian, we split the system into four parts, the left and right waveguides \mathcal{L}_L , \mathcal{L}_R , the ring geometry \mathcal{R} and the source \mathcal{S} . The Hamiltonian of the system is then given by

$$\hat{H} = \hat{H}_{\mathcal{L}_L} + \hat{H}_{\mathcal{R}} + \hat{H}_{\mathcal{L}_R} + \hat{H}_{\mathcal{S}} + \hat{H}_{\mathcal{S}\mathcal{L}_L} + \hat{H}_{\mathcal{L}\mathcal{R}}, \quad (5.1)$$

where the Hamiltonians of the separate subregions are

$$\hat{H}_{\mathcal{L}_L} = \sum_{\alpha=-\infty}^{-1} \left[E_\delta \hat{b}_\alpha^\dagger \hat{b}_\alpha - \frac{E_\delta}{2} (\hat{b}_\alpha^\dagger \hat{b}_{\alpha-1} + \hat{b}_{\alpha-1}^\dagger \hat{b}_\alpha) \right],$$

$$\hat{H}_{\mathcal{L}_R} = \sum_{\alpha=\mathcal{N}_R}^{\infty} \left[E_\delta \hat{b}_\alpha^\dagger \hat{b}_\alpha - \frac{E_\delta}{2} (\hat{b}_\alpha^\dagger \hat{b}_{\alpha+1} + \hat{b}_{\alpha+1}^\dagger \hat{b}_\alpha) \right],$$

$$\begin{aligned}\hat{H}_{\mathcal{S}} &= \mu \hat{b}_{\mathcal{S}}^{\dagger} \hat{b}_{\mathcal{S}}, \\ \hat{H}_{\mathcal{R}} &= \sum_{\alpha=0}^{\mathcal{N}_{\mathcal{R}}-1} \left[(E_{\delta} + V_{\alpha}) \hat{b}_{\alpha}^{\dagger} \hat{b}_{\alpha} + \frac{g}{2} \hat{b}_{\alpha}^{\dagger} \hat{b}_{\alpha}^{\dagger} \hat{b}_{\alpha} \hat{b}_{\alpha} \right] \\ &\quad - \sum_{\alpha=0}^{\mathcal{N}_{\mathcal{R}}-2} \left[\frac{E_{\delta}}{2} \left(\hat{b}_{\alpha+1}^{\dagger} \hat{b}_{\alpha} e^{i\theta} + \hat{b}_{\alpha}^{\dagger} \hat{b}_{\alpha+1} e^{-i\theta} \right) \right] - \frac{E_{\delta}}{2} \left(\hat{b}_0^{\dagger} \hat{b}_{\mathcal{N}_{\mathcal{R}}-1} e^{i\theta} + \hat{b}_{\mathcal{N}_{\mathcal{R}}-1}^{\dagger} \hat{b}_0 e^{-i\theta} \right),\end{aligned}\tag{5.2}$$

and the terms coupling the different regions are

$$\begin{aligned}\hat{H}_{\mathcal{S}\mathcal{L}_L} &= \kappa(t) \hat{b}_{\alpha_{\mathcal{S}}}^{\dagger} \hat{b}_{\mathcal{S}} + \kappa^*(t) \hat{b}_{\mathcal{S}}^{\dagger} \hat{b}_{\alpha_{\mathcal{S}}} \\ \hat{H}_{\mathcal{L}\mathcal{R}} &= -\frac{E_{\delta}}{2} \left(\hat{b}_{-1}^{\dagger} \hat{b}_0 + \hat{b}_0^{\dagger} \hat{b}_{-1} + \hat{b}_{\mathcal{N}_{\mathcal{R}}}^{\dagger} \hat{b}_{\frac{\mathcal{N}_{\mathcal{R}}}{2}} + \hat{b}_{\frac{\mathcal{N}_{\mathcal{R}}}{2}}^{\dagger} \hat{b}_{\mathcal{N}_{\mathcal{R}}} \right).\end{aligned}\tag{5.3}$$

Here, $\hat{b}_{\alpha}^{\dagger}$ and \hat{b}_{α} denote bosonic creation and annihilation operators for particles at site α within the waveguides and the ring structure. The creation and annihilation operators for particles in the reservoir BEC \mathcal{S} are denoted by $\hat{b}_{\mathcal{S}}^{\dagger}$ and $\hat{b}_{\mathcal{S}}$.

Within the waveguide structure we choose the indexing such that negative indices denote the sites in the left semi-infinite waveguide, and $\alpha \geq \mathcal{N}_{\mathcal{R}}$ the ones in the right. The missing indices in the range $0, \dots, \mathcal{N}_{\mathcal{R}} - 1$ label the sites in the ring in clockwise direction, with $\mathcal{N}_{\mathcal{R}}$ being the total number of sites within the ring. We choose $\mathcal{N}_{\mathcal{R}}$ to be an even number, and the sites labeled by $\alpha = 0, \mathcal{N}_{\mathcal{R}}/2$ couple to the left, respective right waveguide. Finally, the site in the left waveguide to which the reservoir \mathcal{S} is coupled is also referred to as $\alpha_{\mathcal{S}}$.

The onsite energies E_{δ} and the hopping terms $-E_{\delta}/2$ are expressed in terms of the energy scale $E_{\delta} = \hbar^2/(m\delta^2)$. Assuming a one-dimensional free motion along the waveguides, this scale arises from discretizing the continuous system by a chain of sites at distance δ , which transforms the kinetic term according to the finite difference discretization scheme

$$\begin{aligned}-\frac{\hbar^2}{2m} \frac{\partial^2 f(x)}{\partial x^2} &\approx -\frac{\hbar^2}{2m} \frac{f(x+\delta) + f(x-\delta) - 2f(x)}{\delta^2} \\ &= E_{\delta} f(x) - \frac{E_{\delta}}{2} (f(x+\delta) + f(x-\delta)).\end{aligned}\tag{5.4}$$

Within the ring, the atoms are subject to a gauge field [21, 22] which acts in an equivalent way as a magnetic field for charged particles. In the Bose-Hubbard Hamiltonian, it appears through an additional phase factor $\exp(\pm i\theta)$ containing Peierl's phase [123], which is multiplied to the hopping parameters. The signs are chosen such that its contribution to the overall phase obtained from hopping along the complete ring in clockwise direction is given by the flux enclosed by the ring, $\mathcal{N}_{\mathcal{R}}\theta = \Phi$.

The source is assumed to be a BEC at temperature $T = 0$ with initially $N(t=0) \rightarrow \infty$ particles at a chemical potential μ . The condensate weakly couples to a single site, labeled by $\alpha_{\mathcal{S}}$. For the numerical work performed by R. Chrétien, the coupling mechanism is controlled through the function $\kappa(t) = \mathcal{O}(E_{\delta}/\sqrt{N(0)})$, which is adiabatically increased from zero to a finite maximum value in infinite time,

$$\kappa = \lim_{t \rightarrow \infty} \kappa(t)\tag{5.5}$$

such that $N(t)|\kappa(t)|^2$ remains constant. As we will argue in subsection 5.1.3, this produces a steady current of particles into the waveguide and towards the Aharonov-Bohm ring and establishes a well-defined scattering state with energy μ and with a well-defined current towards the ring structure after a long enough propagation time [124]. Within the waveguide, we will see that in the mean-field treatment this scattering state is a superposition of plane waves, whose wave number k is related to the chemical potential μ through the dispersion relation of the discretized system

$$E_\delta(1 - \cos(k\delta)) = \mu \quad \Leftrightarrow \quad k = \frac{1}{\delta} \arccos\left(1 - \frac{\mu}{E_\delta}\right). \quad (5.6)$$

This also allows us to associate a wavelength $\lambda = (2\pi)/k$ to the atomic wave.

Within the ring we allow particles to interact with each other through on-site interaction whose strength is controlled by the parameter g . As a physical quantity, this strength is proportional to the s -wave scattering length a_s from the particle-particle scattering problem in 3 dimensions and can be tuned by the means of Feshbach resonances [11]. Further dependencies of this parameter are provided by the confining potential forcing the particles to the one-dimensional motion, see for instance Ref. [31].

Additionally, the ring is subject to a potential describing weak correlated disorder. Numerically, it is produced by

$$V_\alpha = \bar{V}_0 \sum_{\beta=-\frac{\mathcal{N}_R}{2}+1}^{\frac{\mathcal{N}_R}{2}} \sqrt{\frac{\delta}{\sigma\sqrt{\pi}}} \exp\left(-\frac{\delta^2}{2\sigma^2}\beta^2\right) \eta_{\alpha+\beta}, \quad (5.7)$$

where here, and only here, for convenience, the index $\alpha + \beta$ appearing in the summation has to be understood modulo \mathcal{N}_R to again produce a site within the ring. The parameters η_α are independent Gaussian random variables with zero mean and unit variance, such that $\langle \eta_\alpha \eta_{\alpha'} \rangle = \delta_{\alpha\alpha'}$. The sum correlates these random values over a correlation length $\sigma \gg \delta$ while the amplitude \bar{V}_0 controls the disorder strength. This produces a disorder potential which varies slowly over the distance of the correlation length σ . In the ensemble of realizations of disorder, the mean of V_α is 0 and the standard deviation is \bar{V}_0 .

It is worth to specify already here the relation of the different length scales introduced by the disorder. In order to be able to treat the disorder potential semiclassically, we need to demand that the disorder strength is weak compared to μ and that the correlation length σ is large compared to the wavelength λ . Furthermore, to observe AAS oscillations, the length $L = \delta\mathcal{N}_R/2$ of one arm of the ring has to support multiple variations σ of the disorder. Finally, we want to avoid localization effects requiring that L is much smaller than the localization length l_{loc} . For Gaussian correlated disorder, this length is given by [125]

$$l_{\text{loc}} = \frac{\hbar^4 k^2}{2m^2 \bar{V}_0^2 \sigma \sqrt{\pi}} \exp(4k^2 \sigma^2). \quad (5.8)$$

Combining these restrictions and including δ as the smallest length scale of the system, we arrive at

$$\delta \ll \lambda \ll \sigma \ll L \ll l_{\text{loc}}. \quad (5.9)$$

In order to simplify our notation for the next sections, we combine the parameters in such a way that the Hamiltonian takes the compact form

$$\hat{H} = \sum_{\alpha} \left[h_{\alpha} \hat{b}_{\alpha}^{\dagger} \hat{b}_{\alpha} + \frac{g_{\alpha}}{2} \hat{b}_{\alpha}^{\dagger} \hat{b}_{\alpha}^{\dagger} \hat{b}_{\alpha} \hat{b}_{\alpha} \right] + \sum_{\alpha\alpha'} J_{\alpha\alpha'} \hat{b}_{\alpha}^{\dagger} \hat{b}_{\alpha'} + \mu \hat{b}_{\mathcal{S}}^{\dagger} \hat{b}_{\mathcal{S}} + \kappa(t) \hat{b}_{\alpha_{\mathcal{S}}}^{\dagger} \hat{b}_{\mathcal{S}} + \kappa^{*}(t) \hat{b}_{\mathcal{S}}^{\dagger} \hat{b}_{\alpha_{\mathcal{S}}}, \quad (5.10)$$

where h_{α} contains the onsite-energies E_{δ} and disorder V_{α} , and $J_{\alpha\alpha'}$ denotes the hopping between sites, including those towards and from the ring, as well as Peierl's phase $\exp(\pm i\theta)$. Finally, we set $g_{\alpha} = 0$ within the waveguides, and $g_{\alpha} = g$ within the ring.

5.1.2 Mean-field equations

The mean-field equations of the system are given by the Hamilton's equations of motion, Eq. (3.86), we found in the classical " $N \rightarrow \infty$ " limit of the Bose-Hubbard model. In an alternative view, they can also be derived from the Heisenberg equations of motion for the annihilation operators of the system,

$$\begin{aligned} i\hbar \frac{d\hat{b}_{\alpha}(t)}{dt} &= - \left[\hat{H}, \hat{b}_{\alpha}(t) \right] \\ &= h_{\alpha} \hat{b}_{\alpha}(t) + \sum_{\alpha'} J_{\alpha\alpha'} \hat{b}_{\alpha'}(t) + g_{\alpha} \hat{b}_{\alpha}^{\dagger}(t) \hat{b}_{\alpha}(t) \hat{b}_{\alpha}(t) + \delta_{\alpha\alpha_{\mathcal{S}}} \kappa(t) \hat{b}_{\mathcal{S}}(t), \quad (5.11) \\ i\hbar \frac{d\hat{b}_{\mathcal{S}}(t)}{dt} &= - \left[\hat{H}, \hat{b}_{\mathcal{S}}(t) \right] = \mu \hat{b}_{\mathcal{S}}(t) + \kappa^{*}(t) \hat{b}_{\alpha_{\mathcal{S}}}(t). \end{aligned}$$

Here, the mean-field equations arise when substituting the creation and annihilation operators by complex scalar fields, $\hat{b}_{\alpha}(t) \rightarrow \tilde{\Psi}_{\alpha}(t) = \langle \hat{b}_{\alpha}(t) \rangle$ and $\hat{b}_{\mathcal{S}}(t) \rightarrow \tilde{\Psi}_{\mathcal{S}}(t) = \langle \hat{b}_{\mathcal{S}}(t) \rangle$, representing their mean value. Apart from a rescaling $\tilde{\Psi}_{\alpha}(t) = \Phi_{\alpha}(t) \sqrt{N}$, this results in the very same set of equations as in Eq. (3.86). For the study of AAS oscillations, we use the set of equations for $\tilde{\Psi}_{\alpha}$.

Often, especially in the continuous case, one refers to the dynamical mean-field equations, obtained from approximating the bosonic field operators by complex variables, as *Gross-Pitaevskii equation* [24, 25].

It is possible to eliminate the explicit treatment of the source from the dynamical equations. To do so, we make the ansatz $\Psi_{\alpha}(t) = \tilde{\Psi}_{\alpha}(t) e^{-(i/\hbar)\mu t}$ and $\Psi_{\mathcal{S}}(t) = \tilde{\Psi}_{\mathcal{S}}(t) e^{-(i/\hbar)\mu t}$. This transforms the mean-field equations into

$$\begin{aligned} i\hbar \frac{d\Psi_{\alpha}(t)}{dt} &= (h_{\alpha} - \mu) \Psi_{\alpha}(t) + \sum_{\alpha'} J_{\alpha\alpha'} \Psi_{\alpha'}(t) + g_{\alpha} \Psi_{\alpha}^{*}(t) \Psi_{\alpha}(t) \Psi_{\alpha}(t) + \delta_{\alpha\alpha_{\mathcal{S}}} \kappa(t) \Psi_{\mathcal{S}}(t), \\ i\hbar \frac{d\Psi_{\mathcal{S}}(t)}{dt} &= \kappa^{*}(t) \Psi_{\alpha_{\mathcal{S}}}(t). \quad (5.12) \end{aligned}$$

As we argued in the last section, we assume that the coupling $\kappa(t) = \mathcal{O}(E_\delta/\sqrt{N(t)})$ to the source is weak and adiabatically ramped such that $N(t)|\kappa(t)|^2$ becomes a constant in time. Since we assume that initially the number of particles in the source $|\Psi_S(0)|^2 = N(0)$ is much larger than the occupations at the sites in the ring structure, we can conclude from the Eq. (5.12) that $\Psi_S(t) \approx \sqrt{N(0)} \mathcal{T} \exp(-\hbar^{-2} \int_0^t ds |\kappa(s)|^2)$ [124]. Since the coupling is assumed to be small, we can therefore approximate $\Psi_S(t) \approx \sqrt{N(t)}$ as a real value and assume that the phase of $\kappa(t)$ does not depend on time, such that we can also consider the product $\sqrt{N(t)}\kappa(t)$ as a constant in time. This allows us to neglect the second equation in Eq. (5.12) and we arrive at

$$i\hbar \frac{d\Psi_\alpha(t)}{dt} = (h_\alpha - \mu)\Psi_\alpha(t) + \sum_{\alpha'} J_{\alpha\alpha'} \Psi_{\alpha'}(t) + g_\alpha \Psi_\alpha^*(t) \Psi_\alpha(t) \Psi_\alpha(t) + \delta_{\alpha\alpha_S} \underbrace{\kappa(t)\sqrt{N(t)}}_{\text{indep. on } t}. \quad (5.13)$$

As we will see in detail in the next section, the role of the source is to produce a steady current of particles into the system at well-defined energy μ . This current has its source at site α_S , leaving the site in both directions of the waveguide. One part of this steady current scatters through the ring structure, producing back-reflection and transmission of waves. For long enough times, the dynamics are expected to become stationary and the state of the system in the mean-field treatment is then described by a well-defined scattering state solving the nonlinear equation

$$0 = (h_\alpha - \mu)\Psi_\alpha + \sum_{\alpha'} J_{\alpha\alpha'} \Psi_{\alpha'} + g_\alpha \Psi_\alpha^* \Psi_\alpha \Psi_\alpha + \delta_{\alpha\alpha_S} \kappa(t) \sqrt{N(t)}. \quad (5.14)$$

Our theoretical concepts derived in the subsequent sections are based on this equation for the stationary scattering state.

5.1.3 Reflection and Transmission

Within the waveguides and for $\alpha \neq \alpha_S$, Eq. (5.14) takes the form

$$0 = (E_\delta - \mu)\Psi_\alpha - \frac{E_\delta}{2}(\Psi_{\alpha+1} + \Psi_{\alpha-1}), \quad (5.15)$$

whose solution is given by a superposition of plane waves at energy μ . Since we use the source to produce the only plane wave traveling towards the AB ring, the scattering state describing the stationary solution of Eq. (5.14) admits the following form in the waveguides:

$$\Psi_\alpha = \mathcal{A} \begin{cases} e^{i\alpha k\delta} + R(\Phi)e^{-i\alpha k\delta} \\ T(\Phi)e^{i(\alpha - \mathcal{N}_{\mathcal{R}} + 1)k\delta} \end{cases} = \begin{cases} \Psi_{\alpha,+}^{\mathcal{L}} + \Psi_{\alpha,-}^{\mathcal{L}} & \text{for } \alpha_S < \alpha < 0, \\ \Psi_{\alpha,+}^{\mathcal{R}} & \text{for } \alpha \geq \mathcal{N}_{\mathcal{R}}, \end{cases} \quad (5.16)$$

where the wave number k is defined as a function of μ through Eq. (5.6). With $\Psi_{\alpha,\pm}^{\mathcal{X}}$ we denote the contributions of the plane wave associated to a wave number $\pm k$ in the left (X=L) or right (X=R) waveguide,

$$\Psi_{\alpha,+}^{\mathcal{L}} = \mathcal{A}e^{i\alpha k\delta}, \quad \Psi_{\alpha,-}^{\mathcal{L}} = \mathcal{A}R(\Phi)e^{-i\alpha k\delta}, \quad \Psi_{\alpha,+}^{\mathcal{R}} = \mathcal{A}T(\Phi)e^{i(\alpha - \mathcal{N}_{\mathcal{R}} + 1)k\delta}. \quad (5.17)$$

We will later obtain the overall amplitude \mathcal{A} in Eq. (5.16) from a detailed consideration of the source. The complex amplitudes $R(\Phi)$ and $T(\Phi)$, the *reflection and transmission amplitude*, comprise the interference phenomena taking place within the scattering region, converting the incident wave into two outgoing waves, either back-reflected into the incident waveguide, or transmitted to the opposite one. They explicitly depend on the parameters of the scattering region and on the enclosed flux Φ . Their squared modulus $|R(\Phi)|^2$ and $|T(\Phi)|^2$ are referred to as *reflection and transmission probabilities* and they describe the coherent transport of the atomic matter waves through the ring. They are the central objects of interest in observing the AAS oscillations.

To understand the interpretation as probabilities, let us introduce the *particle current density*. Its definition for the continuous one-dimensional system is given by [92]

$$j(x, t) = \frac{\hbar}{2mi} \left(\Psi^*(x, t) \frac{\partial \Psi(x, t)}{\partial x} - \Psi(x, t) \frac{\partial \Psi^*(x, t)}{\partial x} \right), \quad (5.18)$$

from which its version for the Bose-Hubbard model is obtained by discretizing the derivative operator

$$\frac{\partial f(x)}{\partial x} \approx \frac{f(x + \delta) - f(x)}{\delta}. \quad (5.19)$$

This yields that the current density through site α in the waveguide is calculated by

$$j_\alpha = \frac{E_\delta}{2i\hbar} [\Psi_\alpha^* \Psi_{\alpha+1} - \Psi_{\alpha+1}^* \Psi_\alpha]. \quad (5.20)$$

Inserting Eq. (5.16) into Eq. (5.20), we obtain

$$j_\alpha = \frac{E_\delta |\mathcal{A}|^2}{\hbar} \begin{cases} \sin(k\delta) - |R(\Phi)|^2 \sin(k\delta) \\ |T(\Phi)|^2 \sin(k\delta) \end{cases} = \begin{cases} j_{\alpha,+}^{\mathcal{L}_L} + j_{\alpha,-}^{\mathcal{L}_L} & \text{for } \alpha_S + 1 < \alpha < -1, \\ j_{\alpha,+}^{\mathcal{L}_R} & \text{for } \alpha > \mathcal{N}_R, \end{cases} \quad (5.21)$$

where $j_{\alpha,\pm}^{\mathcal{L}_X}$ for $X=L, R$ are the currents calculated by Eq. (5.20) using the individual plane waves $\Psi_{\alpha,\pm}^{\mathcal{L}_X}$, Eq. (5.17).

Within the waveguides, the currents in Eq. (5.21) do not depend on the choice of site α within the ranges specified. Moreover, we are able to interpret reflection and transmission probabilities as the fraction of the incident current which is reflected or transmitted into the outgoing current. Mathematically, we find for $\alpha_S + 1 < \alpha < 0$ and $\alpha' > \mathcal{N}_R$,

$$|R(\Phi)|^2 = \frac{-j_{\alpha,-}^{\mathcal{L}_L}}{j_{\alpha,+}^{\mathcal{L}_L}} = \frac{-(j_\alpha - j_{\alpha,+}^{\mathcal{L}_L})}{j_{\alpha,+}^{\mathcal{L}_L}}, \quad |T(\Phi)|^2 = \frac{j_{\alpha',+}^{\mathcal{L}_R}}{j_{\alpha,+}^{\mathcal{L}_L}}. \quad (5.22)$$

Finally, the conservation of particles translates into conservation of currents, $j_{\alpha',+}^{\mathcal{L}_L} = j_{\alpha,+}^{\mathcal{L}_R} - j_{\alpha,+}^{\mathcal{L}_L}$, from which we conclude immediately $|R(\Phi)|^2 + |T(\Phi)|^2 = 1$.

Either Eq. (5.16) or Eq. (5.22) can be used to calculate reflection and transmission probabilities. Indeed for the numerical treatment, Eq. (5.22) is used, while the theoretical study in the next chapter focuses on finding an analytical expression for $\Psi_{\alpha,-}^{\mathcal{L}_L}$ and $\Psi_{\alpha,+}^{\mathcal{L}_R}$.

However, both approaches require the identification of the amplitude \mathcal{A} of the incident wave generated by the source term.

Let us focus on the left waveguide alone and extend it to an infinite waveguide. The mean-field equation including the source reads

$$0 = (E_\delta - \mu)\Psi_\alpha - \frac{E_\delta}{2}(\Psi_{\alpha+1} + \Psi_{\alpha-1}) + \delta_{\alpha\alpha_S}\kappa(t)\sqrt{N(t)}, \quad (5.23)$$

where the product $\kappa(t)\sqrt{N(t)}$ is understood to be constant in time. The solution to this equation is found to be

$$\Psi_\alpha = \frac{\kappa(t)\sqrt{N(t)}}{\mu - E_\delta(1 - e^{ik\delta})} e^{ik\delta|\alpha - \alpha_S|}. \quad (5.24)$$

Comparing this solution for $\alpha > \alpha_S$ to $\Psi_{\alpha,+}^{\mathcal{L}}$ in Eq. (5.17) allows us to immediately identify the amplitude \mathcal{A} as

$$\mathcal{A} = \frac{\kappa(t)\sqrt{N(t)}}{\mu - E_\delta(1 - e^{ik\delta})} e^{-ik\delta\alpha_S} = \frac{\kappa(t)\sqrt{N(t)}}{i\sqrt{\mu(2E_\delta - \mu)}} e^{i|\alpha_S|k\delta} = \frac{\kappa(t)\sqrt{N(t)}}{iE_\delta \sin(k\delta)} e^{i|\alpha_S|k\delta}, \quad (5.25)$$

where we used Eq. (5.6) as well as

$$E_\delta \sin(k\delta) = \sqrt{\mu(2E_\delta - \mu)} \quad (5.26)$$

to rewrite the solutions. The squared modulus $|\mathcal{A}|^2$ can be interpreted such that the source generates a mean constant particle density in the clean infinite waveguide,

$$\rho^\varnothing \delta = |\Psi_\alpha|^2 = \frac{N(t)|\kappa(t)|^2}{\mu(2E_\delta - \mu)}. \quad (5.27)$$

Using this density, the reflection and transmission probabilities are obtained as

$$|R(\Phi)|^2 = \frac{|\Psi_{\alpha,-}^{\mathcal{L}}|^2}{\rho^\varnothing \delta}, \quad |T(\Phi)|^2 = \frac{|\Psi_{\alpha,+}^{\mathcal{L}}|^2}{\rho^\varnothing \delta}. \quad (5.28)$$

Finally, the current generated by the source is found to be

$$j^\varnothing \equiv j_{\alpha,+}^{\mathcal{L}} = \frac{E_\delta}{\hbar} |\mathcal{A}|^2 \sin(k\delta) = \frac{1}{\hbar} \frac{N(t)|\kappa(t)|^2}{\sqrt{\mu(2E_\delta - \mu)}}. \quad (5.29)$$

5.1.4 Green's function approach and the role of disorder

For a weak enough interaction together with adiabatic ramping of the source, we can treat the stationary scattering problem in Eq. (5.14) as an effectively linear scattering problem. The problem is then formally solved by the ansatz

$$\Psi_\alpha = \sum_{\alpha'} G_{\alpha\alpha'}(\mu) Q_{\alpha'}, \quad (5.30)$$

which involves the (retarded) Green's function for the system without interaction,

$$G_{\alpha\alpha'}(\mu) = \langle \alpha | \hat{G}(\mu) | \alpha' \rangle = \lim_{\varepsilon \rightarrow 0^+} \langle \alpha | (\mu - \hat{\mathcal{H}}_0 + i\varepsilon)^{-1} | \alpha' \rangle \quad (5.31)$$

where $|\alpha\rangle = \hat{b}_\alpha^\dagger |0\rangle$ and

$$\hat{\mathcal{H}}_0 = \sum_\alpha h_\alpha |\alpha\rangle\langle\alpha| + \sum_{\alpha\alpha'} J_{\alpha\alpha'} |\alpha\rangle\langle\alpha'|. \quad (5.32)$$

The source as well as the nonlinear interaction term are combined into

$$Q_\alpha = g_\alpha |\Psi_\alpha|^2 \Psi_\alpha + \delta_{\alpha\alpha_S} \sqrt{\mathcal{N}(t)} \kappa(t). \quad (5.33)$$

This transforms the stationary mean-field equation, Eq. (5.14), for Ψ_α into a self-consistent equation,

$$\Psi_\alpha = \sqrt{\mathcal{N}(t)} \kappa(t) G_{\alpha\alpha_S}(\mu) + \sum_{\alpha'} G_{\alpha\alpha'}(\mu) g_{\alpha'} |\Psi_{\alpha'}|^2 \Psi_{\alpha'}, \quad (5.34)$$

similar to Dyson's equation [90], but with a nonlinear reappearance of Ψ_α on the right hand side. This equation marks the starting point for a perturbation theory in the small interaction parameter g .

In order to start this perturbation theory and to shed light on the involved interference mechanism leading to AAS oscillations, we aim at a suitable semiclassical representation of the Green's function, Eq. (5.31), in terms of interfering classical paths. To do so, let us first consider the infinite discrete waveguide. Its Green's function can either be found by solving the defining equation $(\mu - \hat{H}_0) \hat{G}(\mu) = \mathbf{1}$, or by comparing Eq. (5.24) with Eq. (5.34) for $g_\alpha = 0$. We get

$$G^{\text{free}}(\alpha, \alpha', \mu) = \frac{1}{iE_\delta \sin(k\delta)} e^{ik\delta|\alpha-\alpha'|} = \frac{1}{iE_\delta \sin(k\delta)} e^{\frac{i}{\hbar} S(\alpha, \alpha', \mu)}. \quad (5.35)$$

This Green's function describes plane waves emitted from site α' , since the sign in front of the wave number is specified by $\text{sign}(\alpha - \alpha')$, *i.e.* the relative position of α w.r.t. α' . The argument of the phase factor can also be interpreted as the discrete version of the reduced action $S = \int_{\alpha'}^\alpha \mathbf{p} \, d\mathbf{q}$, which integrates the momentum along the direct path linking α' with α at energy μ . Its discrete version is calculated by (taking $\alpha > \alpha'$)

$$\frac{1}{\hbar} S(\alpha, \alpha', \mu) = \sum_{\alpha''=\alpha'}^\alpha \arccos\left(1 - \frac{\mu}{E_\delta}\right) \delta = \sum_{\alpha''=\alpha'}^\alpha k\delta = k\delta(\alpha - \alpha'). \quad (5.36)$$

This can be generalized to the Green's function of the Aharonov-Bohm ring. We can interpret the junction sites $\alpha = 0, \mathcal{N}_R/2$, at which the waveguides are attached to the ring, as single-site scattering centers. Without disorder, we have free motion along the branches of the ring, thus yielding a multiple scattering problem of the junctions. It can be shown [126] that its solution has the form of a summation over all possible scattering

paths γ , *i.e.* paths linking the sites α' and α with multiple intermediate scattering events at the junctions and plane wave motion between those,

$$G_{\alpha\alpha'}(\mu) = \frac{1}{iE_\delta \sin(k\delta)} \sum_{\gamma: \alpha' \xrightarrow{\mu} \alpha} A_\gamma e^{\frac{i}{\hbar} S_\gamma}. \quad (5.37)$$

Here, $S_\gamma/\hbar = k\delta n_\gamma$ denotes the accumulated reduced action, with n_γ the number of sites passed by the scattering path, thereby counting multiple visits. The amplitude $A_\gamma = r^{n_{\gamma,r}} t^{n_{\gamma,t}}$ weights the paths contribution by the product of powers of the reflection and transmission matrix elements r, t according to the numbers $n_{\gamma,r}$ and $n_{\gamma,t}$ of scattering events at each of the junction sites $\alpha = 0, \mathcal{N}_R/2$. The numerical values for the parameters r and t are obtained from an analysis of the scattering problem at a single Y-junction. This analysis is found in appendix A.5. Note that continuity and current conservation leads to the relations

$$1 + r = t, \quad |r|^2 + 2|t|^2 = 1. \quad (5.38)$$

We now turn the AB ring including the disorder potential. Remember that we assumed that the strength of disorder is weak compared to the chemical potential, $\bar{V}_0 \ll \mu$, and that it is slowly varying on the length scale of the wavelength λ , since the correlation length $\sigma \gg \lambda$ is long compared to the wave length. This allows us to neglect back-reflection within the branches of the AB ring, and the scattering paths in the summation for the Green's function, Eq. (5.37), are left unchanged. Disorder is, however, accounted for in a modification of the accumulated phase. For instance, the action S_u accumulated from a single exploration of the upper (“u”) branch is found to be

$$\begin{aligned} \frac{1}{\hbar} S_u \left(\frac{\mathcal{N}_R}{2} - 1, 0, \mu \right) &= \sum_{\alpha=0}^{\frac{\mathcal{N}_R}{2}-1} \arccos \left(1 - \frac{\mu - V_\alpha}{E_\delta} \right) \\ &\approx \sum_{\alpha=0}^{\frac{\mathcal{N}_R}{2}} \left[\arccos \left(1 - \frac{\mu}{E_\delta} \right) - \frac{1}{\sqrt{\mu(2E_\delta - \mu)}} V_\alpha \right] \\ &= \frac{\mathcal{N}_R}{2} k\delta - \frac{1}{E_\delta \sin k\delta} \sum_{\alpha=0}^{\frac{\mathcal{N}_R}{2}-1} V_\alpha, \end{aligned} \quad (5.39)$$

and similarly for the action S_d accumulated from a single exploration of the lower (“d”) branch.

We can also understand this approximation as to arise from a semiclassical treatment of disorder, where the weak and smooth disorder potential is incorporated into the Green's function by means of semiclassical perturbation theory. This leads to a summation over paths of the unperturbed system, while an additional phase accumulates the disorder potential along the path [95].

For the investigation of AAS oscillations, an average over an ensemble of disorder configurations is required. For our analytical predictions, this can be used for a further

simplification. Within the disorder average, using the statistical properties of V_α , the mean value of the the accumulated phase due to disorder is found to vanish,

$$\left\langle \frac{1}{E_\delta \sin(k\delta)} \sum_{\alpha=0}^{\frac{N_{\mathcal{R}}}{2}} V_\alpha \right\rangle_{\text{dis}} = \frac{1}{E_\delta \sin(k\delta)} \sum_{\alpha=0}^{\frac{N_{\mathcal{R}}}{2}} \langle V_\alpha \rangle_{\text{dis}} = 0. \quad (5.40)$$

However, by choosing the length L of the branches long enough (where long enough depends on the strength \bar{V}_0), we can achieve that the variance of the accumulated phase fulfills

$$\left\langle \left(\frac{1}{E_\delta \sin(k\delta)} \sum_{\alpha=0}^{\frac{N_{\mathcal{R}}}{2}} V_\alpha \right)^2 \right\rangle_{\text{dis}} \gg \pi^2. \quad (5.41)$$

In this case, we can safely assume that $e^{\frac{i}{\hbar}S_u}$, $e^{\frac{i}{\hbar}S_d}$ can be considered as independent random complex numbers, uniformly distributed along the complex unit circle. Finally also including the flux $\Phi = N_R\theta$ through the center of the AB ring, this allows us to replace

$$e^{\frac{i}{\hbar}S_u} = e^{i(\Phi_u \pm \frac{\Phi}{2})}, \quad e^{\frac{i}{\hbar}S_d} = e^{i(\Phi_d \mp \frac{\Phi}{2})} \quad (5.42)$$

where Φ_u , Φ_d are uniformly distributed random phases taken from the interval $[0, 2\pi)$. These phases represent the addition to the overall accumulated phase, which is obtained each time when a scattering path uses the upper, respective lower branch of the ring to travel between junctions. A non-vanishing flux contributes an additional phase $\Phi/2$, where the sign distinguishes between clockwise (+) and anticlockwise (−) direction.

With the above assumptions, we see that details of the individual disorder configurations are comprised in the two parameters Φ_u, Φ_d . Moreover, with the substitution Eq. (5.42) the average over an ensemble of disorder configurations transforms into averaging the phases Φ_u, Φ_d over $[0, 2\pi)$. For instance, the disorder averaged transmission probability is obtained by

$$\langle |T(\Phi_u, \Phi_d, \Phi)|^2 \rangle = \frac{1}{(2\pi)^2} \int_0^{2\pi} d\Phi_u \int_0^{2\pi} d\Phi_d |T(\Phi_u, \Phi_d, \Phi)|^2, \quad (5.43)$$

where $T(\Phi_u, \Phi_d, \Phi)$ is the transmission amplitude of an individual disorder configuration giving rise to phases Φ_u, Φ_d . This reformulation of the disorder average is an important step, as for non-negative integer $n_u, n'_u, n_d, n'_d \in \mathbb{N}_0$, we have the identity

$$\frac{1}{(2\pi)^2} \int_0^{2\pi} d\Phi_u \int_0^{2\pi} d\Phi_d e^{i(n_u - n'_u)\Phi_u + i(n_d - n'_d)\Phi_d} = \delta_{n_u, n'_u} \delta_{n_d, n'_d}. \quad (5.44)$$

Its relevance becomes clear, when we assume that the phase of the integrand in Eq. (5.44) arises as an action difference of scattering paths, as, for instance, in the squared modulus of the Green's function,

$$|G_{\alpha, \alpha'}(\mu)|^2 = \frac{1}{(E_\delta \sin(k\delta))^2} \sum_{\gamma, \gamma': \alpha' \rightarrow \alpha} A_\gamma A_{\gamma'} e^{\frac{i}{\hbar}(S_\gamma - S_{\gamma'})}. \quad (5.45)$$

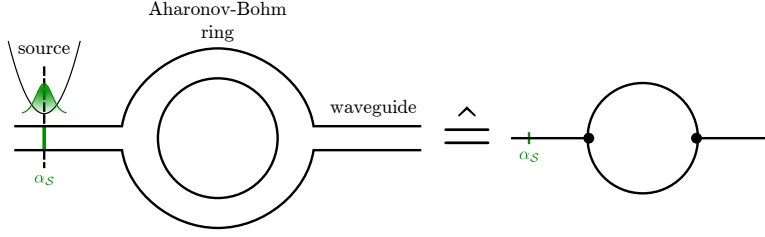


Figure 5.2: The left side shows the AB setup with a BEC as a reservoir coupled to the left waveguide. For weak enough disorder, back-scattering within the ring can be neglected and we can replace the setup by the quantum graph shown on the right. It consists of two semi-infinite bonds representing the waveguides, two vertices representing the junctions between the ring and the waveguides, and two finite bonds for the upper and the lower arm of the ring.

Here, n_u, n_d and n'_u, n'_d from Eq. (5.44) can be understood as to count the number of explorations of the upper and the lower branch of the ring for paths γ and γ' , while complex conjugation of one of the Green's function is responsible for a negative sign in front of n'_u, n'_d . The relevance of Eq. (5.44) is now obvious: Only those pairs of scattering paths survive the disorder average which share an equal number of explorations of the upper, respective lower branch of the ring. This introduces correlations amongst the scattering paths, which allow us to obtain a physical interpretation of AAS oscillations.

At this stage, it is useful to introduce also a graphical, diagrammatic representation to visualize the individual scattering paths γ in Eq. (5.37). For that reason we understand the AB ring as a quantum graph consisting of two semi-infinite waveguides, which are on opposite sides attached to a ring structure via two junctions, see Fig. 5.2. In this quantum graph, a scattering path γ in the coherent summation Eq. (5.37) appears as a sequence of single, full explorations of the branches, with intermediate reflective or transmittive scattering at the junctions. This motivates the definition of the following diagrammatic representations for scattering at the junctions, and the intermediate full explorations of branches in the ring,

$$\begin{aligned}
 \text{Y-junction} &= r, & \text{Junction with arrow} &= \text{Junction with arrow} = t, \\
 \text{Upper ring path} &= e^{i(\Phi_u + \frac{\Phi}{2})}, & \text{Lower ring path} &= e^{i(\Phi_u - \frac{\Phi}{2})}, \\
 \text{Lower ring path} &= e^{i(\Phi_d - \frac{\Phi}{2})}, & \text{Upper ring path} &= e^{i(\Phi_d + \frac{\Phi}{2})}.
 \end{aligned} \tag{5.46}$$

For completeness, note that the beginning and the end of a path lead to additional phases which result either from direct propagation of the initial site to the first contact with one of the junctions, or from the last scattering event at the junctions to the final site. In the diagrammatic representation, we also visualize their contribution by an directed arrow which starts or terminates at a site. To obtain the associated phase factors, we either

use a plane wave in the waveguides, or in the ring we truncate the sum in Eq. (5.39) and add the appropriate phase due to the accumulated flux. Taking for instance $\alpha' = \alpha_S$ and α as a site in the upper part of the ring, the Green's function takes the form

$$\begin{aligned}
 G_{\alpha\alpha_S}(\mu) &= \frac{1}{iE_\delta \sin(k\delta)} \left(\text{diagram 1} + \text{diagram 2} + \text{diagram 3} + \text{diagram 4} + \dots \right) \\
 &= \frac{e^{i|\alpha_S|k\delta}}{iE_\delta \sin(k\delta)} \left(e^{iS(\alpha,0,\mu)+i\alpha\theta} + e^{i(\Phi_u+\frac{\Phi}{2})} e^{iS(\alpha,\frac{N_{\mathcal{R}}}{2},\mu)-i(\frac{N_{\mathcal{R}}}{2}-\alpha)\theta} \right. \\
 &\quad \left. + e^{i(\Phi_d-\frac{\Phi}{2})} e^{iS(\alpha,\frac{N_{\mathcal{R}}}{2},\mu)-i(\frac{N_{\mathcal{R}}}{2}-\alpha)\theta} + e^{i(\Phi_u+\Phi_d)} e^{iS(\alpha,0,\mu)+i\alpha\theta} + \dots \right). \tag{5.47}
 \end{aligned}$$

As we will see in a moment, a detailed consideration of these additional phases is not necessary since for the calculation of reflection and transmission probabilities we find that these phases appear only in pairs canceling each other.

5.2 Numerical predictions for Al'tshuler-Aronov-Spivak (AAS) oscillations

5.2.1 The noninteracting case

We are now at a stage to show and qualitatively explain the AB and AAS oscillations for the noninteracting case. Both phenomena are displayed in Fig. 5.3, which show the transmission probability $|T(\Phi)|^2$ as a function of Φ and for different disorder strengths. The data were obtained by R. Chrétien *et al.* from numerical simulations of the mean-field equation Eq. (5.13) with $g = 0$ and, in case of non-vanishing disorder, were averaged over an ensemble of realizations of disorder. The transmission probability is then calculated through the fraction of currents, Eq. (5.22).

In the case of vanishing disorder in the ring (black line in Fig. 5.3), the transmission probability as a function of the enclosed flux Φ displays oscillations with a periodicity of 2π . Here, the perfect suppression of transmission at $\Phi = \pi$ is attributed to the horizontal axial symmetry of the ring. To understand this, let us first express the transmission probability using Eqs. (5.28) and (5.30) through the Green's function and express the latter by the scattering path representation of the Green's function, Eq. (5.37). For α in the right waveguide, this leads to

$$|T(\Phi)|^2 = E_\delta^2 \sin^2(k\delta) |G_{\alpha\alpha_S}(\mu)|^2 = \sum_{\gamma,\gamma':\alpha_S \rightarrow \alpha} A_\gamma A_{\gamma'}^* e^{\frac{i}{\hbar}(S_\gamma - S_{\gamma'})}. \tag{5.48}$$

Outside the ring, each path displays plane wave motion, and their contributions to the overall action cancel each other within the action difference in Eq. (5.48). Within the ring each of the paths performs an odd number of explorations of the single branches to finally reach the junction coupling to the right waveguide. The phase factor attributed to encircling the flux is thus of the form $\exp(i(2m+1)(\Phi/2))$, where $m \in \mathbb{Z}$. If we mirror a

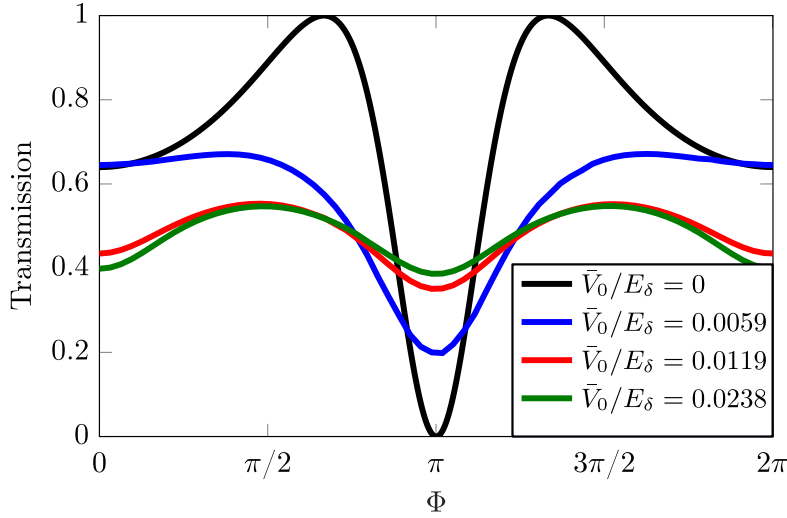


Figure 5.3: Noninteracting simulation of the transmission through the AB ring, Fig. 5.1 (b), as a function of the enclosed dimensionless flux $\Phi = \mathcal{N}_{\mathcal{R}}\theta$ for different strengths \bar{V}_0 of disorder. The curves are obtained from numerically solving Eq. (5.13) with $g/E_\delta = 0$, $\mu/E_\delta = 0.2$ and $\mathcal{N}_{\mathcal{R}} = 200$. In case of $\bar{V}_0 \neq 0$, the data have been averaged over 20000 realizations of the Gaussian correlated disorder with correlation length $\sigma = 20\delta$. In the absence of the disorder potential in the ring, AB oscillations (solid black) with a period 2π appear and show a perfect suppression of the transmission for $\Phi = \pi$. When increasing the disorder strength and averaging over many disorder realizations, the AB oscillations smoothly turn into AAS oscillations of half periodicity π . (*Figure adapted from Ref. [30]*)

path γ along the horizontal axis, we obtain another unique scattering path $\tilde{\gamma}$, for which the amplitude $A_\gamma = A_{\tilde{\gamma}}$ and the flux-independent part of accumulated action remain the same, but since clockwise motion converts into anti-clockwise, the accumulated flux phase of $\tilde{\gamma}$ bears the opposite sign. The phase difference between γ and $\tilde{\gamma}$ is then of the form $\exp(i(2m+1)\Phi)$, which for $\Phi = \pi$ becomes -1 . Upon summation this leads to destructive interference of the contributions of the two paths, and ultimately, since each path has such a unique partner, to a vanishing of the Green's function for $\Phi = \pi$.

By including disorder and increasing its strength, we begin to approach a regime, where our assumptions of the random phases Φ_u, Φ_d in Eq. (5.42) become valid, while the inequalities in Eq. (5.9) still hold true. This is seen in Fig. 5.3 as the smooth conversion of AB oscillations into AAS oscillations with half the period. This doubling of the frequency is ultimately attributed to the disorder average.

As we argued in section 5.1.4, only those pairs of scattering paths γ, γ' in Eq. (5.48) survive the disorder average, which share the same number of explorations of the individual branches. The doubling of the frequency is now best explained at the level of the

reflection probability. Choosing $\alpha = \alpha_S$, we find, using Eqs. (5.28), (5.16), (5.17) and (5.34),

$$\begin{aligned} |R(\Phi_u, \Phi_d, \Phi)|^2 &= E_\delta^2 \sin^2(k\delta) \left| G_{\alpha_S \alpha_S}(\mu) - \Psi_{\alpha_S, +}^{\mathcal{L}_L} \right|^2 \\ &= \sum_{\gamma, \gamma': \alpha_S \rightarrow \alpha} A_\gamma A_{\gamma'}^* e^{\frac{i}{\hbar}(S_\gamma - S_{\gamma'})} \left(= 1 - |T(\Phi_u, \Phi_d, \Phi)|^2 \right), \end{aligned} \quad (5.49)$$

where we subtracted $\Psi_{\alpha_S, +}^{\mathcal{L}_L}$ from the Green's function since this constitutes to the direct path of zero length between α_S and itself. The remaining paths γ, γ' undergo at least one scattering at the left junction to contribute to the reflected wave $\Psi_{\alpha_S, -}^{\mathcal{L}_L}$.

Each of the paths in Eq. (5.49) has to perform an even number of explorations of branches to be able to return to the incident waveguide. The scattering path therefore collects an even number of flux-dependent phases $\Phi/2$, making the overall flux accumulated in the phase of a path a multiple of Φ . To survive the disorder average, a scattering path γ needs to be paired with a partner γ' which shares the same amount of visits both of the upper and the lower branch. An obvious partner is found by setting $\gamma' = \gamma$, producing a flux-independent contribution. Other partners might also exist, which transverse the branches in different order and different directions compared to γ . Since half of the explorations of branches have to be towards the left and the other half towards the right junction in order to return to the incident waveguide, the overall encircled flux of the individual paths can only differ by a multiple of 2Φ . This explains the doubling of the frequency of AAS oscillations compared to AB oscillations.

To illustrate the above arguments, we perform the calculation of the reflection probability by just using the shortest scattering paths with at most three scattering events at the junctions. Using the diagrammatic representation from Eq. (5.46), we find

$$|R(\Phi_u, \Phi_d, \Phi)|^2 = \left| \begin{array}{c} \rightarrow \bullet + \begin{array}{c} \curvearrowright \\ \curvearrowleft \end{array} + \begin{array}{c} \curvearrowleft \\ \curvearrowright \end{array} + \begin{array}{c} \circlearrowleft \\ \circlearrowright \end{array} + \begin{array}{c} \circlearrowright \\ \circlearrowleft \end{array} + \mathcal{O}((r, t)^5) \end{array} \right|^2. \quad (5.50)$$

Within the disorder average, this leads to

$$\begin{aligned} &\left\langle |R(\Phi_u, \Phi_d, \Phi)|^2 \right\rangle_{\text{dis}} \\ &= \left| \rightarrow \bullet \right|^2 + \left| \begin{array}{c} \curvearrowright \\ \curvearrowleft \end{array} \right|^2 + \left| \begin{array}{c} \curvearrowleft \\ \curvearrowright \end{array} \right|^2 + \left| \begin{array}{c} \circlearrowleft \\ \circlearrowright \end{array} + \begin{array}{c} \circlearrowright \\ \circlearrowleft \end{array} \right|^2 + \mathcal{O}((r, t)^{10}) \\ &= |r|^2 + 2|r|^2|t|^4 + 2|t|^6(1 + \cos(2\Phi)) + \mathcal{O}((r, t)^{10}). \end{aligned} \quad (5.51)$$

While the first three diagrammatic terms display interference with themselves, the last term containing time-reversed partners results in the flux-dependent contribution to $\langle |R(\Phi_u, \Phi_d, \Phi)|^2 \rangle_{\text{dis}}$. This also reveals the connection of AAS oscillations to weak localization [127, 128], where the interference of a scattering path with its time-reversed partner leads to an enhancement of the reflection probability, which is sensitive to a time-reversal symmetry affecting mechanism, such as the synthetic gauge field encircled by the ring.

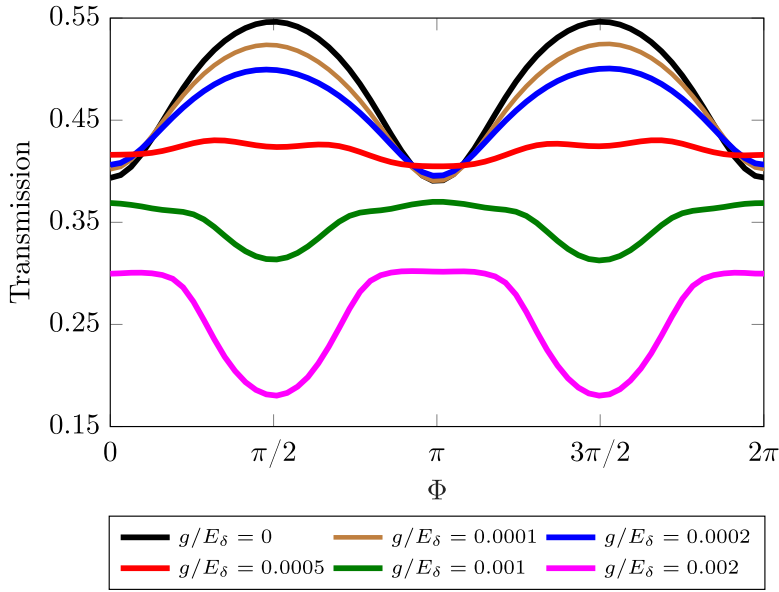


Figure 5.4: Mean-field simulations of the transmission through the disordered AB ring, Fig. 5.1 (b), as a function of the enclosed flux $\Phi = \mathcal{N}_{\mathcal{R}}\theta$ for different strengths of the interaction. The curves are obtained from a Gross-Pitavskii simulation with $\mu/E_{\delta} = 0.2$, $\mathcal{N}_{\mathcal{R}} = 200$, $|\kappa(t)|\sqrt{N(t)}/E_{\delta} = 1$, $\bar{V}_0/E_{\delta} = 0.0238$. The data have been averaged over 20000 realizations of the Gaussian correlated disorder with correlation length $\sigma = 20\delta$. Increasing the interaction strength preserves the π -periodicity of AAS oscillations, but flattens the amplitude for very weak interaction strengths $g/E_{\delta} \leq 0.0002$. For larger interaction strengths, $g/E_{\delta} \geq 0.0002$, the curve is reversed, since former maxima at $\Phi = \pi/2, 3\pi/2$ become minima, thereby transforming the minima at $\Phi = 0, \pi$ into maxima. (Figure adapted from Ref. [30])

5.2.2 Inversion of peaks of the AAS oscillations for interacting cold atoms

We now turn to the interacting case and get a first intuition on the influence of particle-particle interaction on AAS oscillation in the transmission. Fig. 5.4 shows the transmission through the AB setup as a function of the flux Φ . As for the noninteracting scenario, the data have been obtained by R. Chrétien *et al.* by numerically solving the mean-field problem Eq. (5.13). The disorder strength is taken sufficiently strong such that in the noninteracting case AAS-oscillations are observable, see the green line in Fig. 5.3.

The observations we make from the numerical data are the following: when increasing the interaction strength g and averaging over many disorder realizations, the AAS oscillations keep their π -periodicity, but get flattened for a weak interaction strength, $g/E_{\delta} \leq 0.0002$. This indicates that the corrections to the non-interacting AAS oscil-

lations also bear themselves a dependence on the flux Φ , with a maximal amplitude at $\Phi = \pi/2, 3\pi/2$, and minimum at $\Phi = 0, \pi$. When further increasing the interaction strength $g/E_\delta \geq 0.0002$, this ultimately leads to an inversion of the peaks, since the maxima at $\Phi \approx \pi/2, 3\pi/2$ turn into minima, thereby transforming the minimum at $\Phi = \pi$ into a maximum. This is similar to what has been observed in the back-reflection probability in the coherent transport of cold atoms through a two-dimensional disorder potential [28].

We aim at a diagrammatic treatment of the observed AAS oscillation for interacting cold atoms in chapter 6 of this thesis.

5.2.3 Truncated Wigner approximation and its relation to the mean-field approach

Before we start our analytical investigation of AAS oscillations, we like to further motivate our focus on an individual solution of the stationary mean-field equation, Eq. (5.14), by also discussing the truncated Wigner method and its numerical predictions regarding AAS oscillations. A detailed derivation of the truncated Wigner method is found in Ref. [129, 130], see also Ref. [124] for details of its application towards the Bose-Hubbard model. To put the method into context with the semiclassical approximation of the propagator for the Bose-Hubbard Hamiltonian, Eq. (3.83), there are works [33, 35, 36] showing that the truncated Wigner method is equivalent to the so-called *diagonal approximation* in the semiclassical limit “ $N \rightarrow \infty$ ”. This approximation is applied when dealing with a double summation of mean-field solutions, as it appears in the product of the propagator with its complex conjugate version. For the diagonal approximation, the double sum is reduced to a single sum by choosing pairs of identical mean-field solutions. As was the case for the zero-leg-loops in the discussion of OTOCs, see Fig. 4.3, the related quantum phenomena is then described through the dynamics of single mean-field solutions, averaged over their initial conditions.

The truncated Wigner method aims at a description of the dynamics in quantum bosonic many-body systems with a large number of particles. To be more precise, it is used to calculate the time evolution of the quantum average of an observable by expressing it as the phase space average, similar to Eq. (4.5), involving the Wigner function of the time-evolved density operator,

$$\langle \hat{A}(t) \rangle = \text{Tr}(\hat{\rho}(t)\hat{A}) = \int d^{2d}\Psi W(\Psi, \Psi^*, t)A(\Psi, \Psi^*), \quad (5.52)$$

where $\int d^{2d}\Psi = \int d^d \text{Re}(\Psi) \int d^d \text{Im}(\Psi)$ ¹. Here, a more general definition of the Wigner function is used,

$$W(\Psi, \Psi^*, t) = \frac{1}{\pi^{2d}} \int d^{2d}\beta \exp \left[\sum_{i=1}^d (\beta_i^* \Psi_i - \beta_i \Psi_i^*) \right] \text{tr} \left[\hat{\rho}(t) \exp \left(\sum_{i=1}^d (\beta_i \hat{b}_i^\dagger - \beta_i^* \hat{b}_i) \right) \right]. \quad (5.53)$$

¹If we, in analogy to Eq. (3.21), interpret $\Psi = \sqrt{1/2\hbar_{\text{eff}}}(\mathbf{q} + i\mathbf{p})$, we arrive at the formalism as presented in section 4.1.1 for quadrature states.

Accordingly, replacing $\hat{\rho}(t)$ by an arbitrary operator \hat{A} in the above formula yields the Wigner-Weyl transformation $A(\Psi, \Psi^*)$ of this operator. Within this formalism, the von Neumann equation of the density operator, $i\hbar d\hat{\rho}(t)/dt = [\hat{H}, \hat{\rho}](t)$, translates into a partial differential equation for the Wigner function. This equation involves third order derivatives of the Wigner function with respect to \mathbf{q} and \mathbf{p} , which solely originate from the interaction terms in the Hamiltonian. By neglecting these higher order derivatives, *i.e.* “truncating” the equations of motion, one obtains a so-called Fokker-Planck equation, which can be mapped to a set of ordinary differential equations, interpretable as equations of motion of a Hamilton formalism. Along the trajectories which solve these equations of motion, the Wigner function remains constant. Using the conservation of phase space volume, one finally performs a variable transformation in Eq. (5.52) along the classical trajectories to express the Wigner function by its initial value, while the phase space function is now evaluated at the phase space points of the trajectories at time t ,

$$\begin{aligned} \langle \hat{A}(t) \rangle &\approx \int d^{2d} \Psi' W(\Psi', \Psi'^*, 0) A[\Psi(t; \Psi', \Psi'^*), \Psi^*(t; \Psi', \Psi'^*)] \\ &= \left\langle A[\Psi(t; \Psi', \Psi'^*), \Psi^*(t; \Psi', \Psi'^*)] \right\rangle_W, \end{aligned} \quad (5.54)$$

where $\langle \cdot \rangle_W$ denotes the average of the initial conditions with the Wigner function, as shown in Eq. (5.54). This explains the importance of the truncated Wigner method: instead of solving a computationally demanding or even impossible, high-dimensional partial differential problem to obtain the Wigner function at later times, one instead solves ordinary differential equations, whose initial conditions are sampled by the initial Wigner function at time $t = 0$.

To numerically treat AAS oscillations for the disordered AB ring with interacting bosonic particles within the truncated Wigner method, the dynamics described by the Bose-Hubbard Hamiltonian in Eq. (5.10) needs to be limited to a finite number d of sites. This is done by cutting the waveguides after a finite number of sites and introducing absorbing ends to prevent back-reflection. The dynamical equations of motion found within the truncated Wigner method are given by

$$\begin{aligned} i\hbar \frac{d\Psi_\alpha(t)}{dt} &= h_\alpha \Psi_\alpha(t) + \sum_{\alpha'} J_{\alpha\alpha'} \Psi_{\alpha'}(t) + g_\alpha \left(|\Psi_\alpha(t)|^2 - 1 \right) \Psi_\alpha(t) + \delta_{\alpha,\alpha_S} \kappa(t) \Psi_S(t), \\ i\hbar \frac{d\Psi_S(t)}{dt} &= \mu \Psi_S(t) + \kappa^*(t) \Psi_{\alpha_S}(t), \end{aligned} \quad (5.55)$$

where the parameters h_α now also contain the absorbing potential within the waveguides. Compared to the mean-field approach leading to Eq. (5.12), we see that the term related to interaction is treated slightly different. However, in the limit of a large number of particles $N \rightarrow \infty$, the equations coincide, as we can expect a large occupation $|\Psi_\alpha(t)|^2$ of site α , allowing us to neglect the additional term.

Initially, the sites in the waveguides and the ring are unoccupied, while the source contains a Bose-Einstein condensate with a large number N of particles. The latter can

be well approximated by a coherent state with label $\Phi_S = \sqrt{N}$, as described in section 3.1.4. Since the vacuum state is itself a coherent state, the initial many-body state for the full system is a coherent state $|\Phi\rangle$, where $\Phi_\alpha = 0$ for sites α in the waveguides and the ring, and $\Phi_S = \sqrt{N}$.

The Wigner function for a coherent state is a Gaussian density distribution, which can be factorized into Wigner functions of the single sites. It is given by

$$W_{\Phi}((\Psi_\alpha)_\alpha, \Psi_S, (\Psi_\alpha^*)_\alpha, \Psi_S^*) = \underbrace{\left(\frac{2}{\pi}\right) \exp\left(-2|\Psi_S - \sqrt{N}|^2\right)}_{=W_{\text{source}}(\Psi_S, \Psi_S)} \prod_{\alpha} \underbrace{\left(\frac{2}{\pi}\right) \exp\left(-2|\Psi_\alpha|^2\right)}_{W_{\text{system}}((\Psi_\alpha)_\alpha, (\Psi_\alpha^*)_\alpha)}. \quad (5.56)$$

Here, we can understand this Wigner function as a probability density for complex Gaussian random variables. Therefore the average in Eq. (5.54) is obtained by sampling the initial conditions of the dynamical Eqs. (5.55) according to a Gaussian distribution.

To further simplify the problem, it is possible to eliminate the source from the numerical treatment. From Eq. (3.40) we see that the relative uncertainty of the occupation n_S/N for $\Phi_S = \sqrt{N}$ is given by $1/\sqrt{N}$ and decreases with the number of particles. This allows to neglect the fluctuations in Φ_S and treat the source purely classically, $W_{\text{source}}(\Psi_S, \Psi_S) \approx \delta^2(\Psi_S - \sqrt{N})$. Moreover, by taking an appropriate ramping of the coupling $\kappa(t)$, such that $\kappa(t)\sqrt{N(t)}$ becomes a constant, one can completely remove the source from the dynamical equations (5.55) and focus on the sites in the waveguide and the ring,

$$i\hbar \frac{d\Psi_\alpha(t)}{dt} = (h_\alpha - \mu)\Psi_\alpha(t) + \sum_{\alpha'} J_{\alpha\alpha'} \Psi_{\alpha'}(t) + g_\alpha (|\Psi_\alpha(t)|^2 - 1)\Psi_\alpha(t) + \delta_{\alpha, \alpha_S} \kappa(t) \sqrt{N(t)}, \quad (5.57)$$

whose initial conditions are sampled by $W_{\text{system}}((\Psi_\alpha)_\alpha, (\Psi_\alpha^*)_\alpha)$ alone.

To obtain the transmission probability, Eq. (5.22) is used, which requires the calculation of the current, Eq. (5.20). Within the truncated Wigner method, this leads to the calculation of

$$\langle j_\alpha(t) \rangle_W = \frac{E_\delta}{2i\hbar} \langle \Psi_\alpha^*(t) \Psi_{\alpha+1}(t) - \Psi_{\alpha+1}^*(t) \Psi_\alpha(t) \rangle_W. \quad (5.58)$$

The transmission probability is found by first propagating the system long enough to establish a stationary state, and normalizing the obtained current to the incident current, Eq. (5.29) generated by the source,

$$|T(\Phi)|^2 = \lim_{t \rightarrow \infty} \frac{\langle j_\alpha(t) \rangle_W}{j^\emptyset}. \quad (5.59)$$

To investigate AAS oscillations, the above transmission has to be calculated for and averaged over an ensemble of disorder configurations.

Within the truncated Wigner approach, we can moreover first average the fields Ψ_α themselves within the Wigner average Eq. (5.54). This contribution is expected to behave

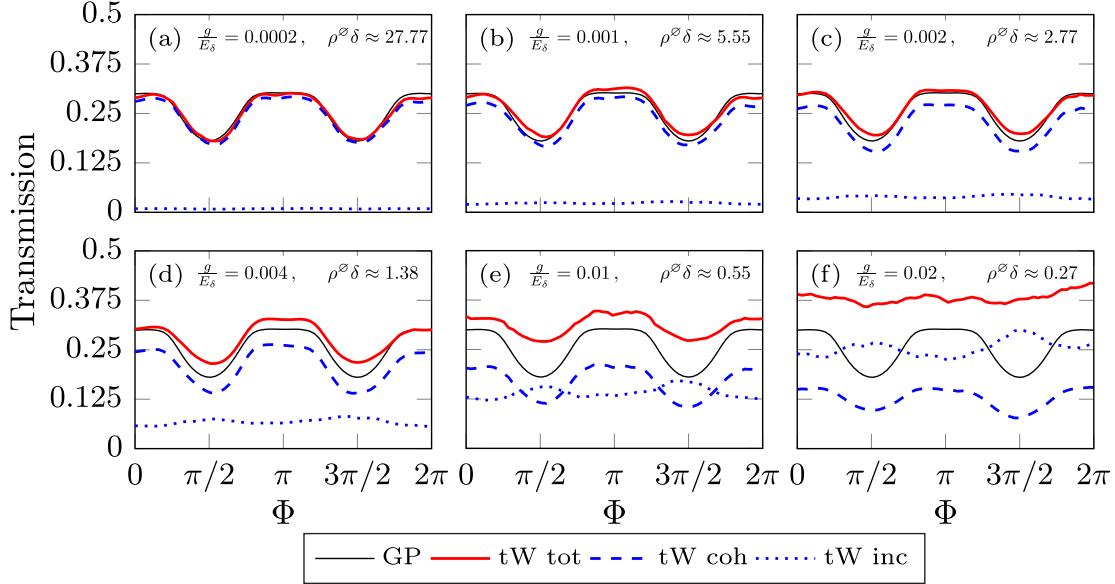


Figure 5.5: The transmission through the AB ring as a function of the enclosed flux $\Phi = \mathcal{N}_R \theta$, shown for different interaction strengths g , while keeping constant the product $(g/E_\delta)\rho^\varnothing \delta = 0.0055$ of interaction strength with the mean particle density generated by the source. Shown are both the results from a truncated Wigner simulation and the numerical solution of Eq. (5.13), with $\mu/E_\delta = 0.2$, $\mathcal{N}_R = 200$, $\bar{V}_0/E_\delta = 0.0238$. Each data point results from an average over 20000 realizations of the Gaussian correlated disorder with correlation length $\sigma = 20\delta$, each with 100 samples of the initial conditions. The particle density $\rho^\varnothing \delta$ generated by the source is related to the coupling strength $N(t)|\kappa(t)|^2$ via Eq. (5.27). For this set of parameters, the inversion of AAS oscillations as a result of interaction has fully developed. By tuning g and $\rho^\varnothing \delta$ we leave the regime where the system is described by a single solution of the mean-field equation, Eq. (5.14), (black line in the figures), and a treatment based on the truncated Wigner method is required. Within this method, the average in Eq. (5.54) over multiple distinct solutions of the mean-field equation leads to a flattening of AAS oscillations. (Figure adapted from Ref. [30])

according to a single solution of the mean-field Eqs. (5.13), whose initial conditions are given by the center of the Gaussian distribution W_{system} . Quantities calculated from these averaged fields are then labeled *coherent*. For instance, the coherent part of the current and the transmission probability is given

$$j_{\alpha}^{\text{coh}}(t) = \frac{iE_{\delta}}{2\hbar} [\langle \Psi_{\alpha+1}^{*}(t) \rangle_W \langle \Psi_{\alpha}(t) \rangle_W - \langle \Psi_{\alpha}^{*}(t) \rangle_W \langle \Psi_{\alpha+1}(t) \rangle_W],$$

$$\left| T^{\text{coh}}(\Phi) \right|^2 = \lim_{t \rightarrow \infty} \frac{j_{\alpha}^{\text{coh}}(t)}{j^{\varnothing}}.$$
(5.60)

The incoherent parts are finally defined by the difference of the quantities, as obtained from the truncated Wigner method, to their coherent parts,

$$j_{\alpha}^{\text{incoh}}(t) = \langle j_{\alpha}(t) \rangle_W - j_{\alpha}^{\text{coh}}(t), \quad \left| T^{\text{incoh}}(\Phi) \right|^2 = |T(\Phi)|^2 - \left| T^{\text{coh}}(\Phi) \right|^2$$
(5.61)

The numerical results obtained with the truncated Wigner method confirm this expectation, as is seen in Fig. 5.5. There the transmission probability (red lines) as a function of the enclosed flux is plotted, as well as its coherent (blue dashed lines) and incoherent part (blue dotted lines), for different values of the interaction strength g/E_{δ} and the mean particle density $\rho^{\varnothing}\delta$, Eq. (5.27), while keeping the product $\rho^{\varnothing}\delta g/E_{\delta}$ fixed. As we will understand in the next chapter, the latter product arises from the perturbation theory motivated by Eq. (5.34), and the above manipulations leave the solution of the stationary mean-field equations, Eq. (5.14) unchanged. Indeed, we see in Fig. 5.5 that the shape of the coherent part of the transmission (dashed blue lines) essentially follows the predictions of the mean-field solution (black lines).

For a large mean particle density $\rho^{\varnothing}\delta$ and weak interaction strength g , Fig. 5.5 (a) to (d), we are in the regime of validity of the mean-field approach, *i.e.* the system is well described by a single solution of the mean-field equation Eq. (5.14). The truncated Wigner method essentially follows this solution. When we decrease the mean particle density $\rho^{\varnothing}\delta$ and simultaneously increase the interaction strength g , we see from the the growing influence of incoherent part (dotted blue lines) that additional solutions of the mean-field equations start to play a role in the average Eq. (5.54), ultimately leading to a complete flattening of AAS oscillations in Fig. 5.5 (e) and (f).

Since the numerical predictions in Fig. 5.5 indicate that the main influence of interaction on AAS oscillations can be understood at the level of a single, central solution of the mean-field equation, this motivates our theoretical investigation in the next chapter.

6 Diagrammatic approach towards Al'tshuler-Aronov-Spivak oscillations

In this chapter we want to present a semiclassical, diagrammatic approach to obtain analytical expressions to explain the role of interaction in Al'tshuler-Aronov-Spivak oscillations in the transport of a bosonic gas through a disordered Aharonov-Bohm ring. The theory is based on the mean-field treatment of the problem and relies on resumming contributions of scattering paths found for the noninteracting system.

In this chapter we present an analytical treatment of AAS oscillations in the coherent transport of cold bosonic atoms through an AB ring with disorder. This treatment aims at solving the stationary mean-field equation by a scattering ansatz, utilizing the Green's function for the noninteracting mean-field Hamiltonian and taking the particle-particle interaction as a weak perturbation, see Eq. (5.34). For an appropriately chosen weak disorder strength, we have seen that the Green's function admits a semiclassical approximation in the form of a summation of all scattering paths linking an initial with a final site, Eq. (5.37). The disorder average itself translates into an average of the flux-independent part of the phases Φ_u , Φ_d accumulated by a path from a single exploration of the upper, respective lower branch of the ring. The main idea for the theory presented here is to perform exact resummations of the intermediate sequential part of the scattering paths, which describes the motion alternating inside the ring between the two junctions to the waveguides. For these resummations we discriminate between the various boundary conditions, *i.e.* the initial and final junction site of the sequence, as well as from which direction a scattering path is allowed to enter and leave the sequence. These considerations allow us to write the Green's function of the noninteracting system and find analytical expressions for the reflection and transmission probability as functions of the flux Φ and disorder phases Φ_u , Φ_d . Furthermore, we are able to tackle the perturbation series for the interacting problem, and can also identify an analytical expression, which, upon average over the disorder phases, yields the corrections for the transmission and reflection probabilities.

The results presented in this chapter mark my contribution to the work studying AAS oscillation in the transport of an interacting bosonic gas through a disordered Aharonov-Bohm ring, and are published in Ref. [30].

6.1 The noninteracting case

We base our theoretical efforts in this chapter on performing the coherent summation over all scattering paths for the noninteracting Green function, Eq. (5.37). It relies on the important observation that for a scattering path both the exploration of the branches and the scattering of the junctions contributes a multiplicative factor to the scattering paths contribution to the sum in Eq. (5.37), leading us to the definition of the diagrammatic rules in Eq. (5.46). This allows us to separate the direct paths between the initial/final site and the junction, and we can focus on the intermediate sequential part oscillating between the two junctions. For instance, for the diagrams depicted in Eq. (5.47)

$$\begin{aligned}
 \alpha_s \xrightarrow{\alpha} + \alpha_s \xrightarrow{\alpha} \text{ (with one loop) } &= \alpha_s \xrightarrow{0} \times \left[\text{direct path} + \text{one loop} \right] \times \alpha_0^{\alpha} \quad (6.1) \\
 \alpha_s \xrightarrow{\alpha} \text{ (with two loops) } + \alpha_s \xrightarrow{\alpha} \text{ (with one loop) } &= \alpha_s \xrightarrow{0} \times \left[\text{one loop} + \text{two loops} \right] \times \alpha_{\frac{N_B}{2}}^{\alpha},
 \end{aligned}$$

where the expressions within the brackets are built only by the elements depicted in Eq. (5.46). They represent the intermediate behaviour of a scattering path, oscillating multiple times in the between between the two junctions.




To sum up these intermediate sequences, we first group the paths depending on which junction they start and end, and how a scattering path may enter and leave the sequence. As we see in the next sections, it is possible to sum up these groups of paths, sharing the same limiting conditions. This leads to new effective diagrams where we encode the common boundary conditions in the shape of the diagram and use the color red to indicate a resummation.

6.1.1 Basic resummation of diagrams

One of these resummed diagrams is given by \uparrow , which can be interpreted as a resummed transmission diagram. Following our description above, it comprises the contribution of the sum of all trajectories which approach the left junction from the lower branch, have an arbitrary number of explorations of upper and lower branches of the AB ring, before they finally leave to the upper branch of the ring. Explicitly writing the sum in terms of diagram, this yields

$$\uparrow = \uparrow + \uparrow \text{ (with one loop) } + \uparrow \text{ (with two loops) } + \uparrow \text{ (with three loops) } + \uparrow \text{ (with four loops) } + \dots \quad (6.2)$$

In the same way we can define the diagrams \downarrow , \updownarrow , \downuparrow as the resummation of paths traversing a junction, while both the beginning and the end of the trajectories remain within the ring. Scattering paths which start and end at the same junction, whose

beginning and end are extendable into the same branch of the ring are represented by , , and . We can interpret these latter diagrams as resummed reflection diagrams.

Quite obviously, after two subsequent visits of any of the branches of the ring, one arrives back at the junction one started. It is therefore easy to see that any of the scattering paths contained in the set of a resummed diagram is constructed by successively extending it through the exploration of two branches, forth to and back from the opposite junction. This is the main idea, leading to self-consistent equations which couple a resummed reflection and transmission diagrams. For instance, we find

$$\begin{aligned} \begin{array}{c} \uparrow \\ \text{red arrow} \end{array} &= \begin{array}{c} \uparrow \\ \text{black arrow} \end{array} + \begin{array}{c} \text{red arrow} \\ \text{black arrow} \end{array} + \begin{array}{c} \text{red arrow} \\ \text{black arrow} \end{array} + \begin{array}{c} \text{red arrow} \\ \text{black arrow} \end{array} + \begin{array}{c} \text{red arrow} \\ \text{black arrow} \end{array}, \\ \begin{array}{c} \text{red arrow} \\ \text{black arrow} \end{array} &= \begin{array}{c} \text{red arrow} \\ \text{black arrow} \end{array} + \begin{array}{c} \text{red arrow} \\ \text{black arrow} \end{array} + \begin{array}{c} \text{red arrow} \\ \text{black arrow} \end{array} + \begin{array}{c} \text{red arrow} \\ \text{black arrow} \end{array} + \begin{array}{c} \text{red arrow} \\ \text{black arrow} \end{array}. \end{aligned} \quad (6.3)$$

The right hand sides of these equations are linear in the resummed red diagrams. To make this point even more clear, we can rewrite the above expressions in a diagrammatic version of a matrix-vector product,

$$\begin{pmatrix} \begin{array}{c} \uparrow \\ \text{red arrow} \end{array} \\ \begin{array}{c} \text{red arrow} \\ \text{black arrow} \end{array} \end{pmatrix} = \begin{pmatrix} \begin{array}{c} \uparrow \\ \text{black arrow} \end{array} \\ \begin{array}{c} \text{red arrow} \\ \text{black arrow} \end{array} \end{pmatrix} + \underbrace{\begin{pmatrix} \begin{array}{c} \text{red arrow} \\ \text{black arrow} \end{array} + \begin{array}{c} \text{red arrow} \\ \text{black arrow} \end{array} \\ \begin{array}{c} \text{red arrow} \\ \text{black arrow} \end{array} + \begin{array}{c} \text{red arrow} \\ \text{black arrow} \end{array} \end{pmatrix}}_{=A(\Phi_u, \Phi_d, \Phi)} \begin{pmatrix} \begin{array}{c} \uparrow \\ \text{red arrow} \end{array} \\ \begin{array}{c} \text{red arrow} \\ \text{black arrow} \end{array} \end{pmatrix}. \quad (6.4)$$

To obtain analytic expressions for the resummed diagrams, we have to solve this equation. This is done by a simple matrix inversion,

$$\begin{pmatrix} \begin{array}{c} \uparrow \\ \text{red arrow} \end{array} \\ \begin{array}{c} \text{red arrow} \\ \text{black arrow} \end{array} \end{pmatrix} = \underbrace{(\mathbb{I} - A(\Phi_u, \Phi_d, \Phi))^{-1}}_{=X(\Phi_u, \Phi_d, \Phi)} \begin{pmatrix} \begin{array}{c} \uparrow \\ \text{black arrow} \end{array} \\ \begin{array}{c} \text{red arrow} \\ \text{black arrow} \end{array} \end{pmatrix} = X(\Phi_u, \Phi_d, \Phi)^{-1} \begin{pmatrix} t \\ r \end{pmatrix}. \quad (6.5)$$

Using the representations from equation (5.46), the matrix $X(\Phi_u, \Phi_d, \Phi)$ is found to be

$$\begin{aligned} X(\Phi_u, \Phi_d, \Phi) &= \begin{pmatrix} 1 - \begin{array}{c} \text{red arrow} \\ \text{black arrow} \end{array} - \begin{array}{c} \text{red arrow} \\ \text{black arrow} \end{array} & - \begin{array}{c} \text{red arrow} \\ \text{black arrow} \end{array} - \begin{array}{c} \text{red arrow} \\ \text{black arrow} \end{array} \\ - \begin{array}{c} \text{red arrow} \\ \text{black arrow} \end{array} - \begin{array}{c} \text{red arrow} \\ \text{black arrow} \end{array} & 1 - \begin{array}{c} \text{red arrow} \\ \text{black arrow} \end{array} - \begin{array}{c} \text{red arrow} \\ \text{black arrow} \end{array} \end{pmatrix} \\ &= \begin{pmatrix} 1 - r^2 e^{2i\Phi_u} - t^2 e^{i(\Phi_u + \Phi_d + \Phi)} & -rte^{i(\Phi_u + \Phi_d - \Phi)} - rte^{2i\Phi_d} \\ -rte^{2i\Phi_u} - rte^{i(\Phi_u + \Phi_d + \Phi)} & 1 - t^2 e^{i(\Phi_u + \Phi_d - \Phi)} - r^2 e^{2i\Phi_d} \end{pmatrix}. \end{aligned} \quad (6.6)$$

Provided that the determinant $D(\Phi_u, \Phi_d, \Phi) = \det[X(\Phi_u, \Phi_d, \Phi)]$ does not vanish, the inverse of this 2×2 matrix exists,

$$\begin{aligned} & X(\Phi_u, \Phi_d, \Phi)^{-1} \\ &= \frac{1}{D(\Phi_u, \Phi_d, \Phi)} \begin{pmatrix} 1 - r^2 e^{2i\Phi_d} - t^2 e^{i(\Phi_u + \Phi_d - \Phi)} & rt(e^{2i\Phi_d} + e^{i(\Phi_u + \Phi_d - \Phi)}) \\ rt(e^{2i\Phi_u} + e^{i(\Phi_u + \Phi_d + \Phi)}) & 1 - r^2 e^{2i\Phi_u} - t^2 e^{i(\Phi_u + \Phi_d + \Phi)} \end{pmatrix}, \end{aligned} \quad (6.7)$$

where

$$\begin{aligned} D(\Phi_u, \Phi_d, \Phi) &= \det(X(\Phi_u, \Phi_d, \Phi)) \\ &= 1 - r^2(e^{2i\Phi_u} + e^{2i\Phi_d}) - 2t^2 e^{i(\Phi_u + \Phi_d)} \cos(\Phi) + (r^2 - t^2)^2 e^{2i(\Phi_u + \Phi_d)}. \end{aligned} \quad (6.8)$$

In order to obtain expressions for the resummed diagrams \blacktriangleleft and \blacktriangleright , we have to insert (6.7) into (6.5). This leads to the matrix-vector product

$$\begin{aligned} & \begin{pmatrix} 1 - r^2 e^{2i\Phi_d} - t^2 e^{i(\Phi_u + \Phi_d - \Phi)} & rt(e^{2i\Phi_d} + e^{i(\Phi_u + \Phi_d - \Phi)}) \\ rt(e^{2i\Phi_u} + e^{i(\Phi_u + \Phi_d + \Phi)}) & 1 - r^2 e^{2i\Phi_u} - t^2 e^{i(\Phi_u + \Phi_d + \Phi)} \end{pmatrix} \begin{pmatrix} t \\ r \end{pmatrix} \\ &= \begin{pmatrix} t(1 + (r^2 - t^2)e^{i(\Phi_u + \Phi_d - \Phi)}) \\ r(1 - (r^2 - t^2)e^{2i\Phi_u}) \end{pmatrix}. \end{aligned} \quad (6.9)$$



Thus, the resummed diagrams are found to be

$$\blacktriangleleft = t \frac{1 + (r^2 - t^2)e^{i(\Phi_u + \Phi_d - \Phi)}}{D(\Phi_u, \Phi_d, \Phi)}, \quad \blacktriangleright = r \frac{1 - (r^2 - t^2)e^{2i\Phi_u}}{D(\Phi_u, \Phi_d, \Phi)}. \quad (6.10)$$

6.1.2 Symmetry arguments to derive other resummed diagrams

The other diagrams, related to transmission through and reflection of a junction, \blacktriangleleft , \blacktriangleright , \blacktriangleright , \blacktriangleleft , \blacktriangleright , and \blacktriangleleft could in principle be calculated in a similar fashion as in the previous paragraph. However, we can also easily obtain them from Eq. (6.10) by making the following observations associated to symmetries of the AB ring:

- Inverting the direction of a resummed diagram is done by inverting each scattering path contained in its sum. For the scattering paths, this inversion does not change the visited branches, but clockwise exploration is converted into anticlockwise, leading to a sign change of the phase Φ . For instance, \blacktriangleleft can be obtained from \blacktriangleright using this rule.
- Mirroring a resummed diagram along the horizontal axis leads to an interchange of the upper with the lower branch of the ring, and thus to an interchange $\Phi_u \leftrightarrow \Phi_d$ of the associated dynamical phases. Furthermore clockwise exploration of the branches turns into anticlockwise and vice versa, we also have to change the sign of Φ again. Using this rule, *e.g.* \blacktriangleright is obtained from \blacktriangleleft .

- Mirroring a diagram along the vertical symmetry axis of the bare ring does not change the explored branches, but interchanges clockwise and anticlockwise motion, which yet again flips the sign in front of Φ . With this rule, we can, for instance obtain  from .

Note that the denominator $D(\Phi_u, \Phi_d, \Phi)$ is invariant under any of the above mentioned transformations. Applying the above rules allows us to immediately derive further diagrams without their explicit calculation as solution of linear equation. For instance

$$\text{Diagram with red arrow pointing up} = t \frac{1 + (r^2 - t^2)e^{i(\Phi_u + \Phi_d - \Phi)}}{D(\Phi_u, \Phi_d, \Phi)} = \text{Diagram with red arrow pointing down}. \quad (6.11)$$

The complete list of diagrams derived from Eq. (6.10) is found in appendix A.6.

6.1.3 Further resummed diagrams

The diagrams calculated in the last section described the resummed transmission and the reflection at a single junction. With their help, we can now also calculate diagrams which link the two junctions at the opposite side of the ring. These diagrams differ in which junction is used as the starting point, and in which branches the scattering paths start and end.

The diagram, which approaches the left junction from the lower branch and, in the end, leaves the right junction again to the lower branch, is diagrammatically calculated by

$$\text{Diagram with red arrow pointing right} = \text{Diagram with red arrow pointing up and black arrow pointing right} + \text{Diagram with red arrow pointing down and black arrow pointing right}. \quad (6.12)$$

To put the above equation in words: to travel from the left junction, which we enter from below, to the right junction, which we exit to the lower branch, we can either in an arbitrary way enter the upper or the lower branch at the left junction and then go directly to the right junction, and both scenarios are summed. (Our in the previous subsection calculated resummed diagrams support us with the word “arbitrary”.)

Inserting the analytical expressions for the diagrams, we find

$$\begin{aligned} \text{Diagram with red arrow pointing right} &= t \frac{1 + (r^2 - t^2)e^{i(\Phi_u + \Phi_d - \Phi)}}{D(\Phi_u, \Phi_d, \Phi)} e^{i(\Phi_u + \frac{\Phi}{2})} t + r \frac{1 - (r^2 - t^2)e^{i2\Phi_u}}{D(\Phi_u, \Phi_d, \Phi)} e^{i(\Phi_d - \frac{\Phi}{2})} r \\ &= e^{-i(\Phi_d + \frac{\Phi}{2})} \frac{r^2 e^{2i\Phi_d} + t^2 e^{i(\Phi_u + \Phi_d + \Phi)} - (r^2 - t^2)^2 e^{2i(\Phi_u + \Phi_d)}}{D(\Phi_u, \Phi_d, \Phi)} \end{aligned} \quad (6.13)$$

$$= e^{-i(\Phi_d + \frac{\Phi}{2})} \left(\frac{1 - r^2 e^{2i\Phi_u} - t^2 e^{i(\Phi_u + \Phi_d - \Phi)}}{D(\Phi_u, \Phi_d, \Phi)} - 1 \right). \quad (6.14)$$

Note that in the last line of Eq. (6.14), we already excluded the inverse of the phase factor associated to a clockwise exploration of the lower branch. We also used the denominator (6.8) to slightly rewrite the result in an alternative form.

In an analogous way, we can calculate the diagram which approaches the left junction from the lower branch, but now leaves the right junction to the upper branch.

$$\begin{aligned}
\begin{array}{c} \text{---} \rightarrow \text{---} \\ | \\ \text{---} \end{array} &= \begin{array}{c} \text{---} \rightarrow \text{---} \\ \curvearrowright \\ \text{---} \end{array} + \begin{array}{c} \text{---} \rightarrow \text{---} \\ \curvearrowleft \\ \text{---} \end{array} \\
&= t \frac{1 + (r^2 - t^2)e^{i(\Phi_u + \Phi_d - \Phi)}}{D(\Phi_u, \Phi_d, \Phi)} e^{i(\Phi_u + \frac{\Phi}{2})} r + r \frac{1 - (r^2 - t^2)e^{i2\Phi_u}}{D(\Phi_u, \Phi_d, \Phi)} e^{i(\Phi_d - \frac{\Phi}{2})} t \\
&= e^{-i(\Phi_u - \frac{\Phi}{2})} \frac{rt(e^{2i\Phi_u} + e^{i(\Phi_u + \Phi_d - \Phi)})}{D(\Phi_u, \Phi_d, \Phi)}. \tag{6.15}
\end{aligned}$$

From equations (6.14), (6.15) and using the symmetry rules presented in subsection 6.1.2 it is easy to derive the remaining resummed diagrams for switching junctions. The list of these diagrams is found in appendix A.6.

So far, both ends of the paths summed over in the previous diagrams terminated within the ring structure. However, for the calculation of the reflection and transmission probabilities $|R(\Phi_u, \Phi_d, \Phi)|^2$ and $|T(\Phi_u, \Phi_d, \Phi)|^2$, Eq. (5.48) and (5.49), we need resummed sequences of paths which connect to the waveguides attached to the ring. Such a resummed diagram is $\begin{array}{c} \text{---} \rightarrow \text{---} \\ | \\ \text{---} \end{array}$, which contains all scattering paths starting in the left waveguide and, in the end, leave the left junction towards the upper branch. Its contribution is calculated by

$$\begin{aligned}
\begin{array}{c} \text{---} \rightarrow \text{---} \\ | \\ \text{---} \end{array} &= \begin{array}{c} \text{---} \rightarrow \text{---} \\ | \\ \text{---} \end{array} + \begin{array}{c} \text{---} \rightarrow \text{---} \\ \curvearrowright \\ \text{---} \end{array} + \begin{array}{c} \text{---} \rightarrow \text{---} \\ \curvearrowleft \\ \text{---} \end{array} \\
&= t + t \left(\frac{1 - r^2 e^{i2\Phi_d} - t^2 e^{i(\Phi_u + \Phi_d - \Phi)}}{D(\Phi_u, \Phi_d, \Phi)} - 1 \right) + t \frac{rt(e^{2i\Phi_d} + e^{i(\Phi_u + \Phi_d - \Phi)})}{D(\Phi_u, \Phi_d, \Phi)} \\
&= t \frac{1 - (r - t)(re^{i2\Phi_d} - te^{i(\Phi_u + \Phi_d - \Phi)})}{D(\Phi_u, \Phi_d, \Phi)}. \tag{6.16}
\end{aligned}$$

It is also advantageous to have diagrams, which start in a waveguide and end at the junction opposite to that. For instance, the diagram which starts in the left waveguide and, in an arbitrary way, travels to the right junction where it leaves to the upper branch, is calculated by

$$\begin{aligned}
\begin{array}{c} \text{---} \rightarrow \text{---} \\ | \\ \text{---} \end{array} &= \begin{array}{c} \text{---} \rightarrow \text{---} \\ \curvearrowright \\ \text{---} \end{array} + \begin{array}{c} \text{---} \rightarrow \text{---} \\ \curvearrowleft \\ \text{---} \end{array} \\
&= t \frac{1 - (r - t)(re^{i2\Phi_d} - te^{i(\Phi_u + \Phi_d - \Phi)})}{D(\Phi_u, \Phi_d, \Phi)} e^{i(\Phi_u + \frac{\Phi}{2})} r \\
&\quad + t \frac{1 - (r - t)(re^{i2\Phi_u} - te^{i(\Phi_u + \Phi_d + \Phi)})}{D(\Phi_u, \Phi_d, \Phi)} e^{i(\Phi_d - \frac{\Phi}{2})} t
\end{aligned}$$

$$= e^{-i(\Phi_u - \frac{\Phi}{2})} t \frac{r e^{i2\Phi_u} + t e^{i(\Phi_u + \Phi_d - \Phi)} - (r-t)(r^2 - t^2) e^{i2(\Phi_u + \Phi_d)}}{D(\Phi_u, \Phi_d, \Phi)}. \quad (6.17)$$

Again, we complete the list of all diagrams, starting or ending in one of the waveguides using the symmetry rules from 6.1.2 and show their results in appendix A.6.

6.1.4 Full reflection and transmission amplitude in the noninteracting case

With the collection of resummed diagrams derived in the last subsections, we are now ready to state a diagrammatic version of the noninteracting Green's function $G_{\alpha\alpha'}(\mu)$ for *any* choice of initial and final sites α, α' . For instance, if the sites α and α' are located in the upper branch of the ring, we get

$$G(\alpha, \alpha', E) = \frac{1}{iE_\delta \sin(k\delta)} \left[\left(\theta(\alpha - \alpha') \overset{\alpha'}{\curvearrowright} \overset{\alpha}{\curvearrowright} + \overset{\alpha}{\curvearrowright} \overset{\alpha'}{\curvearrowright} \right) + \left(\theta(\alpha - \alpha') \overset{\alpha}{\curvearrowleft} \overset{\alpha'}{\curvearrowleft} + \overset{\alpha}{\curvearrowleft} \overset{\alpha'}{\curvearrowleft} \right) + \overset{\alpha'}{\curvearrowright} \overset{\alpha}{\curvearrowright} + \overset{\alpha}{\curvearrowleft} \overset{\alpha'}{\curvearrowleft} \right] \quad (6.18)$$

where the Heaviside function θ discriminates whether α is left ($\alpha < \alpha'$) or right of α' ($\alpha > \alpha'$). In principle, since these representations include a possible partial exploration of branches at the beginning or the end to reach the initial and final sites α, α' , one would need details of the disorder potential in the single branches to obtain the correct quantitative value of the phase. However, as we already argued after Eq. (5.47), due to phase cancellation in the calculation of reflection and transmission probabilities, we can limit our considerations to paths which terminate at the junctions or within one of the waveguides.

By comparing Eq. (5.16) with Eq. (5.30) for the noninteracting case, $g_\alpha = 0$, we see that through the knowledge of the Green's function we can also directly gain access to the reflection and transmission amplitudes. Utilizing the resummed diagrams, we obtain for the reflection amplitude $R^{(0)}(\Phi_u, \Phi_d, \Phi)$ of the full, noninteracting system

$$\rhd = R^{(0)}(\Phi_u, \Phi_d, \Phi) = [iE_\delta \sin(k\delta) G_{\alpha_S \alpha_S}(\mu) - 1] e^{-2i|\alpha_S|k\delta} \quad (6.19)$$

$$\begin{aligned} &= \rhd + \text{diagram 1} + \text{diagram 2} \\ &= r + t^2 \frac{r e^{i2\Phi_u} + t e^{i(\Phi_u + \Phi_d - \Phi)} - (r-t)(r^2 - t^2) e^{i2(\Phi_u + \Phi_d)}}{D(\Phi_u, \Phi_d, \Phi)} \\ &\quad + t^2 \frac{r e^{i2\Phi_d} + t e^{i(\Phi_u + \Phi_d + \Phi)} - (r-t)(r^2 - t^2) e^{i2(\Phi_u + \Phi_d)}}{D(\Phi_u, \Phi_d, \Phi)} \\ &= r + t^2 \frac{r(e^{i2\Phi_u} + e^{i2\Phi_d}) + 2t e^{i(\Phi_u + \Phi_d)} \cos(\Phi) - 2(r-t)(r^2 - t^2) e^{i2(\Phi_u + \Phi_d)}}{D(\Phi_u, \Phi_d, \Phi)}. \end{aligned} \quad (6.20)$$

Note that the term subtracted from the Green's function in the first line attributes to the incoming wave $\Psi_{\alpha_S,+}^{\mathcal{L}} = [\sqrt{N(t)}\kappa(t)]/[iE_\delta \sin(k\delta)]$, while $e^{-2i|\alpha_S|k\delta}$ compensates the phase accumulated from any scattering path when covering the distance between sites α_S and 0 before and after entering the ring structure.

The transmission amplitude $T^{(0)}(\Phi_u, \Phi_d, \Phi)$ is calculated as

$$\bullet \text{---} \bullet \xrightarrow{\text{red arrow}} = T^{(0)}(\Phi_u, \Phi_d, \Phi) = iE_\delta \sin(k\delta) G_{\mathcal{N}_{\mathcal{R}}\alpha_S}(\mu) e^{-i(|\alpha_S|+1)k\delta} \quad (6.21)$$

$$\begin{aligned} &= \begin{array}{c} \text{Diagram 1: } \bullet \text{---} \bullet \xrightarrow{\text{red arrow}} \text{---} \bullet \text{---} \bullet \text{ (curved arrow above)} \\ \text{Diagram 2: } \bullet \text{---} \bullet \text{---} \bullet \text{---} \bullet \text{ (curved arrow below)} \end{array} + \dots \quad (6.22) \\ &= t \frac{1 - (r-t)(re^{i2\Phi_d} - te^{i(\Phi_u + \Phi_d - \Phi)})}{D(\Phi_u, \Phi_d, \Phi)} e^{i(\Phi_u + \frac{\Phi}{2})} t \\ &\quad + t \frac{1 - (r-t)(re^{i2\Phi_u} - te^{i(\Phi_u + \Phi_d + \Phi)})}{D(\Phi_u, \Phi_d, \Phi)} e^{i(\Phi_d - \frac{\Phi}{2})} t \\ &= t^2 \frac{e^{i(\Phi_u + \frac{\Phi}{2})} + e^{i(\Phi_d - \frac{\Phi}{2})} - (r-t)^2 e^{i(\Phi_u + \Phi_d)} (e^{i(\Phi_u - \frac{\Phi}{2})} + e^{i(\Phi_d + \frac{\Phi}{2})})}{D(\Phi_u, \Phi_d, \Phi)}. \end{aligned}$$

Again, the phase factor $e^{-i(|\alpha_S|+1)k\delta}$ compensates the phase accumulated from the scattering paths within the waveguides when covering the distance between sites α_S and 0 and the single jump from site $\mathcal{N}_{\mathcal{R}}/2$ to $\mathcal{N}_{\mathcal{R}}$.

The noninteracting reflection and transmission probability for a certain disorder configuration is now found by taking the squared modulus square of $R^{(0)}(\Phi_u, \Phi_d, \Phi)$ and $T^{(0)}(\Phi_u, \Phi_d, \Phi)$. Averaging these probabilities over all possible phases Φ_u, Φ_d then is expected to display the AAS oscillations.

Since the phases are uniformly distributed between 0 and 2π , this average is an integration,

$$\begin{aligned} \langle |R^{(0)}|^2 \rangle_{\text{dis}}(\Phi) &= \frac{1}{(2\pi)^2} \int_0^{2\pi} d\Phi_u \int_0^{2\pi} d\Phi_d |R^{(0)}(\Phi_u, \Phi_d, \Phi)|^2 \\ \langle |T^{(0)}|^2 \rangle_{\text{dis}}(\Phi) &= \frac{1}{(2\pi)^2} \int_0^{2\pi} d\Phi_u \int_0^{2\pi} d\Phi_d |T^{(0)}(\Phi_u, \Phi_d, \Phi)|^2 \end{aligned} \quad (6.23)$$

Unfortunately, due to the complexity of the expressions in the integrand, we were not able to perform the final integration with analytical means. However, a cheap numerical integration based on Monte-Carlo-methods is reasonable and also allows us to check our model against the full quantum simulation. The pseudo-code for this integration is found in appendix A.7, where we present its result in Fig. 6.1. Its discussion will take place in combination with the interacting theory at the end of the next section.

6.2 The interacting case

6.2.1 Perturbative treatment of interaction

For the diagrammatic representation of the solution Ψ_α of the interacting problem we would like to introduce a similar diagrammatic approach as for the noninteracting case. Our aim is thus to distinguish sets of “interacting scattering paths” according to whether their final point α in the index of Ψ_α is in the upper or lower branch of the Aharonov-Bohm ring, and whether α is approached from its left or right side. This view is motivated from the selfconsistent equation for Ψ_α , Eq. (5.34), where a noninteracting Green’s function, and therefore the scattering paths discussed in the last section, are the objects which terminate at α . Therefore, we write the wave function Ψ_α again as sum of diagrams, which carry a similar interpretation as those discussed in the previous section. For instance, for α in the upper part of the ring, this representation is given by

$$\Psi_\alpha = \frac{\sqrt{N}\kappa(t)}{iE_\delta \sin(k\delta)} e^{ik\delta|\alpha_S|} \left(\text{---} \overset{\alpha}{\curvearrowright} + \text{---} \overset{\alpha}{\curvearrowleft} \right), \quad (6.24)$$

while mirroring horizontally yields the “interacting diagrams” for the lower branch of the ring. The prefactor in Eq. (6.24) is chosen in accordance to the noninteracting solution as obtained by Eq. (5.34) for $g = 0$.

To enable the calculation of the green-colored diagrams, let us introduce further diagrammatic elements to represent the self-consistent Eq. (5.34). Following Ref. [29, 131] we represent the intermediate site α' , at which the mean-field wave interacts with its density $|\Psi_{\alpha'}|^2$, by a box,

$$\blacksquare^{\alpha'}, \quad (6.25)$$

and the complex conjugate, resummed diagrams by dashed lines,

$$\Psi_\alpha^* = -\frac{\sqrt{N}\kappa(t)}{iE_\delta \sin(k\delta)} e^{-ik\delta|\alpha_S|} \left(\text{---} \overset{\alpha}{\curvearrowright} + \text{---} \overset{\alpha}{\curvearrowleft} \right). \quad (6.26)$$

With these building blocks, the self-consistent equation, Eq. (5.34), translates into a set of four coupled diagrammatic equations. One of them is given by

$$\begin{aligned} \text{---} \overset{\alpha}{\curvearrowright} &= \text{---} \overset{\alpha}{\curvearrowright} - ig_{\text{eff}} \sum_{\substack{\alpha' \\ \text{upper} \\ \text{branch}}} \left(\text{---} \overset{\alpha'}{\curvearrowright} + \text{---} \overset{\alpha'}{\curvearrowleft} \right)^2 \left(\text{---} \overset{\alpha'}{\curvearrowright} + \text{---} \overset{\alpha'}{\curvearrowleft} \right) \\ &\quad \times \left(\theta(\alpha - \alpha') \blacksquare^{\alpha'} \overset{\alpha}{\curvearrowright} + \overset{\alpha}{\curvearrowleft} \blacksquare^{\alpha'} + \overset{\alpha}{\curvearrowright} \blacksquare^{\alpha'} \right) \\ &\quad - ig_{\text{eff}} \sum_{\substack{\alpha' \\ \text{lower} \\ \text{branch}}} \left(\text{---} \overset{\alpha'}{\curvearrowright} + \text{---} \overset{\alpha'}{\curvearrowleft} \right)^2 \left(\text{---} \overset{\alpha'}{\curvearrowright} + \text{---} \overset{\alpha'}{\curvearrowleft} \right) \left(\overset{\alpha}{\curvearrowright} \blacksquare^{\alpha'} + \overset{\alpha}{\curvearrowleft} \blacksquare^{\alpha'} \right), \end{aligned} \quad (6.27)$$

where

$$g_{\text{eff}} = g \frac{N(t) |\kappa(t)|^2}{[E_\delta \sin(k\delta)]^3} = \frac{g}{E_\delta} \frac{\rho^\varnothing \delta}{\sin(k\delta)} \quad (6.28)$$

denotes the effective interaction strength and which plays the role of the small parameter for the perturbation series. Apart from the strength g of the interaction it is controlled by the mean density ρ^\varnothing of particles generated in the ring by the source. This reflects the intuitive picture that interaction effects become more prominent for a higher density of particles. Even more, the dependence on $\sqrt{\mu(2 - \mu/E_\delta)} = \sin(k\delta) \approx k\delta$ indicates a more prominent contribution for smaller wave numbers.

By subsequently inserting the set of four diagrammatic equations, such as Eq. (6.27), into each other we obtain a series in powers of the small effective interaction strength g_{eff} , which allows for a perturbative calculation of the interacting wave function.

To obtain the full reflection and transmission amplitudes R^{coh} and T^{coh} for the interacting case we first take the site α in Eq. (6.24) either to be the left or the right junction site. By multiplying a final transmission amplitude t the involved paths leave the ring through the junction to the waveguide where they can travel to the final site within the respective waveguide. Diagrammatically, this is expressed by

$$\begin{aligned} R^{\text{coh}}(\Phi_u, \Phi_d, \Phi) &= \text{green arrow} \cdot = \text{red arrow} \cdot + \text{green arrow with loop} + \text{green arrow with loop}, \\ T^{\text{coh}}(\Phi_u, \Phi_d, \Phi) &= \text{green arrow} = \text{green arrow with loop} + \text{green arrow with loop}. \end{aligned} \quad (6.29)$$

The exact calculation of these expressions in first and higher orders of the effective interaction strength g_{eff} would, in principle, lead to the reflection and transmission probabilities for the interacting case and for a fixed disorder configuration. However, to perform this calculation, we would need exact knowledge of the noninteracting Green's function terminating at sites within the ring, see Eq. (5.34). Their calculation requires the specific disorder potential V_α at the single sites as input to identify the accumulated phase from a partial exploration of one of the branches. For example, we get already in linear order of the perturbation theory, truncating the summation in Eq. (5.39),

$$\text{red arrow with loop}^\alpha = \text{red arrow} \times \exp\left(\frac{i}{\hbar} \sum_{\alpha'=0}^{\alpha} \left(k\delta - \frac{V_{\alpha'}}{E_\delta \sin(k\delta)} + \theta\right)\right). \quad (6.30)$$

Luckily, we can avoid the calculation of these phases as our focus lies on an disorder average of the reflection and transmission probability. As we have argued in section 5.1.4, a consequence of the identity Eq. (5.44) is that only those contributions survive the disorder average which show perfect cancellation of the dynamical phases separately accumulated in each of the two branches. Consequently, since a partial exploration of a branch originates from the presence of an interaction event, we either need to annihilate

this by another, equally sized partial exploration of the same branch, or we extend the partial to a full exploration of the branch with the help of one or many other partial contributions. Quite naturally we find that in the expansion of Eq. (6.27) a structure of the form

$$\begin{array}{c} \leftarrow \leftarrow \leftarrow \\ \leftarrow \leftarrow \leftarrow \\ \leftarrow \leftarrow \leftarrow \end{array} \blacksquare, \quad \begin{array}{c} \leftarrow \leftarrow \leftarrow \\ \leftarrow \leftarrow \leftarrow \\ \leftarrow \leftarrow \leftarrow \end{array} \blacksquare \leftarrow \leftarrow \leftarrow, \quad \begin{array}{c} \leftarrow \leftarrow \leftarrow \\ \leftarrow \leftarrow \leftarrow \\ \leftarrow \leftarrow \leftarrow \end{array} \blacksquare \leftarrow \leftarrow \leftarrow \leftarrow \leftarrow \leftarrow \leftarrow, \quad (6.31)$$

as well as their mirrored and/or complex conjugated versions, produces a non-vanishing phase due to a partial exploration of a branch. To compensate those, we would need a second interaction event which co-moves together with the first and which gives rise to a partial exploration of equal length. However, since each interaction event is accompanied by a summation along the sites of a branch, this scenario reduces two summations to a single one, suppressing these contributions by an order $\mathcal{O}(\mathcal{N}_{\mathcal{R}}^{-1})$ of the inverse number of sites in the ring.

Contrarily, structures similar to the form

$$\begin{array}{c} \leftarrow \leftarrow \leftarrow \\ \leftarrow \leftarrow \leftarrow \\ \leftarrow \leftarrow \leftarrow \end{array} \blacksquare \rightarrow, \quad \begin{array}{c} \leftarrow \leftarrow \leftarrow \\ \leftarrow \leftarrow \leftarrow \\ \leftarrow \leftarrow \leftarrow \end{array} \blacksquare \leftarrow, \quad (6.32)$$

do not have this drawback. In those structures, two arrows are paired, $\leftarrow \rightarrow$, canceling each other the site-dependent dynamical phase. The remaining two arrows appearing at the nonlinearity continue each other, $\rightarrow \blacksquare \rightarrow$, and their dynamical phases add up, thus also removing the explicit position dependence on the intermediate summation variable α' .

It is favorable to only consider diagrammatic constellations which do not contain the structures depicted in (6.31). This is achieved by a redefinition of the interacting diagrams, which equivalently introduces an effective interacting wave function, which only supports constellations of scattering paths only incorporating interaction events with the allowed structures in Eq. (6.32). The redefinition of the diagrams is done by modifying Eq. (6.27) to

$$\begin{aligned} \begin{array}{c} \leftarrow \\ \leftarrow \\ \leftarrow \end{array} \alpha &= \begin{array}{c} \leftarrow \\ \leftarrow \\ \leftarrow \end{array} \alpha + \sum_{\substack{\alpha' \\ \text{upper} \\ \text{branch}}} \begin{array}{c} \leftarrow \\ \leftarrow \\ \leftarrow \end{array} \alpha' \left(\theta(\alpha - \alpha') \begin{array}{c} \leftarrow \\ \leftarrow \\ \leftarrow \end{array} \alpha' \blacksquare \alpha + \begin{array}{c} \leftarrow \\ \leftarrow \\ \leftarrow \end{array} \alpha' \blacksquare \alpha + 2 \begin{array}{c} \leftarrow \\ \leftarrow \\ \leftarrow \end{array} \alpha' \blacksquare \alpha' \right) \\ &+ \sum_{\substack{\alpha' \\ \text{upper} \\ \text{branch}}} \begin{array}{c} \leftarrow \\ \leftarrow \\ \leftarrow \end{array} \alpha' \left(2\theta(\alpha - \alpha') \begin{array}{c} \leftarrow \\ \leftarrow \\ \leftarrow \end{array} \alpha' \blacksquare \alpha + 2 \begin{array}{c} \leftarrow \\ \leftarrow \\ \leftarrow \end{array} \alpha' \blacksquare \alpha + \begin{array}{c} \leftarrow \\ \leftarrow \\ \leftarrow \end{array} \alpha' \blacksquare \alpha' \right) \\ &+ \sum_{\substack{\alpha' \\ \text{lower} \\ \text{branch}}} \begin{array}{c} \leftarrow \\ \leftarrow \\ \leftarrow \end{array} \alpha' \left(\begin{array}{c} \leftarrow \\ \leftarrow \\ \leftarrow \end{array} \alpha' \blacksquare \alpha + 2 \begin{array}{c} \leftarrow \\ \leftarrow \\ \leftarrow \end{array} \alpha' \blacksquare \alpha' \right) + \sum_{\substack{\alpha' \\ \text{lower} \\ \text{branch}}} \begin{array}{c} \leftarrow \\ \leftarrow \\ \leftarrow \end{array} \alpha' \left(2 \begin{array}{c} \leftarrow \\ \leftarrow \\ \leftarrow \end{array} \alpha' \blacksquare \alpha + \begin{array}{c} \leftarrow \\ \leftarrow \\ \leftarrow \end{array} \alpha' \blacksquare \alpha' \right). \end{aligned} \quad (6.33)$$

The factor 2 appearing in the brackets within the sums is a combinatorial factor, which results from the squared factor in Eq. (6.27) and reflects the two possibilities the corresponding diagram can be constructed from picking an element in the factors. We can

write the above equation in a slightly more compact way through the use of vectors with diagrammatic entries and a matrix with the combinatorial weights,

$$\begin{aligned}
 \begin{array}{c} \alpha \\ \curvearrowright \\ \bullet \end{array} &= \begin{array}{c} \alpha \\ \curvearrowright \\ \bullet \\ \color{red}{\curvearrowright} \\ \bullet \end{array} + \sum_{\substack{\alpha' \\ \text{upper} \\ \text{branch}}} \left(\begin{array}{c} \alpha' \\ \curvearrowright \\ \bullet \\ \color{red}{\curvearrowright} \\ \bullet \end{array}, \begin{array}{c} \alpha' \\ \color{red}{\curvearrowright} \\ \bullet \\ \color{red}{\curvearrowright} \\ \bullet \end{array} \right) \begin{pmatrix} 1 & 2 \\ 2 & 1 \end{pmatrix} \begin{pmatrix} \theta(\alpha - \alpha') \begin{array}{c} \alpha' \\ \color{red}{\curvearrowright} \\ \bullet \\ \color{red}{\curvearrowright} \\ \bullet \end{array} + \begin{array}{c} \alpha' \\ \color{red}{\curvearrowright} \\ \bullet \\ \color{red}{\curvearrowright} \\ \bullet \end{array} \\ \begin{array}{c} \alpha \\ \color{red}{\curvearrowright} \\ \bullet \\ \color{red}{\curvearrowright} \\ \bullet \end{array} \end{pmatrix} \\
 &+ \sum_{\substack{\alpha' \\ \text{lower} \\ \text{branch}}} \left(\begin{array}{c} \color{red}{\curvearrowright} \\ \bullet \\ \alpha' \\ \color{red}{\curvearrowright} \\ \bullet \end{array}, \begin{array}{c} \color{red}{\curvearrowright} \\ \bullet \\ \alpha' \\ \color{red}{\curvearrowright} \\ \bullet \end{array} \right) \begin{pmatrix} 1 & 2 \\ 2 & 1 \end{pmatrix} \begin{pmatrix} \begin{array}{c} \alpha \\ \color{red}{\curvearrowright} \\ \bullet \\ \color{red}{\curvearrowright} \\ \bullet \end{array} \\ \begin{array}{c} \alpha \\ \color{red}{\curvearrowright} \\ \bullet \\ \color{red}{\curvearrowright} \\ \bullet \end{array} \end{pmatrix}. \quad (6.34)
 \end{aligned}$$

In an equivalent way, one can find similar equations for the remaining interacting diagrams. Together with Eq. (6.34) this forms a selfconsistent set of four coupled algebraic equations. The missing three are given by

$$\begin{aligned}
 \begin{array}{c} \alpha \\ \color{red}{\curvearrowright} \\ \bullet \end{array} &= \begin{array}{c} \alpha \\ \color{red}{\curvearrowright} \\ \bullet \\ \color{red}{\curvearrowright} \\ \bullet \end{array} \\
 &+ \sum_{\substack{\alpha' \\ \text{upper} \\ \text{branch}}} \left(\begin{array}{c} \alpha' \\ \color{red}{\curvearrowright} \\ \bullet \\ \color{red}{\curvearrowright} \\ \bullet \end{array}, \begin{array}{c} \alpha' \\ \color{red}{\curvearrowright} \\ \bullet \\ \color{red}{\curvearrowright} \\ \bullet \end{array} \right) \begin{pmatrix} 1 & 2 \\ 2 & 1 \end{pmatrix} \begin{pmatrix} \begin{array}{c} \alpha \\ \color{red}{\curvearrowright} \\ \bullet \\ \color{red}{\curvearrowright} \\ \bullet \end{array} \\ \theta(x' - x) \begin{array}{c} \alpha' \\ \color{red}{\curvearrowright} \\ \bullet \\ \color{red}{\curvearrowright} \\ \bullet \end{array} + \begin{array}{c} \alpha' \\ \color{red}{\curvearrowright} \\ \bullet \\ \color{red}{\curvearrowright} \\ \bullet \end{array} \end{pmatrix} \quad (6.35) \\
 &+ \sum_{\substack{\alpha' \\ \text{lower} \\ \text{branch}}} \left(\begin{array}{c} \color{red}{\curvearrowright} \\ \bullet \\ \alpha' \\ \color{red}{\curvearrowright} \\ \bullet \end{array}, \begin{array}{c} \color{red}{\curvearrowright} \\ \bullet \\ \alpha' \\ \color{red}{\curvearrowright} \\ \bullet \end{array} \right) \begin{pmatrix} 1 & 2 \\ 2 & 1 \end{pmatrix} \begin{pmatrix} \begin{array}{c} \alpha \\ \color{red}{\curvearrowright} \\ \bullet \\ \color{red}{\curvearrowright} \\ \bullet \end{array} \\ \begin{array}{c} \alpha \\ \color{red}{\curvearrowright} \\ \bullet \\ \color{red}{\curvearrowright} \\ \bullet \end{array} \end{pmatrix},
 \end{aligned}$$

$$\begin{aligned}
 \begin{array}{c} \alpha \\ \color{red}{\curvearrowright} \\ \bullet \end{array} &= \begin{array}{c} \alpha \\ \color{red}{\curvearrowright} \\ \bullet \\ \color{red}{\curvearrowright} \\ \bullet \end{array} + \sum_{\substack{\alpha' \\ \text{upper} \\ \text{branch}}} \left(\begin{array}{c} \alpha' \\ \color{red}{\curvearrowright} \\ \bullet \\ \color{red}{\curvearrowright} \\ \bullet \end{array}, \begin{array}{c} \alpha' \\ \color{red}{\curvearrowright} \\ \bullet \\ \color{red}{\curvearrowright} \\ \bullet \end{array} \right) \begin{pmatrix} 1 & 2 \\ 2 & 1 \end{pmatrix} \begin{pmatrix} \begin{array}{c} \alpha \\ \color{red}{\curvearrowright} \\ \bullet \\ \color{red}{\curvearrowright} \\ \bullet \end{array} \\ \begin{array}{c} \alpha \\ \color{red}{\curvearrowright} \\ \bullet \\ \color{red}{\curvearrowright} \\ \bullet \end{array} \end{pmatrix} \quad (6.36) \\
 &+ \sum_{\substack{\alpha' \\ \text{lower} \\ \text{branch}}} \left(\begin{array}{c} \color{red}{\curvearrowright} \\ \bullet \\ \alpha' \\ \color{red}{\curvearrowright} \\ \bullet \end{array}, \begin{array}{c} \color{red}{\curvearrowright} \\ \bullet \\ \alpha' \\ \color{red}{\curvearrowright} \\ \bullet \end{array} \right) \begin{pmatrix} 1 & 2 \\ 2 & 1 \end{pmatrix} \begin{pmatrix} \theta(\alpha - \alpha') \begin{array}{c} \alpha' \\ \color{red}{\curvearrowright} \\ \bullet \\ \color{red}{\curvearrowright} \\ \bullet \end{array} + \begin{array}{c} \alpha' \\ \color{red}{\curvearrowright} \\ \bullet \\ \color{red}{\curvearrowright} \\ \bullet \end{array} \\ \begin{array}{c} \alpha \\ \color{red}{\curvearrowright} \\ \bullet \\ \color{red}{\curvearrowright} \\ \bullet \end{array} \end{pmatrix},
 \end{aligned}$$

$$\begin{aligned}
\begin{array}{c} \bullet \\ \hline \bullet \\ \hline \bullet \end{array} \xrightarrow{\alpha'} &= \begin{array}{c} \bullet \\ \hline \bullet \\ \hline \bullet \end{array} \xrightarrow{\alpha'} + \sum_{\text{upper branch}} \left(\begin{array}{c} \bullet \\ \hline \bullet \\ \hline \bullet \end{array} \xrightarrow{\alpha'} + \begin{array}{c} \bullet \\ \hline \bullet \\ \hline \bullet \end{array} \xrightarrow{\alpha'} \right) \begin{pmatrix} 1 & 2 \\ 2 & 1 \end{pmatrix} \begin{pmatrix} \begin{array}{c} \bullet \\ \hline \bullet \\ \hline \bullet \end{array} \xrightarrow{\alpha'} \\ \begin{array}{c} \bullet \\ \hline \bullet \\ \hline \bullet \end{array} \xrightarrow{\alpha'} \end{pmatrix} \\
+ \sum_{\text{lower branch}} \left(\begin{array}{c} \bullet \\ \hline \bullet \\ \hline \bullet \end{array} \xrightarrow{\alpha'} , \begin{array}{c} \bullet \\ \hline \bullet \\ \hline \bullet \end{array} \xrightarrow{\alpha'} \right) \begin{pmatrix} 1 & 2 \\ 2 & 1 \end{pmatrix} \begin{pmatrix} \begin{array}{c} \bullet \\ \hline \bullet \\ \hline \bullet \end{array} \xrightarrow{\alpha'} \\ \theta(\alpha' - \alpha) \begin{array}{c} \bullet \\ \hline \bullet \\ \hline \bullet \end{array} \xrightarrow{\alpha'} + \begin{array}{c} \bullet \\ \hline \bullet \\ \hline \bullet \end{array} \xrightarrow{\alpha'} \end{pmatrix}.
\end{aligned} \tag{6.37}$$

We now return to the calculation of the reflection and transmission amplitudes as described by Eq. (6.29) and insert the above obtained self-consistent equations for the effective interaction diagrams. To simplify the results for the reflection amplitude, we use the diagrammatic identities

$$\begin{aligned}
\begin{array}{c} \bullet \\ \hline \bullet \\ \hline \bullet \end{array} \xrightarrow{\alpha'} &= \begin{array}{c} \bullet \\ \hline \bullet \\ \hline \bullet \end{array} \xrightarrow{\alpha'} + \begin{array}{c} \bullet \\ \hline \bullet \\ \hline \bullet \end{array} \xrightarrow{\alpha'} + \begin{array}{c} \bullet \\ \hline \bullet \\ \hline \bullet \end{array} \xrightarrow{\alpha'}, & \begin{array}{c} \bullet \\ \hline \bullet \\ \hline \bullet \end{array} \xrightarrow{\alpha'} &= \begin{array}{c} \bullet \\ \hline \bullet \\ \hline \bullet \end{array} \xrightarrow{\alpha'} + \begin{array}{c} \bullet \\ \hline \bullet \\ \hline \bullet \end{array} \xrightarrow{\alpha'}, \\
\begin{array}{c} \bullet \\ \hline \bullet \\ \hline \bullet \end{array} \xrightarrow{\alpha'} &= \begin{array}{c} \bullet \\ \hline \bullet \\ \hline \bullet \end{array} \xrightarrow{\alpha'} + \begin{array}{c} \bullet \\ \hline \bullet \\ \hline \bullet \end{array} \xrightarrow{\alpha'}, & \begin{array}{c} \bullet \\ \hline \bullet \\ \hline \bullet \end{array} \xrightarrow{\alpha'} &= \begin{array}{c} \bullet \\ \hline \bullet \\ \hline \bullet \end{array} \xrightarrow{\alpha'} + \begin{array}{c} \bullet \\ \hline \bullet \\ \hline \bullet \end{array} \xrightarrow{\alpha'}.
\end{aligned} \tag{6.38}$$

With these, the equation for the (effective) full interacting reflection amplitude reads

$$\begin{aligned}
R^{(\text{coh, eff})}(\Phi_u, \Phi_d, \Phi) &= \begin{array}{c} \bullet \\ \hline \bullet \\ \hline \bullet \end{array} \xrightarrow{\alpha'} + \begin{array}{c} \bullet \\ \hline \bullet \\ \hline \bullet \end{array} \xrightarrow{\alpha'} + \begin{array}{c} \bullet \\ \hline \bullet \\ \hline \bullet \end{array} \xrightarrow{\alpha'} \\
&= \begin{array}{c} \bullet \\ \hline \bullet \\ \hline \bullet \end{array} \xrightarrow{\alpha'} + \begin{array}{c} \bullet \\ \hline \bullet \\ \hline \bullet \end{array} \xrightarrow{\alpha'} + \begin{array}{c} \bullet \\ \hline \bullet \\ \hline \bullet \end{array} \xrightarrow{\alpha'} - ig_{\text{eff}} \sum_{\text{upper branch}} \left(\begin{array}{c} \bullet \\ \hline \bullet \\ \hline \bullet \end{array} \xrightarrow{\alpha'} , \begin{array}{c} \bullet \\ \hline \bullet \\ \hline \bullet \end{array} \xrightarrow{\alpha'} \right) \begin{pmatrix} 1 & 2 \\ 2 & 1 \end{pmatrix} \begin{pmatrix} \begin{array}{c} \bullet \\ \hline \bullet \\ \hline \bullet \end{array} \xrightarrow{\alpha'} \\ \begin{array}{c} \bullet \\ \hline \bullet \\ \hline \bullet \end{array} \xrightarrow{\alpha'} \end{pmatrix} \\
&\quad - ig_{\text{eff}} \sum_{\text{lower branch}} \left(\begin{array}{c} \bullet \\ \hline \bullet \\ \hline \bullet \end{array} \xrightarrow{\alpha'} , \begin{array}{c} \bullet \\ \hline \bullet \\ \hline \bullet \end{array} \xrightarrow{\alpha'} \right) \begin{pmatrix} 1 & 2 \\ 2 & 1 \end{pmatrix} \begin{pmatrix} \begin{array}{c} \bullet \\ \hline \bullet \\ \hline \bullet \end{array} \xrightarrow{\alpha'} \\ \begin{array}{c} \bullet \\ \hline \bullet \\ \hline \bullet \end{array} \xrightarrow{\alpha'} \end{pmatrix}.
\end{aligned} \tag{6.39}$$

For the effective transmission amplitude we use the following identities to transform our result,

$$\begin{aligned}
\begin{array}{c} \bullet \\ \hline \bullet \\ \hline \bullet \end{array} \xrightarrow{\alpha'} &= \begin{array}{c} \bullet \\ \hline \bullet \\ \hline \bullet \end{array} \xrightarrow{\alpha'} + \begin{array}{c} \bullet \\ \hline \bullet \\ \hline \bullet \end{array} \xrightarrow{\alpha'} + \begin{array}{c} \bullet \\ \hline \bullet \\ \hline \bullet \end{array} \xrightarrow{\alpha'}, & \begin{array}{c} \bullet \\ \hline \bullet \\ \hline \bullet \end{array} \xrightarrow{\alpha'} &= \begin{array}{c} \bullet \\ \hline \bullet \\ \hline \bullet \end{array} \xrightarrow{\alpha'} + \begin{array}{c} \bullet \\ \hline \bullet \\ \hline \bullet \end{array} \xrightarrow{\alpha'} + \begin{array}{c} \bullet \\ \hline \bullet \\ \hline \bullet \end{array} \xrightarrow{\alpha'}, \\
\begin{array}{c} \bullet \\ \hline \bullet \\ \hline \bullet \end{array} \xrightarrow{\alpha'} &= \begin{array}{c} \bullet \\ \hline \bullet \\ \hline \bullet \end{array} \xrightarrow{\alpha'} + \begin{array}{c} \bullet \\ \hline \bullet \\ \hline \bullet \end{array} \xrightarrow{\alpha'}, & \begin{array}{c} \bullet \\ \hline \bullet \\ \hline \bullet \end{array} \xrightarrow{\alpha'} &= \begin{array}{c} \bullet \\ \hline \bullet \\ \hline \bullet \end{array} \xrightarrow{\alpha'} + \begin{array}{c} \bullet \\ \hline \bullet \\ \hline \bullet \end{array} \xrightarrow{\alpha'}.
\end{aligned} \tag{6.40}$$

Then, the integral equation for the resummed transmission amplitude transforms to

$$\begin{aligned}
T^{(\text{coh, eff})}(\Phi_u, \Phi_d, \Phi) &= \text{diagram 1} + \text{diagram 2} \quad (6.41) \\
&= \text{diagram 3} + \text{diagram 4} - ig_{\text{eff}} \sum_{\alpha' \text{ upper branch}} \left(\text{diagram 5}, \text{diagram 6} \right) \begin{pmatrix} 1 & 2 \\ 2 & 1 \end{pmatrix} \begin{pmatrix} \text{diagram 7} \\ \text{diagram 8} \end{pmatrix} \\
&\quad - ig_{\text{eff}} \sum_{\alpha' \text{ lower branch}} \left(\text{diagram 9}, \text{diagram 10} \right) \begin{pmatrix} 1 & 2 \\ 2 & 1 \end{pmatrix} \begin{pmatrix} \text{diagram 11} \\ \text{diagram 12} \end{pmatrix}.
\end{aligned}$$

We like to again emphasize here that contrarily to the noninteracting case the modulus square of the effective reflection and transmission amplitude does not yield the actual reflection probability for a fixed disorder configuration within the ring, since we have neglected contributions to arrive at the above results. It is only after a disorder average that we obtain the correct physical reflection probability.

6.2.2 Effective reflection and transmission amplitudes in linear order in the interaction strength

From Eqs. (6.39) and (6.41) we immediately see, that the correction to the reflection and transmission amplitudes due to first order perturbation theory is found by expressing each resummed interacting diagram by its zeroth order, noninteracting contribution,

$$\text{diagram 13}, \text{diagram 14}, \text{diagram 15}, \text{diagram 16} \rightarrow \text{diagram 17}, \text{diagram 18}, \text{diagram 19}, \text{diagram 20}. \quad (6.42)$$

Within this order the terms in the summation become independent on the summation index α' since the partial explorations of the branches cancel each other, as expected. The summation is then trivially performed and introduces the number of sites $\mathcal{N}_{\mathcal{R}}/2$ in one of the branches of the ring as an additional parameter. The first order correction to the effective reflection amplitude is thus diagrammatically given by

$$\begin{aligned}
\Delta R^{(1)}(\Phi_u, \Phi_d, \Phi) &= R^{(\text{coh, eff}, 1)}(\Phi_u, \Phi_d, \Phi) - R^{(0)}(\Phi_u, \Phi_d, \Phi) \\
&= -ig_{\text{eff}} \frac{\mathcal{N}_{\mathcal{R}}}{2} \left[\begin{aligned} &\left(\text{diagram 21}, \text{diagram 22} \right) \begin{pmatrix} 1 & 2 \\ 2 & 1 \end{pmatrix} \begin{pmatrix} \text{diagram 23} \\ \text{diagram 24} \end{pmatrix} \\ &+ \left(\text{diagram 25}, \text{diagram 26} \right) \begin{pmatrix} 1 & 2 \\ 2 & 1 \end{pmatrix} \begin{pmatrix} \text{diagram 27} \\ \text{diagram 28} \end{pmatrix} \end{aligned} \right]. \quad (6.43)
\end{aligned}$$

The diagrammatic representation allows for an illustrative interpretation of the result. Corrections to the averaged reflection probability arise from scattering paths, which enter the upper or lower branch of the ring in an arbitrary way and coming from an arbitrary junction. Then, somewhere within that branch, we have the interaction with the particle density ρ , which is represented by the paired diagrams. At this stage, combinatorial multiplicities have to be considered. After that the scattering path continues its exploration of the branch until it arrives at the opposite junction, from where it leaves to the incident waveguide in an arbitrary way. The advantage of our approach is that all combinatorial multiplicities of trajectories are accounted for correctly by using resummed diagrams and the multiplicities matrix. Moreover, the word ‘‘arbitrary’’ is mathematically defined through resummed diagrams found for the noninteracting case, which contain any scattering path fulfilling the wished boundary conditions.

The first order correction for the effective transmission amplitude is found to be

$$\begin{aligned}
\Delta T^{(1)}(\Phi_u, \Phi_d, \Phi) &= T^{(\text{coh, eff}, 1)}(\Phi_u, \Phi_d, \Phi) - T^{(0)}(\Phi_u, \Phi_d, \Phi) \\
&= -ig_{\text{eff}} \frac{\mathcal{N}_{\mathcal{R}}}{2} \left[\left(\begin{array}{c} \text{---} \bullet \text{---} \\ \text{---} \bullet \text{---} \end{array} \right), \left(\begin{array}{c} \text{---} \bullet \text{---} \\ \text{---} \bullet \text{---} \end{array} \right) \begin{pmatrix} 1 & 2 \\ 2 & 1 \end{pmatrix} \begin{pmatrix} \text{---} \bullet \text{---} \\ \text{---} \bullet \text{---} \end{pmatrix} \right. \\
&\quad \left. + \left(\begin{array}{c} \text{---} \bullet \text{---} \\ \text{---} \bullet \text{---} \end{array} \right), \left(\begin{array}{c} \text{---} \bullet \text{---} \\ \text{---} \bullet \text{---} \end{array} \right) \begin{pmatrix} 1 & 2 \\ 2 & 1 \end{pmatrix} \begin{pmatrix} \text{---} \bullet \text{---} \\ \text{---} \bullet \text{---} \end{pmatrix} \right]. \tag{6.44}
\end{aligned}$$

Again, a similar interpretation of this diagrammatic expression is possible as in the case of the reflection amplitude.

When we insert into the above formulas the analytical expressions for the resummed noninteracting diagrams found in section 6.1, the results we obtain for the first order corrections are rather lengthy and unhandy formulas. We did not find a possible way to simplify the results to a short analytical expression like in the noninteracting case. For that reason we refrain from an explicit writing of the analytic formulas for the corrections.

6.2.3 Disorder averaged reflection and transmission probabilities in linear order in the interaction strength

In order to obtain reflection and transmission probabilities, we have to take the modulus square of the full interacting reflection and transmission amplitudes. These are then averaged over the disorder phases Φ_u, Φ_d . The result then displays AAS oscillations for including the influence of interaction.

The disorder-averaged reflection probability for the interacting system is, according

to Eq. (5.43), calculated by

$$\begin{aligned}
\left\langle |R^{(\text{coh})}(\Phi_u, \Phi_d, \Phi)|^2 \right\rangle_{\text{dis}} &= \frac{1}{(2\pi)^2} \int_0^{2\pi} d\Phi_u \int_0^{2\pi} d\Phi_d \left| R^{(\text{coh})}(\Phi_u, \Phi_d, \Phi) \right|^2 \\
&= \frac{1}{(2\pi)^2} \int_0^{2\pi} d\Phi_u \int_0^{2\pi} d\Phi_d \left| R^{(0)}(\Phi_u, \Phi_d, \Phi) + \Delta R^{(1)}(\Phi_u, \Phi_d, \Phi) + \mathcal{O}(|g|^2) \right|^2 \\
&= |R^{(0)}(\Phi)|^2 + \Delta |R^{(1)}(\Phi)|^2 + \mathcal{O}(|g|^2), \tag{6.45}
\end{aligned}$$

where

$$|R^{(0)}(\Phi)|^2 = \frac{1}{(2\pi)^2} \int_0^{2\pi} d\Phi_u \int_0^{2\pi} d\Phi_d \left| R^{(0)}(\Phi_u, \Phi_d, \Phi) \right|^2 \tag{6.46}$$

denotes the reflection probability of the noninteracting scenario, and its first order correction in the interaction strength g is given by

$$\Delta |R^{(1)}(\Phi)|^2 = \frac{2}{(2\pi)^2} \int_0^{2\pi} d\Phi_u \int_0^{2\pi} d\Phi_d \text{Re} \left\{ R^{(0)*}(\Phi_u, \Phi_d, \Phi) \delta R^{(1)}(\Phi_u, \Phi_d, \Phi) \right\}. \tag{6.47}$$

We insert the diagrammatic expressions (6.20) and (6.43) into this equation and further assume that the interaction strength g is real. This leads then to

$$\begin{aligned}
\delta R^{(1)}(\Phi) &= \frac{g_{\text{eff}} \mathcal{N}_{\mathcal{R}}}{(2\pi)^2} \int_0^{2\pi} d\Phi_u \int_0^{2\pi} d\Phi_d \text{Im} \left\{ \left(\begin{array}{c} \text{---} \bullet \text{---} + \text{---} \bullet \text{---} \text{---} \bullet \text{---} + \text{---} \bullet \text{---} \text{---} \bullet \text{---} \end{array} \right) \right. \\
&\quad \times \left[\left(\begin{array}{c} \text{---} \bullet \text{---} \text{---} \bullet \text{---} \\ \text{---} \bullet \text{---} \text{---} \bullet \text{---} \end{array} \right) \begin{pmatrix} 1 & 2 \\ 2 & 1 \end{pmatrix} \left(\begin{array}{c} \text{---} \bullet \text{---} \text{---} \bullet \text{---} \\ \text{---} \bullet \text{---} \text{---} \bullet \text{---} \end{array} \right) \right. \\
&\quad \left. \left. + \left(\begin{array}{c} \text{---} \bullet \text{---} \text{---} \bullet \text{---} \\ \text{---} \bullet \text{---} \text{---} \bullet \text{---} \end{array} \right) \begin{pmatrix} 1 & 2 \\ 2 & 1 \end{pmatrix} \left(\begin{array}{c} \text{---} \bullet \text{---} \text{---} \bullet \text{---} \\ \text{---} \bullet \text{---} \text{---} \bullet \text{---} \end{array} \right) \right] \left. \right\}. \tag{6.48}
\end{aligned}$$

Using the symmetry operations explained in section 6.1.2, we can further modify the above integral. Mirroring a diagram along the horizontal axis and then reversing its direction simply interchanges Φ_u with Φ_d in the expressions. Thus, if we also formally exchange Φ_u and Φ_d as integration variables, we find

$$\int_0^{2\pi} d\Phi_u \int_0^{2\pi} d\Phi_d \left(\begin{array}{c} \text{---} \bullet \text{---} + \text{---} \bullet \text{---} \text{---} \bullet \text{---} + \text{---} \bullet \text{---} \text{---} \bullet \text{---} \end{array} \right) \left(\begin{array}{c} \text{---} \bullet \text{---} \\ \text{---} \bullet \text{---} \end{array} \right) \begin{pmatrix} 1 & 2 \\ 2 & 1 \end{pmatrix} \left(\begin{array}{c} \text{---} \bullet \text{---} \text{---} \bullet \text{---} \\ \text{---} \bullet \text{---} \text{---} \bullet \text{---} \end{array} \right)$$

$$\begin{aligned}
&= \int_0^{2\pi} d\Phi_d \int_0^{2\pi} d\Phi_u \left(\text{---} \cdot \text{---} + \text{---} \cdot \text{---} + \text{---} \cdot \text{---} \right) \left(\text{---} \cdot \text{---} , \text{---} \cdot \text{---} \right) \begin{pmatrix} 1 & 2 \\ 2 & 1 \end{pmatrix} \begin{pmatrix} \text{---} \cdot \text{---} \\ \text{---} \cdot \text{---} \end{pmatrix} \\
&= \int_0^{2\pi} d\Phi_d \int_0^{2\pi} d\Phi_u \left(\text{---} \cdot \text{---} + \text{---} \cdot \text{---} + \text{---} \cdot \text{---} \right) \left(\text{---} \cdot \text{---} , \text{---} \cdot \text{---} \right) \begin{pmatrix} 1 & 2 \\ 2 & 1 \end{pmatrix} \begin{pmatrix} \text{---} \cdot \text{---} \\ \text{---} \cdot \text{---} \end{pmatrix}.
\end{aligned} \tag{6.49}$$

This allows us to write the result a little bit more compact,

$$\begin{aligned}
\Delta |R^{(1)}(\Phi)|^2 &= \frac{g_{\text{eff}} \mathcal{N}_{\mathcal{R}}}{4\pi^2} \int_0^{2\pi} d\Phi_u \int_0^{2\pi} d\Phi_d \text{Im} \left\{ \left(\text{---} \cdot \text{---} + \text{---} \cdot \text{---} + \text{---} \cdot \text{---} \right) \right. \\
&\quad \left. \times \left(\text{---} \cdot \text{---} + \text{---} \cdot \text{---} , \text{---} \cdot \text{---} + \text{---} \cdot \text{---} \right) \begin{pmatrix} 1 & 2 \\ 2 & 1 \end{pmatrix} \begin{pmatrix} \text{---} \cdot \text{---} \\ \text{---} \cdot \text{---} \end{pmatrix} \right\}.
\end{aligned} \tag{6.50}$$

In an analogous way we can find the correction to the transmission probability to be

$$\Delta |T^{(1)}(\Phi)|^2 = \frac{2}{(2\pi)^2} \int_0^{2\pi} d\Phi_u \int_0^{2\pi} d\Phi_d \text{Re} \left[T^{(0)*}(\Phi_u, \Phi_d, \Phi) \delta T^{(1)}(\Phi_u, \Phi_d, \Phi) \right], \tag{6.51}$$

which in the diagrammatic representation reads

$$\begin{aligned}
\Delta |T^{(1)}(\Phi)|^2 &= \frac{g_{\text{eff}} \mathcal{N}_{\mathcal{R}}}{(2\pi)^2} \int_0^{2\pi} d\Phi_u \int_0^{2\pi} d\Phi_d \text{Im} \left\{ \left(\text{---} \cdot \text{---} + \text{---} \cdot \text{---} \right) \right. \\
&\quad \left[\left(\text{---} \cdot \text{---} , \text{---} \cdot \text{---} \right) \begin{pmatrix} 1 & 2 \\ 2 & 1 \end{pmatrix} \begin{pmatrix} \text{---} \cdot \text{---} \\ \text{---} \cdot \text{---} \end{pmatrix} \right. \\
&\quad \left. \left. + \left(\text{---} \cdot \text{---} , \text{---} \cdot \text{---} \right) \begin{pmatrix} 1 & 2 \\ 2 & 1 \end{pmatrix} \begin{pmatrix} \text{---} \cdot \text{---} \\ \text{---} \cdot \text{---} \end{pmatrix} \right] \right\}.
\end{aligned} \tag{6.52}$$

Like for the noninteracting case, the analytic expressions obtained as integrand for the disorder averages show a complexity which so far avoided a further analytical evaluation

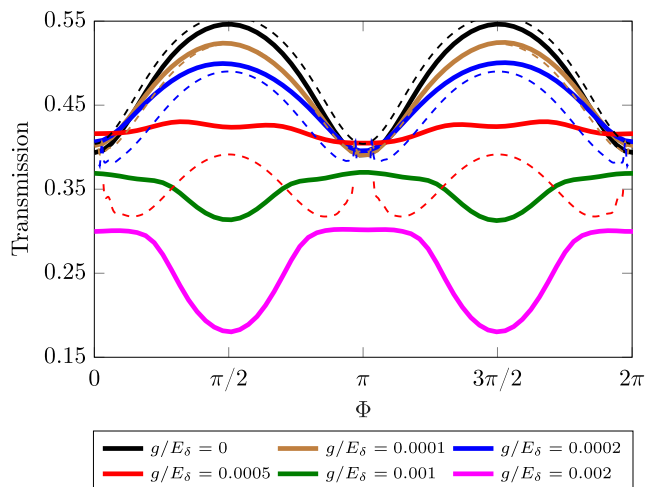
of the disorder average. Also here we used a numerical integration based on Monte-Carlo-methods to check the model against the numerical predictions from a solution of the mean-field equations. The pseudo-code for the numerical integration of Eqs. (6.50) and (6.52) is found in appendix A.7.

6.2.4 Discussion of the results

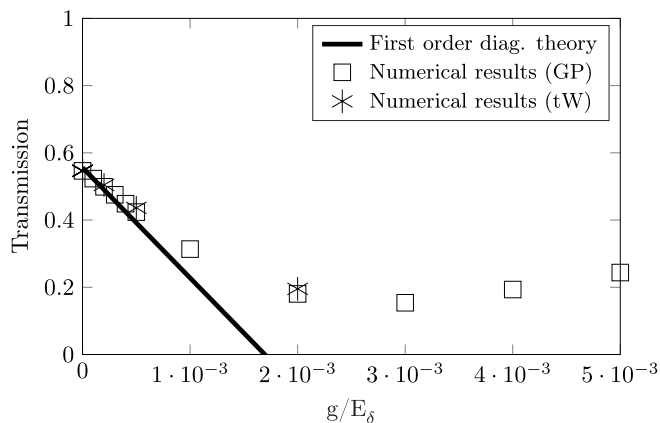
In Fig. 6.1 (a) we show again the results seen in Fig. 5.4, which are obtained from numerically solving the mean-field problem, Eq. (5.13), and compare them to the results obtained from the diagrammatic approach presented in this chapter. We see that for $g = 0$ the Monte-Carlo method produced an average of Eq. (6.23) which is in qualitative and quantitative agreement with the numerical findings for the AAS oscillations, thereby confirming the diagrammatic approach for $g = 0$. For the interacting case, $g \neq 0$, for an enclosed flux in the vicinity of $\Phi = 0$ and $\Phi = \pi$, the Monte-Carlo method produced numerical divergences in the result. We could attribute those to the vanishing of the determinant in Eq. (6.8) for cases when $\Phi_u \approx \Phi_d$, which are not sufficiently compensated by a vanishing of the numerator. These divergences have been excluded from the plots in Fig. 6.1 (a). Away from $\Phi = 0, \pi$, the Monte-Carlo method converges and we can observe a good qualitative and quantitative agreement for weak interaction strengths, $g/E_\delta \leq 0.0002$. For larger interaction strengths, the agreement remains qualitatively good near $\Phi \approx \pi/2$ and $\Phi \approx 3\pi/2$, but otherwise deviates from the numerical findings. Here, including higher order contributions from the perturbative diagrammatic series might improve the match between theory and numerics.

To further investigate the quality of the diagrammatic approach, we plot the transmission probability for $\Phi = \pi/2$ against the interaction strength g in Fig. 6.1 (b). We see that the numerical data indeed show a linear decrease of the AAS amplitude, while its slope is slightly less steep than predicted by the diagrammatic theory. This indicates an overestimation of the influence of interaction by the diagrammatic approach. One possible explanation of this discrepancy might be that in the numerical treatment the on-site energies of the junction sites are also subject to the disorder potential. Therefore, the reflection and transmission amplitudes r and t at the junction sites obtain a dependence on the disorder realization, which the diagrammatic theory is not able to capture. Their consideration might not only resolve the remaining mismatch for weak interaction strengths in Fig. 6.1 (b), but also explain the small but visible discrepancy of the results for $g = 0$ in Fig. 6.1 (a).

While the presented diagrammatic approach is a purely mathematical treatment, its purpose should be seen as to aid in identifying the main mechanism leading to interaction-based corrections of AAS oscillations and to provide a testing ground for a possible future development of a more efficient resummation procedure, which aims at directly summing significant contributions surviving the disorder average, in a similar fashion like ladder and crossed contributions in Refs. [29, 131, 132]. What we find for the ring structure is that the situation is very intriguing, since due to the linear structure of the interaction events in Eq. (6.32), any crossed contribution can here also be understood as a ladder contribution.



(a)



(b)

Figure 6.1: (a) Shown is Fig. 5.4 together with the results obtained from the diagrammatic approach (dashed lines). For $g \neq 0$, the predictions of the diagrammatic theory near $\Phi = 0$ and $\Phi = \pi$ have been excluded, as the numerical Monte-Carlo averaging produced singularities in the results. (b) Transmission probability for $\Phi = \pi/2$ as a function of the interaction strength g . Shown are the predictions from the first-order diagrammatic theory as well as the results of numerical Gross-Pitaevskii and truncated Wigner simulations, where for the latter the numerical parameters are chosen identically to Fig. 5.4 ($\mu/E_\delta = 0.2$, $\mathcal{N}_\mathcal{R} = 200$, averaged over 20000 realisations of correlated disorder with $V_0/E_\delta = 0.0238$ with correlation length $\sigma = 20\delta$). (Preliminary figures, to be published in an update of Ref. [30])

In a similar way to Eq. (5.51), which qualitatively explains the underlying mechanism leading to AAS oscillations in the noninteracting reflection probability, we can take a look at the contribution to $\Delta |R^{(1)}(\Phi)|^2$ in leading order in the powers of (r, t) to obtain a physical understanding of the involved interference mechanism leading to the interaction-based corrections to AAS oscillations. To find this representation, we expand the resummed non-interacting diagrams in Eq. (6.48) in terms of the shortest path contained in them. In leading order in powers of the amplitudes r, t , we find that the diagrammatic contributions surviving the disorder average are given by the diagrammatic product

$$\begin{aligned}
\frac{\Delta |R^{(1)}(\Phi)|^2}{g_{\text{eff}} \mathcal{N}_{\mathcal{R}}} &= \text{Im} \left\{ \begin{array}{l} \leftarrow \cdot \cdot \times \left[\leftarrow \times \left(\text{diagram 1} + \text{diagram 2} \right) \times \left(\text{diagram 3} + 2 \text{diagram 4} \right) \right. \\ \left. + \leftarrow \times \text{diagram 5} \times \left(\text{diagram 6} + 2 \text{diagram 7} \right) \right] \\ + \leftarrow \cdot \cdot \times \left[\leftarrow \times \left(\text{diagram 8} + \text{diagram 9} \right) \times \left(2 \text{diagram 10} + \text{diagram 11} \right) \right. \\ \left. + \leftarrow \times \text{diagram 12} \times \left(2 \text{diagram 13} + \text{diagram 14} \right) \right] \end{array} \right\} \\
&= \text{Im} \left[r^* t \left(t^{*3} e^{-i\Phi} + t^{*2} r^* e^{i\Phi} \right) \left(t^3 e^{i\Phi} + 2t^3 e^{-i\Phi} \right) + r^* t \left(t^{*2} r^* \right) 3t^3 \right. \\
&\quad \left. + r^* t \left(t^{*3} e^{i\Phi} + t^{*2} r^* e^{-i\Phi} \right) \left(2t^3 e^{i\Phi} + t^3 e^{-i\Phi} \right) + r^* t \left(t^{*2} r^* \right) 3t^3 \right] \\
&\quad + \mathcal{O}((r, p)^{10}). \tag{6.53}
\end{aligned}$$

Quite interestingly, the contribution from the left brackets in Eq. (6.48), which contains the diagrams corresponding to $R^{(0)*}(\Phi_u, \Phi_d, \Phi)$, contributes only the constant factor $\leftarrow \cdot \cdot = r^*$. This is further understood when translating the remaining diagrams back into an interacting diagram, which then yield self-averaging contributions such as



$$\tag{6.54}$$

which does not show any net-dependence on the phases Φ_u, Φ_d due to disorder. Such a self-dressing of a diagram was not observed in previous studies [29, 131, 132].

Inserting the numerical values Eq. (A.126) of r, t into Eq. (6.53), we find

$$\Delta |R^{(1)}(\Phi)|^2 = g_{\text{eff}} \mathcal{N}_{\mathcal{R}} (0.00210805 - 0.0252966 \cos(2\Phi)) + \mathcal{O}((r, p)^{10}), \tag{6.55}$$

which would indeed indicate an increase of the reflection probability for $\Phi = \pi/2$, and consequently, the decrease of the transmission probability. Note also that Eq. (6.53) would not yield any contribution in the case of real r, t .

7 Summary and outlook

In this final chapter we want to summarize the topics discussed within this thesis and also grant a further outlook into future research perspectives.

The main focus of this thesis was the study of interacting bosonic quantum many-body systems in the thermodynamic limit of a large number of particles N , and to apply semiclassical techniques in their theoretical treatment to provide an understanding of the interference mechanisms involved in different phenomena. In the limit “ $N \rightarrow \infty$ ” an effective description of the quantum many-body system is found in form of the mean-field wave equations, where interaction, if present, accounts for a term nonlinear in the mean-field matter wave. At the level of these mean-field equations, semiclassical techniques for the conventional semiclassical limit “ $\hbar \rightarrow 0$ ” can be used to find a solution, even if a weak particle-particle interaction is assumed. For stronger interactions, individual mean-field solutions show unstable behaviour upon variations of their initial conditions, and semiclassical techniques derived in Ref. [33], interpreting “ $\hbar_{\text{eff}} = 1/N \rightarrow 0$ ” as a semiclassical limit, allow to explain phenomena as a consequence of many-body interference of contributions related to different mean-field paths.

Within this thesis, we studied two different topics, each of which required one of the above interference mechanisms for its explanation.

In the first topic we dealt with the so-called out-of-time-order correlator (OTOC),

$$C(t) = \left\langle \Psi \left| \left[\hat{V}(t), \hat{W}(0) \right]^\dagger \left[\hat{V}(t), \hat{W}(0) \right] \right| \Psi \right\rangle, \quad (7.1)$$

the expectation value of the squared commutator of two local operators at different times. The OTOC provides a direct probe of chaos in the classical limit of a quantum many-body system. Indeed, for short times, the OTOC allows direct access to the stability of the dynamical solutions of the mean-field equations, while for longer times, it saturates. What we have found is that, to provide a thorough understanding of both the implications of the OTOC as well as for the technical aspects in its semiclassical treatment, we required a detailed review of chaos in classical Hamiltonian systems.

The aim of chapter 2 was to provide the reader with this review of classical Hamiltonian dynamics, with special emphasize put on classically chaotic systems. Calling the solutions of Hamilton’s equations of motion trajectories, we quickly turned to the analysis of their stability upon variations of the initial conditions, which introduced the

stability matrix as the derivative of a trajectory's final point in phase space w.r.t. its initial point. The careful analysis of this matrix led to the introduction of the set of Lyapunov exponents to quantify the growth rate for the at most exponential separation of nearby trajectories. Moreover, associated to each positive Lyapunov exponent λ_i there is a stable and an unstable direction, along which the difference in phase space of two nearby trajectories is exponentially decreasing, respectively growing in time with a rate given by λ_i . For a given trajectory, these directions define a co-traveling basis which spans phase space in the vicinity of this trajectory. This allowed us later in the technical part of the semiclassical treatment of the OTOC to treat the correlations of nearby solutions of the mean-field equations. The end of the chapter marked the precise statement of the defining properties for chaotic classical systems. These properties, mixing and exponential sensitivity to changes in the initial conditions, were later identified to explain the dynamical behaviour of the OTOC.

Chapter 3 was devoted to an introduction of bosonic quantum many-body systems. We reviewed the notion of the bosonic Fock space and introduced quadrature operators, which were needed to define conjugate variables for the later Hamiltonian formalism found as the classical " $\hbar_{\text{eff}} = 1/N \rightarrow 0$ " limit of the quantum system. We then presented the Bose-Hubbard Hamiltonian as the model describing N interacting bosons in a lattice. For this specific choice of Hamiltonian, a recently developed semiclassical theory [33] for the semiclassical limit " $\hbar_{\text{eff}} = 1/N \rightarrow 0$ " is at hand. This theory is based on the semiclassical approximation of the many-body propagator in bosonic Fock space, the matrix elements of the time-evolution operator in quadrature state representation. There, the mean-field wave equations re-emerge as dynamical equations of the Hamiltonian formalism found in the classical " $\hbar_{\text{eff}} \rightarrow 0$ " limit of the quantum system, and the propagator is expressed as a summation over amplitudes with phases accumulated along distinct mean-field solutions. This was our mean to relate the dynamics in the quantum many-body problem to the one found in its mean-field description, and enabled us to investigate the connection between OTOCs and unstable mean-field dynamics. Since an explicit discussion of the role of " $\hbar_{\text{eff}} = 1/N$ " is lacking in the original derivation in Ref. [33], we decided here to review in detail the steps leading to the semiclassical approximation of the propagator, thereby improving the original theory.

Chapter 4 contains the semiclassical treatment of the OTOC and marks the main research contribution of this thesis. To gain intuition, we started this chapter with the derivation of the expected behaviour of the OTOC for short times, using Wigner-Weyl transformations and the expansion of the Moyal bracket to precisely formalize the quantum-classical correspondence principle. Here we could attribute the early-time exponential growth of OTOCs to the appearance of squared elements of the stability matrix, the central quantity we discussed in chapter 2. We further indicated a failure of this expansion at the Ehrenfest time t_E , the time at which details of the order of \hbar_{eff} , such as a minimal wave packet, have spread to a classical size under the unstable chaotic dynamics. We then turned towards the semiclassical analysis of OTOCs, whose starting point was to use the semiclassical approximation of the propagator to express the time-evolution operators inherent in the Heisenberg picture of the operators in Eq. (7.1).

Within this semiclassical treatment, we found that the relevant contributions to the OTOC can be attributed to quadruplets of mean-field solutions which pairwise follow each other during the whole time, while a change of partners takes place during a close encounter of all four trajectories. The constellations with a dominant contribution to the OTOC are schematically depicted in Fig. 4.2 on page 61, and their contribution to the pre- and post-Ehrenfest dynamical behaviour of the OTOC is summarized in Fig. 4.5 on page 75. For times smaller than t_E , we found that the dynamical behaviour of the OTOC is solely attributed to a bundle in which the quadruplet of mean-field solutions effectively follows a single mean-field solution. Through the operators in the OTOC, the correlated motion of the four participants translated into the exponential growth with the Lyapunov exponent of the mean-field dynamics, as expected from the expansion of the Moyal bracket. After the Ehrenfest time, the unstable dynamics of the individual mean-field solutions in the quadruplet exponentially suppresses the contribution of the bundle, while quadruplets undergoing only a temporary encounter prove responsible for the saturation of OTOCs at t_E . Here, uncorrelated and correlated behaviour of the mean-field solutions at initial and final times translated into constant variances in phase space of the classical pendants of the operators of the OTOC, thus giving meaning to the OTOC's saturation value. The Ehrenfest time t_E emerged from this treatment as the minimal time to form a complete and close enough encounter of mean-field solutions to produce a contribution to the OTOC which is non-vanishing in the semiclassical limit " $\hbar_{\text{eff}} \rightarrow 0$ ".

Several implications, which can be drawn from our study of OTOCs, have been already discussed at the end of chapter 4, highlighting also the generality of the involved semiclassical arguments. For future studies, it is promising to extend the formalism presented here to fermionic many-body systems, for which also a semiclassical theory based on the semiclassical propagator in fermionic Fock space [133, 134] is at hand. Another extension of the theory is possible towards quantum many-body systems, whose classical limit displays mixed-regular chaotic motion, and which might be able to shed light on phenomena such as the light-cone spreading of the OTOC, observed for instance in Ref. [59]. An open question so far is also how to appropriately include the notion of temperature into the semiclassical treatment of OTOCs, where first attempts are available [120] for times smaller than t_E . This would allow to address the question of the mechanism underlying the thermal bound of the exponential growth rate predicted in Ref. [43]. One can also aim at introducing further time scales next to the Ehrenfest time and the Lyapunov time, the minimal time for a classical trajectory to experience chaotic dynamics, and study their interplay. An intriguing case is found, for instance, when the quantum system is weakly opened through holes where particles are able to leave the system. A single-particle scenario would be, for instance, a mesoscopic chaotic billiard with attached leads, where the width of the leads is much smaller than the circumference of the billiard. In such systems, the semiclassical contributions arising from classical trajectories are additionally weighted with a factor exponentially decaying with a rate $1/\tau_D$ in time, where the dwell time τ_D denotes the mean time a classical trajectory stays inside, see for instance Ref. [72]. This leads to an interplay of exponential

growth and loss of the OTOC for times before t_E , while exponential decay instead of saturation is expected after t_E . Moreover, the rate of decay of the OTOC due to opening the system is expected to change at the Ehrenfest time, since the correlated motion of the quadruplet as an effective single trajectory is replaced by a pair of two effective trajectories with intermediate temporary correlated motion. Finally, generalizations of OTOCs containing a higher power of commutators [135],

$$\tilde{C}(t) = \left\langle \Psi \left| \left[\hat{V}(t), \hat{W}(0) \right]^r \right| \Psi \right\rangle, \quad (7.2)$$

with $r = 3, 4, \dots$, naturally leads to the introduction of up to $r - 2$ encounters in its semiclassical description. Since each formation of an encounter of four or more solutions requires the Ehrenfest time as a minimal time to significantly contribute to the semiclassical result, this introduces a cascade of interference effects at multiples of the Ehrenfest time.

After our study of OTOCs, we turned in chapters 5 and 6 to a different topic and considered the coherent transport of cold bosonic atoms through an Aharonov-Bohm ring structure. This setup consists of two semi-infinite waveguides attached on opposite sides to a ring structure. The ring is penetrated by a synthetic gauge field with tunable flux Φ , playing the same role for the uncharged atoms like a magnetic field for electrons. Within the ring, the atoms are further subject to both a weak disorder potential and a weak particle-particle interaction. In the non-interacting case, the disorder-averaged transmission probability as a function of the encircled flux displays so-called Al'tshuler-Aronov-Spivak (AAS) oscillations, with double the frequency of the Aharonov-Bohm oscillations – an effect well-known from studies of the electronic pendant of the system. It was our main motivation to study the influence of a weak particle-particle interaction on AAS oscillations. This work has been performed in collaboration with R. Chrétien, J. Dujardin, C. Petitjean and P. Schlagheck, whose numerical results predicted an interaction-based inversion of these oscillations at the level of the mean-field treatment of the system. My contribution to this work was motivated by their results and is presented in chapter 6, where we tried to find and understand the solution of the mean-field equations with the help of semiclassical techniques in the semiclassical limit “ $\hbar \rightarrow 0$ ”.

In chapter 5 we introduced the system and the basic theoretical framework, as well as summarized the results obtained by my collaborators. We presented the Bose-Hubbard Hamiltonian which models the Aharonov-Bohm ring structure and we discussed in detail its parameters, as well as the length scales introduced by this model in order to justify the later use of semiclassical methods in the limit “ $\hbar \rightarrow 0$ ”. We further derived the dynamical mean-field equations for this system, where interaction appears as a term nonlinear in the mean-field matter wave. We showed how to understand the interacting problem as an effective scattering problem, treating the nonlinear interaction term as a perturbation. This allowed us to reformulate the mean-field equation into a self-consistent algebraic equation for the mean-field matter wave involving the Green's function for the non-interacting mean-field problem. This non-interacting Green's function was approximated

semiclassically as a sum over contributions of scattering paths, which enter the ring and in there perform multiple oscillations between the junctions to the attached waveguides. In this approximation, both the enclosed gauge field and the disorder potential attributed to the phase accumulated along the scattering path. Here we argued that the contribution of multiple scattering paths survive the disorder average only if the phases accumulated due to disorder exactly cancel each other. This requires pairs of scattering paths to have a matching number of explorations of the upper, respective lower branch of the ring. With this we were able to arrive at the well-known explanation of AAS oscillations in the noninteracting case: the interference of contributions of scattering paths with time-reversed segments – a similar interference mechanism as in the case of weak localization. When including and increasing particle-particle interaction, numerical results obtained by R. Chrétien *et al.* from a mean-field treatment of the system were shown in Fig. 5.4 on page 101. The results displayed an initial flattening of the oscillations with growing interaction strength, and eventually their inversion, since former maxima are converted into minima, and vice versa.

In chapter 6 we presented a diagrammatic approach to explain the observed influence of interaction to AAS oscillations. Our method was based on exact resummations of intermediate segments within scattering paths. In each of the resummations the segments fulfilled common boundary conditions, including fixing the way the segment is entered and left by the scattering path. This allowed us to derive, for a fixed disorder configuration, analytical expressions for the noninteracting Green's function. Moreover, with their help we could tackle the perturbative series in the weak interaction strength. We calculated their predictions up to linear order in the interaction strength, using the numerical Monte-Carlo method to perform the final average over disorder phases. Here, for weak interaction strengths we could qualitatively and quantitatively reproduce the influence of interaction as observed in the numerical results. Moreover, a hint for the involved interference mechanism leading to the inversion of AAS oscillation could be obtained from a diagrammatic expansion of the interaction-based correction to the reflection probability. There we saw that the constellation of scattering paths with the least number of scattering events at the junctions, but still contributing to the disorder-averaged reflection probability, is given by self-averaging diagrams. In those diagrams, the phase accumulated by one of the scattering paths ending at the interaction event cancels all the phases of the other scattering paths involved in the diagram.

Appendices

A.1 Evaluation of matrix elements of the Bose-Hubbard Hamiltonian

The derivation of a path integral representation of the time evolution operator requires us to evaluate the matrix element $\langle \mathbf{p} | \hat{H} | \mathbf{q} \rangle$. To do so, we first re-express the creation and annihilation operators in the Bose-Hubbard Hamiltonian, Eq. (3.48), by the Hermitian quadrature operators, Eq. (3.21). We obtain

$$\begin{aligned} \hat{H} = & \frac{N}{2} \sum_{i,j=1}^d h_{ij} (\hat{q}_i - i\hat{p}_i) (\hat{q}_j + i\hat{p}_j) \\ & + \frac{N}{4} \sum_{i,j,k,l=1}^d V_{ijkl} (\hat{q}_i - i\hat{p}_i) (\hat{q}_j - i\hat{p}_j) (\hat{q}_k + i\hat{p}_k) (\hat{q}_l + i\hat{p}_l) \end{aligned} \quad (\text{A.1})$$

In a second step, we bring the above Hamiltonian into the so-called *normal ordered form* in which the products of quadrature operators are such that the momentum quadrature operators are found left of the position quadrature operators. In that form, the evaluation of the matrix element becomes trivial, as it simply result in a substitution of quadrature operators by the corresponding scalar components of the labels of the quadrature states $|\mathbf{p}\rangle, |\mathbf{q}\rangle$.

In principle we can perform the ordering by first carrying out the products in the representation Eq. (A.1) and then repeatedly applying the commutation relations, Eq. (3.23). However, this is a rather tedious task due to the sheer number of terms to consider, with additional work needed to afterwards simplify the matrix elements again. An alternative approach is thus desirable and indeed found through the application of a variant of Wick's theorem [136].

Let \hat{A} be an operator expressed as the sum of products of quadrature operators \hat{q}_i and \hat{p}_i , $i \in \{1, \dots, d\}$. We denote by $\{\hat{A}\}_{pq}$ the normal ordering in the quadrature operators. For instance

$$\{\hat{q}_l \hat{p}_j \hat{p}_k + \hat{q}_l \hat{p}_m \hat{q}_n \hat{p}_o\}_{pq} = \hat{p}_j \hat{p}_k \hat{q}_l + \hat{p}_m \hat{p}_o \hat{q}_l \hat{q}_n. \quad (\text{A.2})$$

The statement of Wick's theorem involves the application of so-called *contractions*. The contraction of two arbitrary quadrature operators $\hat{X}, \hat{Y} \in \{\hat{q}_i, \hat{p}_i \mid i \in \{1, \dots, d\}\}$, is defined as the difference between the unordered and the ordered product of these operators, and indicated by an above line linking the operators,

$$\overline{\hat{X}\hat{Y}} = \hat{X}\hat{Y} - \{\hat{X}\hat{Y}\}_{pq}. \quad (\text{A.3})$$

Explicitly, we obtain from this definition

$$\overline{\hat{q}_i \hat{p}_j} = [\hat{q}_i, \hat{p}_j] = \frac{i}{N} \delta_{ij}, \quad \overline{\hat{q}_i \hat{q}_j} = \overline{\hat{p}_i \hat{q}_j} = \overline{\hat{p}_i \hat{p}_j} = 0. \quad (\text{A.4})$$

The definition of a contraction can be extended to linear combinations of quadrature operators. For two operators $A_{\alpha_1}, A_{\alpha_2}$ with $A_{\alpha_l} = \sum_{i=1}^d (a_{\alpha_l, i} \hat{q}_i + b_{\alpha_l, i} \hat{p}_i)$, $l = 1, 2$, with complex coefficients $a_{\alpha_l, i}, b_{\alpha_l, i} \in \mathbb{C}$, we calculate

$$\begin{aligned} \overline{A_{\alpha_1} A_{\alpha_2}} &= A_{\alpha_1} A_{\alpha_2} - \{A_{\alpha_1} A_{\alpha_2}\}_{pq} \quad (\text{A.5}) \\ &= \sum_{i,j=1}^d [(a_{\alpha_1, i} a_{\alpha_2, j} \hat{q}_i \hat{q}_j + a_{\alpha_1, i} b_{\alpha_2, j} \hat{q}_i \hat{p}_j + b_{\alpha_1, i} a_{\alpha_2, j} \hat{p}_i \hat{q}_j + b_{\alpha_1, i} b_{\alpha_2, j} \hat{p}_i \hat{p}_j) \\ &\quad - (a_{\alpha_1, i} a_{\alpha_2, j} \hat{q}_i \hat{q}_j + a_{\alpha_1, i} b_{\alpha_2, j} \hat{p}_j \hat{q}_i + b_{\alpha_1, i} a_{\alpha_2, j} \hat{p}_i \hat{q}_j + b_{\alpha_1, i} b_{\alpha_2, j} \hat{p}_i \hat{p}_j)] \\ &= \sum_{i,j=1}^d a_{\alpha_1, i} b_{\alpha_2, j} \underbrace{[\hat{q}_i, \hat{p}_j]}_{=\frac{i}{N} \delta_{ij}} = \frac{i}{N} \sum_{i=1}^d a_{\alpha_1, i} b_{\alpha_2, i} \quad (\text{A.6}) \end{aligned}$$

It is important to note that the above contractions produce a scalar value, since in the proof of Wick's theorem, this is the essential prerequisite for its applicability.

We are now able to formulate the statement of Wick's theorem: given a set of operators $\{\hat{A}_\alpha, \hat{A}_\beta, \hat{A}_\gamma\}$, each of them a linear combination of quadrature operators, $\hat{A}_\alpha = \sum_{i=1}^d (a_{\alpha, i} \hat{q}_i + b_{\alpha, i} \hat{p}_i)$, the product of these operators can be rewritten as the following sum of normal ordered terms,

$$\begin{aligned} \hat{A}_{\alpha_1} \hat{A}_{\alpha_2} \dots \hat{A}_{\alpha_r} &= \left\{ \hat{A}_{\alpha_1} \hat{A}_{\alpha_2} \dots \hat{A}_{\alpha_r} \right\}_{pq} \\ &\quad + \underbrace{\left\{ \overline{\hat{A}_{\alpha_1} \hat{A}_{\alpha_2} \dots \hat{A}_{\alpha_r}} \right\}_{pq} + \left\{ \overline{\hat{A}_{\alpha_1} \hat{A}_{\alpha_2} \hat{A}_{\alpha_3} \dots \hat{A}_{\alpha_r}} \right\}_{pq} + \dots}_{\text{single contractions}} \\ &\quad + \underbrace{\left\{ \overline{\hat{A}_{\alpha_1} \hat{A}_{\alpha_2} \hat{A}_{\alpha_3} \hat{A}_{\alpha_4} \dots \hat{A}_{\alpha_r}} \right\}_{pq} + \left\{ \overline{\hat{A}_{\alpha_1} \hat{A}_{\alpha_2} \hat{A}_{\alpha_3} \hat{A}_{\alpha_4} \dots \hat{A}_{\alpha_r}} \right\}_{pq} + \dots}_{\text{double contractions}} \\ &\quad + \dots \quad (\text{A.7}) \end{aligned}$$

where we used, since the contractions are scalars, the common simplifying notation in which the operators involved in a contraction are still placed at their original position within the product of other operators. For instance, we interpret¹

$$\hat{A}_{\alpha_1} \hat{A}_{\alpha_2} \overline{\hat{A}_{\alpha_3} \hat{A}_{\alpha_4}} \hat{A}_{\alpha_5} \hat{A}_{\alpha_6} \equiv \overline{\hat{A}_{\alpha_2} \hat{A}_{\alpha_4}} \cdot \overline{\hat{A}_{\alpha_3} \hat{A}_{\alpha_5}} \cdot \hat{A}_{\alpha_1} \hat{A}_{\alpha_6} \quad (\text{A.8})$$

¹The calculation here assumes bosonic operators. In case of fermions, which are not considered here, commuting operators would additionally produce sign changes in the result.

The proof of the theorem is done by induction and is found in the original work of Wick [136] and also in various books covering quantum field theory, *e.g.* Ref. [137]. While these proofs aim at normal ordering of an operator product obtained through time-ordering, it is interesting to note, that an alternative proof exists [138] which indicates a generalization of Wick's theorem allowing its application also to find representations in other ordered products, such as symmetric ordering.

To apply the theorem to the Bose-Hubbard Hamiltonian, we need to calculate the contraction of quadrature operators first. We find

$$\overline{\hat{b}_i \hat{b}_j} = i \frac{N}{2} [\hat{q}_i, \hat{p}_j] = -\frac{\delta_{ij}}{2}, \quad (\text{A.9})$$

$$\overline{\hat{b}_i^\dagger \hat{b}_j} = i \frac{N}{2} [\hat{q}_i, \hat{p}_j] = -\frac{\delta_{ij}}{2}, \quad (\text{A.10})$$

$$\overline{\hat{b}_i \hat{b}_j^\dagger} = -i \frac{N}{2} [\hat{q}_i, \hat{p}_j] = \frac{\delta_{ij}}{2}, \quad (\text{A.11})$$

$$\overline{\hat{b}_i^\dagger \hat{b}_j^\dagger} = -i \frac{N}{2} [\hat{q}_i, \hat{p}_j] = \frac{\delta_{ij}}{2}. \quad (\text{A.12})$$

Finally applying the theorem for the Bose-Hubbard Hamiltonian we obtain

$$\begin{aligned} \hat{H} &= \sum_{i,j=1}^d h_{ij} \left(\left\{ \hat{b}_i^\dagger \hat{b}_j \right\}_{pq} + \left\{ \overline{\hat{b}_i^\dagger \hat{b}_j} \right\}_{pq} \right) \\ &+ \sum_{i,j,k,l=1}^d \frac{V_{ijkl}}{N} \left(\left\{ \hat{b}_i^\dagger \hat{b}_j^\dagger \hat{b}_k \hat{b}_l \right\}_{pq} + \left\{ \overline{\hat{b}_i^\dagger \hat{b}_j^\dagger \hat{b}_k \hat{b}_l} \right\}_{pq} + \left\{ \overline{\hat{b}_i^\dagger \hat{b}_j^\dagger \hat{b}_k} \hat{b}_l \right\}_{pq} + \left\{ \overline{\hat{b}_i^\dagger \hat{b}_j^\dagger \hat{b}_k \hat{b}_l} \right\}_{pq} \right. \\ &\quad + \left\{ \hat{b}_i^\dagger \hat{b}_j^\dagger \overline{\hat{b}_k \hat{b}_l} \right\}_{pq} + \left\{ \hat{b}_i^\dagger \hat{b}_j^\dagger \overline{\hat{b}_k} \hat{b}_l \right\}_{pq} + \left\{ \hat{b}_i^\dagger \hat{b}_j^\dagger \overline{\hat{b}_k \hat{b}_l} \right\}_{pq} \\ &\quad \left. + \left\{ \overline{\hat{b}_i^\dagger \hat{b}_j^\dagger} \overline{\hat{b}_k \hat{b}_l} \right\}_{pq} + \left\{ \overline{\hat{b}_i^\dagger \hat{b}_j^\dagger} \overline{\hat{b}_k} \hat{b}_l \right\}_{pq} + \left\{ \overline{\hat{b}_i^\dagger \hat{b}_j^\dagger} \overline{\hat{b}_k \hat{b}_l} \right\}_{pq} \right) \\ &= \sum_{i,j=1}^d h_{ij} \left(\left\{ \hat{b}_i^\dagger \hat{b}_j \right\}_{pq} - \frac{1}{2} \delta_{ij} \right) \\ &+ \sum_{i,j,k,l=1}^d \frac{V_{ijkl}}{N} \left(\left\{ \hat{b}_i^\dagger \hat{b}_j^\dagger \hat{b}_k \hat{b}_l \right\}_{pq} + \frac{\delta_{ij}}{2} \left\{ \hat{b}_k \hat{b}_l \right\}_{pq} - \frac{\delta_{ik}}{2} \left\{ \hat{b}_j^\dagger \hat{b}_l \right\}_{pq} - \frac{\delta_{il}}{2} \left\{ \hat{b}_j^\dagger \hat{b}_k \right\}_{pq} \right. \\ &\quad - \frac{\delta_{jk}}{2} \left\{ \hat{b}_i^\dagger \hat{b}_l \right\}_{pq} - \frac{\delta_{jl}}{2} \left\{ \hat{b}_i^\dagger \hat{b}_k \right\}_{pq} - \frac{\delta_{kl}}{2} \left\{ \hat{b}_i^\dagger \hat{b}_j \right\}_{pq} \\ &\quad \left. - \frac{\delta_{ij} \delta_{kl}}{4} + \frac{\delta_{ik} \delta_{jl}}{4} + \frac{\delta_{il} \delta_{jk}}{4} \right) \end{aligned} \quad (\text{A.13})$$

The normal ordered form of the Bose-Hubbard Hamiltonian leads to a trivial evaluation

of the matrix elements $\langle \mathbf{p} | \hat{H} | \mathbf{q} \rangle$, effectively substituting operators by scalars,

$$\begin{aligned} \langle \mathbf{p} | \left\{ \dots \hat{b}_i^\dagger \dots \hat{b}_j \dots \right\}_{pq} | \mathbf{q} \rangle &= \left(\dots \sqrt{\frac{N}{2}} (q_i - ip_i) \dots \sqrt{\frac{N}{2}} (q_i + ip_i) \dots \right) \langle \mathbf{p} | \mathbf{q} \rangle \\ &= \left(\dots \sqrt{N} \Phi_i^* \dots \sqrt{N} \Phi_i \dots \right) \langle \mathbf{p} | \mathbf{q} \rangle \end{aligned} \quad (\text{A.14})$$

where we combined the position and the momentum quadrature into a complex variable,

$$\Phi = \frac{1}{\sqrt{2}} (\mathbf{q} + i\mathbf{p}). \quad (\text{A.15})$$

With this notation, we obtain

$$\begin{aligned} \frac{\langle \mathbf{p} | \hat{H} | \mathbf{q} \rangle}{\langle \mathbf{p} | \mathbf{q} \rangle} &= \sum_{i,j=1}^d h_{ij} \left(N \Phi_i^* \Phi_j - \frac{\delta_{ij}}{2} \right) \\ &+ \sum_{i,j,k,l=1}^d \frac{V_{ijkl}}{N} \left(N^2 \Phi_i^* \Phi_j^* \Phi_k \Phi_l + \frac{\delta_{ij}}{2} N \Phi_k \Phi_l - \frac{\delta_{ik}}{2} N \Phi_j^* \Phi_l - \frac{\delta_{il}}{2} N \Phi_j^* \Phi_k \right. \\ &\quad \left. - \frac{\delta_{jk}}{2} N \Phi_i^* \Phi_l - \frac{\delta_{jl}}{2} N \Phi_i^* \Phi_k - \frac{\delta_{kl}}{2} N \Phi_i^* \Phi_j \right. \\ &\quad \left. - \frac{\delta_{ij} \delta_{kl}}{4} + \frac{\delta_{ik} \delta_{jl}}{4} + \frac{\delta_{il} \delta_{jk}}{4} \right) \\ &= \frac{\hbar}{\hbar_{\text{eff}}} \left[\mathcal{H}(\mathbf{q}, \mathbf{p}) + \hbar_{\text{eff}} \mathcal{H}^{(\text{ord})}(\mathbf{q}, \mathbf{p}) \right] \end{aligned} \quad (\text{A.16})$$

where in the last line we used the effective Planck constant $\hbar_{\text{eff}} = 1/N$ and ordered the result in powers of \hbar_{eff} . In this expansion, \mathcal{H} is a function independent on \hbar_{eff} which admits real values, since $h_{ij} = h_{ji}^*$ and $V_{ijkl} = V_{lkji}^*$ due to Hermiticity of \hat{H} . We later identify \mathcal{H} as the Hamilton function of the classical limit of the Bose-Hubbard Hamiltonian in quadrature state representation. The remaining terms are higher powers in \hbar_{eff} originating from our choice of ordering operators \hat{q}_i, \hat{p}_i . Those terms are collected in the complex-valued function $\mathcal{H}^{(\text{ord})}$. By denoting the real and imaginary part of $\mathcal{H}^{(\text{ord})}$ by $\mathcal{H}_{\text{R}}^{(\text{ord})}$ and $\mathcal{H}_{\text{I}}^{(\text{ord})}$, and using the additional assumption $V_{ijkl} = V_{jikl} = V_{ijlk} = V_{jilk}$, we find

$$\mathcal{H}(\mathbf{q}, \mathbf{p}) = \sum_{i,j=1}^d \frac{h_{ij}}{\hbar} \Phi_i^* \Phi_j + \sum_{i,j,k,l=1}^d \frac{V_{ijkl}}{\hbar} \Phi_i^* \Phi_j^* \Phi_k \Phi_l, \quad (\text{A.17})$$

$$\mathcal{H}_{\text{R}}^{(\text{ord})}(\mathbf{q}, \mathbf{p}) = \sum_{i=1}^d \frac{\hbar_{ii}}{2\hbar} + \sum_{i,j,k=1}^d \frac{2V_{ijk i}}{\hbar} \Phi_j^* \Phi_k + \hbar_{\text{eff}} \sum_{i,l=1}^d \left(\frac{V_{illi}}{2\hbar} - \frac{V_{iill}}{4\hbar} \right), \quad (\text{A.18})$$

$$\mathcal{H}_{\text{I}}^{(\text{ord})}(\mathbf{q}, \mathbf{p}) = \frac{1}{2i} \sum_{i,j,k,l=1}^d V_{ijkl} (\delta_{ij} \Phi_k \Phi_l - \delta_{kl} \Phi_i^* \Phi_j^*). \quad (\text{A.19})$$

A.2 Stationary phase approximation applied to the Feynman path integral

In this appendix we want to present the calculation of the semiclassical approximation for the propagator for Bose-Hubbard models. We do this by considering $\lambda = 1/\hbar_{\text{eff}}$ as a large parameter and applying the stationary phase approximation, presented in section 3.3.3, to evaluate the multidimensional integration in the Feynman path integral, Eq. (3.65). The subsequent calculations follow, but are not identical to the original ones for Bose-Hubbard models found in Ref. [33].

For fixed M , the object to evaluate is thus

$$K^{(M)}(\mathbf{q}^{(f)}, \mathbf{q}^{(i)}, t) = \frac{1}{\sqrt{2\pi\hbar_{\text{eff}}^{2dM}}} \int d^d p^{(M)} \int d^d q^{(M-1)} \int d^d p^{(M-1)} \dots \int d^d q^{(1)} \int d^d p^{(1)} \times \exp \left[\frac{i}{\hbar_{\text{eff}}} R^{(M)}(\mathbf{q}, \mathbf{p}, t) - i\varphi^{(M)}(\mathbf{q}, \mathbf{p}, t) \right], \quad (\text{A.20})$$

where we combined the integration variables and the arguments of the propagator into the vectors $\mathbf{q} = (\mathbf{q}^{(0)} = \mathbf{q}^{(i)}, \mathbf{q}^{(1)}, \dots, \mathbf{q}^{(M-1)}, \mathbf{q}^{(M)} = \mathbf{q}^{(f)})$ and $\mathbf{p} = (\mathbf{p}^{(1)}, \dots, \mathbf{p}^{(M)})$. The argument of the phase factor in the integrand, which is multiplied by the large parameter $1/\hbar_{\text{eff}}$, is the *action* and given by

$$R^{(M)}(\mathbf{q}, \mathbf{p}, t) = \sum_{m=1}^M \left[\mathbf{p}^{(m)} \cdot (\mathbf{q}^{(m)} - \mathbf{q}^{(m-1)}) - \frac{\mathcal{H}(\mathbf{q}^{(m)}, \mathbf{p}^{(m)}) + \mathcal{H}(\mathbf{q}^{(m-1)}, \mathbf{p}^{(m)})}{2} \frac{t}{M} \right]. \quad (\text{A.21})$$

The phase of the other oscillatory term in the integrand Eq. (A.20) is given by

$$\varphi^{(M)}(\mathbf{q}, \mathbf{p}, t) = \sum_{m=1}^M \frac{\mathcal{H}_{\text{R}}^{(\text{ord})}(\mathbf{q}^{(m)}, \mathbf{p}^{(m)}) + \mathcal{H}_{\text{R}}^{(\text{ord})}(\mathbf{q}^{(m-1)}, \mathbf{p}^{(m)})}{2} \frac{t}{M}. \quad (\text{A.22})$$

This phase is not multiplied by $1/\hbar_{\text{eff}}$ and thus considered to be part of the smooth function (g in Eq. (3.74)). The result of the stationary phase approximation has to be evaluated in the limit $M \rightarrow \infty$ to arrive at the semiclassical approximation for the propagator.

We differentiate the action, Eq. (A.21), with respect to $p_i^{(m)}$, $m \in \{1, \dots, M\}$, and $q_i^{(m)}$, $m \in \{1, \dots, M-1\}$, for $i \in \{1, \dots, d\}$, and set those derivatives to zero to obtain the stationarity conditions,

$$0 = \frac{\partial R^{(M)}}{\partial p_i^{(m)}}(\mathbf{q}, \mathbf{p}, t) = q_i^{(m)} - q_i^{(m-1)} - \left(\frac{\partial \mathcal{H}}{\partial p_i^{(m)}}(\mathbf{q}^{(m)}, \mathbf{p}^{(m)}) + \frac{\partial \mathcal{H}}{\partial p_i^{(m)}}(\mathbf{q}^{(m-1)}, \mathbf{p}^{(m)}) \right) \frac{t}{2M}, \quad (\text{A.23})$$

$$\begin{aligned}
0 &= \frac{\partial R^{(M)}}{\partial q_i^{(m)}}(\mathbf{q}, \mathbf{p}, t) \\
&= p_i^{(m)} - p_i^{(m+1)} - \left(\frac{\partial \mathcal{H}}{\partial q_i^{(m)}}(\mathbf{q}^{(m)}, \mathbf{p}^{(m)}) + \frac{\partial \mathcal{H}}{\partial q_i^{(m)}}(\mathbf{q}^{(m)}, \mathbf{p}^{(m+1)}) \right) \frac{t}{2M}.
\end{aligned} \tag{A.24}$$

Note that after division of t/M the above equations turn in the limit $M \rightarrow \infty$ into the Hamilton's equations of motion presented in Eq. (3.82). Furthermore, this problem is subject to boundary conditions, $\mathbf{q}^{(M)} = \mathbf{q}^{(f)}$, $\mathbf{q}^{(0)} = \mathbf{q}^{(i)}$, which in the limiting case become $\mathbf{q}(t) = \mathbf{q}^{(f)}$ and $\mathbf{q}(0) = \mathbf{q}^{(i)}$. Contrary to an initial value problem, we thus expect to find multiple solutions to Eqs. (A.23), (A.24) subject to the above boundary conditions.

Let us denote a solution of the stationarity conditions Eqs. (A.23), (A.24) by $\mathbf{q}_\gamma = (\mathbf{q}_\gamma^{(0)}, \dots, \mathbf{q}_\gamma^{(M)})$, $\mathbf{p}_\gamma = (\mathbf{p}_\gamma^{(1)}, \dots, \mathbf{p}_\gamma^{(M)})$, and distinguish different solutions by Greek subscripts. Similar to before, we include the boundary conditions into the solution vector by setting $\mathbf{q}_\gamma^{(0)} = \mathbf{q}^{(i)}$ and $\mathbf{q}_\gamma^{(M)} = \mathbf{q}^{(f)}$.

In principle, we could now directly apply Eq. (3.80) to obtain the stationary phase approximation for $K^{(M)}(\mathbf{q}^{(f)}, \mathbf{q}^{(i)}, t)$. However, for taking the limit $M \rightarrow \infty$ we would need to evaluate the determinant through a Laplace expansion. Already for $d = 1$, this is a rather tedious task, see for instance Ref. [100] where this is done to derive a semiclassical approximation for the propagator in coherent state representation. An alternative route to the result is found by evaluating the multidimensional integration step by step rather than at once.

Following the method description for the stationary phase approximation we express the action through its second order Taylor expansion around the stationary points. This leads to the following integration over the fluctuations around the stationary solutions,

$$\begin{aligned}
K^{(M)}(\mathbf{q}^{(f)}, \mathbf{q}^{(i)}, t) &= \frac{1}{\sqrt{2\pi\hbar_{\text{eff}}^{2dM}}} \sum_{\gamma} \exp\left(\frac{i}{\hbar_{\text{eff}}} R^{(M)}(\mathbf{q}_\gamma, \mathbf{p}_\gamma, t) - i\varphi^{(M)}(\mathbf{q}_\gamma, \mathbf{p}_\gamma, t)\right) \\
&\times \int d^d \delta p^{(M)} \int d^d \delta q^{(M-1)} \int d^d \delta p^{(M-1)} \dots \int d^d \delta q^{(1)} \int d^d \delta p^{(1)} \\
&\times \exp\left[\frac{i}{2\hbar_{\text{eff}}} \sum_{m=1}^{M-1} \begin{pmatrix} \delta \mathbf{p}^{(m)} \\ \delta \mathbf{q}^{(m)} \end{pmatrix}^\top \begin{pmatrix} \mathbf{R}_{\gamma, \mathbf{p}^{(m)} \mathbf{p}^{(m)}} & \mathbf{R}_{\gamma, \mathbf{p}^{(m)} \mathbf{q}^{(m)}} \\ \mathbf{R}_{\gamma, \mathbf{q}^{(m)} \mathbf{p}^{(m)}} & \mathbf{R}_{\gamma, \mathbf{q}^{(m)} \mathbf{q}^{(m)}} \end{pmatrix} \begin{pmatrix} \delta \mathbf{p}^{(m)} \\ \delta \mathbf{q}^{(m)} \end{pmatrix}\right] \\
&\times \exp\left[\frac{i}{\hbar_{\text{eff}}} \sum_{m=1}^{M-1} \delta \mathbf{p}^{(m+1)\top} \mathbf{R}_{\gamma, \mathbf{p}^{(m+1)} \mathbf{q}^{(m)}} \delta \mathbf{q}^{(m)}\right] \\
&\times \exp\left[\frac{i}{2\hbar_{\text{eff}}} \delta \mathbf{p}^{(M)\top} \mathbf{R}_{\gamma, \mathbf{p}^{(M)} \mathbf{p}^{(M)}} \delta \mathbf{p}^{(M)}\right],
\end{aligned} \tag{A.25}$$

where we used an abbreviating notation for the second order derivatives of the action,

$$\mathbf{R}_{\gamma, \mathbf{v}^{(m)} \mathbf{w}^{(m')}} = \frac{\partial^2 R^{(M)}}{\partial \mathbf{v}^{(m)} \partial \mathbf{w}^{(m')}}(\mathbf{q}_\gamma, \mathbf{p}_\gamma, t), \quad \mathbf{v}, \mathbf{w} \in \{\mathbf{p}, \mathbf{q}\}. \tag{A.26}$$

These matrices have dimension $d \times d$ and contain second derivatives of the Hamilton function \mathcal{H} , which we abbreviate by

$$\mathcal{H}_{\gamma, \mathbf{vw}}^{(m, m')} = \frac{\partial^2 \mathcal{H}}{\partial \mathbf{v} \partial \mathbf{w}} \left(\mathbf{q}_\gamma^{(m)}, \mathbf{p}_\gamma^{(m')} \right), \quad \mathbf{v}, \mathbf{w} \in \{\mathbf{p}, \mathbf{q}\}. \quad (\text{A.27})$$

In Eq. (A.25) we only wrote the non-vanishing submatrices of the second derivatives of the action. In our abbreviated notation, those are given by

$$\mathbf{R}_{\gamma, \mathbf{p}^{(m)} \mathbf{p}^{(m)}} = -\frac{\mathcal{H}_{\gamma, \mathbf{pp}}^{(m, m)} + \mathcal{H}_{\gamma, \mathbf{pp}}^{(m-1, m)}}{2} \frac{t}{M}, \quad (\text{A.28})$$

$$\mathbf{R}_{\gamma, \mathbf{p}^{(m)} \mathbf{q}^{(m)}} = \mathbf{1} - \frac{\mathcal{H}_{\gamma, \mathbf{pq}}^{(m, m)}}{2} \frac{t}{M} = \left(\mathbf{1} - \frac{\mathcal{H}_{\gamma, \mathbf{qp}}^{(m, m)}}{2} \frac{t}{M} \right)^\top = \mathbf{R}_{\gamma, \mathbf{q}^{(m)} \mathbf{p}^{(m)}}^\top, \quad (\text{A.29})$$

$$\mathbf{R}_{\gamma, \mathbf{q}^{(m)} \mathbf{q}^{(m)}} = -\frac{\mathcal{H}_{\gamma, \mathbf{qq}}^{(m, m)} + \mathcal{H}_{\gamma, \mathbf{qq}}^{(m, m+1)}}{2} \frac{t}{M}, \quad (\text{A.30})$$

$$\begin{aligned} \mathbf{R}_{\gamma, \mathbf{p}^{(m+1)} \mathbf{q}^{(m)}} &= -\mathbf{1} - \frac{\mathcal{H}_{\gamma, \mathbf{pq}}^{(m, m+1)}}{2} \frac{t}{M} \\ &= \left(-\mathbf{1} - \frac{\mathcal{H}_{\gamma, \mathbf{qp}}^{(m, m+1)}}{2} \frac{t}{M} \right)^\top = \mathbf{R}_{\gamma, \mathbf{q}^{(m)} \mathbf{p}^{(m+1)}}^\top. \end{aligned} \quad (\text{A.31})$$

To obtain an analytic expression for Eq. (A.25) we use the following result for multi-dimensional Gaussian integrals with a quadratic and a linear term in the phase factor [113]: Let B be a real symmetric, invertible matrix, c a real vector and α a positive real number. Then

$$\int d^d x \exp \left[\frac{i}{2\alpha} (\mathbf{x}^\top B \mathbf{x} + 2\mathbf{c}^\top \mathbf{x}) \right] = \sqrt{\frac{(2\pi\alpha)^d}{|\det(B)|}} \exp \left(i \frac{\pi}{4} \beta(B) - \frac{i}{2\alpha} \mathbf{c}^\top B^{-1} \mathbf{c} \right), \quad (\text{A.32})$$

where $\beta(B)$ is the difference in the number of positive and negative eigenvalues of the matrix B . Note that the result on the r.h.s. has an exponent quadratic in the vector c . Since in the iterated integrations in Eq. (A.25) the vector \mathbf{c} contains fluctuation vectors of a subsequent integration, this will lead to modifications of the quadratic forms involved in the Gaussian integrals.

To illustrate, starting from $m = 1$, we perform a d -dimensional integrations over $\delta \mathbf{p}^{(m)}$ and then $\delta \mathbf{q}^{(m)}$ using Eq. (A.32). Setting $\mathbf{X}^{(1)} = \mathbf{R}_{\gamma, \mathbf{p}^{(1)} \mathbf{p}^{(1)}}$ we find

$$\begin{aligned} & \int d^d \delta \mathbf{q}^{(m)} \int d^d \delta \mathbf{p}^{(m)} \exp \left[\frac{i}{2\hbar_{\text{eff}}} \delta \mathbf{q}^{(m)\top} \mathbf{R}_{\gamma, \mathbf{q}^{(m)} \mathbf{q}^{(m)}} \delta \mathbf{q}^{(m)} + \frac{i}{\hbar_{\text{eff}}} \delta \mathbf{p}^{(m+1)\top} \mathbf{R}_{\gamma, \mathbf{p}^{(m+1)} \mathbf{q}^{(m)}} \delta \mathbf{q}^{(m)} \right] \\ & \quad \times \exp \left[\frac{i}{2\hbar_{\text{eff}}} \delta \mathbf{p}^{(m)\top} \mathbf{X}^{(m)} \delta \mathbf{p}^{(m)} + \frac{i}{\hbar_{\text{eff}}} \delta \mathbf{q}^{(m)\top} \mathbf{R}_{\gamma, \mathbf{q}^{(m)} \mathbf{p}^{(m)}} \delta \mathbf{p}^{(m)} \right] \\ &= \frac{(2\pi\hbar_{\text{eff}})^d}{\sqrt{|\det(\mathbf{X}^{(m)}) \det(\mathbf{Y}^{(m)})|}} \exp \left[i \frac{\pi}{4} \left(\beta(\mathbf{X}^{(m)}) + \beta(\mathbf{Y}^{(m)}) \right) \right] \\ & \quad \times \exp \left[-\frac{i}{2\hbar_{\text{eff}}} \delta \mathbf{p}^{(m+1)\top} \left(\mathbf{R}_{\gamma, \mathbf{p}^{(m+1)} \mathbf{q}^{(m)}} \mathbf{Y}^{(m)-1} \mathbf{R}_{\gamma, \mathbf{q}^{(m)} \mathbf{p}^{(m+1)}} \right) \delta \mathbf{p}^{(m+1)} \right] \end{aligned} \quad (\text{A.33})$$

where $\mathbf{Y}^{(m)}$ denotes the effective quadratic matrix for the integration over $\delta\mathbf{q}^{(m)}$. It is given by

$$\begin{aligned} \mathbf{Y}^{(m)} &= \mathbf{R}_{\gamma, \mathbf{q}^{(m)} \mathbf{q}^{(m)}} - \mathbf{R}_{\gamma, \mathbf{q}^{(m)} \mathbf{p}^{(m)}} \mathbf{X}^{(m)-1} \mathbf{R}_{\gamma, \mathbf{p}^{(m)} \mathbf{q}^{(m)}} \\ &= -\frac{\mathcal{H}_{\gamma, \mathbf{q}\mathbf{q}}^{(m,m)} + \mathcal{H}_{\gamma, \mathbf{q}\mathbf{q}}^{(m,m+1)}}{2} \frac{t}{M} - \left(\mathbf{1} - \frac{\mathcal{H}_{\gamma, \mathbf{q}\mathbf{p}}^{(m,m)}}{2} \frac{t}{M} \right) \mathbf{X}^{(m)-1} \left(\mathbf{1} - \frac{\mathcal{H}_{\gamma, \mathbf{p}\mathbf{q}}^{(m,m)}}{2} \frac{t}{M} \right). \end{aligned} \quad (\text{A.34})$$

From the result in Eq. (A.33) we not only obtain prefactors, but can also see, that the matrix $\mathbf{X}^{(m+1)}$ in the following integration is modified according to

$$\begin{aligned} \mathbf{X}^{(m+1)} &= \mathbf{R}_{\gamma, \mathbf{p}^{(m+1)} \mathbf{p}^{(m+1)}} - \mathbf{R}_{\gamma, \mathbf{p}^{(m+1)} \mathbf{q}^{(m)}} \mathbf{Y}^{(m)-1} \mathbf{R}_{\gamma, \mathbf{q}^{(m)} \mathbf{p}^{(m+1)}} \\ &= -\frac{\mathcal{H}_{\gamma, \mathbf{p}\mathbf{p}}^{(m+1,m+1)} + \mathcal{H}_{\gamma, \mathbf{p}\mathbf{p}}^{(m,m+1)}}{2} \frac{t}{M} \\ &\quad - \left(-\mathbf{1} - \frac{\mathcal{H}_{\gamma, \mathbf{p}\mathbf{q}}^{(m,m+1)}}{2} \frac{t}{M} \right) \mathbf{Y}^{(m)-1} \left(-\mathbf{1} - \frac{\mathcal{H}_{\gamma, \mathbf{q}\mathbf{p}}^{(m,m+1)}}{2} \frac{t}{M} \right). \end{aligned} \quad (\text{A.35})$$

Including the final integration over $\delta\mathbf{p}^{(m)}$, we obtain for the propagator

$$\begin{aligned} K^{(M)}(\mathbf{q}^{(f)}, \mathbf{p}^{(i)}, t) &= \sum_{\gamma} \exp\left(\frac{i}{\hbar_{\text{eff}}} R^{(M)}(\mathbf{q}_{\gamma}, \mathbf{p}_{\gamma}, t) - i\varphi^{(M)}(\mathbf{q}_{\gamma}, \mathbf{p}_{\gamma}, t)\right) \\ &\quad \times \frac{\exp\left[i\frac{\pi}{4} \left[\beta(\mathbf{X}^{(M)}) + \sum_{m=1}^{M-1} (\beta(\mathbf{Y}^{(m)}) + \beta(\mathbf{X}^{(m)})) \right]\right]}{\sqrt{(2\pi\hbar_{\text{eff}})^d \left| \det(\mathbf{X}^{(M)}) \prod_{m=1}^{M-1} \det(\mathbf{Y}^{(m)}) \det(\mathbf{X}^{(m)}) \right|}}. \end{aligned} \quad (\text{A.36})$$

Taking the limit $M \rightarrow \infty$ requires further work, as we have to find analytical expressions for the involved matrices $\mathbf{X}^{(m)}$, $\mathbf{Y}^{(m)}$.

For large M , we can express the involved quantities through their Taylor expansion in the small parameter $1/M$. Note that according to the stationarity conditions, Eqs. (A.23), (A.24), we have $(\mathbf{q}_{\gamma}^{(m+1)}, \mathbf{p}_{\gamma}^{(m+1)}) = (\mathbf{q}_{\gamma}^{(m)}, \mathbf{p}_{\gamma}^{(m)}) + \mathcal{O}(M^{-1})$, reflecting the interpretation of the solutions as discretizations of continuous paths. Inserted into the second derivatives of the Hamilton function, we thus find, for instance, $\mathcal{H}_{\gamma, \mathbf{q}\mathbf{q}}^{(m,m+1)} = \mathcal{H}_{\gamma, \mathbf{q}\mathbf{q}}^{(m,m)} + \mathcal{O}(M^{-1})$. Within the second derivatives of the action, Eqs. (A.28) to (A.31), the second derivatives of the Hamilton function come along with M^{-1} . Thus, for a Taylor expansion of the coupled recursive matrix equations, Eqs. (A.34), (A.35), up to linear order in $1/M$, we can simplify the result by evaluating the second derivatives of the Hamilton functions at the phase space point $(\mathbf{q}^{(m)}, \mathbf{p}^{(m)})$ associated with the current $t^{(m)} = mt/M$. We find for $\mathbf{Y}^{(m)}$

$$\begin{aligned} \mathbf{Y}^{(m)} &= -\mathbf{X}^{(m)-1} \\ &\quad + \left(-\mathcal{H}_{\gamma, \mathbf{q}\mathbf{q}}^{(m,m)} + \frac{\mathcal{H}_{\gamma, \mathbf{q}\mathbf{p}}^{(m,m)}}{2} \mathbf{X}^{(m)-1} + \mathbf{X}^{(m)-1} \frac{\mathcal{H}_{\gamma, \mathbf{p}\mathbf{q}}^{(m,m)}}{2} \right) \frac{t}{M} + \mathcal{O}\left(\frac{1}{M^2}\right), \end{aligned} \quad (\text{A.37})$$

and for $\mathbf{X}^{(m)}$

$$\begin{aligned} \mathbf{X}^{(m+1)} &= -\mathbf{Y}^{(m)-1} \\ &\quad - \left(\mathcal{H}_{\gamma, \mathbf{p}\mathbf{p}}^{(m,m)} + \frac{\mathcal{H}_{\gamma, \mathbf{p}\mathbf{q}}^{(m,m)}}{2} \mathbf{Y}^{(m)-1} + \mathbf{Y}^{(m)-1} \frac{\mathcal{H}_{\gamma, \mathbf{q}\mathbf{p}}^{(m,m)}}{2} \right) \frac{t}{M} + \mathcal{O}\left(\frac{1}{M^2}\right), \end{aligned} \quad (\text{A.38})$$

To proceed, we use the geometric series for matrices $(\mathbf{1} - \varepsilon A)^{-1} = \mathbf{1} + \varepsilon A + \mathcal{O}(\varepsilon^2)$ for a matrix A and $\varepsilon > 0$ small enough, we can find a relation for the inverse of $\mathbf{Y}^{(m)}$,

$$\begin{aligned} \mathbf{Y}^{(m)-1} &= -\mathbf{X}^{(m)} \\ &\quad - \left(-\mathbf{X}^{(m)} \mathcal{H}_{\gamma, \mathbf{q}\mathbf{q}}^{(m,m)} \mathbf{X}^{(m)} + \mathbf{X}^{(m)} \frac{\mathcal{H}_{\gamma, \mathbf{q}\mathbf{p}}^{(m,m)}}{2} + \frac{\mathcal{H}_{\gamma, \mathbf{p}\mathbf{q}}^{(m,m)}}{2} \mathbf{X}^{(m)} \right) \frac{t}{M} + \mathcal{O}\left(\frac{1}{M^2}\right). \end{aligned} \quad (\text{A.39})$$

Inserting the latter into Eq. (A.38) we obtain a recursive relation for $\mathbf{X}^{(m)}$,

$$\begin{aligned} \mathbf{X}^{(m+1)} &= \mathbf{X}^{(m)} - \left(\mathcal{H}_{\gamma, \mathbf{p}\mathbf{p}}^{(m,m)} + \mathbf{X}^{(m)} \mathcal{H}_{\gamma, \mathbf{q}\mathbf{q}}^{(m,m)} \mathbf{X}^{(m)} \right) \frac{t}{M} \\ &\quad + \left(\mathbf{X}^{(m)} \mathcal{H}_{\gamma, \mathbf{q}\mathbf{p}}^{(m,m)} + \mathcal{H}_{\gamma, \mathbf{p}\mathbf{q}}^{(m,m)} \mathbf{X}^{(m)} \right) \frac{t}{M} + \mathcal{O}\left(\frac{1}{M^2}\right). \end{aligned} \quad (\text{A.40})$$

By subtracting $\mathbf{X}^{(m)}$ from both sides and then dividing by t/M we recover on the l.h.s. a difference quotient. In the limit $M \rightarrow \infty$ this results in an ordinary differential equation for the matrix $X(s)$,

$$\dot{X}(s) = -\mathcal{H}_{\gamma, \mathbf{p}\mathbf{p}}(s) - X(s) \mathcal{H}_{\gamma, \mathbf{q}\mathbf{q}}(s) X(s) + X(s) \mathcal{H}_{\gamma, \mathbf{q}\mathbf{p}}(s) + \mathcal{H}_{\gamma, \mathbf{p}\mathbf{q}}(s) X(s), \quad (\text{A.41})$$

subject to the initial condition $\mathbf{X}(0) = \mathbf{0}$ ($= \lim_{M \rightarrow \infty} \mathbf{X}^{(1)}$), and the second derivatives of the Hamilton function now evaluated at the phase space point of the (now continuous) trajectory γ ,

$$\mathcal{H}_{\gamma, \mathbf{v}\mathbf{w}}(s) = \frac{\partial^2 \mathcal{H}}{\partial \mathbf{v} \partial \mathbf{w}}(\mathbf{q}_\gamma(s), \mathbf{p}_\gamma(s)), \quad \mathbf{v}, \mathbf{w} \in \{\mathbf{q}, \mathbf{p}\}. \quad (\text{A.42})$$

The solution to Eq. (A.41) is found to be (see Ref. [33])

$$\mathbf{X}(s) = -\frac{\partial \mathbf{q}}{\partial \mathbf{p}_0}(s; \mathbf{q}_\gamma(0), \mathbf{p}_\gamma(0)) \cdot \left[\frac{\partial \mathbf{p}}{\partial \mathbf{p}_0}(s; \mathbf{q}_\gamma(0), \mathbf{p}_\gamma(0)) \right]^{-1}, \quad (\text{A.43})$$

where $\partial \mathbf{q} / \partial \mathbf{p}_0$, $\partial \mathbf{q} / \partial \mathbf{p}_0$ are submatrices of the stability matrix $M(s; \mathbf{q}_\gamma(0), \mathbf{p}_\gamma(0))$, Eq. (2.10), for the trajectory γ .²

²Be reminded that within the usage of the stability matrix, which encodes a trajectory's sensitivity towards variations in the initial phase space coordinates, the trajectory γ has to be treated as if it was defined by an initial value problem rather than a boundary problem. For that reason, if one wants to check that Eq. (A.43) fulfills the differential equation, Eq. (A.41), one has to use Eq. (2.13) to calculate the temporal derivative \dot{X} .

Before we can now use the above result, Eq. (A.43), for $\mathbf{X}(s)$, we have to prepare the product of denominators in Eq. (A.36). Using the linearized expression for $\mathbf{Y}^{(m)}$, Eq. (A.37), we calculate

$$\begin{aligned}
& \left| \prod_{m=1}^{M-1} \det(Y^{(m)}) \det(X^{(m)}) \right| \tag{A.44} \\
&= \left| \prod_{m=1}^{M-1} \det \left(\mathbf{1} + \left(\mathcal{H}_{\gamma, \mathbf{q}\mathbf{q}}^{(m,m)} \mathbf{X}^{(m)} - \frac{\mathcal{H}_{\gamma, \mathbf{q}\mathbf{p}}^{(m,m)}}{2} - \mathbf{X}^{(m)-1} \frac{\mathcal{H}_{\gamma, \mathbf{p}\mathbf{q}}^{(m,m)}}{2} \mathbf{X}^{(m)} \right) \frac{t}{M} + \mathcal{O}\left(\frac{1}{M^2}\right) \right) \right| \\
&= \left| \det \left[\exp \left[\sum_{m=1}^{M-1} \left(\mathcal{H}_{\gamma, \mathbf{q}\mathbf{q}}^{(m,m)} \mathbf{X}^{(m)} - \frac{\mathcal{H}_{\gamma, \mathbf{q}\mathbf{p}}^{(m,m)}}{2} - \mathbf{X}^{(m)-1} \frac{\mathcal{H}_{\gamma, \mathbf{p}\mathbf{q}}^{(m,m)}}{2} \mathbf{X}^{(m)} \right) \frac{t}{M} + \mathcal{O}\left(\frac{1}{M}\right) \right] \right] \right|.
\end{aligned}$$

We now use that $\det(\exp(\mathbf{A})) = \exp(\text{tr}(\mathbf{A}))$ and eliminate $\mathbf{X}^{(m)-1}$ by exploiting the cycling property of the trace. We find

$$\begin{aligned}
& \lim_{M \rightarrow \infty} \frac{1}{\sqrt{\left| \prod_{m=1}^{M-1} \det(Y^{(m)}) \det(X^{(m)}) \right|}} \tag{A.45} \\
&= \lim_{M \rightarrow \infty} \left| \exp \left[-\frac{1}{2} \sum_{m=1}^{M-1} \left(\text{tr} \left\{ \mathcal{H}_{\gamma, \mathbf{q}\mathbf{q}}^{(m,m)} \mathbf{X}^{(m)} \right\} - \text{tr} \left\{ \mathcal{H}_{\gamma, \mathbf{q}\mathbf{p}}^{(m,m)} \right\} \right) \frac{t}{M} + \mathcal{O}\left(\frac{1}{M}\right) \right] \right| \\
&= \left| \exp \left(-\frac{1}{2} \int_0^t ds \text{tr} [\mathcal{H}_{\gamma, \mathbf{q}\mathbf{q}}(s) \mathbf{X}(s) - \mathcal{H}_{\gamma, \mathbf{q}\mathbf{p}}(s)] \right) \right|.
\end{aligned}$$

The argument of the trace can be simplified using the equation of motion of the stability matrix, Eq. (2.13). We calculate (omitting all arguments of the functions except time for readability)

$$\begin{aligned}
& \int_0^t ds \text{tr} [\mathcal{H}_{\gamma, \mathbf{q}\mathbf{q}}(s) \mathbf{X}(s) - \mathcal{H}_{\gamma, \mathbf{q}\mathbf{p}}(s)] \\
&= \text{tr} \left[\int_0^t ds \left[-\frac{\partial^2 \mathcal{H}}{\partial \mathbf{q} \partial \mathbf{q}}(s) \frac{\partial \mathbf{q}}{\partial \mathbf{p}_0}(s) \left(\frac{\partial \mathbf{p}}{\partial \mathbf{p}_0}(s) \right)^{-1} - \frac{\partial^2 \mathcal{H}}{\partial \mathbf{q} \partial \mathbf{p}}(s) \frac{\partial \mathbf{p}}{\partial \mathbf{p}_0}(s) \left(\frac{\partial \mathbf{p}}{\partial \mathbf{p}_0}(s) \right)^{-1} \right] \right] \\
&= \text{tr} \left[\int_0^t ds \left(\frac{d}{ds'} \Big|_s \frac{\partial \mathbf{p}}{\partial \mathbf{p}_0}(s') \right) \left(\frac{\partial \mathbf{p}}{\partial \mathbf{p}_0}(s) \right)^{-1} \right] = \text{tr} \left[\ln \left(\frac{\partial \mathbf{p}}{\partial \mathbf{p}_0}(t) \right) \right]. \tag{A.46}
\end{aligned}$$

We thus obtain

$$\lim_{M \rightarrow \infty} \frac{1}{\sqrt{\left| \prod_{m=1}^{M-1} \det(Y^{(m)}) \det(X^{(m)}) \right|}} = \frac{1}{\sqrt{\left| \det \left(\frac{\partial \mathbf{p}}{\partial \mathbf{p}_0}(t) \right) \right|}}. \tag{A.47}$$

Together with $X^{(M)} \rightarrow X(t)$, we thus obtain for the complete propagator

$$\begin{aligned} K(\mathbf{q}^{(f)}, \mathbf{p}^{(i)}, t) &= \lim_{M \rightarrow \infty} K^{(M)}(\mathbf{q}^{(f)}, \mathbf{p}^{(i)}, t) \\ &= \sum_{\gamma} \exp\left(\frac{i}{\hbar_{\text{eff}}} R_{\gamma}(\mathbf{q}^{(f)}, \mathbf{q}^{(i)}, t) - i\varphi_{\gamma}(\mathbf{q}^{(f)}, \mathbf{q}^{(i)}, t)\right) \frac{\exp[-i\frac{\pi}{4}\mu_{\gamma}]}{\sqrt{(2\pi\hbar_{\text{eff}})^d \left| \det\left(\frac{\partial \mathbf{q}}{\partial \mathbf{p}_0}(t)\right) \right|}}. \end{aligned} \quad (\text{A.48})$$

where we collected the additional phases from the Gaussian integrations into a single variable, the *Maslov index* μ_{γ} . It has been shown that this index allows also for a geometrical interpretation. It counts the number of divergencies of the prefactor, which are interpreted as number of conjugate points along γ , *i.e.* points, where a bundle of classical trajectories fulfilling the boundary problem can be found [1, 2].

Furthermore, in the limit $M \rightarrow \infty$ the discretized action $R^{(M)}$ is replaced by Hamilton's principal function $R_{\gamma}(\mathbf{q}^{(f)}, \mathbf{q}^{(i)}, t) = R[\mathbf{q}_{\gamma}(s), \mathbf{p}_{\gamma}(s)]$, which is labeled with the index γ of the trajectory, and which depends on the boundary conditions of the trajectory. We also introduced

$$\begin{aligned} \varphi_{\gamma}(\mathbf{q}^{(f)}, \mathbf{q}^{(i)}, t) &= \varphi[\mathbf{q}_{\gamma}(s), \mathbf{p}_{\gamma}(s)] \\ &= \int_0^t ds \left[\sum_{i=1}^d \frac{h_{ii}}{2\hbar} + \sum_{i,j,k=1}^d \frac{2V_{ijk}}{\hbar} \Phi_{\gamma,j}^*(s) \Phi_{\gamma,k}(s) \right] \end{aligned} \quad (\text{A.49})$$

where the integrand is simply the phase space function $\mathcal{H}^{(\text{ord})}(\mathbf{q}(s), \mathbf{p})$, Eq. (A.18) with terms proportional to \hbar_{eff} neglected. It can easily be checked, that we can express this phase through derivatives of the classical Hamilton function \mathcal{H} (compare also Ref. [100])

$$\begin{aligned} \varphi_{\gamma}(\mathbf{q}^{(f)}, \mathbf{q}^{(i)}, t) &= \frac{1}{2} \int_0^t ds \text{tr} \left[\frac{\partial^2 \mathcal{H}}{\partial \Phi \partial \Phi^*}(\mathbf{q}_{\gamma}(s), \mathbf{p}_{\gamma}(s)) \right] \\ &= \frac{1}{4} \int_0^t ds \text{tr} \left[\frac{\partial^2 \mathcal{H}}{\partial \mathbf{q} \partial \mathbf{q}}(\mathbf{q}_{\gamma}(s), \mathbf{p}_{\gamma}(s)) + \frac{\partial^2 \mathcal{H}}{\partial \mathbf{p} \partial \mathbf{p}}(\mathbf{q}_{\gamma}(s), \mathbf{p}_{\gamma}(s)) \right]. \end{aligned} \quad (\text{A.50})$$

To arrive at the final form of the propagator we use the second derivatives of the principal function to re-express the determinant in the denominator

$$\frac{1}{\left| \det\left(\frac{\partial \mathbf{q}}{\partial \mathbf{p}_0}\right) \right|} = \left| \det\left(\frac{\partial \mathbf{p}^{(i)}}{\partial \mathbf{q}^{(f)}}\right) \right| = \left| \det\left(\frac{\partial^2 R_{\gamma}}{\partial \mathbf{q}^{(i)} \partial \mathbf{q}^{(f)}}\right) \right|. \quad (\text{A.51})$$

We end up with the following representation of the propagator

$$K^{(\text{sc})}(\mathbf{q}^{(f)}, \mathbf{p}^{(i)}, t) = \sum_{\gamma: \mathbf{q}^{(i)} \xrightarrow{t} \mathbf{q}^{(f)}} A_{\gamma}(\mathbf{q}^{(f)}, \mathbf{q}^{(i)}, t) \exp\left(\frac{i}{\hbar_{\text{eff}}} R_{\gamma}(\mathbf{q}_{\gamma}, \mathbf{p}_{\gamma}, t)\right), \quad (\text{A.52})$$

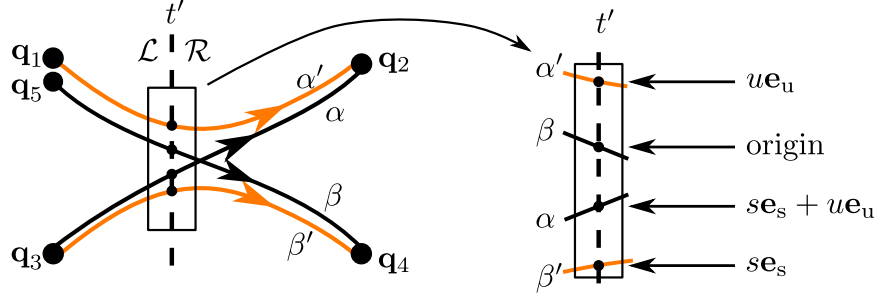


Figure A.1: On the left: Trajectories from the integral representation Eq. (4.23) of the OTOC. By choosing a time t' within the encounter, we divide the trajectories involved in the diagram into a left (\mathcal{L}) and a right (\mathcal{R}), representing the trajectories before and after the time t' .

On the right: At t' We use stable and unstable directions of the phase space point $\mathbf{x}_\beta(t')$ of the trajectory β at t' to quantify the distance of $\mathbf{x}_\beta(t')$ to the phase space points of the other trajectories α, α', β' at the same time.

with the complex amplitude

$$A_\gamma(\mathbf{q}^{(f)}, \mathbf{q}^{(i)}, t) = \sqrt{\frac{1}{(2\pi\hbar_{\text{eff}})^d} \left| \det \left(\frac{\partial^2 R_\gamma}{\partial \mathbf{q}^{(i)} \partial \mathbf{q}^{(f)}} (\mathbf{q}^{(f)}, \mathbf{q}^{(i)}, t) \right) \right|} \exp \left[-i \left(\frac{\pi}{4} \mu_\gamma + \varphi_\gamma(\mathbf{q}^{(f)}, \mathbf{q}^{(i)}, t) \right) \right], \quad (\text{A.53})$$

which is considered slowly varying upon variations of the arguments $(\mathbf{q}^{(f)}, \mathbf{q}^{(i)}, t)$. In its final representation the semiclassical approximation Eq. (A.52) resembles the well known structure of the semiclassical Van Vleck-Gutzwiller propagator known from single-particle systems in the semiclassical limit “ $\hbar \rightarrow 0$ ” [1, 2].

A.3 Calculation of the action difference

In this section we want to review the action difference due to an encounter of many trajectories in phase space. In its methods, it is almost identical to the derivation found in Refs. [81, 109], with the only difference that it explicitly discusses the question of an additional linearization due to a slight mismatch in the initial coordinates of two trajectories. An alternative calculation of the action difference based on geometrical considerations in phase space is found in Refs. [33, 69, 139]. For simplicity of the expressions, we restrict ourselves to a single pair of a stable and unstable directions, $\mathbf{e}_s(\mathbf{x})$ and $\mathbf{e}_u(\mathbf{x})$. The generalization to the multidimensional case is straightforward.

The situation is depicted in figure A.1. As we describe in detail in section 4.2.3, before and after the encounter trajectories closely follow each other as pairs. Within the encounter region, the trajectories interchange their partners. To describe this scenario, we

choose one trajectory as the reference trajectory, here $\beta : \mathbf{q}_5 \rightarrow \mathbf{q}_4$, as well as a time t' within the encounter, and use the stable and unstable direction $\mathbf{e}_s(\mathbf{x}_\beta(t'))$ and $\mathbf{e}_u(\mathbf{x}_\beta(t'))$ to quantify the relative distance of the phase space points $\mathbf{x}_{\beta'}(t')$, $\mathbf{x}_\alpha(t')$, $\mathbf{x}_{\alpha'}(t')$ of the other trajectories. The precise distance is illustrated in Fig. A.1. We want to calculate the difference in the actions associated to the above depicted situation. For that reason, we note that the time t' divides the diagram in a left and a right part, containing the dynamics of the trajectories before and after t' . Quantities associated with the left part will be indexed by \mathcal{L} , and accordingly \mathcal{R} for the right part. The classical actions of the single trajectories can be divided in two parts, since they integrate the classical Lagrange function over time, see Eq. (2.5),

$$R_\gamma(\mathbf{q}^{(f)}, \mathbf{q}^{(i)}, t) = R_\gamma^{\mathcal{L}}(\mathbf{q}_\gamma(t'), \mathbf{q}^{(i)}, t') + R_\gamma^{\mathcal{R}}(\mathbf{q}^{(f)}, \mathbf{q}_\gamma(t'), t - t'), \quad (\text{A.54})$$

where $\gamma \in \{\alpha, \alpha', \beta, \beta'\}$, and $\mathbf{q}^{(i)}$, $\mathbf{q}^{(f)}$ represent the corresponding initial and final position quadrature variable of the trajectory. $\mathbf{q}_\gamma(t') = \mathbf{q}_\gamma(t'; \mathbf{q}^{(f)}, \mathbf{q}^{(i)}, t)$ denotes the position quadrature of the trajectory γ at the intermediate time t' . By relating this intermediate position quadrature with the reference trajectory we can bring the stable and unstable directions of the reference trajectory into play. Using a Taylor expansion, this allows us to express the action difference in terms of the stable and unstable coordinates s and u .

For the subsequent calculations we abbreviate

$$\mathbf{e}_s^{(\beta)}(t') \equiv \mathbf{e}_s(\mathbf{x}_\beta(t'; \mathbf{q}_4, \mathbf{q}, t)), \quad \mathbf{e}_u^{(\beta)}(t') \equiv \mathbf{e}_u(\mathbf{x}_\beta(t'; \mathbf{q}_4, \mathbf{q}, t)). \quad (\text{A.55})$$

The position and the momentum quadrature sector, see Eq. (4.15) is abbreviated as

$$\mathbf{e}_{s,\mathbf{q}}^{(\beta)}(t') = \left[\mathbf{e}_s^{(\beta)}(t') \right]_{\mathbf{q}}, \quad \mathbf{e}_{s,\mathbf{p}}^{(\beta)}(t') = \left[\mathbf{e}_s^{(\beta)}(t') \right]_{\mathbf{p}} \quad (\text{A.56})$$

and accordingly for $\mathbf{e}_{u,\mathbf{q}}^{(\beta)}(t')$, $\mathbf{e}_{u,\mathbf{p}}^{(\beta)}(t')$. Using Eq. (A.54) we can divide the action difference into a left and a right part,

$$\begin{aligned} \Delta R &= -R_{\alpha'}(\mathbf{q}_2, \mathbf{q}_1, t) + R_\alpha(\mathbf{q}_2, \mathbf{q}_3, t) - R_{\beta'}(\mathbf{q}_4, \mathbf{q}_3, t) + R_\beta(\mathbf{q}_4, \mathbf{q}_5, t) \\ &= \Delta R^{\mathcal{L}} + \Delta R^{\mathcal{R}}, \end{aligned} \quad (\text{A.57})$$

where the partial action differences, already using stable and unstable coordinates, are found to be

$$\begin{aligned} \Delta R^{\mathcal{L}} &= R_\beta^{\mathcal{L}}[\mathbf{q}_\beta(t'), \mathbf{q}_5, t'] - R_{\alpha'}^{\mathcal{L}}[\mathbf{q}_\beta(t') + u\mathbf{e}_{u,\mathbf{q}}^{(\beta)}(t'), \mathbf{q}_1, t'] \\ &\quad + R_\alpha^{\mathcal{L}}[\mathbf{q}_\beta(t') + s\mathbf{e}_{s,\mathbf{q}}^{(\beta)}(t') + u\mathbf{e}_{u,\mathbf{q}}^{(\beta)}(t'), \mathbf{q}_3, t'] - R_{\beta'}^{\mathcal{L}}[\mathbf{q}_\beta(t') + s\mathbf{e}_{s,\mathbf{q}}^{(\beta)}(t'), \mathbf{q}_3, t'] \\ \Delta R^{\mathcal{R}} &= R_\beta^{\mathcal{R}}[\mathbf{q}_4, \mathbf{q}_\beta(t'), t - t'] - R_{\beta'}^{\mathcal{R}}[\mathbf{q}_4, \mathbf{q}_\beta(t') + s\mathbf{e}_{s,\mathbf{q}}^{(\beta)}(t'), t - t'] \\ &\quad + R_\alpha^{\mathcal{R}}[\mathbf{q}_2, \mathbf{q}_\beta(t') + s\mathbf{e}_s^{(\beta)}(t') + u\mathbf{e}_u^{(\beta)}(t'), t - t'] - R_{\alpha'}^{\mathcal{R}}[\mathbf{q}_2, \mathbf{q}_\beta(t') + u\mathbf{e}_u^{(\beta)}(t'), t - t'] \end{aligned} \quad (\text{A.58})$$

We want to expand terms involved in the action differences $\Delta R^{\mathcal{L}}$, $\Delta R^{\mathcal{R}}$, around small differences in their initial and final condition. One of the two expansion points is $\mathbf{q}_\beta(t')$.

Furthermore, we want to replace \mathbf{q}_1 and \mathbf{q}_5 by $\mathbf{q} = (\mathbf{q}_1 + \mathbf{q}_5)/2$. This is justified as we assume that \mathbf{q}_1 is close to \mathbf{q}_5 since otherwise a large action difference can not be avoided, leading to a canceling contribution to the integration Eq. (4.23).

To increase readability in the subsequent Taylor expansion, we from now on omit the arguments of trajectory-related quantities. If any quantity has only a trajectory index $\alpha, \alpha', \beta, \beta'$, its arguments are the defining arguments of the trajectories, for instance $(\mathbf{q}_4, \mathbf{q}_5, t)$ in case of the trajectory β . If additionally to the trajectory index there is an indicator for the left or right part, \mathcal{L} or \mathcal{R} , we mean the part of the trajectory, which ends or starts at the time t' . Accordingly, the arguments are those containing the intermediate position quadrature, as indicated by the terms in equations (A.58).

The zeroth order contribution vanishes as this assumes sequentially equal trajectories and thus pairwise vanishing actions in the above difference. In linear order we obtain for the left part, remembering the properties Eqs. (2.6), (2.7) of the classical action,

$$\begin{aligned} \Delta R^{\mathcal{L},(1)} &= \mathbf{p}_\beta^{(i)} \cdot (\mathbf{q}_1 - \mathbf{q}_5) - \mathbf{p}_\beta^{(f)\mathcal{L}} \cdot u\mathbf{e}_{u,\mathbf{q}}^{(\beta)} + \mathbf{p}_\alpha^{(f)\mathcal{L}} \cdot u\mathbf{e}_{u,\mathbf{q}}^{(\beta)} \\ &= \mathbf{p}_\beta^{(i)} \cdot (\mathbf{q}_1 - \mathbf{q}_5) + \left(\mathbf{p}_\alpha^{(f)\mathcal{L}} - \mathbf{p}_\beta^{(f)\mathcal{L}} \right) \cdot u\mathbf{e}_{u,\mathbf{q}}^{(\beta)}. \end{aligned} \quad (\text{A.59})$$

The difference of the momentum quadratures taken at t' and therefore can be also expressed through stable and unstable directions,

$$\mathbf{p}_\alpha^{(f)\mathcal{L}} - \mathbf{p}_\beta^{(f)\mathcal{L}} = s\mathbf{e}_{s,\mathbf{p}}^{(\beta)} + u\mathbf{e}_{u,\mathbf{p}}^{(\beta)}. \quad (\text{A.60})$$

Therefore

$$\Delta R^{\mathcal{L},(1)} = \mathbf{p}_\alpha^{(i)} \cdot (\mathbf{q}_1 - \mathbf{q}_5) + \left[s\mathbf{e}_{s,\mathbf{p}}^{(\beta)} + u\mathbf{e}_{u,\mathbf{p}}^{(\beta)} \right] \cdot u\mathbf{e}_{u,\mathbf{q}}^{(\beta)}. \quad (\text{A.61})$$

The action difference for the right part is calculated accordingly

$$\Delta R^{\mathcal{R},(1)} = \mathbf{p}_\beta^{(i)\mathcal{R}} \cdot s\mathbf{e}_{s,\mathbf{q}}^{(\beta)} - \mathbf{p}_\alpha^{(i)\mathcal{R}} \cdot s\mathbf{e}_{s,\mathbf{q}}^{(\beta)} = - \left[s\mathbf{e}_{s,\mathbf{p}}^{(\beta)} + u\mathbf{e}_{u,\mathbf{p}}^{(\beta)} \right] \cdot s\mathbf{e}_{s,\mathbf{q}}^{(\beta)}. \quad (\text{A.62})$$

Together, we obtain

$$\begin{aligned} \Delta R^{(1)} &= \mathbf{p}_\beta^{(i)} \cdot (\mathbf{q}_1 - \mathbf{q}_5) - \left[s\mathbf{e}_{s,\mathbf{p}}^{(\beta)} + u\mathbf{e}_{u,\mathbf{p}}^{(\beta)} \right] \cdot \left[s\mathbf{e}_{s,\mathbf{q}}^{(\beta)} - u\mathbf{e}_{u,\mathbf{q}}^{(\beta)} \right] \\ &= \mathbf{p}_\beta^{(i)} \cdot (\mathbf{q}_1 - \mathbf{q}_5) - s^2 \mathbf{e}_{s,\mathbf{p}}^{(\beta)} \cdot \mathbf{e}_{s,\mathbf{q}}^{(\beta)} + u^2 \mathbf{e}_{u,\mathbf{p}}^{(\beta)} \cdot \mathbf{e}_{u,\mathbf{q}}^{(\beta)} + su \overbrace{\left[\mathbf{e}_{u,\mathbf{q}}^{(\beta)} \cdot \mathbf{e}_{u,\mathbf{p}}^{(\beta)} - \mathbf{e}_{u,\mathbf{p}}^{(\beta)} \cdot \mathbf{e}_{s,\mathbf{q}}^{(\beta)} \right]}^{=1}, \end{aligned} \quad (\text{A.63})$$

where the last line uses the normalization Eq. (2.33) of the directions $\mathbf{e}_s^{(\alpha)}, \mathbf{e}_u^{(\alpha)}$.

Remarkably, due to our use of the classical relations in Eq. (A.60) we find that the linear order Taylor expansion result in an expression which contain quadratic orders in s and u . To be consistent, this requires also the consideration of terms found in second order in the Taylor expansion, which produce quadratic corrections in s and u . For that

reason, in the calculation of the left part we do not require further derivatives w.r.t. the initial conditions. We find

$$\Delta R^{\mathcal{L}(2)} = -\frac{1}{2}u\mathbf{e}_{\mathbf{u},\mathbf{q}}^{(\beta)\top} \frac{\partial \mathbf{p}_{\beta}^{(f)\mathcal{L}}}{\partial \mathbf{q}^{(f)}} u\mathbf{e}_{\mathbf{u},\mathbf{q}}^{(\beta)} - \frac{1}{2}u\mathbf{e}_{\mathbf{u},\mathbf{q}}^{(\beta)\top} \frac{\partial \mathbf{p}_{\alpha}^{(f)\mathcal{L}}}{\partial \mathbf{q}^{(f)}} u\mathbf{e}_{\mathbf{u},\mathbf{q}}^{(\beta)}. \quad (\text{A.64})$$

The derivatives involving final position and momentum quadratures can be used to change the sector $\mathbf{e}_{\mathbf{u},\mathbf{q}}^{(\alpha)}$ into $\mathbf{e}_{\mathbf{u},\mathbf{p}}^{(\alpha)}$, since

$$\frac{\partial \mathbf{p}_{\beta}^{(f)\mathcal{L}}}{\partial \mathbf{q}^{(f)}} u\mathbf{e}_{\mathbf{u},\mathbf{q}}^{(\beta)} + \frac{\partial \mathbf{p}_{\alpha}^{(f)\mathcal{L}}}{\partial \mathbf{q}^{(f)}} u\mathbf{e}_{\mathbf{u},\mathbf{q}}^{(\beta)} = \mathbf{p}_{\alpha'}^{(f)\mathcal{L}} - \mathbf{p}_{\beta}^{(f)\mathcal{L}} - \mathbf{p}_{\beta'}^{(f)\mathcal{L}} + \mathbf{p}_{\alpha}^{(f)\mathcal{L}} = 2u\mathbf{e}_{\mathbf{u},\mathbf{p}}^{(\beta)}. \quad (\text{A.65})$$

Thus

$$\Delta R^{\mathcal{L}(2)} = -u^2 \mathbf{e}_{\mathbf{u},\mathbf{q}}^{(\beta)\top} \mathbf{e}_{\mathbf{u},\mathbf{p}}^{(\beta)}. \quad (\text{A.66})$$

For the right side, we get, also using a similar argument as shown in Eq. (A.65),

$$\Delta R^{\mathcal{R},(2)} = \frac{1}{2}s\mathbf{e}_{\mathbf{s},\mathbf{q}}^{(\beta)\top} \frac{\partial \mathbf{p}_{\beta}^{(i)\mathcal{R}}}{\partial \mathbf{q}^{(i)}} s\mathbf{e}_{\mathbf{s},\mathbf{q}}^{(\beta)} + \frac{1}{2}s\mathbf{e}_{\mathbf{s},\mathbf{q}}^{(\beta)\top} \frac{\partial \mathbf{p}_{\alpha}^{(i)\mathcal{R}}}{\partial \mathbf{q}^{(i)}} s\mathbf{e}_{\mathbf{s},\mathbf{q}}^{(\beta)} = s^2 \mathbf{e}_{\mathbf{s},\mathbf{q}}^{(\beta)\top} \mathbf{e}_{\mathbf{s},\mathbf{p}}^{(\beta)}. \quad (\text{A.67})$$

Combining $\Delta R^{\mathcal{L},(2)}$ and $\Delta R^{\mathcal{R},(2)}$ we thus find for the second order contribution

$$\Delta R^{(2)} = s^2 \mathbf{e}_{\mathbf{s},\mathbf{q}}^{(\beta)\top} \mathbf{e}_{\mathbf{s},\mathbf{p}}^{(\beta)} - u^2 \mathbf{e}_{\mathbf{s},\mathbf{q}}^{(\beta)\top} \mathbf{e}_{\mathbf{s},\mathbf{p}}^{(\beta)}. \quad (\text{A.68})$$

The action difference due to an encounter of trajectories is thus given by

$$\Delta R \approx \Delta R^{(1)} + \Delta R^{(2)} = \mathbf{p}_{\beta}^{(i)} \cdot (\mathbf{q}_1 - \mathbf{q}_5) + su. \quad (\text{A.69})$$

A.4 Calculation of encounter-related integrals

In this appendix we present the technical details for the various integrations associated with the encounter regions in the diagram classes (a) to (d) in Fig. 4.2.

A.4.1 Frequently used integrals in the calculations of encounters

Let a, b be positive and dimensionless real parameters. The *sine integral* is defined by[113]

$$\text{Si}(z) = \int_0^z dz' \frac{\sin(z')}{z'}. \quad (\text{A.70})$$

During the subsequent calculations of encounter diagrams we frequently face the subsequent integrals. Their evaluation involves the sine integral and its derivatives.

$$\bullet \int_{-a}^a ds \int_{-b}^b du e^{\frac{i}{\hbar_{\text{eff}}} su} = 4\hbar_{\text{eff}} \text{Si}\left(\frac{ab}{\hbar_{\text{eff}}}\right), \quad (\text{A.71})$$

$$\begin{aligned}
& \bullet \int_{-a}^a ds \int_{-b}^b du s^2 e^{\frac{i}{\hbar_{\text{eff}}} su} = -4\hbar_{\text{eff}} a^2 \text{Si}''\left(\frac{ab}{\hbar_{\text{eff}}}\right) \\
& = 4\hbar_{\text{eff}}^3 \frac{1}{b^2} \sin\left(\frac{ab}{\hbar_{\text{eff}}}\right) - 4\hbar_{\text{eff}}^2 \frac{a}{b} \cos\left(\frac{ab}{\hbar_{\text{eff}}}\right), \tag{A.72}
\end{aligned}$$

$$\begin{aligned}
& \bullet \int_{-a}^a ds \int_{-b}^b du s u e^{\frac{i}{\hbar_{\text{eff}}} su} = -4\hbar_{\text{eff}}^2 i \left(y^2 \frac{d}{dy} \frac{\text{Si}(y)}{y} \Big|_{y=\frac{ab}{\hbar_{\text{eff}}}} \right) \\
& = 4\hbar_{\text{eff}}^2 i \left[\text{Si}\left(\frac{ab}{\hbar_{\text{eff}}}\right) - \sin\left(\frac{ab}{\hbar_{\text{eff}}}\right) \right], \tag{A.73}
\end{aligned}$$

$$\begin{aligned}
& \bullet \int_{-a}^a ds \int_{-b}^b du s^2 u^2 e^{\frac{i}{\hbar_{\text{eff}}} su} = -4\hbar_{\text{eff}}^3 \left(y^3 \frac{d^2}{dy^2} \frac{\text{Si}(y)}{y} \Big|_{y=\frac{ab}{\hbar_{\text{eff}}}} \right) \\
& = -4\hbar_{\text{eff}}^3 \left[\frac{ab}{\hbar_{\text{eff}}} \cos\left(\frac{ab}{\hbar_{\text{eff}}}\right) - 3 \sin\left(\frac{ab}{\hbar_{\text{eff}}}\right) + 2 \text{Si}\left(\frac{ab}{\hbar_{\text{eff}}}\right) \right]. \tag{A.74}
\end{aligned}$$

A.4.2 Encounter integral of the four-leg diagram

In this section we perform the evaluation of the encounter integral, Eq. (4.52), for the 4-leg encounters. This multidimensional integral is given by

$$F^{(4\text{le})}(t) = \frac{1}{(2\pi\hbar_{\text{eff}})^{d-2}} \int_{-c}^c d^{d-2}s \int_{-c}^c d^{d-2}u e^{\frac{i}{\hbar_{\text{eff}}}\mathbf{s}\cdot\mathbf{u}t - t_{\text{enc}}(\mathbf{s},\mathbf{u})} \Theta[t - t_{\text{enc}}(\mathbf{s},\mathbf{u})]. \tag{A.75}$$

In order to resolve the max-function in the definition Eq. (4.32) of $t_{\text{enc}}(\mathbf{s},\mathbf{u})$, we split the integrations over \mathbf{s}, \mathbf{u} , leading to the summation

$$F^{(4\text{le})}(t) = \sum_{i,j=1}^{d-2} F_{ij}^{(4\text{le})}(t), \tag{A.76}$$

where

$$\begin{aligned}
F_{ij}^{(4\text{le})}(t) &= \frac{1}{(2\pi\hbar_{\text{eff}})^{d-2}} \int_{-c}^c ds_i \int_{-c}^c du_j \frac{t - t_{\text{enc}}(s_i u_j)}{t_{\text{enc}}(s_i u_j)} \Theta[t - t_{\text{enc}}(s_i u_j)] \\
&\quad \times \left(\prod_{\substack{k,k'=1 \\ k \neq i, k' \neq j}}^{d-2} \int_{-|s_i|}^{|s_i|} ds_k \int_{-|u_j|}^{|u_j|} du_{k'} \right) e^{\frac{i}{\hbar_{\text{eff}}}\mathbf{s}\cdot\mathbf{u}}. \tag{A.77}
\end{aligned}$$

Within the integrand, s_i and u_j are the first components of the stable and unstable vectors \mathbf{s}, \mathbf{u} to reach the critical value c when being involved in time, and thus, they determine the encounter time $t_{\text{enc}}(s_i u_j) = (1/\lambda) \log(c^2/|s_i u_j|)$ within the integrand.

For the evaluation of Eq. (A.77), one has to distinguish the cases $i \neq j$ from $i = j$ in order to correctly interpret the product over k, k' . The integrations over s_k and $u_{k'}$

are easily performed, either by a simple integration of an exponential for $k = j$, $k' = i$, $i \neq j$, or by sorting the products such that $k = k'$ and then using Eq. (A.71). For the final integration over s_i, u_j , one first transforms for both variables the integration over the subinterval $[-c, 0]$ to $[0, c]$ by inverting the sign of the integration variables. The resulting integrations are then over positive s_i, u_j , for which we use the variable transformation [70]

$$(s_i, u_j) \rightarrow (S, \sigma) = \left(\frac{s_i u_j}{c^2}, \frac{c}{u_j} \right), \text{ with } \left| \frac{\partial(s_i, u_j)}{\partial(S, \sigma)} \right| = \frac{c^2}{\sigma}, \quad (\text{A.78})$$

$$\text{and } 0 < S < 1, \quad 1 < \sigma < \frac{1}{S}.$$

The integration over σ leads to the cancellation of $t_{\text{enc}}(s_i u_j)$ in the denominator. The argument of the Heaviside step function Θ demands $t > (1/\lambda) \log(S^{-1})$, which is equivalent to $S > \exp(-\lambda t)$, thus raising the lower integration limit for S . We get as intermediate result for $i = j$

$$F_{ii}^{(4\text{le})}(t) = \left(\frac{2}{\pi} \right)^{d-2} \int_{e^{-\lambda t}}^1 dS \left(\lambda t - \log \left(\frac{1}{S} \right) \right) \text{Si}^{d-3} \left(\frac{c^2 S}{\hbar_{\text{eff}}} \right) \cos \left(\frac{c^2 S}{\hbar_{\text{eff}}} \right) \frac{c^2}{\hbar_{\text{eff}}}, \quad (\text{A.79})$$

and for $i \neq j$

$$F_{ij}^{(4\text{le})}(t) = \left(\frac{2}{\pi} \right)^{d-2} \int_{e^{-\lambda t}}^1 dS \left(\lambda t - \log \left(\frac{1}{S} \right) \right) \text{Si}^{d-4} \left(\frac{c^2 S}{\hbar_{\text{eff}}} \right) \frac{\sin^2 \left(\frac{c^2 S}{\hbar_{\text{eff}}} \right)}{S}. \quad (\text{A.80})$$

We now perform the summation over indices i, j to obtain an integral expression for $F^{(4\text{le})}$. Within that, we combine

$$\begin{aligned} & (d-2)(d-3) \text{Si}^{d-4} \left(\frac{c^2 S}{\hbar_{\text{eff}}} \right) \frac{\sin^2 \left(\frac{c^2 S}{\hbar_{\text{eff}}} \right)}{S} + (d-2) \text{Si}^{d-3} \left(\frac{c^2 S}{\hbar_{\text{eff}}} \right) \cos \left(\frac{c^2 S}{\hbar_{\text{eff}}} \right) \frac{c^2}{\hbar_{\text{eff}}} \\ &= \frac{d}{dS} S \frac{d}{dS} \text{Si}^{d-2} \left(\frac{c^2 S}{\hbar_{\text{eff}}} \right), \end{aligned} \quad (\text{A.81})$$

and arrive at

$$F^{(4\text{le})}(t) = \left(\frac{2}{\pi} \right)^{d-2} \int_{e^{-\lambda t}}^1 dS \left(\lambda t - \log \left(\frac{1}{S} \right) \right) \frac{d}{dS} S \frac{d}{dS} \text{Si}^{d-2} \left(\frac{c^2 S}{\hbar_{\text{eff}}} \right). \quad (\text{A.82})$$

By a partial integration, we shift the outer derivative to the first factor in the integrand. As $d(t - \log(S^{-1}))/dS = 1/S$ cancels the factor S , the remaining integration is easily performed. To obtain more physical insight at this stage, it is worth to utilize the identity $c^2/\hbar_{\text{eff}} = \exp(\lambda t_{\text{E}})$ to introduce the Ehrenfest time, Eq. (A.77), into our results. Using this, the final result reads

$$\begin{aligned} F^{(4\text{le})}(t) &= \left(\frac{2}{\pi} \right)^{d-2} \lambda t (d-2) \text{Si}^{d-3} \left(e^{\lambda t_{\text{E}}} \right) \sin \left(e^{\lambda t_{\text{E}}} \right) \\ &\quad - \left(\frac{2}{\pi} \right)^{d-2} \left[\text{Si}^{d-2} \left(e^{\lambda t_{\text{E}}} \right) - \text{Si}^{d-2} \left(e^{\lambda(t_{\text{E}}-t)} \right) \right]. \end{aligned} \quad (\text{A.83})$$

In the semiclassical limit $\hbar_{\text{eff}} \ll c^2$, t_E in Eq. (4.30) is large compared to the Lyapunov time $t_L = \lambda^{-1}$, implying a separation of time scales for the OTOC. Thus, $\exp(\lambda t_E) \gg 1$, and this has several consequences:

- $\sin[\exp(\lambda t_E)]$ is highly oscillatory and can be neglected in the phase space average (4.50).
- $\text{Si}[\exp(\lambda t_E)]$ is well approximated by the asymptotic limit of the sine integral for large, positive arguments, $\text{Si}[\exp(\lambda t_E)] \approx \frac{\pi}{2}$ [113].
- For $t < t_E$ Taylor-expansion around $t/t_E = 0$ yields

$$\text{Si}^{d-2}\left(e^{\lambda t_E}\right) - \text{Si}^{d-2}\left(e^{\lambda(t_E-t)}\right) \approx (d-2) \text{Si}^{d-3}\left(e^{\lambda t_E}\right) \sin\left(e^{\lambda t_E}\right) \lambda t, \quad (\text{A.84})$$

where the term linear in t is the same highly oscillatory term as in the first item and can be neglected. (Alternatively, if not neglected, it would exactly cancel the oscillatory term for small t .)

- For $t > t_E$ we have $\exp[\lambda(t_E - t)] \ll 1$, and thus, by Taylor-expanding $\text{Si}(y)$ around $y = 0$, we get

$$\text{Si}^{d-2}\left(e^{\lambda(t_E-t)}\right) \approx e^{(d-2)\lambda(t_E-t)}, \quad (\text{A.85})$$

which is exponentially fast decaying for $t > t_E$ and thus can be neglected against the terms originating from the second item.

Combining the above considerations, we can well approximate

$$F^{(4\text{e})}(t) \approx \begin{cases} 0 & \text{if } t < t_E \\ -1 & \text{if } t > t_E \end{cases} \approx -\Theta(t - t_E). \quad (\text{A.86})$$

Hence the diagram class of the 4-leg-encounters only contributes after a certain minimal time, the Ehrenfest time t_E . It is after this time that a description solely based on classical dynamics breaks down, as interference contributions due to trajectory constellations with encounter regions with an action difference of the order $\mathcal{O}(\hbar_{\text{eff}})$ start to exist.

A.4.3 Encounter integral of the two-leg diagram with the encounter at the beginning

The relevant encounter integral we have to solve for diagram (b) in Fig. 4.2 is given by Eq. (4.57) and reads

$$F_{ll'}^{(2\text{e},(b))}(t) = \frac{1}{(2\pi\hbar_{\text{eff}})^{d-2}} \int_{-c}^c d^{d-2}s \int_{-c}^c d^{d-2}u e^{\frac{i}{\hbar_{\text{eff}}}\mathbf{s}\cdot\mathbf{u}} s_l s_{l'} \times \int_0^{t_s(\mathbf{s})} dt' \frac{\Theta\left[t - t_{\text{enc}}^{(\text{eff})}(t', \mathbf{u})\right]}{t_{\text{enc}}^{(\text{eff})}(t', \mathbf{u})} e^{2\lambda t'}, \quad (\text{A.87})$$

with the effective encounter time $t_{\text{enc}}^{(\text{eff})}(t', \mathbf{u}) = t' + t_u(\mathbf{u})$. The stable and unstable time $t_s(\mathbf{s})$ and $t_u(\mathbf{u})$ are functions of the moduli of the components of \mathbf{s} , \mathbf{u} , see Eq. (4.31).

For $l \neq l'$ we can immediately conclude $F_{ll'}^{(2\text{le},(\text{b}))}(t) = 0$, as the variable transformation $(s_l, u_l) \rightarrow -(s_l, u_l)$ results in $F_{ll'}^{(2\text{le},(\text{b}))}(t) = -F_{ll'}^{(2\text{le},(\text{b}))}(t)$.

Thus only the case $l = l'$ needs to be considered. Like before in the calculation of the encounter integral $F^{(4\text{le})}$ of the four-leg diagram, we have to resolve the maximum functions used in the definition of $t_s(\mathbf{s})$ and $t_u(\mathbf{u})$, Eq. (4.31). We therefore split

$$F_{ll}^{(2\text{le},(\text{b}))}(t) = \sum_{i,j=1}^{d-2} F_{l,ij}^{(2\text{le},(\text{b}))}(t), \quad (\text{A.88})$$

where

$$F_{l,ij}^{(2\text{le},(\text{b}))}(t) = \frac{1}{(2\pi\hbar_{\text{eff}})^{d-2}} \int_{-c}^c ds_i \int_{-c}^c du_j \int_0^{t_s(s_i)} dt' \frac{\Theta[t - t_{\text{enc}}^{(\text{eff})}(t', u_j)]}{t_{\text{enc}}^{(\text{eff})}(t', u_j)} \times \left(\prod_{\substack{k,k'=1 \\ k \neq i, k' \neq j}}^{d-2} \int_{-|s_i|}^{|s_i|} ds_k \int_{-|u_j|}^{|u_j|} du_{k'} \right) s_l^2 e^{\frac{i}{\hbar_{\text{eff}}} \mathbf{s} \cdot \mathbf{u}} e^{2\lambda t'}. \quad (\text{A.89})$$

Within the integrand, s_i and u_j determine the stable time $t_s(s_i) = (1/\lambda) \log(c/|s_i|)$ and the encounter time $t_{\text{enc}}^{(\text{eff})}(t', u_j) = t' + (1/\lambda) \log(c/|u_j|)$. For correctly treating the product of integrations in the last line of Eq. (A.89), we must distinguish the cases $i = j$ from $i \neq j$, and moreover the cases when l happens to be one of the indices i or j . Using Eqs. (A.71) and (A.72), the integrations over s_k , $u_{k'}$ for $k \neq i$, $k' \neq j$ are readily performed. For the last integrals over s_i , u_j and t' , we again, through a sign-changing transformation, convert the integration over the subinterval $[-c, 0]$ into one over $[0, c]$. Then we use the transformation[70, 72]

$$(s_i, u_j, t') \rightarrow (T, S, \sigma) = \left(t' + t_u(u_j), \frac{s_i u_j}{c^2}, \frac{c}{u_j} \right), \quad \text{with} \quad \left| \frac{\partial(s_i, u_j, t')}{\partial(T, S, \sigma)} \right| = \frac{c^2}{\sigma} \quad (\text{A.90})$$

and $0 \leq T < \infty$, $0 \leq S \leq e^{-\lambda T}$, $1 \leq \sigma \leq e^{\lambda T}$.

The integration over σ leads to a cancellation of the effective encounter time T in the denominator. The Heaviside step function transforms to $\Theta(t - T)$, which introduces an upper bound in the integration over T .

We find that the results have the common structure

$$F_{l,ij}^{(2\text{le},(\text{b}))}(t) = \left(\frac{2}{\pi} \right)^{d-2} c^2 \lambda \int_0^t dT e^{2\lambda T} \int_0^{e^{-\lambda T}} dS f_{l,ij}(S), \quad (\text{A.91})$$

and we have to distinguish the following five cases:

- for $i = j = l$:

$$f_{l,l}(S) = \text{Si}^{d-3} \left(\frac{c^2 S}{\hbar_{\text{eff}}} \right) \cos \left(\frac{c^2 S}{\hbar_{\text{eff}}} \right) S^2 \frac{c^2}{\hbar_{\text{eff}}}, \quad (\text{A.92})$$

- for $i = j$ with $i, j \neq l$:

$$f_{l,ii}(S) = \text{Si}^{d-4} \left(\frac{c^2 S}{\hbar_{\text{eff}}} \right) \cos \left(\frac{c^2 S}{\hbar_{\text{eff}}} \right) \left[\frac{\hbar_{\text{eff}}}{c^2} \sin \left(\frac{c^2 S}{\hbar_{\text{eff}}} \right) - S \cos \left(\frac{c^2 S}{\hbar_{\text{eff}}} \right) \right], \quad (\text{A.93})$$

- for $i \neq j$ with $i, j \neq l$:

$$f_{l,ij}(S) = \text{Si}^{d-5} \left(\frac{c^2 S}{\hbar_{\text{eff}}} \right) \frac{\sin^2 \left(\frac{c^2 S}{\hbar_{\text{eff}}} \right)}{S} \frac{\hbar_{\text{eff}}}{c^2} \left[\frac{\hbar_{\text{eff}}}{c^2} \sin \left(\frac{c^2 S}{\hbar_{\text{eff}}} \right) - S \cos \left(\frac{c^2 S}{\hbar_{\text{eff}}} \right) \right], \quad (\text{A.94})$$

- for $i \neq j$ with $i = l$:

$$f_{l,lj}(S) = \text{Si}^{d-4} \left(\frac{c^2 S}{\hbar_{\text{eff}}} \right) S \sin^2 \left(\frac{c^2 S}{\hbar_{\text{eff}}} \right), \quad (\text{A.95})$$

- for $i \neq j$ with $j = l$:

$$f_{l,il}(S) = \text{Si}^{d-4} \left(\frac{c^2 S}{\hbar_{\text{eff}}} \right) \frac{\sin \left(\frac{c^2 S}{\hbar_{\text{eff}}} \right)}{S} \times \left[2 \frac{\hbar_{\text{eff}}}{c^2} S \cos \left(\frac{c^2 S}{\hbar_{\text{eff}}} \right) + \left(S^2 - 2 \left(\frac{\hbar_{\text{eff}}}{c^2} \right)^2 \right) \sin \left(\frac{c^2 S}{\hbar_{\text{eff}}} \right) \right]. \quad (\text{A.96})$$

The sum in Eq. (A.88) over all indices to obtain $F_l^{(2\text{le},(b))}(t)$ directly translates into a summation of $f_{l,ij}(x)$ via Eq. (A.91). The latter sum can be conveniently rewritten as

$$\sum_{i,j=1}^{d-2} f_{l,ij}(S) = -\frac{d}{dS} S^3 \frac{d}{dS} \text{Si}^{d-3} \left(\frac{c^2 S}{\hbar_{\text{eff}}} \right) \text{Si}'' \left(\frac{c^2 S}{\hbar_{\text{eff}}} \right). \quad (\text{A.97})$$

This identity allows one to easily perform the remaining integrals over S and T . We obtain

$$F_l^{(2\text{le},(b))}(t) = -\left(\frac{2}{\pi} \right)^{d-2} c^2 \left[\text{Si}^{d-3} \left(e^{\lambda t_E} \right) \text{Si}'' \left(e^{\lambda t_E} \right) - \text{Si}^{d-3} \left(e^{\lambda(t_E-t)} \right) \text{Si}'' \left(e^{\lambda(t_E-t)} \right) \right]. \quad (\text{A.98})$$

The result contains the second derivative $\text{Si}''(z) = \cos(z)/z - \sin(z)/z^2$ of the sine integral, which are oscillatory functions. We consider again the limiting cases:

- For $t \ll t_E$ we get $\exp[\lambda(t_E-t)] \approx \exp(\lambda t_E)$, and $\text{Si}''[\exp(\lambda t_E)]$ only contains highly oscillatory factors, which we can neglect in the semiclassical limit $\hbar_{\text{eff}} \ll c^2$.

- For $t \gg t_E$ we expand around $\exp[\lambda(t_E - t)] \approx 0$

$$\text{Si}^{d-3}(e^{\lambda(t_E-t)}) \text{Si}''(e^{\lambda(t_E-t)}) \approx \text{Si}'''(0)e^{(d-2)\lambda(t_E-t)}, \quad (\text{A.99})$$

where $\text{Si}'''(0) = -5/3$. As for the 4-leg encounter, this contribution is exponentially small compared to the contribution of the four-leg diagram.

For times $t \ll t_E$ and $t \gg t_E$ the diagrams in Fig. 4.2 (b) are negligible in the semiclassical limit. Only for $t \approx t_E$, the above terms can, in principle, produce non-negligible contributions. However, for these times the results depend on the (sharp) cutoff value c of the encounter integrations, indicating that the quantitative result of the encounter integration is not very meaningful. However, qualitatively, our results indicate that the interference mechanism behind diagram (b) accounts, together with other diagrams, for the smooth crossover between the pre- and post-Ehrenfest time behavior of OTOCs.

A.4.4 Encounter integral of the two-leg diagram with the encounter at the end

The relevant encounter integrals we have to solve for diagram (c) in Fig. 4.2 are given in Eq. (4.59) and (4.60) and read

$$F^{(2\text{le},(c))}(t) = \frac{1}{(2\pi\hbar_{\text{eff}})^{d-2}} \int_{-c}^c d^{d-2}s \int_{-c}^c d^{d-2}u e^{\frac{i}{\hbar_{\text{eff}}}\mathbf{s}\cdot\mathbf{u}} \times \int_{t-t_u(\mathbf{u})}^t dt' \frac{\Theta[t - t_{\text{enc}}^{(\text{eff})}(t', \mathbf{s})]}{t_{\text{enc}}^{(\text{eff})}(t', \mathbf{s})}, \quad (\text{A.100})$$

$$F_{ll'}^{(2\text{le},(c))}(t) = \frac{1}{(2\pi\hbar_{\text{eff}})^{d-2}} \int_{-c}^c d^{d-2}s \int_{-c}^c d^{d-2}u e^{\frac{i}{\hbar_{\text{eff}}}\mathbf{s}\cdot\mathbf{u}} u_l u_{l'} \times \int_{t-t_u(\mathbf{u})}^t dt' \frac{\Theta[t - t_{\text{enc}}^{(\text{eff})}(t', \mathbf{s})]}{t_{\text{enc}}^{(\text{eff})}(t', \mathbf{s})} e^{2\lambda(t-t')}, \quad (\text{A.101})$$

where the effective encounter time is taken as $t_{\text{enc}}^{(\text{eff})}(t', \mathbf{s}) = (t - t') + t_s(\mathbf{s})$. The stable and unstable times $t_s(\mathbf{s})$, $t_u(\mathbf{u})$ are defined in Eq. (4.31).

In a first step, we interchange the variable names for stable and unstable coordinates, $\mathbf{s} \leftrightarrow \mathbf{u}$, which formally interchanges $t_s(\mathbf{s}) \leftrightarrow t_u(\mathbf{u})$. Then we perform a variable transformation $t' \rightarrow t - t'$, which inverts the arrow of time. These steps convert the calculations for an encounter at the end to those for an encounter at the beginning of the trajectories, and we immediately obtain $F_{ll'}^{(2\text{le},(c))}(t) = F_{ll'}^{(2\text{le},(b))}(t)$. It thus remains to calculate $F^{(2\text{le},(c))}(t)$, which in its transformed version reads

$$F^{(2\text{le},(c))}(t) = \frac{1}{(2\pi\hbar_{\text{eff}})^{d-2}} \int_{-c}^c d^{d-2}s \int_{-c}^c d^{d-2}u e^{\frac{i}{\hbar_{\text{eff}}}\mathbf{s}\cdot\mathbf{u}} \int_0^{t_s(\mathbf{s})} dt' \frac{\Theta[t - t_{\text{enc}}^{(\text{eff})}(t', \mathbf{u})]}{t_{\text{enc}}^{(\text{eff})}(t', \mathbf{u})}. \quad (\text{A.102})$$

In the very same spirit as for four-leg diagrams in section A.4.2, we split

$$F^{(2le,(c))}(t) = \sum_{i,j=1}^{d-2} F_{ij}^{(2le,(c))}(t) \quad (\text{A.103})$$

to resolve the max-functions inherent in $t_s(\mathbf{s})$ and $t_u(\mathbf{u})$ in Eqs. (4.31). Within $F_{ij}^{(2le,(c))}(t)$ all integrations except for the ones over (s_i, u_j, t') are as easily performed as in section A.4.2. For these remaining integrals we use the variable transformation in Eq. (A.90). We obtain

$$F_{ij}^{(2le,(c))}(t) = \frac{1}{(2\pi\hbar_{\text{eff}})^{d-2}} \lambda \int_0^t dT \int_0^{e^{-\lambda T}} dS f_{ij}^{(2le,(c))}(S), \quad (\text{A.104})$$

where

- for $i = j$:

$$f_{ii}^{(2le,(c))}(S) = \text{Si}^{d-3} \left(\frac{c^2 S}{\hbar_{\text{eff}}} \right) \cos \left(\frac{c^2 S}{\hbar_{\text{eff}}} \right) \frac{c^2}{\hbar_{\text{eff}}}, \quad (\text{A.105})$$

- for $i \neq j$:

$$f_{ij}^{(2le,(c))}(t) = \text{Si}^{d-4} \left(\frac{c^2 S}{\hbar_{\text{eff}}} \right) \frac{\sin^2 \left(\frac{c^2 S}{\hbar_{\text{eff}}} \right)}{S}. \quad (\text{A.106})$$

Summing over indices, we find

$$\sum_{i,j=1}^{d-2} f_{ij}^{(2le,(c))}(S) = \frac{d}{dS} S \frac{d}{dS} \text{Si}^{d-2} \left(\frac{c^2 S}{\hbar_{\text{eff}}} \right), \quad (\text{A.107})$$

which allows us to easily evaluate the final integrations over S and T . We eventually obtain

$$F^{(2le,(c))}(t) = \left(\frac{2}{\pi} \right)^{d-2} \left[\text{Si}^{d-2} \left(e^{\lambda t_E} \right) - \text{Si}^{d-2} \left(e^{\lambda(t_E - t)} \right) \right]. \quad (\text{A.108})$$

Following the same arguments as in the section about the four-leg diagram, this term is only contributing for times larger than the Ehrenfest time t_E and can be approximated by $F^{(2le,(c))}(t) \approx \Theta(t - t_E)$ in the semiclassical limit. Both, the diagram (c) and (d) in Fig. 4.2 contribute a constant term to the OTOC for $t > t_E$.

A.4.5 Encounter integral of the zero-leg diagram

The relevant encounter integrals we have to solve for diagram (a) in Fig. 4.2 are given by Eq. (4.64) and (4.65). They read

$$F_{ll'}^{(0le,1)}(t) = \frac{1}{(2\pi\hbar_{\text{eff}})^{d-2}} \int_0^t dt' e^{2\lambda t'} \int_{-ce^{-\lambda t'}}^{ce^{-\lambda t'}} d^{d-2} s \int_{-ce^{-\lambda(t-t')}}^{ce^{-\lambda(t-t')}} d^{d-2} u \frac{e^{\frac{i}{\hbar_{\text{eff}}} \mathbf{s} \cdot \mathbf{u}}}{t} s_l s_{l'}, \quad (\text{A.109})$$

$$F_{l'l'mm'}^{(0le,2)}(t) = \frac{1}{(2\pi\hbar_{\text{eff}})^{d-2}} \int_0^t dt' e^{2\lambda t'} \int_{-ce^{-\lambda t'}}^{ce^{-\lambda t'}} d^{d-2}s \int_{-ce^{-\lambda(t-t')}}^{ce^{-\lambda(t-t')}} d^{d-2}u \frac{e^{\frac{i}{\hbar_{\text{eff}}}\mathbf{s}\cdot\mathbf{u}}}{t} s_l s_{l'} u_m u_{m'}. \quad (\text{A.110})$$

Using the same reasoning as before for two-leg diagrams, based on the variable transformation $(s_l, u_l) \rightarrow -(s_l, u_l)$ we can immediately conclude that $F_{l'l'}^{(0le,1)}(t) = 0$ for $l \neq l'$. Using further Eqs. (A.71, A.72) we find

$$F_{ll'}^{(0le,1)}(t) = -\left(\frac{2}{\pi}\right)^{d-2} c^2 \text{Si}^{d-3}\left(e^{\lambda(t_E-t)}\right) \text{Si}''\left(e^{\lambda(t_E-t)}\right). \quad (\text{A.111})$$

As has been argued after Eq. (A.98), this term can be neglected in the cases $t \ll t_E$ and $t \gg t_E$, but qualitatively, the underlying interference mechanism is involved in the crossover regime at $t \approx t_E$.

For $F_{l'l'mm'}^{(0le,2)}$ four indices are involved, and we find three classes of non-vanishing integrals, which are treated using all the Eqs. (A.71) – (A.74).

(a) For $l = l'$, $m = m'$ with $l \neq m$ we get

$$F_{llmm}^{(0le,2)}(t) = \left(\frac{2}{\pi}\right)^{d-2} c^4 \text{Si}^{d-4}\left(e^{\lambda(t_E-t)}\right) \left[\text{Si}''\left(e^{\lambda(t_E-t)}\right)\right]^2. \quad (\text{A.112})$$

(b) If the set of indices $\{l, l'\} = \{m, m'\}$ are equal without being all the same, *i.e.* $l \neq l'$, we get

$$F_{l'l'mm'}^{(0le,2)}(t) = -\left(\frac{2}{\pi}\right)^{d-2} c^4 \text{Si}^{d-4}\left(e^{\lambda(t_E-t)}\right) e^{2\lambda(t-t_E)} \left[\text{Si}\left(e^{\lambda(t_E-t)}\right) - \sin\left(e^{\lambda(t_E-t)}\right)\right]^2. \quad (\text{A.113})$$

(c) If all indices are the same, we get

$$\begin{aligned} F_{llll}^{(0le,2)}(t) = & -\left(\frac{2}{\pi}\right)^{d-2} c^4 \text{Si}^{d-4}\left(e^{\lambda(t_E-t)}\right) e^{2\lambda(t-t_E)} \\ & \times \left[2 \left[\text{Si}\left(e^{\lambda(t_E-t)}\right) - \sin\left(e^{\lambda(t_E-t)}\right) \right]^2 + \sin\left(e^{\lambda(t_E-t)}\right) \text{Si}\left(e^{\lambda(t_E-t)}\right) \right. \\ & \left. - 2 \sin^2\left(e^{\lambda(t_E-t)}\right) + \cos\left(e^{\lambda(t_E-t)}\right) \text{Si}\left(e^{\lambda(t_E-t)}\right) e^{\lambda(t_E-t)} \right]. \end{aligned} \quad (\text{A.114})$$

In case (a) the result contains the factor $\text{Si}''[\exp[\lambda(t_E-t)]]$ and thus, like $F_{ll}^{(0le,1)}(t)$, can be neglected for both $t \ll t_E$ and $t \gg t_E$. For case (b) we have for $t \ll t_E$:

$$\text{Si}\left(e^{\lambda(t_E-t)}\right) - \sin\left(e^{\lambda(t_E-t)}\right) \approx \text{Si}\left(e^{\lambda t_E}\right) \approx \frac{\pi}{2}, \quad (\text{A.115})$$

i.e. the highly oscillatory term $\sin[\exp[\lambda(t_E - t)]]$ is neglected and we use the asymptotic value for Si. For $t \gg t_E$, we obtain from a Taylor expansion around $\exp[\lambda(t_E - t)] \approx 0$

$$\text{Si}\left(e^{\lambda(t_E - t)}\right) - \sin\left(e^{\lambda(t_E - t)}\right) \approx \frac{1}{9}e^{3\lambda(t_E - t)}. \quad (\text{A.116})$$

Therefore, as $\text{Si}[\exp[\lambda(t_E - t)]] \approx \exp[\lambda(t_E - t)]$, we find

$$F_{l'l'mm'}^{(0le,2)}(t) \approx -\frac{1}{81}\left(\frac{2}{\pi}\right)^{d-2}c^4e^{d\lambda(t_E - t)}. \quad (\text{A.117})$$

i.e. the contribution becomes exponentially suppressed after the Ehrenfest time. We can thus approximate

$$F_{l'l'mm'}^{(0le,2)}(t) \approx -c^4e^{2\lambda(t - t_E)}\Theta(t_E - t) = -\hbar_{\text{eff}}^2e^{2\lambda t}\Theta(t_E - t). \quad (\text{A.118})$$

Note that since we have $\{l, l'\} = \{m, m'\}$ we get an additional combinatorial factor 2 when reducing the fourfold sum over l, l', m, m' in Eq. (4.63) to a twofold one over l, l' with $l \neq l'$. The case of equal indices $l = l'$ is still excluded from this summation, but using case (c), which also contains the same contribution as case (b) (explicitly including the prefactor 2), we can complete the summation. It remains to discuss the additional terms in the last lines of Eq. (A.114). Those can be neglected for $t \ll t_E$ as they all contain highly oscillatory factors. For $t \gg t_E$ we find

$$\begin{aligned} & \sin\left(e^{\lambda(t_E - t)}\right)\text{Si}\left(e^{\lambda(t_E - t)}\right) - 2\sin^2\left(e^{\lambda(t_E - t)}\right) \\ & + \cos\left(e^{\lambda(t_E - t)}\right)\text{Si}\left(e^{\lambda(t_E - t)}\right)e^{\lambda(t_E - t)} \approx -\frac{1}{9}e^{4\lambda(t_E - t)}. \end{aligned} \quad (\text{A.119})$$

This leads to a suppression of $F_{lll}^{(0le,2)}(t)$ for $t \gg t_E$, which is less strong than the one for $F_{l'l'mm'}^{(0le,2)}(t)$ in Eq. (A.117), but still exponential. Thus, the overall exponential suppression reads

$$F_{lll}^{(0le,2)}(t) \approx \frac{1}{9}e^{(d-2)\lambda(t_E - t)}. \quad (\text{A.120})$$

A.5 Scattering matrix elements for a discretized Y-junction

In this appendix, we derive the scattering matrix elements for scattering at a discretized Y-junction. The situation is depicted in Fig. A.2. Three semi-infinite, identical leads with on-site energies E_δ and hopping $-E_\delta/2$ are attached to a symmetric Y-junction, which is modeled by a single site $\alpha = 0$ with on-site energy E_Y and hopping $-E_\delta/2$ to any of the waveguides. The Hamiltonian of the system can be split into five parts,

$$\hat{H} = \hat{H}_{\mathcal{L}_{\text{in}}} + \hat{H}_{\mathcal{L}_{\text{out}}} + \hat{H}_{\mathcal{L}_{\text{out}'}} + \hat{H}_Y + \hat{H}_{\mathcal{L}_Y}. \quad (\text{A.121})$$

The three waveguides and the junction are modeled by

$$\hat{H}_{\mathcal{L}_X} = \sum_{\alpha} \left[E_\delta |\alpha\rangle\langle\alpha| - \frac{E_\delta}{2} (|\alpha\rangle\langle\alpha + 1| + |\alpha\rangle\langle\alpha - 1|) \right], \quad \hat{H}_Y = E_Y |0\rangle\langle 0| \quad (\text{A.122})$$

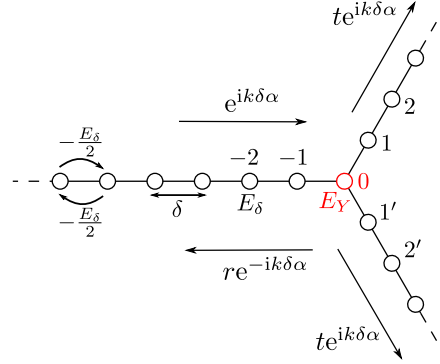


Figure A.2: Three semi-infinite, identical leads with on-site energies E_δ and hopping $-E_\delta/2$ are attached to a symmetric Y-junction formed by a single site $\alpha = 0$ with on-site energy E_Y and hopping $-E_\delta/2$ to any of the waveguides. An incoming plane wave $e^{ik\delta\alpha}$ in one of the waveguides transmits and reflects into the outgoing waves $re^{ik\delta\alpha}$ and $te^{ik\delta\alpha}$.

with $\alpha = -1, \dots, -\infty$ for X=in, and $\alpha = 1, 2, \dots$, or $\alpha = 1', 2'$ for $X \in \{\text{out}, \text{out}'\}$. In order to simplify notation, the Hamiltonians of the waveguides already partially couple to the junction site. The missing hopping terms are contained in $\hat{H}_{\mathcal{L}Y}$.

Within the waveguides, any scattering state, as a solution of the stationary Schrödinger equation $\mu |\psi\rangle = \hat{H} |\psi\rangle$, is found to be a superposition of the plane waves $e^{\pm ik\delta\alpha}$, with $\cos(k\delta) = 1 - \mu/E_\delta$, either traveling towards or away from the scattering center \hat{H}_Y . The incoming waves are linked to the outgoing ones through the elements of the scattering matrix. For the symmetric Y-junction, these elements take only one of two possible values r and t , describing either reflection or transmission through the junction. To obtain their values, we focus on a scattering state with a single incoming contribution, say, in the left waveguide in Fig. A.2. The ansatz for this scattering state is thus, already using continuity for $\alpha = 0$, and setting the amplitude of the incoming wave to 1,

$$\psi_\alpha = \begin{cases} e^{ik\delta\alpha} + re^{-ik\delta\alpha}, & \text{for } \alpha = -1, -2, \dots, \\ 1 + r = t, & \text{for } \alpha = 0, \\ te^{ik\delta\alpha}, & \text{for } \alpha = 1, 2, \dots, \text{ or } \alpha = 1', 2', \dots \end{cases} \quad (\text{A.123})$$

The values of r and t are obtained from considering the stationary Schrödinger equation at site $\alpha = 0$,

$$\mu\psi_0 = E_Y\psi_0 - \frac{E_\delta}{2}(\psi_{-1} + \psi_1 + \psi_{1'}). \quad (\text{A.124})$$

Inserting the ansatz Eq. (A.123) and using the continuity condition $1 + r = t$, we can solve this equation for r and t . We find

$$r = -\frac{1 - \frac{E_Y}{E_\delta} + \frac{1}{2}e^{ik\delta}}{1 - \frac{E_Y}{E_\delta} + e^{ik\delta} - \frac{1}{2}e^{-ik\delta}}, \quad t = \frac{i \sin(k\delta)}{1 - \frac{E_Y}{E_\delta} + e^{ik\delta} - \frac{1}{2}e^{-ik\delta}}. \quad (\text{A.125})$$

Within the numerical simulations, the parameters $\mu = 0.2E_\delta$ and $E_Y = E_\delta$ have been chosen. This leads to

$$r = -\frac{43}{97} + i\frac{24}{97}, \quad t = \frac{54}{97} + i\frac{24}{97}, \quad (\text{A.126})$$

which we use as input to compare analytical with the numerical results.

A.6 List of resummed diagrams

Here we list all resummed diagrams we find in section 6.1 as well as the diagrams we obtain from them through the application of the arguments listed in 6.1.2.

The diagrams representing the resummation of all paths which in the end either transverse or reflect of one of the junctions, are related to Eq. (6.10) and are found to be

$$\begin{aligned} \begin{array}{c} \uparrow \\ \bullet \\ \leftarrow \\ \bullet \\ \downarrow \end{array} &= t \frac{1 + (r^2 - t^2)e^{i(\Phi_u + \Phi_d - \Phi)}}{D(\Phi_u, \Phi_d, \Phi)} = \begin{array}{c} \bullet \\ \leftarrow \\ \bullet \\ \downarrow \end{array}, & \begin{array}{c} \bullet \\ \leftarrow \\ \bullet \\ \downarrow \end{array} &= r \frac{1 - (r^2 - t^2)e^{i2\Phi_u}}{D(\Phi_u, \Phi_d, \Phi)} = \begin{array}{c} \bullet \\ \leftarrow \\ \bullet \\ \downarrow \end{array}, \end{aligned} \quad (\text{A.127})$$

$$\begin{aligned} \begin{array}{c} \bullet \\ \leftarrow \\ \bullet \\ \downarrow \end{array} &= t \frac{1 + (r^2 - t^2)e^{i(\Phi_u + \Phi_d + \Phi)}}{D(\Phi_u, \Phi_d, \Phi)} = \begin{array}{c} \bullet \\ \leftarrow \\ \bullet \\ \downarrow \end{array}, & \begin{array}{c} \bullet \\ \leftarrow \\ \bullet \\ \downarrow \end{array} &= r \frac{1 - (r^2 - t^2)e^{i2\Phi_d}}{D(\Phi_u, \Phi_d, \Phi)} = \begin{array}{c} \bullet \\ \leftarrow \\ \bullet \\ \downarrow \end{array}. \end{aligned} \quad (\text{A.128})$$

The next classes of diagrams describe resummations of contributions of paths starting and ending within the ring, but at opposite junctions. These are obtained from Eqs. (6.14), (6.15), and found to be

$$\begin{array}{c} \leftarrow \\ \bullet \\ \leftarrow \\ \bullet \end{array} = e^{-i(\Phi_d - \frac{\Phi}{2})} \left(\frac{1 - r^2 e^{i2\Phi_u} - t^2 e^{i(\Phi_u + \Phi_d + \Phi)}}{D(\Phi_u, \Phi_d, \Phi)} - 1 \right), \quad (\text{A.129})$$

$$\begin{array}{c} \bullet \\ \rightarrow \\ \bullet \\ \rightarrow \end{array} = e^{-i(\Phi_u - \frac{\Phi}{2})} \left(\frac{1 - r^2 e^{i2\Phi_d} - t^2 e^{i(\Phi_u + \Phi_d + \Phi)}}{D(\Phi_u, \Phi_d, \Phi)} - 1 \right), \quad (\text{A.130})$$



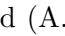
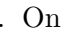
$$\begin{array}{c} \bullet \\ \leftarrow \\ \bullet \\ \leftarrow \end{array} = e^{-i(\Phi_u + \frac{\Phi}{2})} \left(\frac{1 - r^2 e^{i2\Phi_d} - t^2 e^{i(\Phi_u + \Phi_d - \Phi)}}{D(\Phi_u, \Phi_d, \Phi)} - 1 \right), \quad (\text{A.131})$$

$$\begin{array}{c} \bullet \\ \rightarrow \\ \bullet \\ \rightarrow \end{array} = e^{-i(\Phi_u - \frac{\Phi}{2})} \frac{rt(e^{2i\Phi_u} + e^{i(\Phi_u + \Phi_d - \Phi)})}{D(\Phi_u, \Phi_d, \Phi)} \quad (\text{A.132})$$

$$= e^{-i(\Phi_d + \frac{\Phi}{2})} \frac{rt(e^{2i\Phi_d} + e^{i(\Phi_u + \Phi_d + \Phi)})}{D(\Phi_u, \Phi_d, \Phi)} = \begin{array}{c} \bullet \\ \rightarrow \\ \bullet \\ \rightarrow \end{array}, \quad (\text{A.133})$$

$$\begin{array}{c} \bullet \\ \leftarrow \\ \bullet \\ \leftarrow \end{array} = e^{-i(\Phi_u + \frac{\Phi}{2})} \frac{rt(e^{2i\Phi_u} + e^{i(\Phi_u + \Phi_d + \Phi)})}{D(\Phi_u, \Phi_d, \Phi)} \quad (\text{A.134})$$

$$= e^{-i(\Phi_d - \frac{\Phi}{2})} \frac{rt(e^{2i\Phi_d} + e^{i(\Phi_u + \Phi_d - \Phi)})}{D(\Phi_u, \Phi_d, \Phi)} = \begin{array}{c} \bullet \\ \leftarrow \\ \bullet \\ \leftarrow \end{array}. \quad (\text{A.135})$$

The equivalence of the expressions for  and , as well as for  and  is an interesting application of the system's symmetries. On the other hand, the diagrams can be obtained from each other by a single reflection along the horizontal symmetry axis, which results in equations (A.133) and (A.135). On the other hand, these expressions should coincide with equations (A.132) and (A.134), since the diagrams also result from each other by a reflection along the vertical symmetry axis and a subsequent time-reversal, which together flips the sign in front of the gauge field phase Φ twice, leaving the overall result invariant under this combined operation. Indeed, the equivalence of (A.133) with (A.132, as well as (A.135) with (A.134) holds, as one can easily check.

Starting from Eq. (6.16), we find

$$\begin{array}{c} \text{red arrow pointing right with red arrow pointing up from tip} \\ \bullet \end{array} = t \frac{1 - (r - t)(re^{i2\Phi_d} - te^{i(\Phi_u + \Phi_d - \Phi)})}{D(\Phi_u, \Phi_d, \Phi)} = \begin{array}{c} \text{red arrow pointing right with red arrow pointing down from tip} \\ \bullet \end{array}, \quad (\text{A.136})$$

$$\begin{array}{c} \text{red arrow pointing left with red arrow pointing up from tip} \\ \bullet \end{array} = t \frac{1 - (r - t)(re^{i2\Phi_u} - te^{i(\Phi_u + \Phi_d + \Phi)})}{D(\Phi_u, \Phi_d, \Phi)} = \begin{array}{c} \text{red arrow pointing left with red arrow pointing down from tip} \\ \bullet \end{array}, \quad (\text{A.137})$$

$$\begin{array}{c} \text{red arrow pointing right with red arrow pointing up from tip} \\ \bullet \end{array} = t \frac{1 - (r - t)(re^{i2\Phi_d} - te^{i(\Phi_u + \Phi_d + \Phi)})}{D(\Phi_u, \Phi_d, \Phi)}, \quad (\text{A.138})$$

$$\begin{array}{c} \text{red arrow pointing left with red arrow pointing up from tip} \\ \bullet \end{array} = t \frac{1 - (r - t)(re^{i2\Phi_u} - te^{i(\Phi_u + \Phi_d - \Phi)})}{D(\Phi_u, \Phi_d, \Phi)}. \quad (\text{A.139})$$

The other remaining resummed diagrams of the same type are:

$$\begin{array}{c} \text{red arrow pointing right with red arrow pointing up from tip} \\ \bullet \end{array} = e^{-i(\Phi_u - \frac{\Phi}{2})} t \frac{re^{i2\Phi_u} + te^{i(\Phi_u + \Phi_d - \Phi)} - (r - t)(r^2 - t^2)e^{i2(\Phi_u + \Phi_d)}}{D(\Phi_u, \Phi_d, \Phi)} = \begin{array}{c} \text{red arrow pointing right with red arrow pointing down from tip} \\ \bullet \end{array} \quad (\text{A.140})$$

$$\begin{array}{c} \text{red arrow pointing left with red arrow pointing up from tip} \\ \bullet \end{array} = e^{-i(\Phi_d + \frac{\Phi}{2})} t \frac{re^{i2\Phi_d} + te^{i(\Phi_u + \Phi_d + \Phi)} - (r - t)(r^2 - t^2)e^{i2(\Phi_u + \Phi_d)}}{D(\Phi_u, \Phi_d, \Phi)} = \begin{array}{c} \text{red arrow pointing left with red arrow pointing down from tip} \\ \bullet \end{array} \quad (\text{A.141})$$

$$\begin{array}{c} \text{red arrow pointing right with red arrow pointing up from tip} \\ \bullet \end{array} = e^{-i(\Phi_u + \frac{\Phi}{2})} t \frac{re^{i2\Phi_u} + te^{i(\Phi_u + \Phi_d + \Phi)} - (r - t)(r^2 - t^2)e^{i2(\Phi_u + \Phi_d)}}{D(\Phi_u, \Phi_d, \Phi)} \quad (\text{A.142})$$

$$\begin{array}{c} \text{red arrow pointing left with red arrow pointing up from tip} \\ \bullet \end{array} = e^{-i(\Phi_d - \frac{\Phi}{2})} t \frac{re^{i2\Phi_d} + te^{i(\Phi_u + \Phi_d - \Phi)} - (r - t)(r^2 - t^2)e^{i2(\Phi_u + \Phi_d)}}{D(\Phi_u, \Phi_d, \Phi)}. \quad (\text{A.143})$$

A.7 Numerical averaging of reflection and transmission probabilities

The main idea for numerically calculating the averaged reflection and transmission probability is to calculate the integrals in (6.50) and (6.52) using, e.g., a Monte-Carlo simu-

lation. The most expensive part of this calculation is the evaluation of the exponentials $e^{i\Phi_u}$, $e^{i\Phi_d}$, $e^{i\Phi}$, since these are nonlinear functions. Our aim is thus to express the integrand in equations (6.50) and (6.52) through functions of the exponentials $e^{i\Phi_u}$, $e^{i\Phi_d}$, $e^{i\frac{\Phi}{2}}$ instead of the phases Φ_u , Φ_d , Φ . As a consequence, in every cycle of the calculation, the phase factors have only to be calculated once.

Basic functions

When looking at the basic resummed diagrams in equations (6.50) and (6.52), we see, that we need to implement the following ones:

$$\begin{aligned}
 \begin{array}{c} \uparrow \\ \bullet \\ \leftarrow \end{array} &= \begin{array}{c} \rightarrow \\ \bullet \\ \leftarrow \end{array}, \quad \begin{array}{c} \leftarrow \\ \bullet \\ \downarrow \end{array} = \begin{array}{c} \rightarrow \\ \bullet \\ \leftarrow \end{array}, \quad \begin{array}{c} \leftarrow \\ \bullet \\ \leftarrow \end{array}, \\
 \begin{array}{c} \uparrow \\ \bullet \\ \rightarrow \end{array} &= \begin{array}{c} \rightarrow \\ \bullet \\ \rightarrow \end{array}, \quad \begin{array}{c} \rightarrow \\ \bullet \\ \downarrow \end{array} = \begin{array}{c} \rightarrow \\ \bullet \\ \rightarrow \end{array}, \quad \begin{array}{c} \leftarrow \\ \bullet \\ \leftarrow \end{array}.
 \end{aligned} \tag{A.144}$$

Thus, a review of our calculations in section 6.1 motivates the definition of the following functions

$$\begin{aligned}
 w(z_u, z_d, z) &= 1 - r^2(z_u^2 + z_d^2) - t^2 z_u z_d (z + z^*) + (r^2 - t^2)^2 z_u^2 z_d^2 \\
 &= 1 - r^2(z_u^2 + z_d^2) - t^2 z_u z_d (z + z^*) + (r + t)^2 z_u^2 z_d^2, \\
 f_1(z_u, z_d, z) &= t(1 - (r - t)(r z_d^2 - t z_u z_d z^*)) \\
 &= t(1 + r z_d^2 - t z_u z_d z^*), \\
 f_2(z_u, z_d, z) &= t(r z_u^2 + t z_u z_d z^* - (r - t)(r^2 - t^2) z_u^2 z_d^2) \\
 &= t(r z_u^2 + t z_u z_d z^* - (r + t) z_u^2 z_d^2).
 \end{aligned} \tag{A.145}$$

We used here that, due to continuity of the wave functions at the junctions, we have

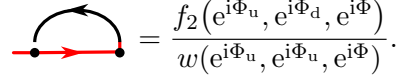
$$1 + r = t \leftrightarrow r - t = -1. \tag{A.146}$$

Then, the common denominator and the basic diagrams are given by

$$\begin{aligned}
 D(\Phi_u, \Phi_d, \Phi) &= w(e^{i\Phi_u}, e^{i\Phi_d}, e^{i\Phi}) \tag{A.147} \\
 \begin{array}{c} \uparrow \\ \bullet \\ \leftarrow \end{array} &= \begin{array}{c} \rightarrow \\ \bullet \\ \leftarrow \end{array} = \frac{f_1(e^{i\Phi_u}, e^{i\Phi_d}, e^{i\Phi})}{w(e^{i\Phi_u}, e^{i\Phi_d}, e^{i\Phi})}, \quad \begin{array}{c} \rightarrow \\ \bullet \\ \rightarrow \end{array} = \begin{array}{c} \rightarrow \\ \bullet \\ \rightarrow \end{array} = \frac{1}{e^{i(\Phi_u - \frac{\Phi}{2})}} \frac{f_2(e^{i\Phi_u}, e^{i\Phi_d}, e^{i\Phi})}{w(e^{i\Phi_u}, e^{i\Phi_d}, e^{i\Phi})}, \\
 \begin{array}{c} \leftarrow \\ \bullet \\ \downarrow \end{array} &= \begin{array}{c} \rightarrow \\ \bullet \\ \leftarrow \end{array} = \frac{f_1(e^{i\Phi_d}, e^{i\Phi_u}, e^{-i\Phi})}{w(e^{i\Phi_u}, e^{i\Phi_d}, e^{i\Phi})}, \quad \begin{array}{c} \rightarrow \\ \bullet \\ \downarrow \end{array} = \begin{array}{c} \rightarrow \\ \bullet \\ \rightarrow \end{array} = \frac{1}{e^{i(\Phi_d + \frac{\Phi}{2})}} \frac{f_2(e^{i\Phi_d}, e^{i\Phi_u}, e^{-i\Phi})}{w(e^{i\Phi_u}, e^{i\Phi_d}, e^{i\Phi})}, \\
 \begin{array}{c} \leftarrow \\ \bullet \\ \leftarrow \end{array} &= \frac{f_1(e^{i\Phi_u}, e^{i\Phi_d}, e^{-i\Phi})}{w(e^{i\Phi_u}, e^{i\Phi_d}, e^{i\Phi})}, \quad \begin{array}{c} \leftarrow \\ \bullet \\ \leftarrow \end{array} = \frac{1}{e^{i(\Phi_u + \frac{\Phi}{2})}} \frac{f_2(e^{i\Phi_u}, e^{i\Phi_d}, e^{-i\Phi})}{w(e^{i\Phi_u}, e^{i\Phi_d}, e^{i\Phi})}.
 \end{aligned}$$

In the expressions in the second column, we could, in principle, add the additional phase factor in front of the fraction to the definition of f_2 . However, we deliberately excluded

it, first, to avoid an additional dependence on $e^{i\frac{\Phi}{2}}$ and second since this factor usually gets canceled by a subsequent free Green's function in the diagrammatic equations or vanishes due to calculating the modulus square. E.g. we have



$$\text{Diagram} = \frac{f_2(e^{i\Phi_u}, e^{i\Phi_d}, e^{i\Phi})}{w(e^{i\Phi_u}, e^{i\Phi_u}, e^{i\Phi})}.$$

Pseudo-code for numerical calculation of the averaged probabilities

The following scheme performs the numerical averaging

1. **Define the functions w , f_1 , f_2 as above.** To save computation time, it might be worth to first calculate and store the repeatedly appearing, constant factors r^2 , t^2 , $(r+t)$, $(r+t)^2$.
2. **Create a vector containing the phases $e^{i\Phi}$:** Choose a suitable large number $N_1 \in \mathbb{N}$ to divide the interval $[0, 2\pi]$ and set $\mathbf{v} = (v_l)_{l=1, \dots, N_1}$ with $v_l = e^{i\frac{l}{N_1}2\pi}$. We interpret $v_l = e^{i\Phi}$ with $\Phi = \frac{l}{N_1}2\pi$. (Since the result is expected to be symmetric with respect to $\Phi \leftrightarrow -\Phi$, it would be enough to discretize the smaller interval $[0, \pi]$, which speeds up the calculation. However, one can use the additional information as a check for the numerical procedure.)
3. **Initialize two empty vectors $\Delta\mathcal{R}^{(k)} = \mathbf{0}$, $\Delta\mathcal{T}^{(k)} = \mathbf{0}$,** which will be used for summing reflection and transmission probabilities at fixed gauge field in first order. (Do not confuse the subscript here, which indicates the iteration number, with the subscripts of the main text, which indicates the order in the perturbation theory).
4. **Loop over disorder configurations:** Choose a second large number N_2 of disorder configurations for the average. For each $k \in \{1, \dots, N_2\}$, do
 - a) Draw Φ_u, Φ_d from a uniform distribution in $[0, 2\pi)$ and calculate $z_u = e^{i\Phi_u}$, $z_d = e^{i\Phi_d}$.
 - b) Loop over gauge field strengths: For $l \in \{1, \dots, N_1\}$, do
 - i. Calculate the common denominator

$$d = w(z_u, z_d, v_l). \quad (\text{A.148})$$

- ii. Calculate the numerator functions

$$\begin{aligned} f_{11} &= f_1(z_u, z_d, v_l), & f_{21} &= f_2(z_u, z_d, v_l), \\ f_{12} &= f_1(z_d, z_u, v_l^*), & f_{22} &= f_2(z_d, z_u, v_l^*), \\ f_{13} &= f_1(z_u, z_d, v_l^*), & f_{23} &= f_2(z_u, z_d, v_l^*). \end{aligned} \quad (\text{A.149})$$

iii. Calculate their modulus squared

$$\begin{aligned}
\alpha_{11} &= |d|^2 \cdot \overrightarrow{f_1} = f_{11} f_{11}^*, & \alpha_{21} &= |d|^2 \cdot \overrightarrow{f_2} = f_{21} f_{21}^*, \\
\alpha_{12} &= |d|^2 \cdot \overrightarrow{f_2} = f_{12} f_{12}^*, & \alpha_{22} &= |d|^2 \cdot \overrightarrow{f_1} = f_{22} f_{22}^*, \\
\alpha_{13} &= |d|^2 \cdot \overrightarrow{f_3} = f_{13} f_{13}^*, & \alpha_{23} &= |d|^2 \cdot \overrightarrow{f_3} = f_{23} f_{23}^*.
\end{aligned} \tag{A.150}$$

iv. Update $\Delta\mathcal{R}^{(k)}$, $\Delta\mathcal{T}^{(k)}$ according to equations (6.50) and (6.52)

$$\begin{aligned}
\Delta\mathcal{R}_l^{(k)} &= \Delta\mathcal{R}_l^{(k-1)} + \text{Im} \left\{ \left(r + t \frac{f_{21} + f_{22}}{d} \right)^* \right. \\
&\quad \left. \times \frac{1}{d^3 d^*} (\alpha_{11} + \alpha_{23}, \alpha_{13} + \alpha_{21}) \begin{pmatrix} 1 & 2 \\ 2 & 1 \end{pmatrix} \begin{pmatrix} f_{11} \cdot f_{23} \\ f_{21} \cdot f_{13} \end{pmatrix} \right\} \\
\Delta\mathcal{T}_l^{(k)} &= \Delta\mathcal{T}_l^{(k-1)} + \text{Im} \left\{ \left[\frac{t}{d} (f_{11} z_u \sqrt{z} + f_{21} z_d \sqrt{z}^*) \right]^* \right. \\
&\quad \times \left[\frac{1}{d^3 d^*} (\alpha_{11}, \alpha_{21}) \begin{pmatrix} 1 & 2 \\ 2 & 1 \end{pmatrix} \begin{pmatrix} f_{11}^2 z_u \sqrt{z} \\ f_{21}^2 \frac{1}{z_u \sqrt{z}^*} \end{pmatrix} \right. \\
&\quad \left. \left. + \frac{1}{d^3 d^*} (\alpha_{12}, \alpha_{22}) \begin{pmatrix} 1 & 2 \\ 2 & 1 \end{pmatrix} \begin{pmatrix} f_{12}^2 z_d \sqrt{z}^* \\ f_{22}^2 \frac{1}{z_d \sqrt{z}} \end{pmatrix} \right] \right\} \\
&= \Delta\mathcal{T}_l^{(k-1)} + \text{Im} \left\{ \left[\frac{t}{d} (f_{11} z_u z + f_{21} z_d) \right]^* \right. \\
&\quad \times \frac{1}{d^3 d^*} \left[(\alpha_{11}, \alpha_{21}) \begin{pmatrix} 1 & 2 \\ 2 & 1 \end{pmatrix} \begin{pmatrix} f_{11}^2 z_u z \\ f_{21}^2 z_u^* z \end{pmatrix} \right. \\
&\quad \left. \left. + (\alpha_{12}, \alpha_{22}) \begin{pmatrix} 1 & 2 \\ 2 & 1 \end{pmatrix} \begin{pmatrix} f_{12}^2 z_d \\ f_{22}^2 z_d^* \end{pmatrix} \right] \right\}
\end{aligned} \tag{A.151}$$

where for the transmission we interpret the complex square root as $\sqrt{z} = e^{i\frac{\Phi}{2}}$ and $\sqrt{z}^* = e^{-i\frac{\Phi}{2}}$. In the second line of the transmission we got rid of these roots by extracting \sqrt{z} from the first, complex conjugate factor,

$$(f_{11} z_u \sqrt{z} + f_{21} z_d \sqrt{z}^*)^* = \sqrt{z} (f_{11} z_u z + f_{21} z_d)^*, \tag{A.152}$$

and multiplying the remaining part of the expression with it.

5. Multiply the vectors $\Delta\mathcal{R}^{(N_2)}$ and $\Delta\mathcal{T}^{(N_2)}$ with $\mathcal{N}_{\mathcal{R}} g \rho^\varnothing / (N_2 \sin(k\delta))$

$$\langle \Delta\mathbf{R} \rangle = \frac{g \mathcal{N}_{\mathcal{R}} \rho}{N_2 \sin(k\delta)} \Delta\mathcal{R}^{(N_2)}, \quad \langle \Delta\mathbf{T} \rangle = \frac{g \mathcal{N}_{\mathcal{R}} \rho}{N_2 \sin(k\delta)} \Delta\mathcal{T}^{(N_2)} \tag{A.153}$$

After the integration has converged, the theoretically expected correction to the reflection and transmission probabilities is, as a function of the gauge field, represented by the vectors $\langle \Delta\mathbf{R} \rangle$ and $\langle \Delta\mathbf{T} \rangle$.

List of publications

- J. Rammensee, J. D. Urbina, and K. Richter, “Many-Body Quantum Interference and the Saturation of Out-of-Time-Order Correlators”, *Phys. Rev. Lett.* **121**, 124101 (2018). [Chapter 4]
- R. Chrétien, J. Rammensee, J. Dujardin, C. Petitjean, and P. Schlagheck, “Al’tshuler-Aronov-Spivak oscillations of bosonic matter-wave beams in the presence of interaction”, arXiv:1812.05999 (2018). [Chapter 6]

Notation

In this section we present our notation of frequently used mathematical expressions

- $\mathbb{N} = \{1, 2, 3, \dots\}$ is the set of positive integers. 0 is included in $\mathbb{N}_0 = \mathbb{N} \cup \{0\}$.
- Variables in boldface, *e.g.* \mathbf{n} , \mathbf{x} , Φ , are understood as vectors. Components in a basis are labeled with an index, *e.g.* n_i . If we denote the set of indices as \mathcal{I} the following representations are equivalent:

$$\mathbf{x} = (x_i)_{i \in \mathcal{I}} = (x_i)_i.$$

- Vectors are understood as column vectors. They are transformed to row vectors by transposing, \mathbf{x}^\top . If additionally, the vector's components are complex conjugated, we call the vector Hermitian conjugate and write $\mathbf{x}^\dagger = (\mathbf{x}^\top)^*$, where the complex conjugation of a variable or the components of a vector or matrix is indicated by the superscript $*$.
- Since vectors and matrices often appear as functions, *e.g.* $\mathbf{M}(\mathbf{x}; t)$ we use the dot \cdot in order to highlight a matrix product. Occasionally, we also use the same symbol for the real scalar product of two vectors, whenever this simplifies the notation, *i.e.* we have the identity $\mathbf{x}^\top \mathbf{x}' = \mathbf{x} \cdot \mathbf{x}'$.
- The norm of a vector is calculated as

$$\|\mathbf{x}\| = \sqrt{\sum_{i \in \mathcal{I}} |x_i|^2} = \sqrt{\mathbf{x}^\dagger \mathbf{x}}$$

- A scalar function differentiated by a vector is understood as gradient,

$$\frac{\partial f}{\partial \mathbf{q}} = \left(\frac{\partial f}{\partial q_i} \right)_i^\top$$

The second derivative results in a matrix,

$$\left(\frac{\partial^2 f}{\partial \mathbf{q} \partial \mathbf{p}} \right)_{ij} = \frac{\partial^2 f}{\partial q_i \partial p_j}.$$

In this notation, the Taylor expansion of a function is up to second order written as

$$f(\mathbf{q} + \mathbf{y}) = f(\mathbf{q}) + \frac{\partial f}{\partial \mathbf{q}} \mathbf{y} + \frac{1}{2} \mathbf{y}^\top \frac{\partial^2 f}{\partial \mathbf{q} \partial \mathbf{q}} \cdot \mathbf{y} + \mathcal{O}(\|\mathbf{y}\|^3).$$

- A vector-valued function $\mathbf{f} = (f_i)_i^\top$ differentiated by a scalar is a vector

$$\frac{d\mathbf{f}}{ds} = \left(\frac{df_i}{ds} \right)_i^\top.$$

The differentiation by a vector is interpreted as a matrix

$$\left(\frac{\partial \mathbf{f}}{\partial \mathbf{q}} \right)_{ij} = \frac{\partial f_i}{\partial q_j}.$$

Again, this notation is motivated from the Taylor expansion

$$\mathbf{f}(\mathbf{q} + \mathbf{y}) = \mathbf{f}(\mathbf{q}) + \frac{\partial \mathbf{f}}{\partial \mathbf{q}} \cdot \mathbf{y} + \mathcal{O}(\|\mathbf{y}\|^2).$$

- A differentiation with respect to the time variable is indicated by a dot,

$$\dot{\mathbf{q}}(t) = \frac{d\mathbf{q}}{dt}(t)$$

- In integrations we omit the integration volume if it is \mathbb{R}^d . The dimension of the vector space is indicated by the integration measure,

$$\int d^d q = \int_{\mathbb{R}^d} d^d q$$

- If the integration volume is the product $[a, b]^d$ of a one-dimensional interval $[a, b]$, we use the shorthand notation

$$\int_a^b d^d q = \int_{[a,b]^d} d^d q = \int_a^b dq_1 \cdot \int_a^b dq_d \quad (7.154)$$

Bibliography

- [1] M. C. Gutzwiller, *Chaos in classical and quantum mechanics* (Springer, 1991).
- [2] M. Brack, and R. K. Bhaduri, *Semiclassical physics*, Frontiers in physics (Westview, 2003).
- [3] H. U. Baranger, R. A. Jalabert, and A. D. Stone, “Weak localization and integrability in ballistic cavities”, *Phys. Rev. Lett.* **70**, 3876 (1993).
- [4] K. Richter, and M. Sieber, “Semiclassical Theory of Chaotic Quantum Transport”, *Phys. Rev. Lett.* **89**, 206801 (2002).
- [5] Y. Gefen, Y. Imry, and M. Y. Azbel, “Quantum oscillations and the Aharonov-Bohm effect for parallel resistors”, *Phys. Rev. Lett.* **52**, 129 (1984).
- [6] Y. Aharonov, and D. Bohm, “Significance of Electromagnetic Potentials in the Quantum Theory”, *Phys. Rev.* **115**, 485 (1959).
- [7] B. L. Al’tshuler, A. G. Aronov, and B. Z. Spivak, “The Aaronov-Bohm effect in disordered conductors”, *JETP Lett.* **33**, 94 (1981).
- [8] M. H. Anderson, J. R. Ensher, M. R. Matthews, C. E. Wieman, and E. A. Cornell, “Observation of Bose-Einstein Condensation in a Dilute Atomic Vapor”, *Science* **269**, 198 (1995).
- [9] K. B. Davis, M. O. Mewes, M. R. Andrews, N. J. Van Druten, D. S. Durfee, D. M. Kurn, and W. Ketterle, “Bose-Einstein condensation in a gas of sodium atoms”, *Phys. Rev. Lett.* **75**, 3969 (1995).
- [10] K. V. Krutitsky, “Ultracold bosons with short-range interaction in regular optical lattices”, *Phys. Rep.* **607**, 1 (2016).
- [11] C. J. Pethick, and H. Smith, *Bose-Einstein Condensation in Dilute Gases* (Cambridge University Press, 2008).
- [12] M. Greiner, O. Mandel, T. Esslinger, T. W. Hänsch, and I. Bloch, “Quantum phase transition from a superfluid to a Mott insulator in a gas of ultracold atoms”, *Nature* **415**, 39 (2002).
- [13] T. Stöferle, H. Moritz, C. Schori, M. Köhl, and T. Esslinger, “Transition from a strongly interacting 1D superfluid to a Mott insulator”, *Phys. Rev. Lett.* **92**, 1 (2004).

-
- [14] I. Spielman, W. Phillips, and J. Porto, “Mott-Insulator Transition in a Two-Dimensional Atomic Bose Gas”, *Phys. Rev. Lett.* **98**, 080404 (2007).
- [15] A. Ramanathan, K. C. Wright, S. R. Muniz, M. Zelan, W. T. Hill, C. J. Lobb, K. Helmerson, W. D. Phillips, and G. K. Campbell, “Superflow in a toroidal Bose-Einstein condensate: An atom circuit with a tunable weak link”, *Phys. Rev. Lett.* **106**, 1 (2011).
- [16] V. Milner, J. L. Hanssen, W. C. Campbell, and M. G. Raizen, “Optical billiards for atoms”, *Phys. Rev. Lett.* **86**, 1514 (2001).
- [17] K. Henderson, C. Ryu, C. MacCormick, and M. G. Boshier, “Experimental demonstration of painting arbitrary and dynamic potentials for Bose-Einstein condensates”, *New J. Phys.* **11** (2009).
- [18] W. Guerin, J. F. Riou, J. P. Gaebler, V. Josse, P. Bouyer, and A. Aspect, “Guided quasicontinuous atom laser”, *Phys. Rev. Lett.* **97**, 1 (2006).
- [19] A. Couvert, M. Jeppesen, T. Kawalec, G. Reinaudi, R. Mathevet, and D. Guéry-Odelin, “A quasi-monomode guided atom laser from an all-optical Bose-Einstein condensate”, *Europhys. Lett.* **83** (2008).
- [20] J. Billy, V. Josse, Z. Zuo, A. Bernard, B. Hambrecht, P. Lugan, D. Clément, L. Sanchez-Palencia, P. Bouyer, and A. Aspect, “Direct observation of Anderson localization of matter waves in a controlled disorder”, *Nature* **453**, 891 (2008).
- [21] G. Juzeliunas, P. Åhberg, J. Ruseckas, and A. Klein, “Effective magnetic fields in degenerate atomic gases induced by light beams with orbital angular momenta”, *Phys. Rev. A* **71**, 1 (2005).
- [22] J. Dalibard, F. Gerbier, G. Juzeliunas, and P. Öhberg, “Colloquium: Artificial gauge potentials for neutral atoms”, *Rev. Mod. Phys.* **83**, 1523 (2011).
- [23] C. Chin, R. Grimm, P. Julienne, and E. Tiesinga, “Feshbach resonances in ultracold gases”, *Rev. Mod. Phys.* **82**, 1225 (2010).
- [24] E. Gross, “Structure of Quantized Vortex”, *Nuovo Cim.* **20**, 454 (1961).
- [25] L. P. Pitaevskii, “Vortex Lines in an Imperfect Bose Gas”, *Sov. Phys. JETP-USSR* **13**, 451 (1961).
- [26] F. Jendrzejewski, K. Müller, J. Richard, A. Date, T. Plisson, P. Bouyer, A. Aspect, and V. Josse, “Coherent Backscattering of Ultracold Atoms”, *Phys. Rev. Lett.* **109**, 195302 (2012).
- [27] C. D’Errico, M. Fattori, M. Zaccanti, M. Inguscio, M. Modugno, G. Modugno, C. Fort, L. Fallani, and G. Roati, “Anderson localization of a non-interacting Bose-Einstein condensate”, *Nature* **453**, 895 (2008).

- [28] M. Hartung, T. Wellens, C. A. Müller, K. Richter, and P. Schlagheck, “Coherent backscattering of bose-einstein condensates in two-dimensional disorder potentials”, *Phys. Rev. Lett.* **101**, 1 (2008).
- [29] T. Hartmann, J. Michl, C. Petitjean, T. Wellens, J.-D. Urbina, K. Richter, and P. Schlagheck, “Weak localization with nonlinear bosonic matter waves”, *Ann. Phys.* **327**, 1998 (2012).
- [30] R. Chrétien, J. Rammensee, J. Dujardin, C. Petitjean, and P. Schlagheck, *Al’tshuler-Aronov-Spivak oscillations of bosonic matter-wave beams in the presence of interaction*, 2018, arXiv:1812.05999.
- [31] T. Ernst, T. Paul, and P. Schlagheck, “Transport of ultracold Bose gases beyond the Gross-Pitaevskii description”, *Phys. Rev. A* **81**, 1 (2010).
- [32] T. Hartmann, “Transport of Bose-Einstein condensates through two dimensional cavities”, PhD thesis (Universität Regensburg, Universitätsverlag Regensburg, Apr. 2015).
- [33] T. Engl, “A Semiclassical Approach to Many-Body Interference in Fock-Space”, PhD thesis (Universität Regensburg, Universitätsverlag Regensburg, 2015).
- [34] T. Engl, J. Dujardin, A. Argüelles, P. Schlagheck, K. Richter, and J. D. Urbina, “Coherent Backscattering in Fock Space: A Signature of Quantum Many-Body Interference in Interacting Bosonic Systems”, *Phys. Rev. Lett.* **112**, 140403 (2014).
- [35] J. Dujardin, T. Engl, J. D. Urbina, and P. Schlagheck, “Describing many-body bosonic waveguide scattering with the truncated Wigner method”, *Ann. Phys.* **527**, 629 (2015).
- [36] J. Dujardin, T. Engl, and P. Schlagheck, “Breakdown of Anderson localization in the transport of Bose-Einstein condensates through one-dimensional disordered potentials”, *Phys. Rev. A* **93**, 1 (2016).
- [37] A. R. Kolovsky, and A. Buchleitner, “Quantum chaos in the Bose-Hubbard model”, *Europhys. Lett.* **68**, 632 (2004).
- [38] M. Hiller, T. Kottos, and T. Geisel, “Wave-packet dynamics in energy space of a chaotic trimeric Bose-Hubbard system”, *Phys. Rev. A* **79**, 1 (2009).
- [39] A. C. Cassidy, D. Mason, V. Dunjko, and M. Olshanii, “Threshold for chaos and thermalization in the one-dimensional mean-field Bose-Hubbard model”, *Phys. Rev. Lett.* **102**, 1 (2009).
- [40] A. Kitaev, *Hidden correlations in the hawking radiation and thermal noise*, <https://www.youtube.com/watch?v=0Q9qN8j7EZI>, Talk at Breakthrough Physics Prize Symposium, Nov. 10 2014.

-
- [41] Y. Sekino, and L. Susskind, “Fast scramblers”, J. High Energy Phys. **2008**, 65 (2008).
- [42] S. H. Shenker, and D. Stanford, “Black holes and the butterfly effect”, J. High Energy Phys. **2014**, 67 (2014).
- [43] J. Maldacena, S. H. Shenker, and D. Stanford, “A bound on chaos”, J. High Energy Phys. **2016**, 106 (2016).
- [44] A. I. Larkin, and Y. N. Ovchinnikov, “Quasiclassical Method in the Theory of Superconductivity”, Soviet Physics JETP **28**, 1200 (1969).
- [45] S. H. Shenker, and D. Stanford, “Multiple shocks”, J. High Energy Phys. **2014** (2014).
- [46] G. Zhu, M. Hafezi, and T. Grover, “Measurement of many-body chaos using a quantum clock”, Phys. Rev. A **94**, 062329 (2016).
- [47] B. Swingle, G. Bentsen, M. Schleier-Smith, and P. Hayden, “Measuring the scrambling of quantum information”, Phys. Rev. A **94**, 1 (2016).
- [48] M. Campisi, and J. Goold, “Thermodynamics of quantum information scrambling”, Phys. Rev. E **95**, 062127 (2017).
- [49] M. Garttner, J. G. Bohnet, A. Safavi-Naini, M. L. Wall, J. J. Bollinger, and A. M. Rey, “Measuring out-of-time-order correlations and multiple quantum spectra in a trapped-ion quantum magnet”, Nat. Phys. **13**, 781 (2017).
- [50] J. Li, R. Fan, H. Wang, B. Ye, B. Zeng, H. Zhai, X. Peng, and J. Du, “Measuring out-of-time-order correlators on a nuclear magnetic resonance quantum simulator”, Phys. Rev. X **7**, 1 (2017).
- [51] B. Swingle, “Unscrambling the physics of out-of-time-order correlators”, Nat. Phys. **14**, 988 (2018).
- [52] R. A. Jalabert, and H. M. Pastawski, “Environment-independent decoherence rate in classically chaotic systems”, Phys. Rev. Lett. **86**, 2490 (2001).
- [53] E. B. Rozenbaum, S. Ganeshan, and V. Galitski, “Lyapunov Exponent and Out-of-Time-Ordered Correlator’s Growth Rate in a Chaotic System”, Phys. Rev. Lett. **118**, 086801 (2017).
- [54] D. Bagrets, A. Altland, and A. Kamenev, “Power-law out of time order correlation functions in the SYK model”, Nucl. Phys. B **921**, 727 (2017).
- [55] T. Scaffidi, and E. Altman, *Semiclassical Theory of Many-Body Quantum Chaos and its Bound*, 2017, arXiv:1711.04768.

- [56] E. J. Torres-Herrera, A. M. García-García, and L. F. Santos, “Generic dynamical features of quenched interacting quantum systems: Survival probability, density imbalance, and out-of-time-ordered correlator”, *Phys. Rev. B* **97**, 1 (2018).
- [57] J. Cotler, N. Hunter-Jones, J. Liu, and B. Yoshida, “Chaos, complexity, and random matrices”, *J. High Energy Phys.* **2017**, 48 (2017).
- [58] A. Del Campo, J. Molina-Vilaplana, and J. Sonner, “Scrambling the spectral form factor: Unitarity constraints and exact results”, *Phys. Rev. D* **95**, 1 (2017).
- [59] A. Bohrdt, C. B. Mendl, M. Endres, and M. Knap, “Scrambling and thermalization in a diffusive quantum many-body system”, *New J. Phys.* **19**, 063001 (2017).
- [60] H. Shen, P. Zhang, R. Fan, and H. Zhai, “Out-of-time-order correlation at a quantum phase transition”, *Phys. Rev. B* **96**, 054503 (2017).
- [61] K. Hashimoto, K. Murata, and R. Yoshii, “Out-of-time-order correlators in quantum mechanics”, *J. High Energy Phys.* **2017**, 138 (2017).
- [62] P. Ehrenfest, “Bemerkung über die angenäherte Gültigkeit der klassischen Mechanik innerhalb der Quantenmechanik”, *Zeitschrift für Phys.* **45**, 455 (1927).
- [63] G. Berman, and G. Zaslavsky, “Condition of stochasticity in quantum nonlinear systems”, *Phys. A* **91**, 450 (1978).
- [64] G. Dvali, D. Flassig, C. Gomez, A. Pritzel, and N. Wintergerst, “Scrambling in the black hole portrait”, *Phys. Rev. D* **88**, 124041 (2013).
- [65] S. Tomsovic, and E. J. Heller, “Semiclassical dynamics of chaotic motion: Unexpected long-time accuracy”, *Phys. Rev. Lett.* **67**, 664 (1991).
- [66] I. L. Aleiner, and A. I. Larkin, “Divergence of classical trajectories and weak localization”, *Phys. Rev. B* **54**, 14423 (1996).
- [67] O. Agam, I. Aleiner, and A. Larkin, “Shot Noise in Chaotic Systems: “Classical” to Quantum Crossover”, *Phys. Rev. Lett.* **85**, 3153 (2000).
- [68] M. Sieber, and K. Richter, “Correlations between Periodic Orbits and their Role in Spectral Statistics”, *Phys. Scr.* **T90**, 128 (2001).
- [69] S. Müller, S. Heusler, P. Braun, F. Haake, and A. Altland, “Periodic-orbit theory of universality in quantum chaos”, *Phys. Rev. E* **72**, 046207 (2005).
- [70] P. W. Brouwer, and S. Rahav, “Semiclassical theory of the Ehrenfest time dependence of quantum transport in ballistic quantum dots”, *Phys. Rev. B* **74**, 075322 (2006).

-
- [71] P. Jacquod, and R. S. Whitney, “Semiclassical theory of quantum chaotic transport: Phase-space splitting, coherent backscattering, and weak localization”, *Phys. Rev. B* **73**, 195115 (2006).
- [72] D. Waltner, M. Gutiérrez, A. Goussev, and K. Richter, “Semiclassical mechanism for the quantum decay in open chaotic systems”, *Phys. Rev. Lett.* **101**, 1 (2008).
- [73] J.-D. Urbina, J. Kuipers, S. Matsumoto, Q. Hummel, and K. Richter, “Multiparticle Correlations in Mesoscopic Scattering: Boson Sampling, Birthday Paradox, and Hong-Ou-Mandel Profiles”, *Phys. Rev. Lett.* **116**, 100401 (2016).
- [74] T. Engl, J. D. Urbina, and K. Richter, “Periodic mean-field solutions and the spectra of discrete bosonic fields: Trace formula for Bose-Hubbard models”, *Phys. Rev. E* **92**, 062907 (2015).
- [75] R. Dubertrand, and S. Müller, “Spectral statistics of chaotic many-body systems”, *New J. Phys.* **18**, 033009 (2016).
- [76] M. Akila, D. Waltner, B. Gutkin, P. Braun, and T. Guhr, “Semiclassical Identification of Periodic Orbits in a Quantum Many-Body System”, *Phys. Rev. Lett.* **118**, 164101 (2016).
- [77] S. Tomsovic, P. Schlagheck, D. Ullmo, J.-D. Urbina, and K. Richter, “Post-Ehrenfest many-body quantum interferences in ultracold atoms far out of equilibrium”, *Phys. Rev. A* **97**, 061606 (2018).
- [78] E. Ott, *Chaos in Dynamical Systems* (Cambridge University Press, 1993).
- [79] M. Tabor, *Chaos and Integrability in Nonlinear Dynamics: An Introduction* (Wiley-Interscience, 1989).
- [80] A. M. O. de Almeida, *Hamiltonian Systems: Chaos and Quantization* (Cambridge University Press, 1990).
- [81] M. Turek, “Semiclassics beyond the diagonal approximation”, PhD thesis (Universität Regensburg, 2004).
- [82] P. Gaspard, *Chaos, Scattering and Statistical Mechanics* (Cambridge University Press, 1998).
- [83] M. Fecko, *Differential Geometry and Lie Groups for Physicists* (Cambridge University Press, 2006).
- [84] V. Oseledets, “Oseledets theorem”, *Scholarpedia* **3**, revision #142085, 1846 (2008).
- [85] R. L. Devaney, *Introduction to Chaotic Dynamical Systems* (Benjamin-Cummings Publishing Co., Subs. of Addison Wesley Longman, US, 1986).

-
- [86] S. Wiggins, *Introduction to Applied Nonlinear Dynamical Systems and Chaos* (Springer, 2003).
- [87] J. Banks, J. Brooks, G. Cairns, G. Davis, and P. Stacey, “On Devaney’s Definition of Chaos”, *Am. Math. Mon.* **99**, 332 (1992).
- [88] V. D. Tô, “A Note on Devaney’s Definition of Chaos”, *J. Dyn. Syst. Geom. Theor.* **2**, 23 (2004).
- [89] J. W. Negele, and H. Orland, *Quantum Many-particle Systems* (Taylor & Francis Inc, Nov. 27, 1998), 476 pp.
- [90] H. Bruus, and K. Flensberg, *Many-Body Quantum Theory in Condensed Matter Physics: An Introduction* (Oxford University Press, 2004), 435 pp.
- [91] W. Nolting, *Grundkurs Theoretische Physik 5/1: Quantenmechanik - Grundlagen* (Springer, 2001).
- [92] G. Münster, *Quantentheorie* (Walter de Gruyter, Inc., 2006).
- [93] G. S. Agarwal, *Quantum Optics*, Quantum Optics (Cambridge University Press, 2013).
- [94] C. Gardiner, and P. Zoller, *Quantum Noise* (Springer Berlin Heidelberg, Aug. 27, 2004), 476 pp.
- [95] L. S. Schulman, *Techniques and Applications of Path Integration* (Wiley-VCH, 1996).
- [96] F. Bruckmann, and J. D. Urbina, *Rigorous construction of coherent state path integrals through dualization*, 2018, arXiv:1807.10462.
- [97] H. Kleinert, *Path Integrals in Quantum Mechanics, Statistics, Polymer Physics, and Financial Markets, Third Edition* (World Scientific Publishing Company, 2004).
- [98] H. G. Solari, “Semiclassical treatment of spin system by means of coherent states”, *J. Math. Phys.* **28**, 1097 (1987).
- [99] E. A. Kochetov, “SU(2) coherent-state path integral”, *J. Math. Phys.* **36**, 4667 (1995).
- [100] M. Baranger, M. A. M. de Aguiar, F. Keck, H. J. Korsch, and B. Schellhaaß, “Semiclassical approximations in phase space with coherent states”, *J. Phys. A* **34**, 7227 (2001).
- [101] F. Dalfovo, S. Giorgini, L. P. Pitaevskii, and S. Stringari, “Theory of Bose-Einstein condensation in trapped gases”, *Rev. Mod. Phys.* **71**, 463 (1999).

-
- [102] J. Rammensee, J. D. Urbina, and K. Richter, “Many-Body Quantum Interference and the Saturation of Out-of-Time-Order Correlators”, *Phys. Rev. Lett.* **121**, 124101 (2018).
- [103] D. A. Roberts, and D. Stanford, “Diagnosing Chaos Using Four-Point Functions in Two-Dimensional Conformal Field Theory”, *Phys. Rev. Lett.* **115**, 131603 (2015).
- [104] W. B. Case, “Wigner functions and Weyl transforms for pedestrians”, *Am. J. Phys.* **76**, 937 (2008).
- [105] T. L. Curtright, and C. K. Zachos, “Quantum Mechanics in Phase Space”, *Asia Pacific Phys. Newsl.* **01**, 37 (2012).
- [106] D. J. Luitz, and Y. Bar Lev, “Information propagation in isolated quantum systems”, *Phys. Rev. B* **96**, 1 (2017).
- [107] T. Rakovszky, F. Pollmann, and C. W. von Keyserlingk, “Diffusive Hydrodynamics of Out-of-Time-Ordered Correlators with Charge Conservation”, *Phys. Rev. X* **8**, 031058 (2018).
- [108] Q. Hummel, B. Geiger, J. D. Urbina, and K. Richter, *Reversible quantum information spreading in many-body systems near criticality*, 2018, arXiv:1812.09237.
- [109] M. Turek, and K. Richter, “Leading off-diagonal contribution to the spectral form factor of chaotic quantum systems”, *J. Phys. A* **36**, L455 (2003).
- [110] S. Müller, S. Heusler, P. Braun, and F. Haake, “Semiclassical approach to chaotic quantum transport”, *New J. Phys.* **9**, 1 (2007).
- [111] S. Pappalardi, A. Russomanno, B. Žunkovič, F. Iemini, A. Silva, and R. Fazio, “Scrambling and entanglement spreading in long-range spin chains”, *Phys. Rev. B* **98**, 134303 (2018).
- [112] D. Spohner, “Spectral form factor of hyperbolic systems: leading off-diagonal approximation”, *J. Phys. A* **36**, 7269 (2003).
- [113] I. S. Gradshteyn, and I. M. Ryzhik, *Table of Integrals, Series, and Products*, edited by A. Jeffrey, and D. Zwillinger, Seven, Table of Integrals, Series, and Products Series (Elsevier Science, 2007).
- [114] D. Waltner, *Semiclassical Approach to Mesoscopic Systems* (Springer-Verlag GmbH, 2012).
- [115] P. W. Brouwer, and S. Rahav, “Towards a semiclassical justification of the ‘effective random matrix theory’ for transport through ballistic chaotic quantum dots”, *Phys. Rev. B* **74**, 085313 (2006).

-
- [116] X. Han, and B. Wu, “Ehrenfest breakdown of the mean-field dynamics of Bose gases”, *Phys. Rev. A* **93**, 023621 (2016).
- [117] W. P. Schleich, *Quantum Optics in Phase Space* (Wiley VCH Verlag GmbH, Feb. 9, 2001).
- [118] F. Borgonovi, F. M. Izrailev, and L. F. Santos, “Exponentially fast dynamics of chaotic many-body systems”, *Phys. Rev. E* **99**, 010101 (2019).
- [119] S. Tomsovic, “Complex saddle trajectories for multidimensional quantum wave packet and coherent state propagation: Application to a many-body system”, *Phys. Rev. E* **98**, 023301 (2018).
- [120] J. Kurchan, “Quantum Bound to Chaos and the Semiclassical Limit”, *J. Stat. Phys.* **171**, 965 (2018).
- [121] O. Yevtushenko, G. Lütjering, D. Weiss, and K. Richter, “Weak Localization in Antidot Arrays: Signature of Classical Chaos”, *Phys. Rev. Lett.* **84**, 542 (2000).
- [122] P. W. Brouwer, “Semiclassical theory of the Ehrenfest-time dependence of quantum transport”, *Phys. Rev. B* **76**, 165313 (2007).
- [123] R. Peierls, “Zur Theorie des Diamagnetismus von Leitungselektronen”, *Zeitschrift für Phys.* **80**, 763 (1933).
- [124] J. Dujardin, A. Argüelles, and P. Schlagheck, “Elastic and inelastic transmission in guided atom lasers: A truncated Wigner approach”, *Phys. Rev. A* **91**, 1 (2015).
- [125] T. Paul, M. Albert, P. Schlagheck, P. Leboeuf, and N. Pavloff, “Anderson localization of a weakly interacting one-dimensional Bose gas”, *Phys. Rev. A* **80**, 1 (2009).
- [126] M. G. Da Luz, E. J. Heller, and B. K. Cheng, “Exact form of Green functions for segmented potentials”, *J. Phys. A* **31**, 2975 (1998).
- [127] B. L. Altshuler, D. Khmel'nitzkii, A. I. Larkin, and P. A. Lee, “Magnetoresistance and Hall effect in a disordered two-dimensional electron gas”, *Phys. Rev. B* **22**, 5142 (1980).
- [128] S. Datta, *Electronic Transport in Mesoscopic Systems* (Cambridge University Press, Sept. 15, 2014), 396 pp.
- [129] P. B. Blakie, A. S. Bradley, M. J. Davis, R. J. Ballagh, and C. W. Gardiner, “Dynamics and statistical mechanics of ultra-cold Bose gases using c-field techniques”, *Adv. Phys.* **57**, 363 (2008).

-
- [130] M. J. Steel, M. K. Olsen, L. I. Plimak, P. D. Drummond, S. M. Tan, M. J. Collett, D. F. Walls, and R. Graham, “Dynamical quantum noise in trapped Bose-Einstein condensates”, *Phys. Rev. A* **58**, 4824 (1998).
- [131] T. Wellens, “Nonlinear coherent backscattering”, *Appl. Phys. B* **95**, 189 (2009).
- [132] T. Geiger, A. Buchleitner, and T. Wellens, “Microscopic scattering theory for interacting bosons in weak random potentials”, *New J. Phys.* **15** (2013) <http://dx.doi.org/10.1088/1367-2630/15/11/115015>.
- [133] T. Engl, P. Plöchl, J. D. Urbina, and K. Richter, “The semiclassical propagator in fermionic Fock space”, *Theor. Chem. Acc.* **133**, 1563 (2014).
- [134] T. Engl, J. D. Urbina, K. Richter, and P. Schlagheck, “Many-body spin echo”, *Phys. Rev. A* **98**, 013630 (2018).
- [135] F. Haehl, R. Loganayagam, P. Narayan, and M. Rangamani, “Classification of out-of-time-order correlators”, *SciPost Phys.* **6**, 001 (2019).
- [136] G. C. Wick, “The Evaluation of the Collision Matrix”, *Phys. Rev.* **80**, 268 (1950).
- [137] M. E. Peskin, and D. V. Schroeder, *Introduction To Quantum Field Theory* (Perseus Books Group, 1995), 864 pp.
- [138] L. Diósi, “Wick theorem for all orderings of canonical operators”, *J. Phys. A* **51**, 365201 (2018).
- [139] S. Müller, “Periodic-Orbit Approach to Universality in Quantum Chaos”, PhD thesis (Universitaet Duisburg-Essen, Sept. 2005), p. 165, [arXiv:0512058 \[nlin\]](https://arxiv.org/abs/0512058).

Acknowledgments

“The whole is more than just the sum of its parts” – this sentence is most certainly true when reviewing the experience I had when working in the group of Prof. Dr. Klaus Richter for the last years. The very pleasant and stimulating atmosphere in this group is the result of the cooperative attitudes shown by its members. I truly believe that without this environment, this thesis would not have been possible. Upon its completion, I would therefore like to express my gratitude to all the people which supported me over the years.

On top of all, I would like to thank my supervisor Prof. Dr. Klaus Richter for giving me the opportunity to be part of this group, and for being the character he is, the center of the group’s atmosphere. During my time as a PhD student it was him, who gave me valuable guidance and helpful suggestions whenever I needed those.

Many thanks also go to Juan-Diego Urbina for all the help he provided, for all the discussions about physics (and non-physics) we had and for all the motivating words, when those are needed. I was very lucky to be able to work with him. I highly appreciate the efforts he went through in proof-reading almost the complete thesis. Many thanks go also to the rest of the current and former members of the semiclassical gang, Remy Dubertrand, Thomas Engl, Benjamin Geiger, Quirin Hummel, Jack Kuipers, Camilo-Alfonso Moreno-Jaimes, as well as Fabian Stöger and Dominik Vierl for the opportunity of working with them and for all the discussion which helped enlighten the field for me.

I am grateful to Prof. Dr. Schlagheck for inviting me to Liège to directly work with Renaud Chrétien and Cyril Petitjean on a very intriguing problem. I felt very welcome in Belgium, thanks to them.

For proofreading parts of the thesis I want to say thanks to Raphael Kozlovsky, Juan-Diego Urbina, Remy Dubertrand and Dominik Vierl.

Working as one of the system administrators over the years, I also joined forces with many colleagues who helped with the daily struggle in IT. Many thanks go to Jan Bundesmann, Sven Essert, Jacob Fuchs, Tobias Frank, Raphael Kozlovsky, Viktor Krückl, Lisa Hesse, and the crew of admins of the chairs Grifoni and of the particle physics department, and thanks for sparing me from most of the admin work during the time of intense writing. For helping with the tough cases, I am very thankful to have Michael Hartung as the person to call in the computer center.

Finally, my thanks goes to the complete group of the chairs Richter and Fabian, for providing the stimulating atmosphere I experienced in this group. I grew friend with many of their members over the years, and I hope that this friendship will last for year.

Not gratitude, but love goes to my parents Johann and Emma Michl, and especially to my wife Heike for their support and their patience with me, especially during the last weeks of writing this thesis. Thanks for just being there.

Index

- AAS, *see* Al'tshuler-Aronov-Spivak
- AB, *see* Aharonov-Bohm
- Aharonov-Bohm oscillations, 86
- Al'tshuler-Aronov-Spivak oscillations, 86
- annihilation operator
 - commutation relation, 32
- annihilation operator
 - definition, 31
- BEC, *see* Bose-Einstein-condensate
- Bose-Einstein condensate, 86
- Bose-Hubbard models
 - definition, 39
- boundary problem, 16
- chaos
 - definition, 25
- coherent states, 37
- configuration space, 15
- constant of motion
 - definition, 23
 - global, 23
- creation operator
 - commutation relation, 32
 - definition, 31
- current density, 92
- disorder
 - average, 96
 - correlation length, 89
 - Gaussian correlated, 89
- Ehrenfest time, 64
- encounter region
 - encounter time, 65
 - stable time, 65
 - time-reversal symmetry, 81
 - unstable time, 65
- encounter regions, 60
- ergodic phase space average, 69
- ergodicity, 27
- finite differences, 88
- Fock space, 31
- Fock state
 - definition, 30
 - quadrature state representation, 37
- functional independence, 23
- Green's function, 94
 - free, 94
 - scattering paths, 95
- Gross-Pitaevskii equation, 49, 90
- Hamilton function, 15
- Hamilton's equation of motion, 16
- Hamilton's principal function, 17
- harmonic oscillator
 - ladder operators, 33
- harmonic oscillator, 33
 - classical limit, 34
- hyperbolic dynamics
 - definition, 27
 - uniformly, 27
- initial value problem, 16
- invariant measure, 25
- involution, 23
- local stretching rate, 20
- Lorentz gas, 84
- Lyapunov exponent

- definition, 19
 - pairing rule, 22
 - spectrum, 78
 - spectrum , 19
- Lyapunov time, 27
- mean-field equation, 49, 90
 - stationary, 91
- mixing, 26
- multiplicative cocycle, 19
- neutral direction, 20
 - relation to constants of motion, 25
- number state, *see* Fock state
- occupation number representation, *see*
 - second quantization
- OTOC
 - billiard, 84
 - definition, 51
 - diagrams
 - zero-leg, 61
 - short-time limit, 55
 - squared commutator, 52
- out-of-time-order-correlator, *see* OTOC
- particle current density, 92
- Peierl's phase, 88
- phase space
 - definition, 16
 - point, 16
 - variables, 16
- Poisson bracket, 23, 54
- propagator
 - definition, 41
 - path integral representation, 46
 - semiclassical approximation, 49
- quadrature
 - operators, 34
- Quantum Chaos, 8
 - many-body, 9
- reflection
 - amplitude, 92
 - probability, 92
- scattering paths, 95
- second quantization, 30
- semigroup property, 41
- Si
 - seesine integral, 69
- sine integral, 69, 147
- Solari-Kolchetov phase, 49
- source
 - current density, 93
 - particle density, 93
- stability matrix
 - definition, 18
- stability matrix
 - equations of motion, 19
 - formal solution, 19
 - inverse, 21
- stable direction, 20
- star product, 53
- stationary phase approximation
 - stationarity condition, 46
 - stationarity point, 46
- stationary phase approximation, 46
- symplectic structure
 - fundamental matrix, 16
- time evolution operator, 40
- time-ordered exponential, 19, 41
- trajectory, 16
- transmission
 - amplitude, 92
 - probability, 92
- truncated Wigner approximation, 102
- unstable direction, 19
- Wigner function, 53, 102